Manfred Nachtnebel, Mag. rer. nat, Bakk. rer. nat.

In situ experiments with polymeric materials in the environmental scanning electron microscope

DOCTORAL THESIS

to achieve the university degree of

Doktor der technischen Wissenschaften

Submitted to

Graz University of Technology

Supervisor:

Dipl.-Ing., Dr.techn. Univ.-Doz., Peter Pölt

Co-Supervisor:

Dipl.-Ing. Dr. Armin Zankel

Institute of Electron Microscopy and Nanoanalysis (FELMI)

Graz, March 2017

¡Viva la vida!

AFFIDAVIT

I declare that I have authored this thesis independently, that I have not used other than the declared sources/resources, and that I have explicitly indicated all material which has been quoted either literally or by content from the source used. The text document uploaded to TUGRAZonline is identical to the present doctoral thesis.

_____ _____

Date Signature

EIDESSTATTLICHE ERKÄRUNG

Ich erkläre an Eides statt, dass ich die vorliegende Arbeit selbstständig verfasst, andere als die angegebenen Quellen/Hilfsmittel nicht benutzt, und die den benutzten Quellen wörtlich und inhaltlich entnommenen Stellen als solche kenntlich gemacht habe. Das in TUGRAZonline hochgeladene Textdokument ist mit der vorliegenden Dissertation identisch.

_____ _____

Datum Unterschrift

Kurzfassung

Die vorliegende Doktorarbeit behandelt zwei Themen, die *in situ* Charakterisierung von Mikrofiltrationsmembranen und das Bruchverhalten von modifiziertem Polypropylen basierend auf der 3D-Rekonstruktion der beschädigten Region. In beiden Fällen besteht das untersuchte Material aus Polymeren, wobei das Niederdruck Rasterelektronenmikroskop (Engl. ESEM: environmental scanning electron microscope) hierbei als Hauptuntersuchungsgerät eingesetzt wird. Dieses spezielle Mikroskop wurde gewählt, weil es die Abbildung von elektrisch nichtleitenden Proben erlaubt. Diese können somit mit hoher Vergrößerung und großer Schärfentiefe aufgenommen werden, ohne dass eine leitfähige Schicht auf der Probenoberfläche aufgebracht werden muss. Des Weiteren erlaubt es Untersuchungen an feuchten Proben und daher auch die Analyse der Interaktion zwischen Wasser und unterschiedlichen Materialien. Im Allgemeinen ermöglicht es die Realisierung von dynamischen Untersuchungen und zusätzlich die simultane Messung und damit auch die Korrelation zwischen gemessenen makroskopischen und mikroskopischen Parametern und den mikroskopischen Strukturen des Materials. Diese Strukturen können einerseits schon im Material vorhanden sein oder sich während des physikalischen oder chemischen Untersuchungsverlaufes ausbilden.

Der erste Teil beschäftigt sich mit asymmetrischen mehrschichtigen Mikrofiltrationsflachmembranen, welche aus einer Mischung von Polyethersulfon und Polyvinylpyrrolidon bestehen, und deren Schädigung durch eine chemische Behandlung. In Wasserreinigungsanlagen aber auch bei industriellen Anwendungen werden diese Membranen regelmäßig mit unterschiedlichen Chemikalien gereinigt und desinfiziert, um eine Langzeitnutzung zu gewährleisten. Untersuchungen haben ergeben, dass die Chemikalien neben dem reinigenden Effekt auch das Membranmaterial schädigen und somit deren Effizienz über die Zeit senken können. Aber die meisten gebräuchlichen Untersuchungsmethoden, wie der Vergleich der Reinwasser-Durchlässigkeit von ungebrauchten und chemisch behandelten Proben, liefert nur einen generellen Überblick über die Membranschädigung über das gesamte Membranvolumen. Sie liefern daher keine Information darüber, welche Schicht bei einer mehrschichtigen Membran am stärksten geschädigt wird. Dies ist aber für deren Design und Weiterentwicklung wichtig. Um diese ortsaufgelöste Information zu erhalten wurde in das ESEM eine speziell entwickelte Kühlbühne eingesetzt, welche eine *in situ* Befeuchtung und Trocknung ermöglicht. Diese erlaubt eine simultane Aufnahme von hoch aufgelösten Bildern, von entweder einer der beiden Membranoberflächen oder deren Querschnitt, und der Messung der Temperaturprofile beider Membranoberflächen durch hochpräzise Thermoelemente während des gesamten Befeuchtungs- und Trocknungsprozesses. Die Korrelation von allen während der Versuche aufgenommenen Parametern liefert neue Informationen über die Interaktion zwischen dem Wasser und den Membran- und Porenwänden in den verschiedenen Schichten. Die Untersuchungen zeigten, dass durch die chemische Behandlung hauptsächlich die Membranoberfläche angegriffen wird und nicht so sehr die eigentliche Filtrationsschicht.

Dieses Ergebnis konnte durch zwei weitere Messmethoden bestätigt werden. Die Erste war ortsaufgelöste Transmissions-IR-Spektroskopie, welche es erlaubt die Verteilung von Polyethersulfon und Polyvinylpyrrolidon über den Querschnitt hochaufgelöst darzustellen. Diese Verteilungen liefern aber nur Flächeninformationen, während die Befeuchtungs- und Trocknungsversuche ein größeres Volumen miteinbeziehen und daher eine größere

statistische Signifikanz aufweisen. Die zweite Methode umfasste die kapillare Einsaugung von Wassertropfen an der Membranoberfläche. Hierbei wird ein Wassertropfen auf die Oberfläche aufgebracht und die Zeit, welche für die Einsaugung benötigt wird, mittels Videoaufnahme gemessen.

Ein Verlust der hydrophilen Eigenschaften direkt an der Oberfläche, aufgrund der Abnahme der Polyvinylpyrrolidon-Konzentration der Polymermischung, konnte für die Schädigung der behandelten Membranen verantwortlich gemacht werden. Die Ergebnisse ergaben auch, dass eine höhere Konzentration der eingesetzten Chemikalien eine stärkere Schädigung hervorrief, als eine höher angesetzte Behandlungsdosis (Konzentration · Zeit) bei niedrigerer Konzentration. Des Weiteren wurde verifiziert, dass auch die verwendeten Chemikalien einen großen Einfluss auf die Membranschädigung haben.

Der zweite Teil der Doktorarbeit behandelt die physikalischen Auswirkungen auf Polymere durch mechanische Beanspruchung. Zu diesem Zwecke wurden drei verschiedene Mischungen mit einer Polypropylen (PP) Matrix Zugversuchen mittels einer Zugbühne unterzogen, welche in der Probenkammer des ESEM montiert werden kann. Dies erlaubt bereits die Beobachtung der sich ausbildenden mikroskopischen Strukturen am Rissende und deren Fortpflanzung während des Zugversuches. Dennoch können damit nur Oberflächenstrukturen beobachtet werden, wohingegen keine Informationen über die Rissbildung, das Risswachstum und die Rissfortpflanzung innerhalb der Matrix erhalten werden können. Des Weitern sind die meisten mikroskopischen Untersuchungen von Polymerbrüchen beschränkt auf Aufnahmen der Rissoberfläche, nachdem die Probe komplett durchgerissen wurde. Aber von solchen Aufnahmen lassen sich schwer Aussagen treffen, welche mikroskopischen Prozesse nun hauptsächlich für die Bruchbildung verantwortlich sind und welche eventuell ein die Rissausbreitung hemmen. Um beide Probleme zu lösen, wurden alle Proben, nachdem die Zugversuche bei einer vordefinierten Kraft weit unter dem Maximum der Kraft (Engl.: Yield) angehalten wurden, mittels *In situ* Ultramikrotomie (Engl. SBEM: serial block-face scanning electron microscopy) präpariert. Diese Technik ermöglicht eine 3D Rekonstruktion der schon geschädigten Region. Da es sich bei den Proben um Modifizierungen von PP mit entweder EPR-Teilchen (Engl.: ethylene propylene rubber) oder LLDPE-Teilchen (Engl.: linear low density polyethylene) handelt, waren die wesentlichen Parameter einerseits die Größe, Form und Verteilung dieser Füllstoffpartikel und andererseits die Größe und Verteilung der Risse welche sich während der Zugversuche gebildet haben. Deren Rekonstruktion liefert Informationen über die räumliche Beziehung beider Strukturen, der Teilchen und Risse. Ein theoretischer Lösungsansatz basierend auf experimentellen Untersuchungen, welche bereits 1985 ausgeführt wurden, ergab, dass der Abstand (Oberfläche zu Oberfläche) zwischen den Teilchen in Teilchen-modifizierten Polymeren festlegt, ob sich die Mischung zäh oder spröde verhält. Diese Theorie ist nun stark umstritten. Aber theoretische Berechnungen zeigten auch, dass die Spannungskonzentration zwischen den Teilchen stark überhöht ist, wenn der Abstand zwischen den Teilchen kleiner ist der doppelte Partikeldurchmesser. Also Resultat sollten sich Risse vorzugsweise in Regionen mit kleinem Teilchenabstand ausbilden.

Die Experimente zeigten bei den Zugtests ein komplett unterschiedliches Rissverhalten der EPR- und LLDPE modifizierten PP-Proben. Während sich in der EPR modifizierten Probe sich weit ausbreitende Risse in der PP-Matrix ausbildeten, konnte bei der zweiten Mischung eine Ablösung der LLDPE-Partikel von der Matrix als Hauptschädigungsmechanismus festgestellt

werden. Des Weiteren wurden bei der LLDPE-modifizierten Probe nur sehr schmale, senkrecht zur Zugrichtung verlaufende, Regionen beschädigt. Das 3D-Abstandsfeld der Füllstoffteilchen, berechnet aus den 3D-Rekonstruktionen der Füllstoffteilchen, wurde benutzt um die dreidimensionale Verteilung der Teilchenabstände zu bestimmen. Es zeigte sich, dass sowohl für runde als auch ellipsenförmige EPR-Teilchen sich die Risse vorzugsweise in Regionen mit hoher Teilchenkonzentration befinden, d.h. Regionen mit kleinem Teilchenabstand. Dementsprechend scheint der Teilchenabstand ein wichtiger Parameter zu sein, welcher die Rissbildung, das Risswachstum und die Rissausbreitung beeinflusst, zumindest bei Kräften weit unterhalb des Yield. Andererseits führte in den LLDPE-modifizierten Proben die Ablösung der Teilchen von der Matrix zu Hohlräume in der Probe. Nicht überraschend bildeten sich große Hohlräume, deren Durchmesser jene der Teilchen deutlich übersteigen konnten, bevorzugt in Regionen mit hoher Partikelkonzentration aus. Zusätzlich konnte eine Scherung der elliptischen LLDPE Partikel in den geschädigten Bereichen beobachtet werden. Der Partikelabstand scheint daher bei beiden Modifikationen ein entscheidender Parameter für den Ablauf des Bruchverhaltens des Materials zu sein.

Abstract

This thesis deals with two different topics, the *in situ* characterisation of polymeric microfiltration membranes and the fracture behaviour of modified polypropylene based on 3D reconstructions of the damaged regions. In both cases the materials investigated were polymers, and the environmental scanning electron microscope (ESEM) played an essential role in the investigations. This special microscope was chosen because it enables the imaging of the surfaces of non-conductive samples at high magnification and great depth of focus without the need for a conductive coating. Furthermore it facilitates the investigation of wet samples and thus the study of the interaction of water with solids. More generally it enables the realisation of *in situ* investigations, which can provide a correlation between measured macroscopic parameters and characteristics and microscopic structures, both already present in the material but also developing during the progress of physical or chemical processes.

The first topic concerns asymmetrically layered flat sheet microfiltration membranes, consisting of a blend of polyethersulfone and polyvinylpyrrolidone, and their response to chemical treatments. In industrial applications of these membranes various chemicals are typically used to regularly clean and disinfect the membranes for long term use. Nevertheless, different studies have shown that besides the cleaning effect, these chemicals also damage the membrane material, thus lowering membrane performance over time. But most customary investigation methods like comparisons of the pure water permeability of pristine and chemically treated membrane samples provide only a general overview of membrane degradation integrated over the whole membrane volume. Thus they give no information about the membrane layer of a multilayered membrane in which the degradation mainly occurred. But this is important for the design and development of new membranes. To gain this spatially resolved information, a specially designed and home-made cooling stage was used enabling *in situ* wetting and drying of the membranes. It allows the simultaneous recording of high resolution images of either one membrane surface or its cross-section and the measurement of temperature profiles at both membrane surfaces using two high precision thermocouples during the whole wetting and drying cycle. The correlation of all the parameters obtained in these experiments provides new information about the interaction between water and the pore walls in the different membrane layers. The investigations revealed that the major changes in the membrane material caused by the chemical treatment occurred directly at the membrane surface and not in the separation layer.

This finding was verified and confirmed by two other methods. The first one was spatially resolved transmission IR-spectroscopy, which allowed the distribution of both polyethersulfone and polyvinylpyrrolidone to be mapped across the cross-sections of the membranes. But these maps provide only areal information, whereas the wetting and drying experiments involve a large volume and the results thus have a higher statistical significance. The second method involved water droplet imbibition tests at the membrane surfaces, applying water droplets onto the membrane surface and measuring the time it took them to be absorbed by the membrane by video recording.

A loss in hydrophilicity directly at the surface, caused by a decrease in the polyvinylpyrrolidone concentration, was found to be responsible for the degradation of the treated membranes. The results also proved that a higher concentration of the chemical agent caused a higher membrane degradation than a higher treatment dose (concentration · time)

at a lower concentration. The type of chemical used also had a great influence on membrane degradation.

The second topic of this thesis focuses on the physical impact of an applied force on a polymeric material. To this aim, three different blends with a polypropylene (PP) matrix were subjected to a tensile test at a stage mounted in the specimen chamber of an ESEM. This already enables the observation of the microscopic structures forming at the crack tip and their evolution during the progress of the tensile test. Nevertheless, only the surface structure can be observed, while no information can be gained about the crack initiation, the crack growth and propagation in the bulk of the material. Also most of the microscopic investigations of polymer fracturing are restricted to the imaging of the fracture surface after the sample has completely fractured. But from such images it is difficult to conclude which microscopic processes were mainly responsible for the fracturing and which may even tend to prevent crack growth. To cope with both problems, the samples were sectioned by serial block-face scanning electron microscopy (SBEM) after stopping the tensile test at a predefined force far below the yield. This technique enables the 3D reconstruction of the already damaged regions. As the samples were PP modified by either ethylene-propylene rubber (EPR) or linear low density polyethylene (LLDE) particles, the features of interest were the size, shape and distribution of the filler particles, and the size and distribution of the cracks and crazes caused by the tensile tests. The reconstruction provides information about the spatial relationship between the two features, the particles and cracks. A theoretical approach based on experimental investigations performed as early as 1985 states that the interparticle (surface to surface) distance in particle modified polymers is the main parameter that determines whether a polymer blend will be tough or brittle. This theory is now strongly contested. But theoretical calculations also show that stress concentration is strongly increased if the distance between the particles is smaller than twice the particle diameter. As a result, cracks / crazes should preferentially be formed in regions with small interparticle distances.

In our experiments a completely different fracture behaviour between the PP samples modified with EPR and those modified with LLDPE particles was found after performance of the tensile tests. Whereas widespread cracks / crazes formed inside the PP matrix blended with EPR, debonding of the particles from the matrix was identified as the main damage mechanism in the LLDPE modified samples. And also in the latter case only small straight regions perpendicular to the applied force were damaged. The 3D distance field of the particles, calculated by use of the 3D reconstruction of the filler particles, was used as a measure for the interparticle distance distributions. It became definitely apparent for both spherical as well as for elongated EPR particles that the cracks were preferentially located in regions with higher particle concentrations, i.e. with short interparticle distances. Thus the interparticle distance seems to be a very important parameter governing both crack growth and crack propagation, at least at stresses below the yield. Particle debonding caused the formation of voids in LLDPE modified PP. Not surprisingly, large voids with diameters exceeding the particle diameter emerged preferentially in regions with high particle concentrations. Additionally, at the deformed regions a shearing of the elongated LLDPE particles was observed. The interparticle distance may thus for both modifications be a vital parameter determining the fracture behaviour of the respective material.

Danksagung

Auf dieser Seite möchte ich mich bei allen bedanken, ohne die es mit Sicherheit sehr viel schwieriger gewesen wäre diese Dissertation fertigzustellen. Auch wenn diese Danksagung eventuell nach einer Reihung aussehen möge, möchte ich gleich vorwegnehmen, dass dies nicht der Fall ist. Alle haben mich auf unterschiedlichste Art und Wiese unterstützt, mich in meinen letzten Jahren begleitet/geleitet/unterhalten/motiviert/geprägt, sodass ich allen meinen gleich großen Dank aussprechen möchte!

Dir Peter, möchte ich vor Allem für deinen wissenschaftlichen wie auch sprachlichen Input und deine fortwährende Unterstützung danken. Ohne Ersteren wären viele Arbeiten und Untersuchungen sicher nicht so wunderbar verlaufen, wie sie es schlussendlich alle sind. Auch für den wissenschaftlichen Freiraum, den du mir stets gelassen hast, um mich in dieser Arbeit einzubringen und zu verwirklichen möchte ich dir danken. Für die Möglichkeit am FELMI-ZFE diese Tätigkeiten auszuführen, möchte ich Ferdinand danken, welcher es mir mit bedachten Worten sogar ermöglicht hat, ein viertes Jahr an diesem wunderbaren Institut mitzuarbeiten. Armin, bei dir möchte ich mich besonders für dein stets offenes Ohr und deine fantastische Unterstützung bei all meinen Arbeiten bedanken. Deine wunderbare Art, gewisse Dinge anzugehen bzw. auch kritisch zu hinterfragen, hat sehr zum wissenschaftlichen Erfolg dieser Arbeit, als auch zum Wohlfühl-Faktor hier am Institut beigetragen. Dir Claudia, möchte ich für deine Beharrlichkeit, Geduld sowie den fantastischen Einfällen bei der Probenpräparation danken. Für die wunderbare Zeit am Institut, mitten und auch fernab der Arbeit möchte ich hier stellvertretend meinen BürokollegInnen danken: Beginnend bei Toni, Steffi, Arno über Dani, Luki und Georg, welche nicht nur für das wunderbare Büroklima und die Unterhaltung, sondern auch bei schnellen Fragen für gute Antworten sorgten. An dieser Stelle möchte ich mich bei der ganzen FELMI-ZFE Crew für deren nette und unkomplizierte Art mir weiter zu helfen bedanken, welche mir viele Arbeiten sehr erleichtert hat.

Familiär möchte ich mich bei meiner Weggefährtin Laura bedanken. Vor allem für deine herrliche Art, sowie deinem Verständnis, wenn die Arbeit ab und zu einmal etwas länger gedauert hat als ursprünglich geplant. Auch meinen Eltern Johanna und Manfred möchte ich an dieser Stelle danken, denn ohne eure Hilfe und ständige Unterstützung wäre ich sicherlich nicht hier wo ich jetzt bin. Bei meinen Geschwistern und Freunden möchte ich mich für die wunderbare Zeit außerhalb der Arbeit bedanken, aber auch für den einen oder anderen Denkanstoß, welcher sich bei den Diskussionen am Feierabend ergeben hat.

¡Vlv! MGN

Abbreviations

2D	Two dimensions
3D	Three dimensions
.OH	Hydroxyl radicals
ADC	Area difference coefficient
ATR	Attenuated total reflectance
AV	Acceleration voltage
BSE	Backscattered electrons
C-SEM	Conventional -scanning electron microscope
CA	Citric acid
CLAHE	Contrast limited adaptive histogram equalization
CPU	Central processing unit
EDT	Euclidean distance transformation
EDS	Energy dispersive X-ray spectroscopy
EDX	Energy dispersive X-ray
EPR	Ethylene-propylene rubber
ESEM	Environmental scanning electron microscope
FD	Flow direction
FEC	Fractional equivalent coefficient
FEG	Field emission gun
FFT	Fast Fourier transform
FT-IR	Fourier transform-infrared spectroscopy
GT	Ground truth
iPP	Isotactic polypropylene
LLDPE	Linear-low density polyethylene
MFI	Melt flow index
NaClO	Sodium hypochlorite
NaOH	Sodium hydroxide
NLM	Non-local mean
PES	Polyethersulfone
PLA	Pressure limiting aperture
PLS	Pressure limiting system
PVP	Polyvinylpyrrolidone
RAM	Random access memory
RuO4	Ruthenium tetroxide
SBEM	Serial block-face scanning electron microscopy
SE	Secondary electrons
SEM	Scanning electron microscope
SS	Spot size
TEM	Transmission electron microscope
WD	Working distance
WEKA	Waikato Environment for Knowledge Analysis

Motivation

The usage of polymers is very common in nearly every field of application due to their high physical and chemical resistivity. But investigations on such soft materials are often based on macroscopic parameters such as results obtained from stress-strain tests. Hence the results mostly yield characteristics which are integrated over the cross-section of the sample. More sophisticated techniques are required to obtain detailed knowledge of different internal or spatially resolved processes. This thesis investigates two different processes for two different polymeric materials.

The first investigation addresses flat sheet microfiltration membranes and the spatially resolved analysis of the impact of typical cleaning and disinfection agents. These membranes are mainly made of polyethersulfone (PES) and are modified with polyvinylpyrrolidone (PVP) to make them more hydrophilic. Because of their different fields of application they must be regularly cleaned to preserve their efficiency. Previous studies found a decrease in membrane performance after such treatments and attributed this among other causes to PVP degradation [1], [2]. The results gave a comprehensive insight into the overall degradation mechanism caused by the usage of chemicals. These studies did not, however, demonstrate whether this degradation is homogenous over the whole cross-section or is concentrated in a specific region. To overcome this issue a new investigation method was thus used which enables the *in situ* wetting and drying of the membrane inside an environmental scanning electron microscope (ESEM). The combination of the simultaneously recorded microscopic and macroscopic parameters enables to obtain spatially resolved results. Hence it is possible to investigate the membrane property changes after different membrane treatments.

The second topic focuses on the investigation of the fracture behaviour of isotactic polypropylene (iPP) modified with ethylene-propylene rubber (EPR) or linear-low density polyethylene (LLDPE). The former blend is used, e.g., in the automotive industry [3]. Its resistance to physical impacts was tested with different macroscopic methods such as the previously mentioned tensile tests. Also *in situ* tensile tests inside an ESEM only reveal high resolution images of the crack tip and do not provide an insight into the material and the cracks formed there. But the information of the spatial relationship between the filler particles and the cracks can lead to a better understanding of the mechanisms of crack formation in such blends. Therefore, serial block face scanning electron microscopy (SBEM) was used to obtain 3D reconstructions of the filler particles and cracks formed after a tensile test. This leads to new information about the distribution, distance and geometry of the filler particles and cracks.

Table of contents

1. The environmental scanning electron microscope

Since the introduction of scanning electron microscopes (SEM) in the 1960s many different types have become available which can be operated under different conditions. A conventional SEM (C-SEM) operates under high vacuum at a pressure below 10^{-4} Torr to avoid electron scattering inside the electron column and specimen chamber. Therefore, the specimen must be vacuum friendly, i.e. it should not contain volatiles. This restricts the types of samples that can be investigated, to e.g. wet, biological or degassing materials. This limitation can be overcome by the use of a higher pressure range inside the specimen chamber. In the 1940s Ardenne and D. Beischer published [4] a new method for examining samples inside an electron microscope under atmospheric gas or water vapour. In the following decades the instruments and techniques were substantially extended and improved. The pressure in the specimen chamber of modern environmental scanning electron microscopes (ESEM[1]) can be up to 20 Torr, whereas a high vacuum is still present in the probe forming electron column. A pressure limiting system (PLS) must be used to maintain this pressure difference. This system can, e.g., consist of pressure limiting apertures (PLA) and a differential pumping system [5]. A schematic of such a system can be seen in Fig. 1. Different gases can be employed in the specimen chamber. The limitations here are mostly due to practical reasons, e.g. they must be non-toxic, inflammable and non-reactive with the ESEM's components. The usage of suitable gases has two main advantages: the compensation of negative charging by positive gas ions at non-conductive sample surfaces and the possibility to investigate wet samples or even liquids. In general, the pressure range inside the specimen chamber is varied between 0.1 Torr and 10 Torr. The usage of higher pressures is generally avoided, because a strong increase in electron scattering causes a likewise strong decrease of the signal-to-noise ratio, as most of the electrons are scattered. The usage of a cooling system and water vapour as the chamber gas, however, enables the investigation of wet samples. This option makes the ESEM highly interesting for *in situ* experiments, e.g. dynamic wetting and drying of different kinds of materials. A cooling stage is necessary to avoid condensation of water vapour at the chamber walls and the detectors. Unless otherwise indicated, the main literature source used for this section is the book by Stokes [6].

Commercially available accessories additionally allow the recording of various microscopic as well as macroscopic parameters and characteristics. Examples include tensile stages, heating or cooling stages or the *in situ* ultramicrotome for 3D reconstructions, to name just a few [7]–[10]. Additional home-made experimental setups enable the study of specific reactions, such as the controlled wetting of cellulose fibres or the measurement of the osmotic pressure of single yeast cells [11].

[1] The term ESEM is a brand of the manufacturer FEI (Eindhoven, the Netherlands) and will be used in this thesis as the general term for SEMs which can be operated at higher specimen chamber pressure than high vacuum (e.g. VP-SEM (variable-pressure SEM) by Zeiss AG (Oberkochen, Germany) or LVSEM (low vacuum SEM) by JEOL Ltd. (Akishima, Japan)).

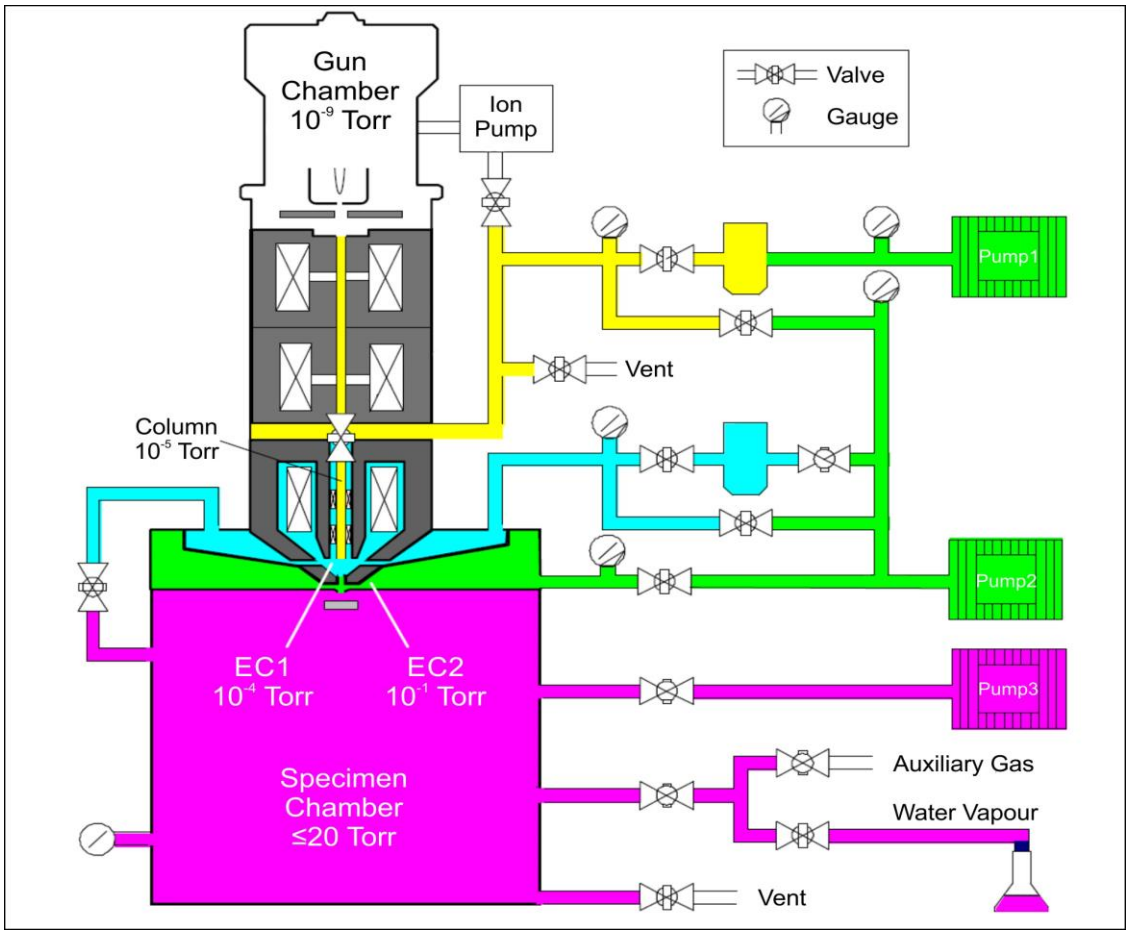

Fig. 1: Schematic of the vacuum system of an ESEM (first environmental chamber (EC1) and second environmental chamber (EC2)); adapted from [12].

The present work was carried out using a Quanta 600 ESEM (FEI, Eindhoven, the Netherlands) equipped with a field emission gun (FEG). This instrument allows samples to be investigated in the conventional high vacuum mode (≤10^{-4} Torr), the low vacuum mode (pressure range from 0.1 Torr to 1 Torr) or the ESEM mode with a chamber pressure up to 20 Torr [12]. Fig. 1 demonstrates that the pressure continuously decreases from the specimen chamber up to the gun chamber (electron source) with pressures down to approximately 10^{-9} Torr. This high vacuum is necessary to prevent scattering of the primary beam electrons at gas atoms or molecules in the microscope column and keep them focused. Also, a gas present in the gun could be ionised due to high local electric fields, which could lead to electrostatic discharges and thus cause damage. But as mentioned above, the usage of a PLS makes it possible that the pressure inside the specimen chamber can be much higher than in the other parts of the microscope.

The gas in the specimen chamber has positive as well as negative effects, which must be taken into account. One of the positive effects is the charge compensation at the surface of electrically non-conductive materials. These materials are negatively charged by primary electron irradiation and the missing charge carrier transport to mass. But as schematically shown in Fig. 2, this negative charge can be compensated by the positively charged gas ions generated by the collisions of primary electrons with gas atoms and the resulting ionisation of

these gas atoms. This enables direct imaging of non-conductive materials without the necessity of a conductive coating or use of the second crossover energy as electron energy. At the second crossover energy the number of incoming electrons is equal to the emitted SE and BSE electrons. A detailed description of this method and tabulated values for, e.g., the second crossover energy can be found in Goldstein [13]. Another table with second crossover energies, especially for various polymers, can be found in J.H. Butler *et al.* [14]. But this method works only for homogeneous and approximately flat materials. The second crossover energy is not only dependent on the material, but also on the tilt angle. Coating must be avoided, of course, in the case of *in situ* experiments, but also when the analysis concerns very small features, which could be masked by an additional surface layer. Also, artefacts induced by the coating process can never be completely excluded, especially not in the case of soft materials like polymers.

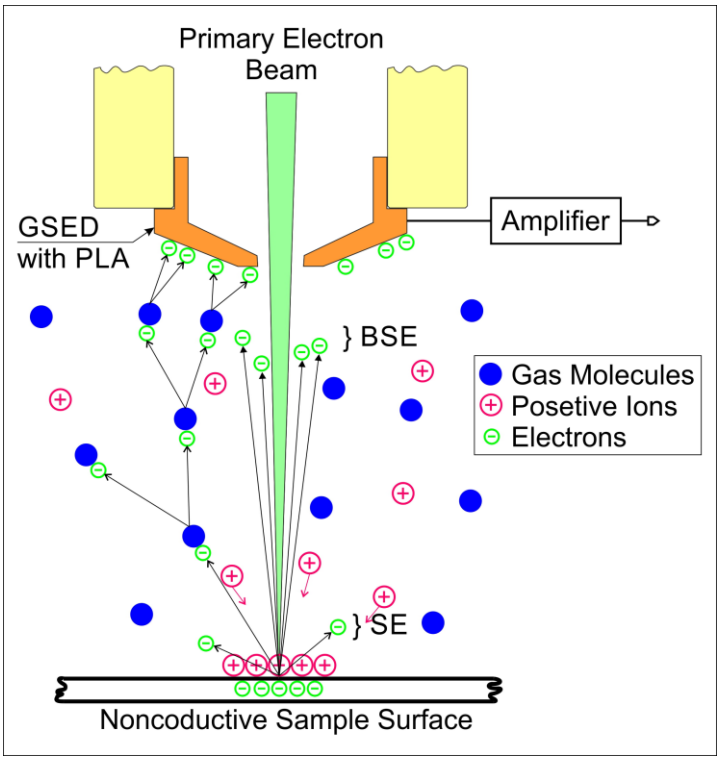

Fig. 2: Schematic of the generation of positive ions due to scattering of primary beam electrons at the gas molecules and the resulting charge compensation at the sample surface.

The suitability of water vapour as chamber gas reveals the second advantage of an ESEM compared to a C-SEM. If a sample inside the chamber is cooled below the dew point at a given water vapour pressure, condensation will take place. Hence it is possible to investigate wet samples without the sample drying out, and to perform dynamic wetting and drying experiments by varying the pressure or the temperature. Pressure variations are generally preferred, because these occur immediately, whereas the time necessary for temperature changes is dependent on the thermal conductivity of the materials. Thus the sample temperature is usually kept constant and only the vapour pressure is varied between pressure

values below and above the dew point, see phase diagram in Fig. 3. This approach was used, e.g., for the dynamic *in situ* microfiltration membrane characterisation (see chapter 2). But as mentioned before, the drawback of using a gaseous environment is the scattering of primary electrons out of the focused beam. Monte Carlo simulations allow this scattering to be calculated for different operating parameters of the microscope. The simulations in the centre of Fig. 3 show the electron scattering and skirting exemplarily for three different gas pressures [6]. It can immediately be seen that the higher the pressure the stronger the scattering and the larger the skirting radius. The corresponding lateral distribution of the signal intensity can be seen at the bottom of Fig. 3. The signal/noise ratio decreases with increasing pressure. But the signal/noise ratio also depends on several other parameters, such as the working distance, the electron energy, the type of gas:

$$\frac{I_0}{I_{total}} \sim e^{-\frac{kpd}{TE}} . \qquad (1)$$

Nevertheless, the resolution stays the same even at a pressure of 6 Torr so that images at high magnification and with sufficient contrast can be taken in this pressure range. The resolution is often limited by radiation damage to beam sensitive samples. This has to be taken into account especially for polymers, if high acceleration voltages and a water vapour environment are used. Royall *et al.* [15] proved that the beam damage increases in the presence of water vapour because of the formation of highly mobile free radicals, e.g. hydroxyl radicals (.OH). The amount of radicals increases with an increase of the acceleration voltage (AV), hence the use of lower beam energies is recommended. Another benefit of using lower energies is the decrease in electron penetration depth into the sample, which increases the sensitivity to resolve fine structures at the surface. However, the lower the electron energy, the stronger is the scattering of the electrons by the gas atoms. Thus, contrary to the high vacuum mode, one cannot use arbitrarily low electron energies in the low vacuum range.

The broad pressure range makes the ESEM a versatile tool for a variety of investigations, both static and dynamic, at the micro- and mesoscale. It is especially suitable for investigating non-conductive materials such as soft materials, because in many cases no special sample preparation is required. Also the ability to examine samples in the wet state makes it indispensable for the investigation of filtration membranes, as described in more detail in in chapter 2.4.1.

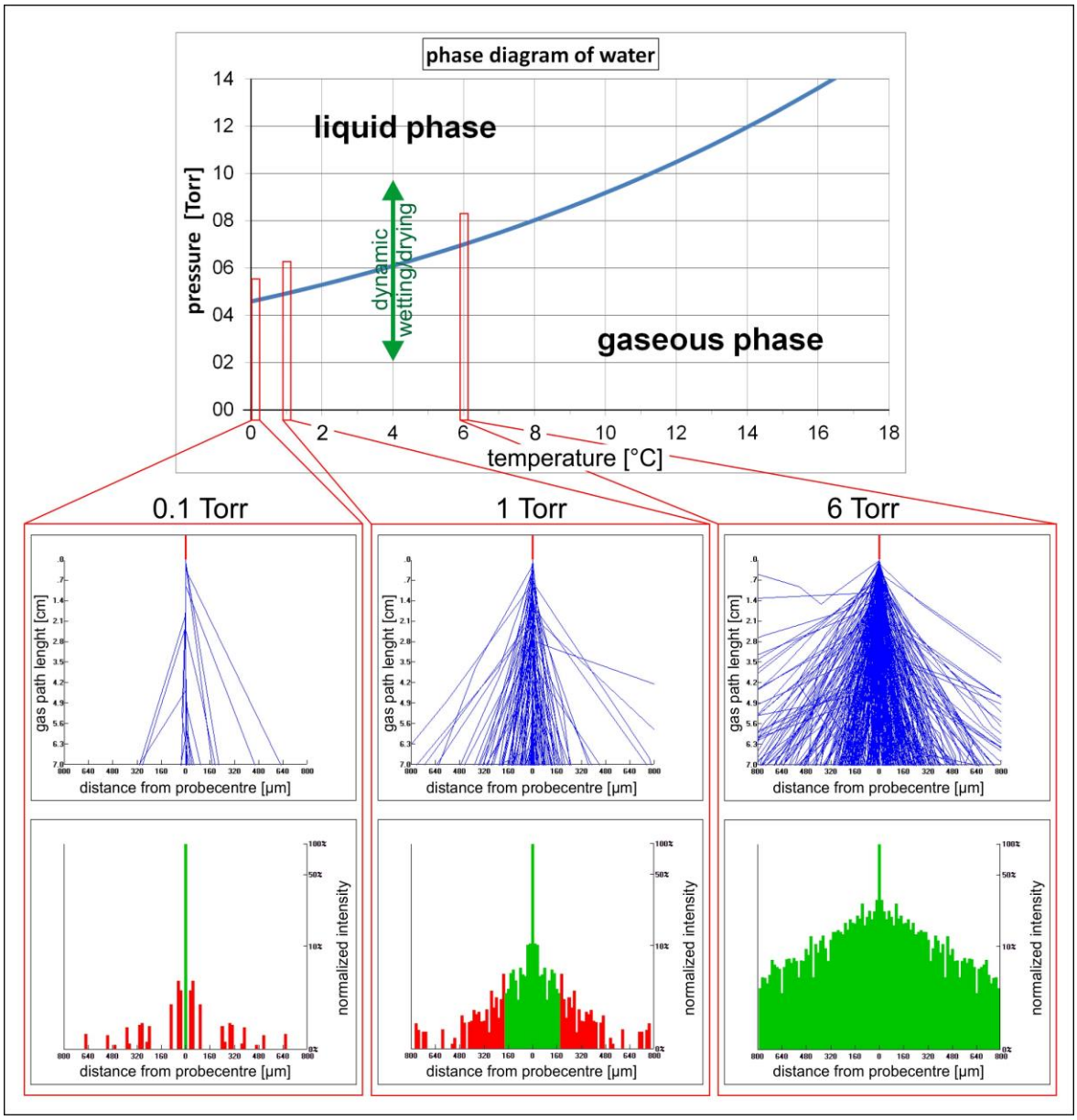

Fig. 3: Top: phase diagram of water in the typical ESEM pressure region; centre: electron scattering simulations inside the specimen chamber at the pressures marked in the phase diagram (AV: 7 kV, WD: 7 mm); bottom: the corresponding lateral distribution of the electrons at the sample surface and signal/noise ratio, where the green regions comprise 90 % of the primary electrons.

2. *In situ* characterisation of microfiltration membranes

2.1. Introduction

A wide range of industries uses microfiltration membranes for separation purposes like the purification of wastewater or at downstream applications in biotechnology [16], [17]. They are best known for their excellent filtration performance while simultaneously standing out due to their low power consumption. The materials used for production include a large variety of materials, e.g. ceramics, metals and polymers. Polymers are preferentially used as they are easy to manufacture and the pore size and its distribution over the cross-section of the membrane can easily be adjusted. A frequently used polymeric material for such membranes is polyethersulfone (PES) with polyvinylpyrrolidone (PVP) as additive for increasing the overall hydrophilicity [18]. Practically all areas of application eventually lead to membrane fouling because process solutions, particles, bacteria and all other types of impurities in the liquid are deposited on the membrane surface and in the pores. As a consequence, the membrane gradually loses its effectiveness. The membranes must therefore be regularly cleaned and disinfected for long term usage. Several cleaning agents are used for this purpose, typically sodium hypochlorite (NaClO) and sodium hydroxide (NaOH) [19]. Occasionally citric acid (CA) can also be found as a cleaning agent in the literature [20]. Many investigations have been carried out studying the impact of the cleaning agents on membrane performance. All the studies revealed signs of membrane degradation, accompanied by a decrease in membrane performance after treatment with cleaning agents. The investigations used a variety of characterisation methods to examine the ageing mechanism, for example pure water permeability, tensile strain at break or ATR-IR measurements. But the results of nearly all these measurements are parameters which are integrated over the whole membrane volume. Reingruber *et al.* [21] developed a technique for the investigation of flat sheet membranes in the specimen chamber of an ESEM by wetting and subsequent drying of the membrane. It enables the acquisition of high resolution images at one membrane surface, while simultaneously measuring the temperature characteristics at both surfaces. By correlating these microscopic and macroscopic parameters, spatially resolved results about the membrane structure can be obtained. This new method will be used in this thesis to investigate the impact of cleaning agents on membrane degradation in more detail. The results will be discussed and compared to results from other techniques.

2.2. Microfiltration membrane production [22]

A great variety of production processes can be used for the manufacturing of synthetic flat sheet membranes. Examples of these processes include sintering of powder consisting of particles with a given size, stretching of (semi) crystalline polymers, coating of different materials or the phase inversion process. Phase inversion is a frequently used technique, where the precipitation of the membrane material can be controlled via solvent evaporation, thermal alterations or by immersion in a non-solvent. The latter method involves casting the dope solution onto a carrier foil and subsequently immersing the foil in the non-solvent. A schematic representation of this process is shown in Fig. 4. In this process precipitation takes place due to the exchange of solvent and non-solvent inside the coagulation bath, leading to

a controlled transformation of the polymer from liquid to solid. This technique allows the fabrication of all kinds of morphologies with a wide variety of polymeric blends. As mentioned in chapter 2.1, the investigated flat-sheet microfiltration membranes consist mainly of PES. Additionally, PVP is added to increase the overall hydrophilicity, which improves the performance of the membranes if used, e.g., in water treatment plants. This blend is also often preferred because of its high resistance to many physical and chemical treatments [23]. It is typically fabricated using the phase separation process, which can also lead to highly anisotropic cross-section morphologies [24]. These anisotropic membranes show a significantly improved filtration performance, and additionally a high transmembrane flow-rate and a high filter capacity. The phase separation process is generally based on thermodynamic principles, which will be briefly discussed in the following.

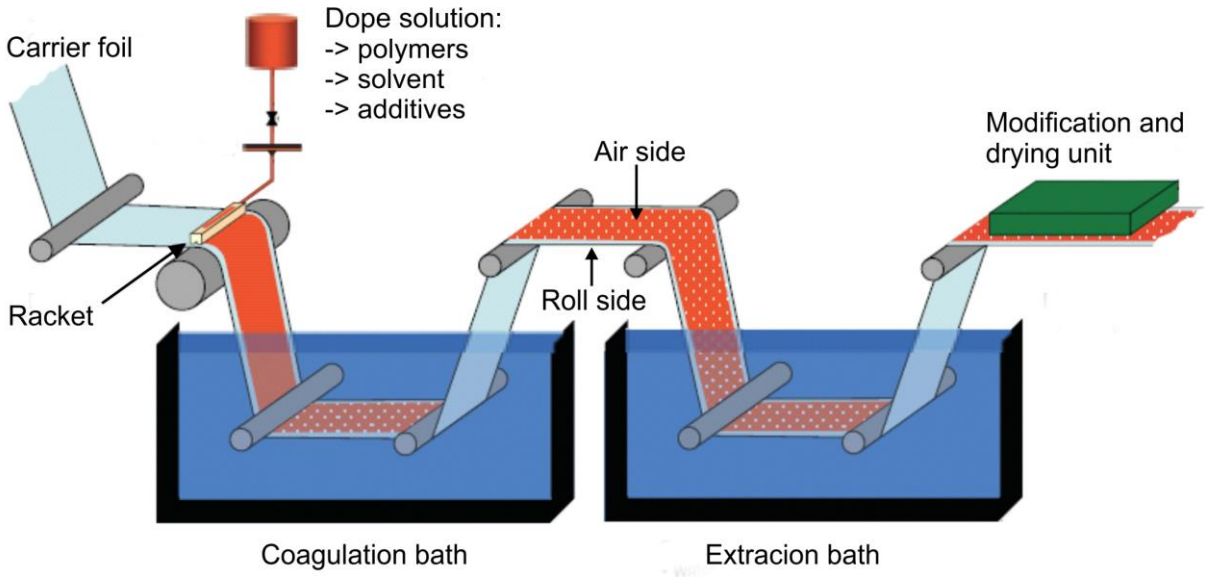

Fig. 4: Schematic of the production process of flat-sheet microfiltration membranes.

Phase separation in polymeric systems starts with a thermodynamically stable solution which needs to be segregated. The three components used in the solution for the immersion precipitation process are a polymer, a solvent and a non-solvent. In fact, the typical composition of industrially fabricated membranes is more complex, but here only the basic principles of the process will be discussed. The state function can be used to specify whether a system is in equilibrium or whether it might change spontaneously. The change of the free enthalpy or the Gibbs free energy of mixing G_m can be used as a criterion to determine whether the mixing process is spontaneous or not:

$$\Delta G_m = \Delta H_m - T\,\Delta S_m \tag{2}$$

where ΔH_m is the enthalpy of mixing, T the temperature and ΔS_m the entropy of mixing. For a two component system like polymer – solvent, mixing will spontaneously occur if the free

enthalpy of mixing is negative, $\Delta G_m < 0$. As this equation only applies to systems at constant pressure and temperature, only a change in enthalpy or entropy can lead to a phase separation. But in contrast to the mixing of ideal gases, where the molecules are relatively small, a dissimilarity of the mixing molecules can be found in polymer solutions. In 1941, Flory and Huggins [25], [26] therefore independently published a new equation for the free enthalpy change where this circumstance was taken into account:

$$\Delta G_m = R\,T\,(x_A \ln \emptyset_A + x_B \ln \emptyset_B + x_A \emptyset_B \chi) \tag{3}$$

with R the gas constant, T the absolute temperature, x_A the number of moles of the volume fraction $\emptyset_A$ (e.g. the polymer), x_B the number of moles of the volume fraction $\emptyset_B$ (e.g. the solvent) and χ the Flory-Huggins parameter. This parameter is a measure of the thermodynamic interaction between the different components indicating if they are miscible. The reaction between the components is athermal in case $\chi = 0$ (ideal mixture), endothermal for $\chi > 0$ and exothermal for $\chi < 0$. As mentioned above, the dope solution typically consists of three components (polymer, solvent and non-solvent), hence there are three interaction parameters which must be taken into account in determining whether the mixture is miscible or whether miscibility gaps appear [27]. Conventionally a three component phase diagram is used for discussing the thermodynamic processes in the membrane precipitation process. An example of such a phase diagram can be seen in Fig. 5, where each corner represents one of the three pure components. The process of membrane formation starts here at point A, with a mixture of polymer and solvent. The membrane must go through several steps to reach the final membrane composition at equilibrium point D. Membrane formation is basically due to the exchange of the solvent with the non-solvent, which is why the production process is referred to as non-solvent induced phase separation (NIPS) [24]. As the concentration of the solvent continuously decreases from A to D, a demixing of polymer and solvent takes place. The first precipitation takes place at point B, where the membrane formation line crosses the binodal line F – E, which represents the line where a phase transition takes place. The concentration of the solvent in the mixture further decreases, leading to a steady increase in the polymer rich phase and its viscosity, until point C is reached. Here the viscosity of the precipitated polymer is high enough to be regarded as solid, which prevents further movement of the polymer bulk. The proceeding exchange of solvent and non-solvent results in a shrinkage in the polymer phase until, ultimately, the final membrane composition at point D is reached. The porosity and the layer arrangement of the membrane can be influenced by different parameters. The key parameters in the present process include the choice of the three main components, the position of point D, the temperature or the production velocity, to name but a few.

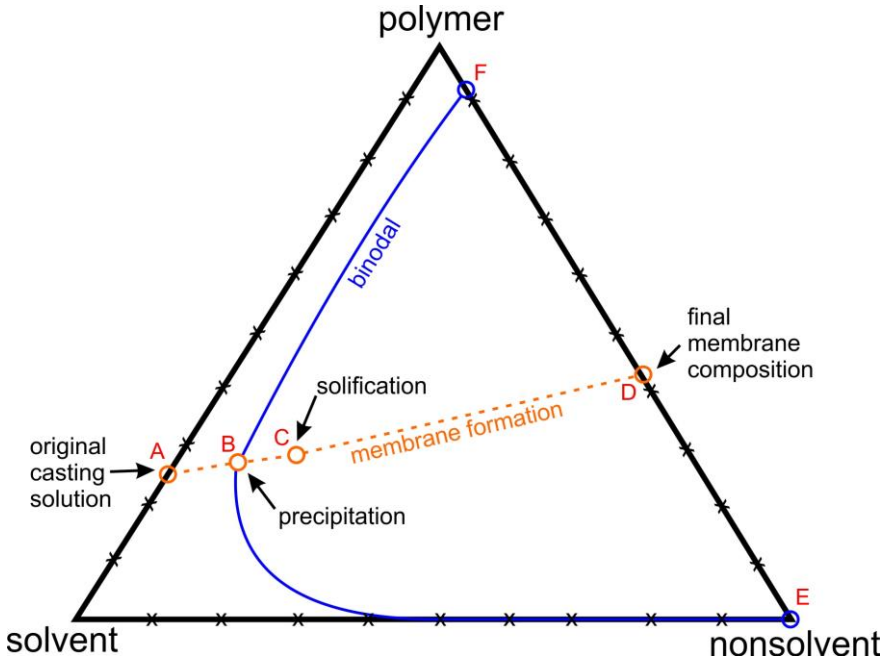

Fig. 5: Schematic of a phase diagram for a three component system, detailed description can be found in the text; adapted from [28]**.**

2.3. The Membranes investigated

Using the production method described in chapter 2.2 it is possible to manufacture different types of membranes such as flat sheet or hollow fibre membranes that feature differences in structure and mean pore size. The variation of different operation parameters allows the production of a broad range of filtration membranes including microfiltration, ultrafiltration and gas separation membranes. The investigations in this thesis are mainly focused on microfiltration membranes with an asymmetrical layer arrangement. They are, amongst others, applied in the field of biology and medicine as well as in the beverage industry. Due to their asymmetrical structure they show a significantly better filtration performance than other membranes of the same type [24]. The asymmetrical structure of the two membranes investigated can be clearly seen in the SEM images of the cross-sections and the corresponding schematics of the pore size distributions in Fig. 6. The DuraPES® 600 has a nominal pore size of 0.6 µm and the MicroPES® 2F has a nominal pore size of 0.2 µm [29], [30] (Membrana, Wuppertal, Germany). But the two membranes differ not only in their nominal pore sizes, but also in their pore size distribution. The DuraPES® 600 consists of roughly three different layers, whereas the MicroPES® 2F consists of four. The overall thickness also differs: (110 ± 10) µm for the MicroPES® 2F, (140 ± 10) µm for the DuraPES® 600. In both membranes, the separation layer (i.e. the layer with the smallest pores, where filtration actually takes place) is positioned close to the air side, which is the top surface during the production process (see Fig. 4).

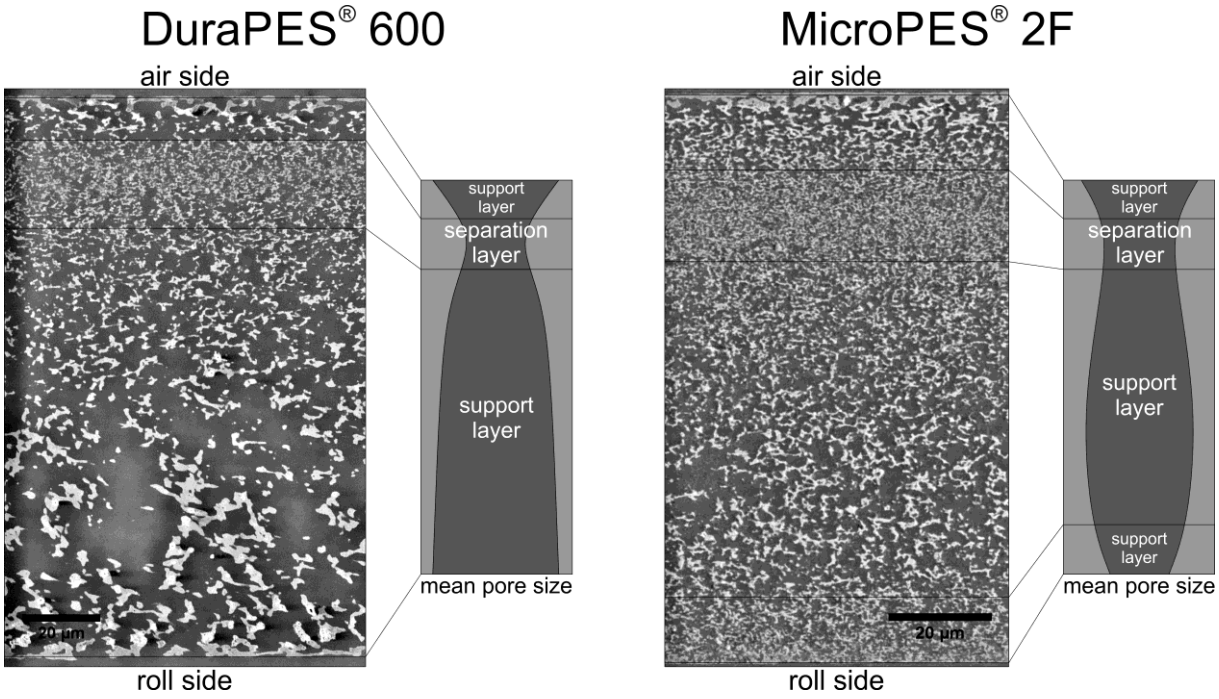

Fig. 6: SEM images of the cross-sections and corresponding schematics of the pore size distribution of the two membranes investigated; left: DuraPES® 600; right: MicroPES® 2F.

These two flat sheet membranes were analysed in pristine and treated conditions in order to analyse the impact of different cleaning agents. The three different techniques used were *in situ* wetting and drying in the ESEM, mapping by FT-IR spectrometry and droplet tests using a micro-pipette. By combining these three methods, it should be possible to elucidate which layer in a multi-layered membrane is most strongly affected by degradation or fouling. A detailed description of all three methods can be found in chapters 2.4.1, 2.4.2 and 2.4.3. How, in principle, the chemicals used in the cleaning process alter the main components of the membranes is described in chapter 2.3.1.

In addition to these two flat sheet membranes, another type of flat sheet membrane (Université de Rennes 1, Rennes, France), hollow fibre membranes (Membrana, Wuppertal, Germany) and multi-pore membranes (Université de Poitiers, Poitiers, France) were investigated by FT-IR spectroscopy only. The membrane cross-sections of all three types can be seen in Fig. 7. All these membranes also feature an anisotropic layer arrangement. The separation layer of the hollow fibre and multi-pore membranes is situated close to the inner pore walls. Like the two flat sheet membranes discussed above, these two membranes were treated with cleaning agents to investigate the amount of degradation caused by the treatment. A detailed description of all chemical treatments can be found in chapter 2.3.2.

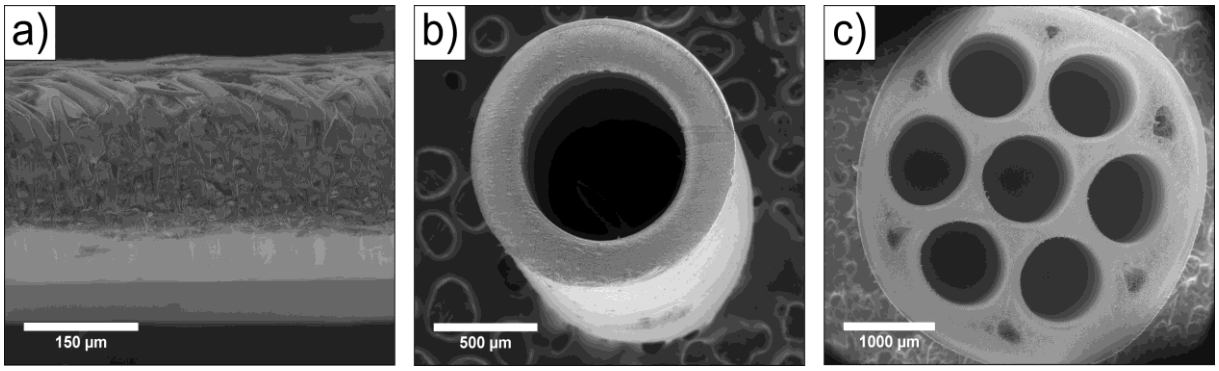

Fig. 7: Cross-sections of membranes investigated by FT-IR: a) flat sheet membranes, b) hollow fibre membranes and c) multi-pore membranes.

2.3.1. Membrane degradation caused by chemical treatment

Sustainable development has also become an important issue in the field of membrane separation. In the light of this, existing membrane types have been modified and new types of membranes composed of a variety of materials have been developed to improve both membrane performance and lifetime. Part of these improvements is also the introduction of highly anisotropic membrane structures, which should also lower the power consumption of the membrane module in operation [24]. A careful choice of the membrane materials has also enhanced their long-term resistance to damage caused by different chemical treatments. Chemicals must be used for regular membrane cleaning to avoid fouling, bacterial contamination and for disinfection purposes [20]. One of the most frequently used chemicals is sodium hypochlorite (NaClO), because it forms in an aqueous solution of sodium hypochlorite (NaOH) at the one hand and hypochlorite acid (HClO) at the other hand. Hence it is well known for its high disinfection potential in comparison with other cleaners [1]. Other cleaning agents used include NaOH and, infrequently, citric acid (CA) for the same purpose. By implementing proper cleaning procedures, membranes can be used for several years in various applications. But several studies have revealed a degradation in membrane performance caused by the chemical agents used in the cleaning process [31], [32]. As discussed in chapter 2.2, the investigated microfiltration membranes consist mainly of PES, with an addition of PVP to enhance its hydrophilicity. Prulho *et al.* [33] studied the ageing of PES/PVP blends by soaking both pure components and the blend into an aqueous hypochlorite solution. In case of pure PVP, the hydroxyl radicals (.OH) involved led to degradation and the radical oxidation formed succinimide groups, see Fig. 8. Treatment with a hypochlorite solution thus led to an oxidation of the polymer accompanied by cross-linking and chain scissioning.

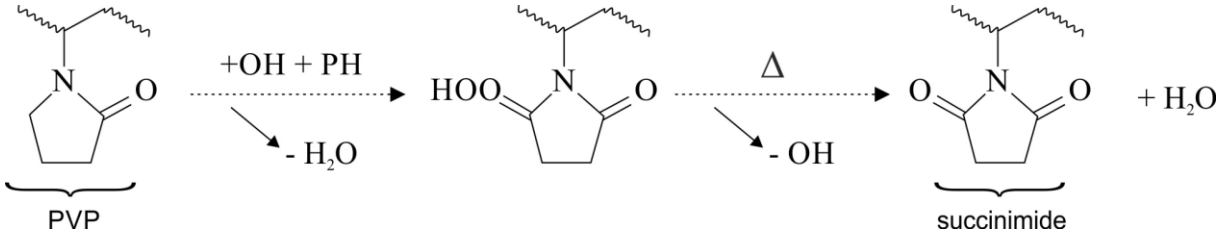

Fig. 8: Schematic of the PVP degradation in contact with radicals, adapted from [33]**.**

The treatment of pure PES had no measurable effect on the polymer under the same conditions. The authors ascribe this circumstance to the absence of aliphatic assistants in the PES structure. The use of higher hypochlorite doses led to the formation of phenol groups, see Fig. 9. Chain scissioning in the PES structure seems to take place only in the presence of sufficiently high hypochlorite concentrations [34].

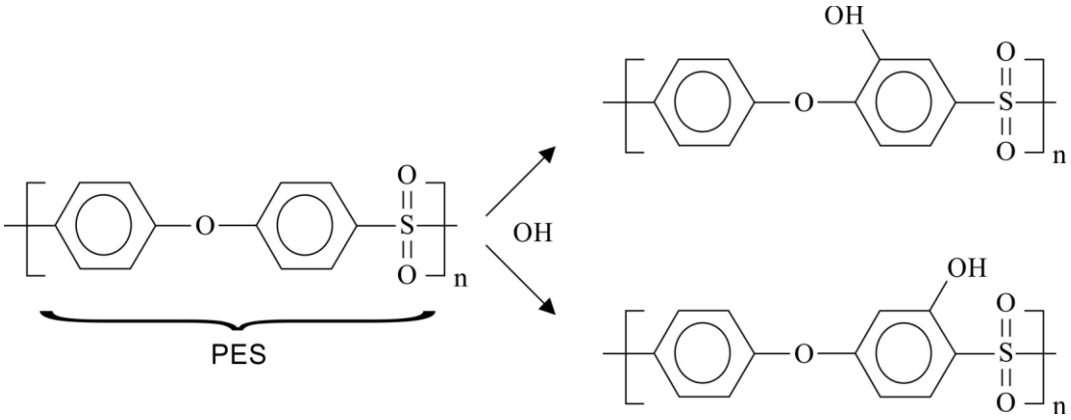

Fig. 9: Schematic of the mechanism of phenol formation in PES through higher concentrated radicals, adapted from [33]**.**

In the context of the PES/PVP blend hypochlorite treatment, Prulho *et al.* suggested that primarily an oxidation of the PVP component had taken place [33]. The hydroxylation of the aromatic rings in the PES led to both chain scission and cross-linking reactions in the blend. But this oxidation of PES was only verifiable at very high PVP concentrations of around 50 %, whereas usually the concentrations are much lower. As mentioned before, however, a decrease in membrane performance was also found in membranes with low PVP concentration after hypochlorite treatment. Several mechanisms could be responsible for this decrease, for example irreversible ring chlorination, surface pitting and cracking or chain scission at the sulfonic linkage, to name but a few. The methods used for membrane characterisation after degradation often include SEM investigations for observing changes in surface morphology, FT-IR ATR measurements for detecting changes in the membrane composition, and tensile tests or flux tests for verifying changes of general membrane properties. All these measurements produce parameters which are integrated over the membrane cross-section or provide only local information. New methods are thus used and

developed in this thesis to produce spatially resolved results of the membrane ramification. In the following chapters they will be introduced and discussed in detail.

2.3.2. Chemical membrane treatment

To investigate the impact of frequently used membrane cleaning agents on membrane degradation, two types of flat-sheet microfiltration membranes were soaked in three different typical cleaning agents. The concentrations and exposure times were varied to obtain different doses (i.e. concentration × time, [ppm.day]). Higher chemical concentrations were used than in on-site chemical cleaning to keep the exposure times short. The three chemicals used were sodium hypochlorite (NaClO) with 16 % free chlorine, ≥ 99 % sodium hydroxide (NaOH) and ≥ 99.9 % citric acid (CA). They were diluted with ultrapure water (14.7 MΩ cm) from Barnstead™ NANOpure™ (Thermo-Fisher Scientific, Waltham, USA) to obtain the desired concentrations of:

- NaClO: 4000 ppm, 15,000 ppm and 30,000 ppm
- NaOH: 3000 ppm
- CA: 2000 ppm.

Not only the concentration varied for every agent, but also the pH values: the NaClO solution was set to pH 9, NaOH to pH 10 and CA to pH 3. As mentioned in chapter 2.3, the two membranes investigated are DuraPES® 600 and MicroPES® 2F from Membrana GmbH (Wuppertal, Germany). Both feature an asymmetrical layer arrangement, where the separation layer is located close to the air side. They were cut into strips of 5 x 15 mm², which were soaked in the respective solutions. Conventionally the cleaning solution is applied to the membrane by e.g. backflushing [35], but the main aim was not to clean the membrane, but to cause changes in the membrane properties due to the chemical treatment. The solutions were monitored throughout the soaking time in order to identify any changes in their composition. No changes in pH value were registered for NaOH and CA, only a slight change from pH 9 to pH 8 was detected for the NaClO solution after 24 h. Thereafter no further change was observed. After the treatment the membranes were rinsed for a minimum of 30 min with ultrapure water to get rid of the chemical solutions and subsequently dried under high vacuum (< 10^{-4} Torr).

2.4. Investigation methods

Three different methods were used for the characterisation of both pristine and treated polymeric membranes. Although based on different principles they all have the same aim: to acquire the impact of different kinds of chemicals on the membrane material.

2.4.1. *In situ* wetting in the ESEM

The *in situ* investigations in the ESEM were carried out using a specially designed and manufactured experimental setup providing controlled wetting and drying of flat sheet membranes. The method was developed by Reingruber *et al.* [21] and enables the simultaneous recording of microscopic as well as macroscopic parameters. The combination yields spatially resolved results providing information on where exactly degradation or fouling mainly occurred in a multi-layered membrane. A schematic representation of the experimental setup can be seen in Fig. 10. This setup was developed because the commercially available cooling stage did not meet the requirements for the *in situ* investigation of membranes. It consists of a Peltier element that cools a small metal cup holding the sample. The membranes were fixed at the rim of the cup by an adhesive tape. By decreasing the cup temperature below the dew point of water at a given water vapour pressure, condensation took place in the cup and finally wetted the membrane, whose temperature was higher than that of the cup due to its poor heat conductivity. This arrangement did not allow repeatable temperature profiles at the membrane and was thus not suitable for the wetting and drying experiments. A new experimental setup was therefore developed and constructed to overcome these complexities. The membrane is fixed between two brass clamps, which can be cooled. Due to the poor heat conductivity of the membrane, the temperature of the membrane increases with the distance between the clamps and peaks in the middle between the two cooling clamps. Additionally, the setup enables the attachment of two micro-thermocouples at both surfaces of the membrane and thus local temperature measurements. The thickness of the membranes is between 110 µm and 150 µm, so the diameter of the thermocouples must be as small as possible. As the heat conductivity of the contact wires must also be as low as possible, K-type (chromel, alumel) micro-thermocouples of around 30 µm diameter (CHAL-0005, Omega®, Newport, UK) were applied. The contact between the thermocouples and the membrane surface is ensured only by the spring force of the contact wires. The thermocouples must therefore be mounted carefully. But the flexible contact wires ensure a permanent contact with the surface, even if the membrane bends due to the contact with water. The temperature logger used (HH147, Omega, Newport, UK) enabled measurements with a time resolution of 1 s.

The whole setup is designed in a way that it can be easily mounted on the specimen stage in the same way as normal samples. Also, the ESEM built-in temperature controller can be used to drive the two series-connected Peltier elements to the specified temperature. The actual temperature was measured by Pt100 thermocouples, which were first electrically insulated and then mounted inside the cooling clamps. The cooling clamps themselves were electrically grounded with a spring contact to the microscope stage. The heat sink was a 43 x 43 x 18 mm³ stainless steel block connected to the specimen stage. In addition, two brass plates were screwed onto the top and bottom of the heat sink for mounting the Peltier elements - and micro-thermocouple connectors. The entire wiring required from the connectors to the external temperature logger was made of the same two materials as the thermocouples to avoid voltage differences between the materials. This allowed highly accurate temperature measurements of the two membrane surfaces and the two cooling clamps. Two different sets of cooling clamps were constructed. One set enabled the membrane to be clamped in a horizontal position to record images of the top membrane surface, while the other set was used

to clamp the membrane in a vertical position for imaging the membrane cross-section. Fig. 11 shows the temperature characteristics and a few SEM images of a representative wetting and drying process. Only a brief discussion of the whole procedure will be provided in this thesis, a detailed discussion can be found in [36].

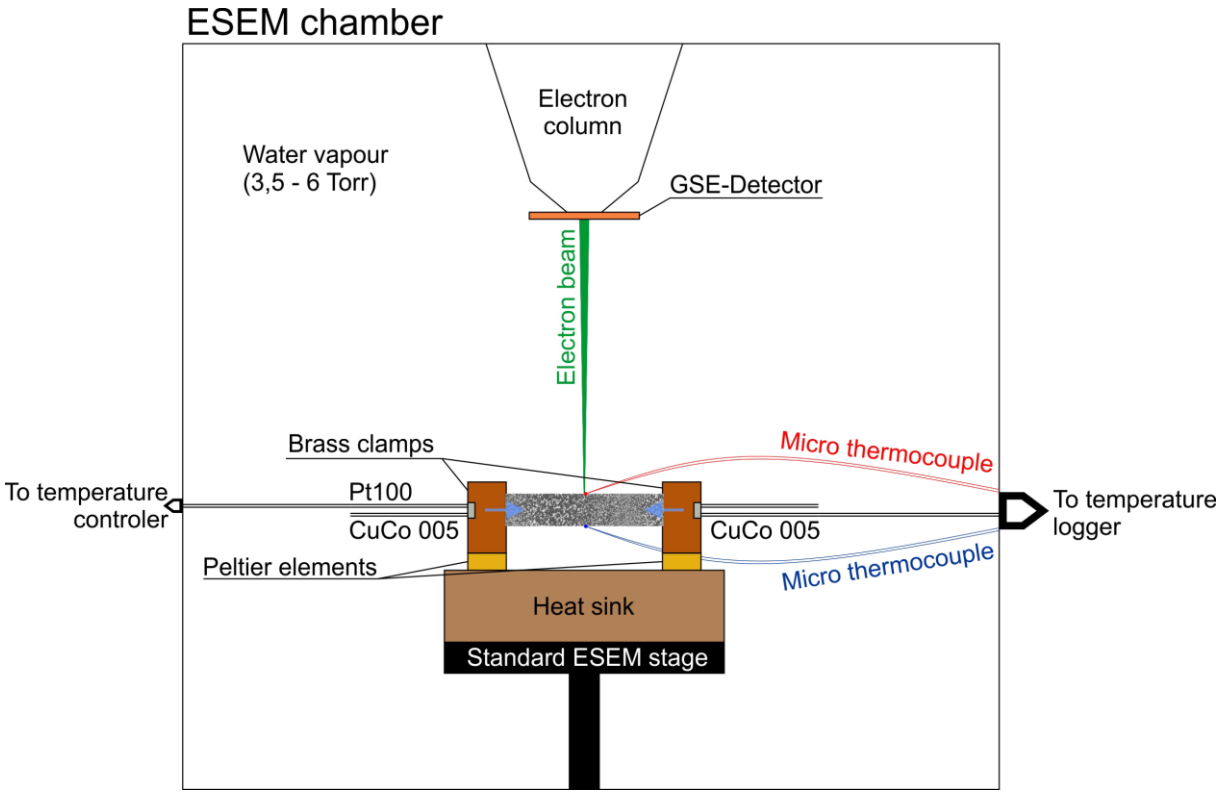

Fig. 10: Schematic of the setup for the *in situ* wetting and drying experiments in the ESEM; detailed description can be found in the text.

At At the beginning, the cooling clamps were set to the ambient temperature of 22°C to ensure that the membrane is completely dry. Afterwards three purging cycles, consisting of pressure changes between 1 and 8 Torr, were performed at section 1 in the temperature profile of Fig. 11 to ensure that the water vapour atmosphere definitely conforms to the preassigned pressure of 1 Torr. The purging mainly accelerates the approach of the gas equilibrium in the specimen chamber after pressure changes. At the start of the actual drying and wetting experiment, the temperature of the cooling clamps was set to 4 °C with the water vapour pressure still remaining at 1 Torr (section 2 of Fig. 11). To enable the condensation of water at the cooling clamps the water vapour pressure was increased above the dew point, which is dependent on the cooling clamp temperature, thus above 5.7 Torr in the present case. To ensure the condensation of water the pressure in section 3 was set to 6 Torr. Subsequently the condensed water at the clamps started to penetrate into the membrane at the contact areas with the clamps due to the capillary forces, finally fully wetting it. It can be assumed that the membrane is fully wetted, because all images recorded at the membrane surfaces show that the membrane is fully covered with water, see images A in Fig. 11. Additionally, both

membrane surfaces reach the same temperature as the cooling clamps, indicating that they have the same temperature as the condensed water. Only data from the drying process were used for the analysis of the membrane structure and properties. Wetting starts at the cross-sections of the membranes which are in contact with the cooling clamps, whereas drying occurs through vaporisation of the water through the membrane surfaces. Only the latter process equals the flow of water through the membrane. To initialise membrane drying in section 4, the pressure was decreased below the dew point, to 3.5 Torr, causing the water to evaporate. Because of the evaporation heat the temperature at both the membrane surfaces and the cooling clamps drops below 0 °C. As ultrapure water vapour was used in the ESEM, the condensed water is nearly free of impurities which could act as nuclei for freezing. This is also the reason why boiling was never observed, despite the low pressure. Thus we assume that we get water in the super-cooled state without ice formation. Also, ice formation was never observed at the cooling clamps and the membrane surfaces during all tests. But as we see only the surface pores directly, ice formation in the membrane interior cannot be completely excluded. Nevertheless, because the whole drying process is highly reproducible the possible formation of ice should not disturb the analysis.

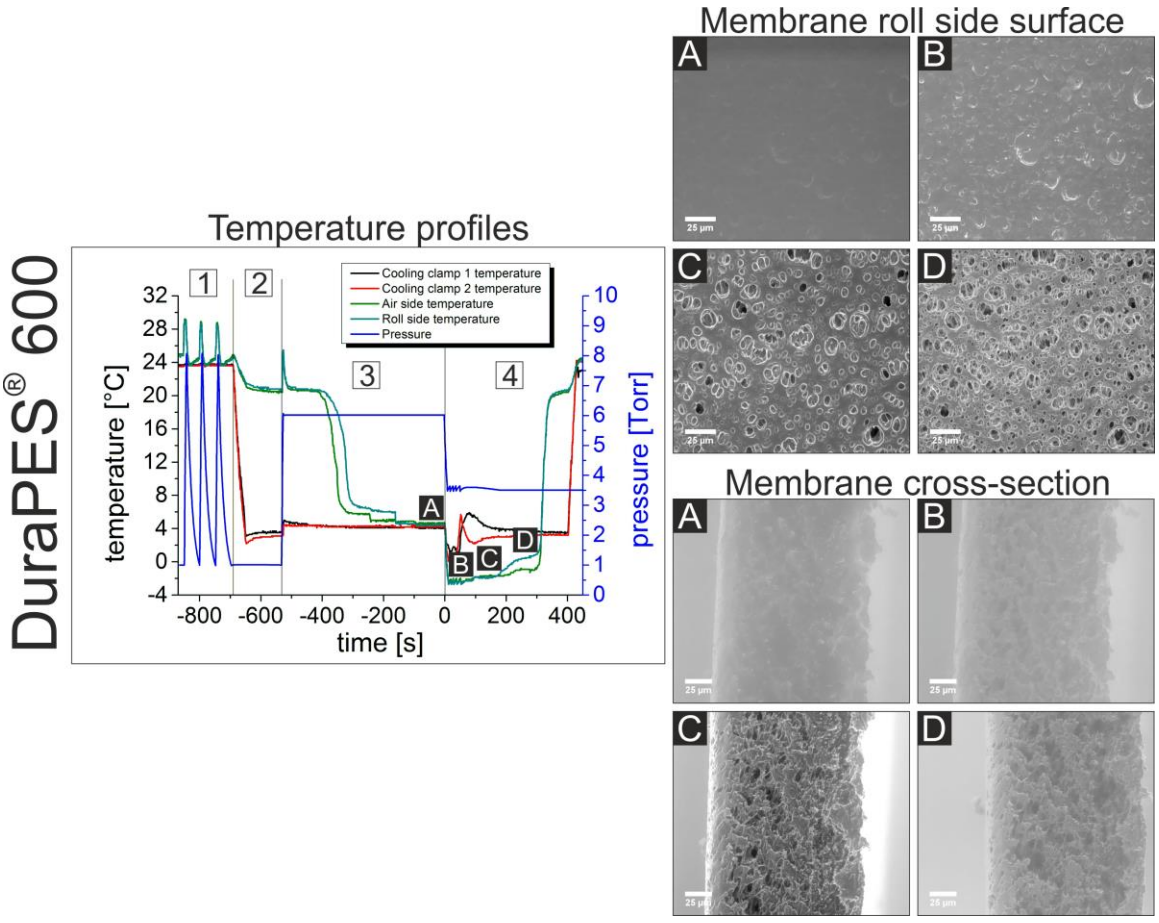

Fig. 11: Whole wetting and drying cycle of a DuraPES 600®. Left: temperature profiles, right: SEM images of the surface at the roll side of the membrane (top) and the cross-section of the membrane (bottom) at the positions marked in the profile. Detailed explanation in text.

High resolution images of one membrane surface and the temperature profiles at both membrane surfaces can be recorded simultaneously throughout the drying process. Because of the asymmetrical layer arrangement of every membrane they also show a distinct temperature profile [21]. These profiles mirror the structure of the inner parts of the membrane. The SEM images provide information about the number and size distribution of the dry pores on the membrane surface during the wetting and drying process as a function of time. In correlation with the temperature profiles, qualitative information about the thicknesses of the different layers, their pore size and the asymmetry of the layer arrangement can be gained. By comparing the results of pristine and treated membranes it should be possible to elucidate which layer was mainly / most strongly affected by the treatment. The same should be true for membrane fouling. The differences between the respective temperature profiles are caused by changes in the interaction between the water and the membrane surface and the pore walls and are also a qualitative measure of the amount of damage caused by the treatment, be it cleaning or fouling.

2.4.2. Spatially resolved IR spectroscopy [37]

As mentioned in chapter 2.1, the membranes investigated consist mainly of PES blended with PVP to increase the hydrophilicity of the membrane. Fourier transform infrared spectroscopy (FT-IR) was used to obtain information about the chemical composition and distribution of the PVP in the membrane. A Hyperion 3000 FT-IR microscope with a Tensor 27 spectrometer (Bruker, Billerica, USA) was used for the analyses. This instrument offers different features such as the macro- or transmission mode or the recording of spectra maps. The spectra shown in Fig. 12 were recorded using attenuated total reflectance infrared spectroscopy (ATR-IR, diamond crystal). The complete IR spectra recorded at the air side of the two membranes DuraPES® 600 and MicroPES® 2F can be seen at the bottom of the figure. Because the intensities of the individual bands are, amongst others, dependent on the composition of the blend, the surface roughness, the sample thickness in transmission and the contact pressure of the crystal in ATR mode, the spectra were normalised to the maximum peak to make them better comparable. The spectra of both membranes show the same bands, hence both membranes have the same composition. Additionally the spectra of the two pure components PES and PVP were recorded with the same technique, see Fig. 12 a) and b). They were used to identify IR bands that are characteristic of the respective component, but do not overlap with a peak of the other component and thus can be used for integration over a specific wavenumber range, providing a qualitative value for the concentration. The IR bands considered most suitable were 1578 cm^{-1} (integration range: (1563 – 1593) cm^{-1}) for PES and 1666 cm-1 (integration range: (1635 – 1695) cm^{-1}) for PVP.

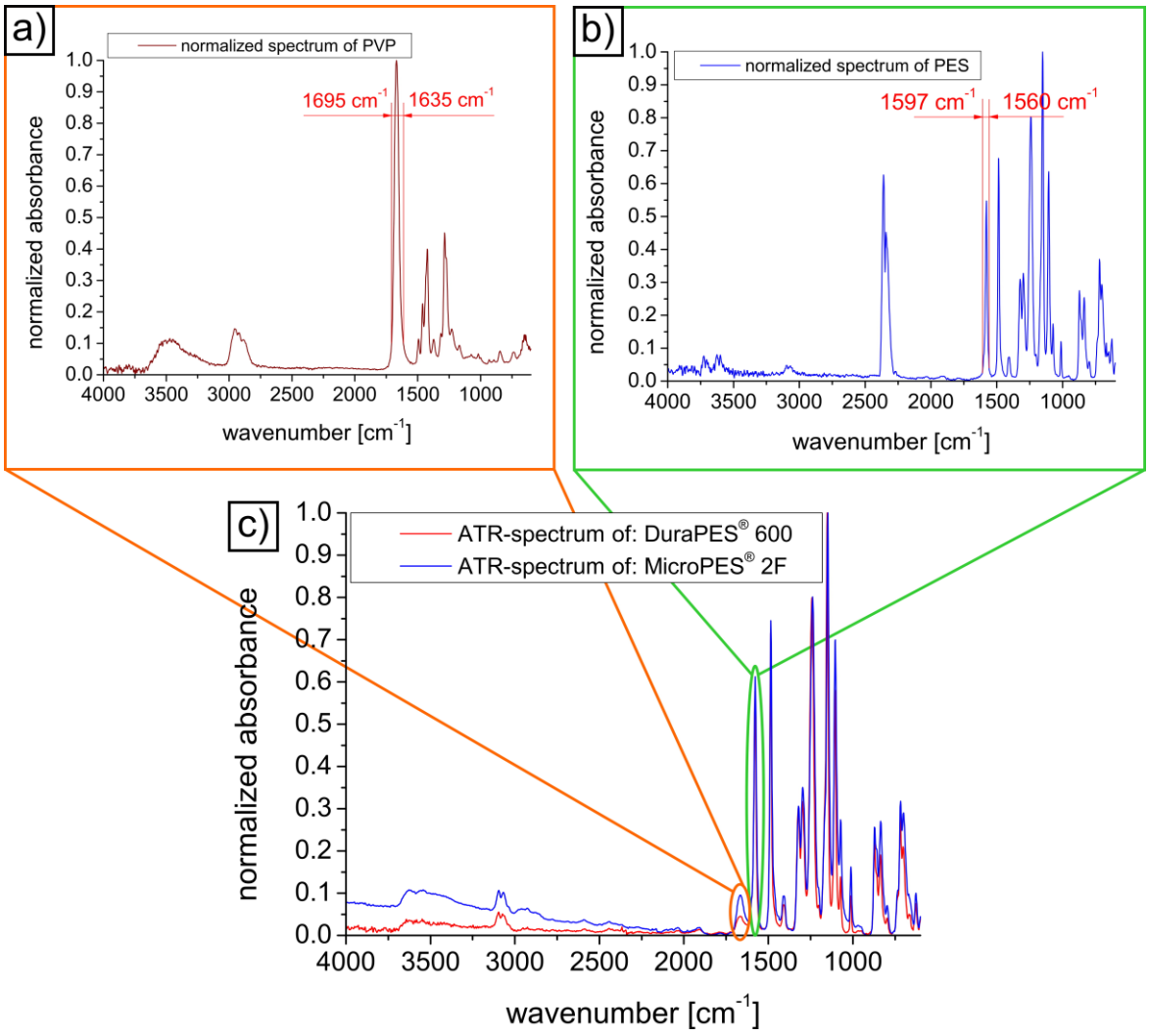

Fig. 12: Normalised FT-IR spectra of a) pure PES, b) pure PVP K30 c): DuraPES® 600 and MicroPES® 2F, characteristic peaks for PES and PVP are marked; detailed description in text.

The goal of the IR investigations is to map the PVP distribution over the cross-sections of different types of membranes, both pristine and after treatment with cleaning agents, for a comparison with the results gained from the wetting and drying experiments in the ESEM. The spectra maps make it possible to extract the distribution of all components from one map. As mentioned before, two different modes are available: macro imaging and transmission mode imaging. Ultramicrotomy was used in both cases to obtain either a flat surface or a thin slice. The membranes must therefore be embedded in a resin to prevent distortion of the highly porous and deformable membranes during the cutting/slicing process. The type of resin to be used for embedding is highly dependent on the material and the subject of investigation. A. Glauert [38] gives a list of recommendations which properties the embedding media should have: they should polymerise uniformly, have a little volume change on polymerisation, be easy to section and stable under the investigation conditions. In the present case another requirement is that the bands of the resin do not overlap with the characteristic peaks of PES and PVP marked in Fig. 12 a) and b). Therefore, several resins were examined using ATR-IR to compare them with the IR spectra of the pure main membrane components, see Fig. 13.

Because the PVP concentration in the membranes is much lower than the PES concentration (see Fig. 12 c)), the IR bands of the resin especially should not overlap with the main band of PVP chosen at 1666 cm^{-1}. EpoHeat® (Buehler, Lake Bluff, USA) proved to be most suitable because it is the resin with the fewest IR bands overlapping with those of PVP and PES.

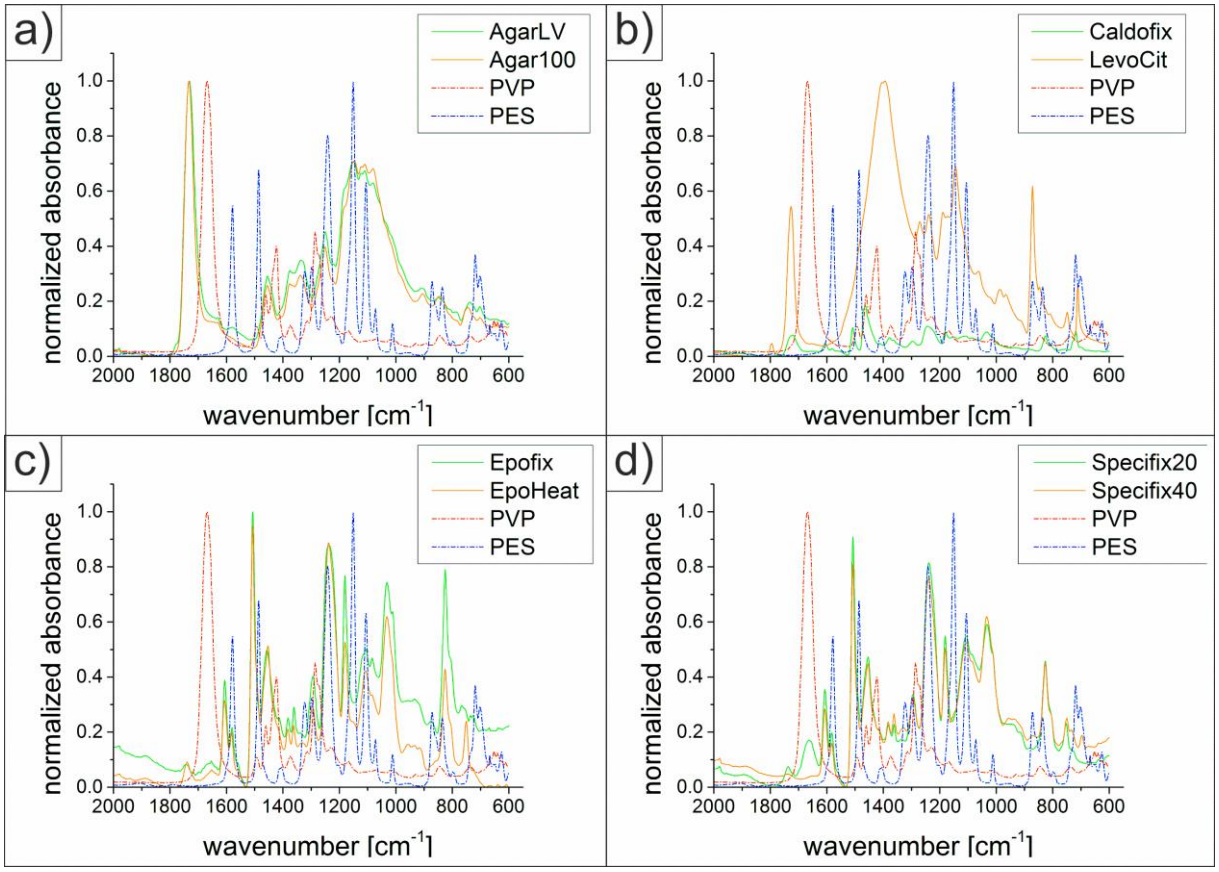

Fig. 13: Comparison of IR spectra of both pure PES and PVP with different resins (only the wavenumber range 2000 cm^{-1} to 550 cm^{-1} is shown).

Opus spectroscopy software (Bruker, Billerica, USA) was used for the analysis of the recorded spectra. Different options can be chosen for the integration over the selected bands. It is important to always use the same integration technique in order to make the analyses comparable. The different available techniques were thus compared to establish the most suitable one. The baseline adjusted integration showed the best results for the integration over the PES band. In this method, the base line connects the minima within the integration range at both sides. A schematic of this method, applied to the characteristic PVP band, and called “integration method 1” in this work, can be seen in Fig. 14 left. The yellow area represents the result after integration and is a qualitative value for the concentration. The same method was used for integration over the PVP band marked in Fig. 12 a) in a MicroPES® 2F spectrum. A comparison of the light microscopic image with the PVP map also revealed a non-zero PVP concentration outside the membrane area. This could be due to the small peak in the EpoHeat® spectrum in the integration region or due to inclusions in the resin. To get rid of this signal,

another integration method was used to obtain the PVP concentration in the IR recordings. Referred to as “integration method 2”, it also takes the intensity at a specific frequency (1677 cm^{-1}) into account, while the base line is subtracted. In the lower left schematic in Fig. 14 the calculated intensity is marked as a green line. The corresponding PVP map shows that the PVP signals inside the resin disappear, but the PVP distribution inside the membrane is similar to that for method 1. As the integrated area is much smaller than by use of method 1, the intensity values in the map are of course also much smaller. To get a better comparison of the two PVP maps they were calculated as grey-value images using the Opus software, and subsequently the images were converted to a surface view with Fiji [39]. In the surface view the grey-level distribution in the images is converted to a 3D model, where the height in the plot represents the PVP concentration. It can be clearly seen that the PVP concentration outside the membrane drops to zero by using integration method 2, but within the membrane area the two distributions are highly comparable.

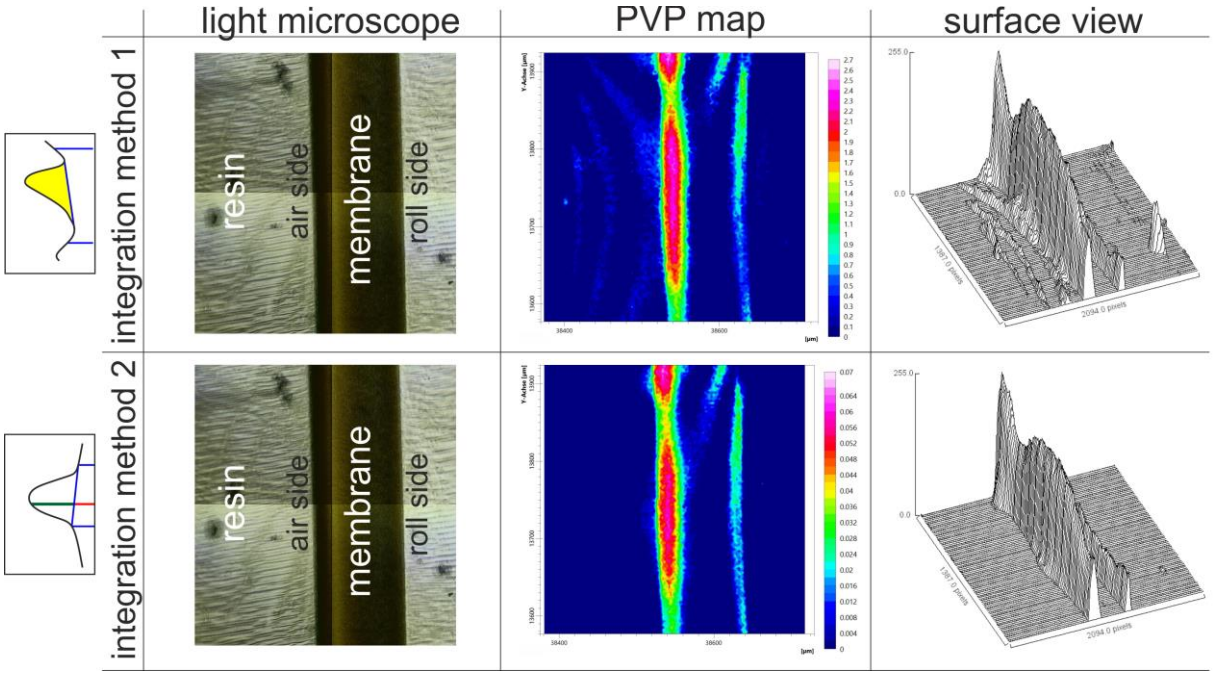

Fig. 14: Comparison of two different integration methods available in the Opus software and used for calculating PVP distributions at the cross-section of the MicroPES® 2F membrane in transmission mode; left: light microscopic image, centre: corresponding PVP distribution, right: surface view of the PVP distribution (calculated from the converted grey-level PVP image); detailed description in text.

By using integration method 1 for the PES and integration method 2 for the PVP intensity, reliable maps for both materials can be generated. It has already been mentioned that two modes are available for the recording of IR maps of larger areas. At first, macro ATR imaging was used to record spectrum maps of the cross-sections of the membranes. For this purpose, a germanium or diamond crystal is pressed against the flat sample surface in the region of interest. The measurable area per record is around (170 x 170) µm². If the region of interest is larger than this area, the specimen stage can be programmed to automatically move to neighbouring positions and to take a series of aligned images. The focal plane array detector

used consists of a matrix of (64 x 64) single detectors giving a pixel resolution of approximately (2.6 x 2.6) µm². Because of the diffraction limit, however, the lateral resolution is only around 6 µm at the PES integration band used. Fig. 15 shows a macro ATR image recorded at the cross-section of a DuraPES® 600 membrane. A slight misalignment of the separate single images can already be seen in the IR result. But a comparison of the length of the membrane cross-section obtained from the light microscopic image with that measured at the IR image reveals a strong difference between them. The light microscopic images were always taken prior to IR mapping. Hence the difference in the lengths will be due to the pressure exerted by the germanium crystal on the sample surface, causing a severe distortion. This distortion may be strongly enhanced by an incomplete filling of the inner small pores with resin because in this case the crystal would cause a deep dent in the membrane cross-section accompanied by a contraction of the lateral dimension of the cross-section. Even if it were possible to map both the PES and PVP distribution (see also Fig. 15, insert) in the investigated membrane this distortion would not allow a reliable interpretation of the results.

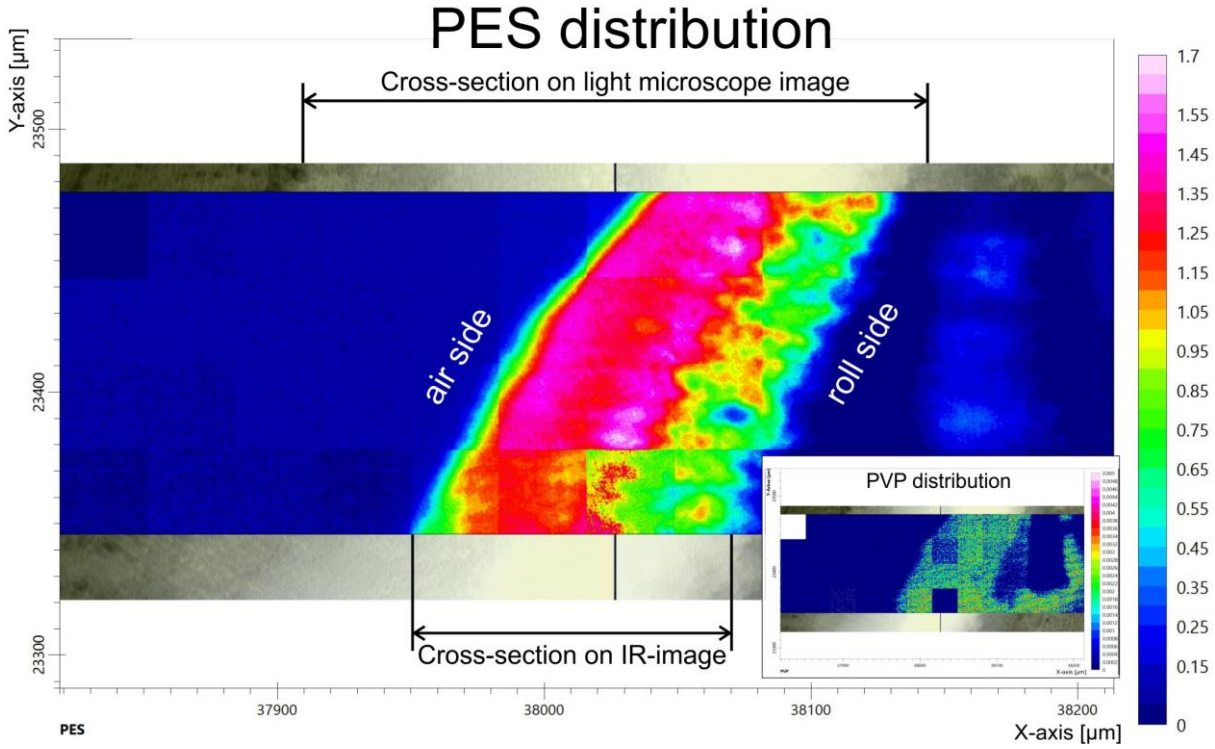

Fig. 15: IR map of the PES distribution at the cross-section of a DuraPES® 600 membrane embedded in resin, with the map recorded by ATR-macro mode using a germanium crystal. A comparison of the cross-section at the light microscopic (background) and the IR image reveals a clear distortion caused by the pressure exerted by the crystal. Insert: same position as the main image, but for PVP distribution.

To overcome the distortion problem in the macro imaging mode, samples were also prepared to record IR maps in transmission mode. Microtomy allows slices of samples to be cut with a thickness from around 30 nm up to several ten µm. Several tests with slices of varying thicknesses were performed to determine the suitable slice thickness yielding a suitable PVP signal in the recorded spectra. The first tests were performed with a slice

thickness of 10 µm. But these samples did not yield an intensity high enough to obtain reliable maps of the PVP concentration of the membranes. By increasing the slice thickness to 20 µm the signal intensity was high enough to obtain usable maps for both the MicroPES® 2F and DuraPES® 600 membranes. Much greater thicknesses would not be possible because then the samples would no longer be IR transmissive. Fig. 16 shows the results for the DuraPES® 600 membrane. The pore size distribution over the cross-section can clearly be seen in the PES map. As PES is the main material of the membrane it should be approximately evenly distributed. But due to different porosities in the separation layer and the support layer, the membrane material per volume unit changes across the cross-section, leading to a variation in the signal intensity. This intensity variation increases with the pore size variations across the cross-section. The PVP / PES ratio is also calculated in order to compensate for this variation in the PVP maps and for a possible slice thickness variation due to sample preparation. This technique makes it possible to investigate pristine flat-sheet membranes, but also other types of membranes like hollow fibres or multi-pore membranes. Additionally, it allows a space-resolved examination of the degradation of membranes at their cross-sections following chemical treatment.

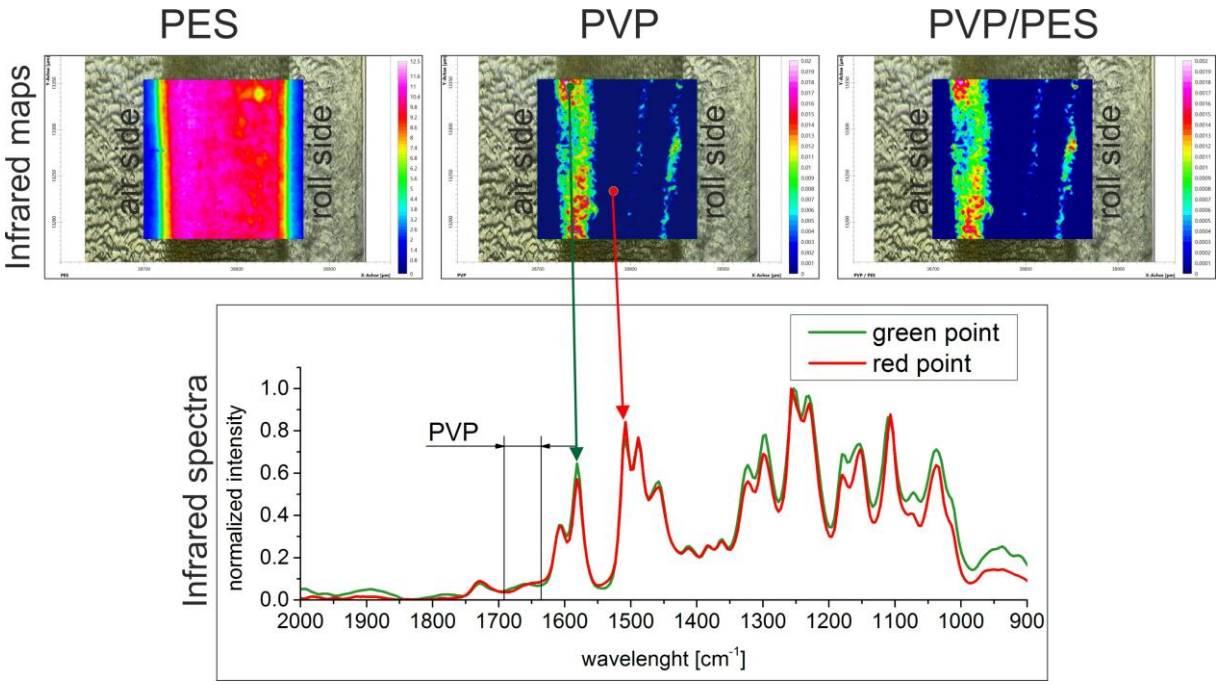

Fig. 16: Top: IR-maps of PES, PVP and PVP / PES in transmission mode at the cross-section of the DuraPES® 600 flat sheet membrane; the corresponding light microscopic image can be seen in the background; bottom: IR spectra at the points marked in the PVP image.

2.4.3. Droplet absorption test

The contact angle measurement is an established method to examine membranes regarding their hydrophilicity at the membrane surface[40]. To this end, an ultrapure water droplet is dropped onto the membrane surface and the contact angle of the droplet on the membrane

surface is measured with special equipment. This technique was slightly modified, however, because the necessary setup was not available. Instead of measuring the contact angle, the imbibition time of a small droplet was recorded. To obtain reliable measurements the same amount of ultrapure water must be dropped on the same side of the investigated membrane (air or roll side) for each measurement and the imbibition process must be recorded with high temporal and spatial resolution. A light microscope with a CCD camera mounted on it was used to record the imbibition process. The camera, a Nikon D7000 (Nikon, Tokyo, Japan), can take high resolution videos at a frame rate of 25 images per second (i.e. one image every 40 ms). A Biohit Proline® Plus pipette from Sartorius (0.5 – 10 µl, increment of 0.01µl) was used to be able to always apply the same amount of ultrapure water (1 µl) and thus a droplet of the same size. The ultrapure water was obtained with the same equipment as described in chapter 2.3.2. With this setup it is possible to obtain reliable imbibition times for different flat-sheet membranes. One imbibition test at a pristine MicroPES® 2F membrane can be seen in Fig. 17.

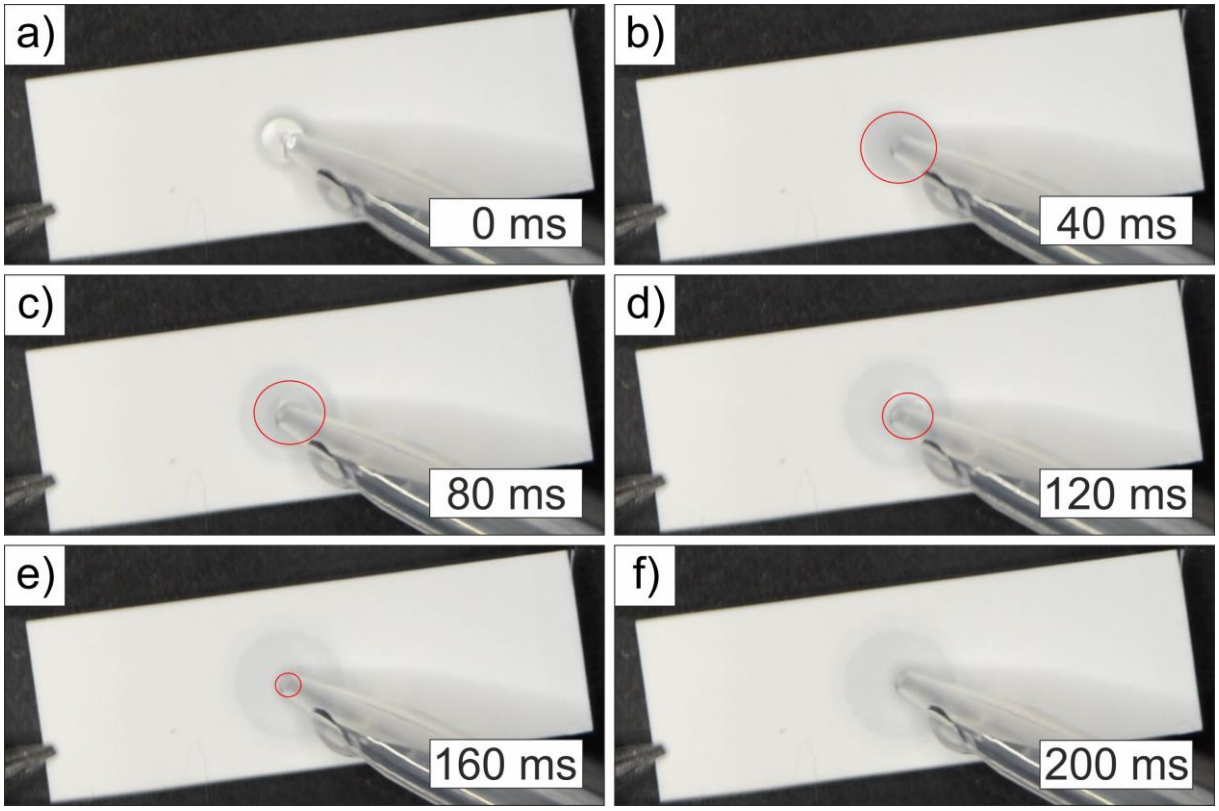

Fig. 17: Image sequence of droplet imbibition at the air side of a pristine MicroPES® 2F membrane. Red rings indicate the droplet perimeter at the elapsed time after applying the water droplet on the surface: a) time zero where the droplet gets in contact with the membrane, b) – f) subsequent image sequence with a time increment of 40 ms.

Any change in the surface properties of a membrane caused by a specific treatment will change the imbibition time and can thus be observed. But any changes observed by this method will not run directly parallel to those monitored by the wetting and drying experiment. This is due to the fact that the imbibition of water is a time dependent process which relies

mainly on the sorptivity of the membrane and not on the capillary forces, which govern the drying of the membrane [41]:

$$I = S \cdot \sqrt{t}\,, \tag{4}$$

with I the cumulative infiltration, i.e. the absorbed liquid per area at time t, and S the sorptivity. The sorptivity for a single capillary tube can also be written as:

$$S = \left(\frac{r}{2}\right) \cdot \left(\frac{\gamma\ \cos\theta}{\mu}\right)^{1/2} \cdot \sqrt{t}\,, \tag{5}$$

whit r the radius of the capillary, μ the viscosity and γ the surface tension of the liquid and θ the contact angle between the liquid and the surface. As the same amount of ultrapure water was used in each test, the influence of the water properties can be neglected. It can also be assumed that the pore diameter does not change after the contact with chemicals, see Fig. 18 in chapter 2.4.1. Thus only the surface tension or contact angle can be responsible for a change in imbibition time. A change in time reveals a change in the hydrophilicity of the membrane surface. This test will not provide information about potential degradation in the inner parts of the membrane.

2.5. Experimental results and discussion

The three investigation methods explicated in the preceding sections will now be used for the examination of the two different flat-sheet membranes introduced in section 2.3. To analyse the impact of different cleaning agents, both pristine and chemically treated membranes were tested. A comparison of the results should provide information about the amount of degradation caused by the treatment of the membranes and also disclose which membrane layer was strongest affected by the cleaning agents. A vital parameter is also the minimum dose of the cleaning agents necessary to cause an amount of degradation which is measurable with the methods used. Further investigations of hollow-fibre and multi-pore membranes were performed only with FT-IR.

2.5.1. Temperature characteristics

Because the membranes investigated are highly porous, with pore sizes down to 200 nm, capillary forces play a major role in the wetting and drying process. The capillary height of a liquid column is given by the Young-Laplace equation:

$$h = \frac{2\,\gamma \cos\theta}{\rho\ g\ r}\,, \tag{6}$$

with g the gravitational acceleration, r the mean pore radius, θ the contact angle, γ the surface tension, ρ the density of the liquid and h the resulting liquid column height, which can be related to the pore length. Because ultrapure water was used in all experiments, the parameters ρ as well as g can be omitted in the discussions below. To check if the chemical treatment caused any structural changes of the membrane such as pore size or surface roughness, SEM images of the cross-sections of both pristine and treated membranes were recorded. Membranes treated with the highest dose used in the experiments for the respective agent were prepared for this comparison. Fig. 18 shows SEM images of all four cross-sections overlaid with the corresponding moving average of the normalised pixel intensity profile. These profiles were generated by first performing segmentation of the cross-sections and calculating the average pixel intensity of every vertical line of the image. Subsequently, all profiles were normalised to their maximum and the respective moving average calculated to ensure comparability (program used for the calculation: Origin 9.0G, OriginLab, Northampton, MA).These profiles were used to obtain a qualitative parameter to verify structural changes in addition to the visual comparison of the cross-sections. A qualitative interpretation is acceptable, because only small areas of the membranes were used for the calculation of the intensity profiles. Nevertheless, both the visual impressions of the images and the intensity profiles of the treated membranes agree with those obtained from the pristine membranes. Thus, chemical treatment does not induce major changes in the mean pore size nor the pore size distribution across the cross-sections. From these results it can be inferred that in eq. (6) the contact angle and the surface tension are the only parameters which can undergo changes in the event of membrane degradation and thus are responsible for changes in the corresponding temperature profiles recorded during the wetting and drying experiments. It should be mentioned, however, that at the drying profile the vaporisation of water is additionally dependent on the temperature of the liquid, the water vapour pressure of the surrounding and its temperature difference to the liquid. These parameters should not have an influence on the results because the investigations were always performed in the same controlled experimental environment. Therefore, any changes in the temperature profile can be attributed to changes in the properties of the materials, especially their hydrophilicity.

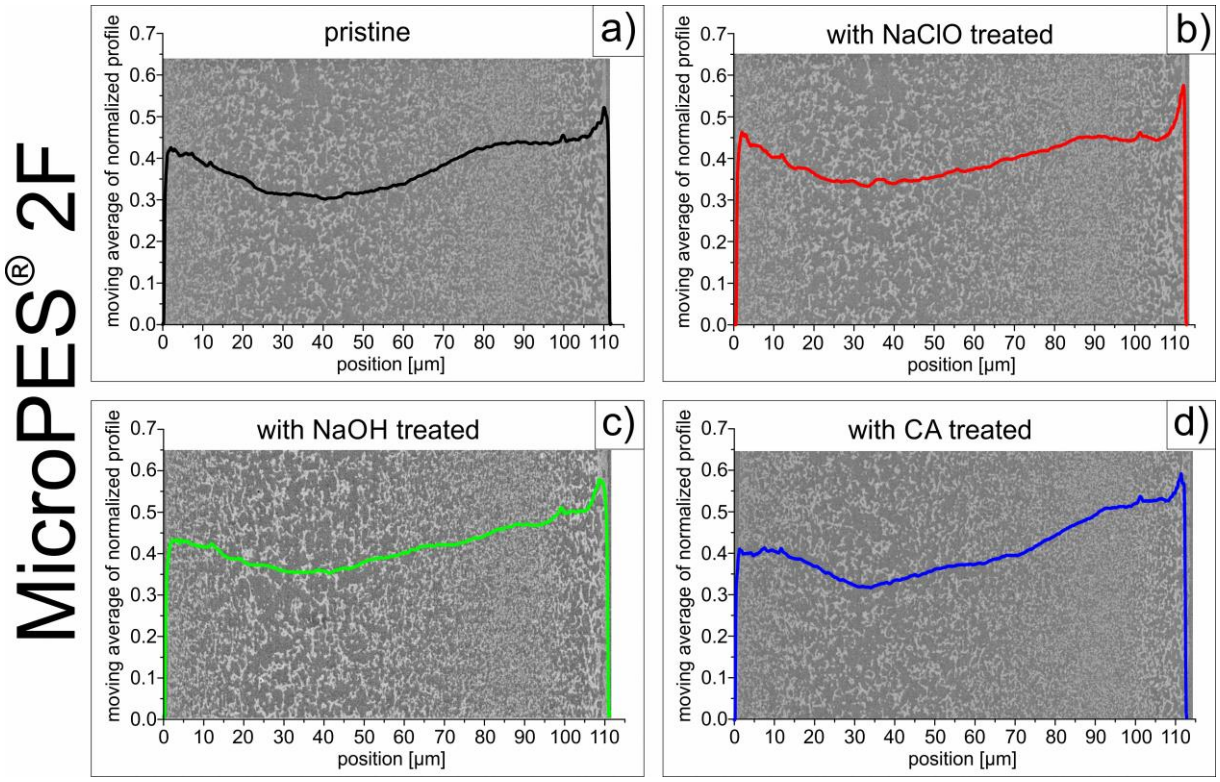

Fig. 18: SEM images of the cross-sections and corresponding moving average of the normalised histogram profile of a pristine MicroPES 2F membrane and the same membrane treated with different cleaning agents: a) pristine, b) 30,000 ppm.day NaClO (30,000 ppm concentration), c) 12,000 ppm.day NaOH (4,000 ppm concentration) and d) 8,000 ppm.day Ca (2,000 ppm concentration).

Because the experimental setup developed and used by Reingruber *et al.* [21] got slightly modified to increase its stability against damage, first tests were performed to examine if any differences in the temperature profiles recorded by both setups were detectable. For that purpose temperature profiles of both pristine membranes were recorded with the modified setup and the results were compared to those stated in the publication [21]. Additionally the reproducibility of the measurements got reviewed recording profiles from 4 different pristine MicroPES® 2F membrane samples and comparing the results. Fig. 19 proves that the reproducibility is definitely very excellent, and that the accuracy of the measurements relating to the overall drying time is better than plus/minus 5 s. In comparison to the results from Reingruber, the shape of the profiles was the same, but the complete drying of the membrane lasted longer (e.g. approximately 10 % for the MicroPES® 2F). Therefore, it is important to use the same setup every time, because any changes affect the resulting temperature profile. Especially changes in the area of the membrane strips and the pressure change will cause changes in the drying time. But a high reproducibility can be obtained by using for all measurements the same experimental setup, the same sample size and the same environmental conditions in the ESEM.

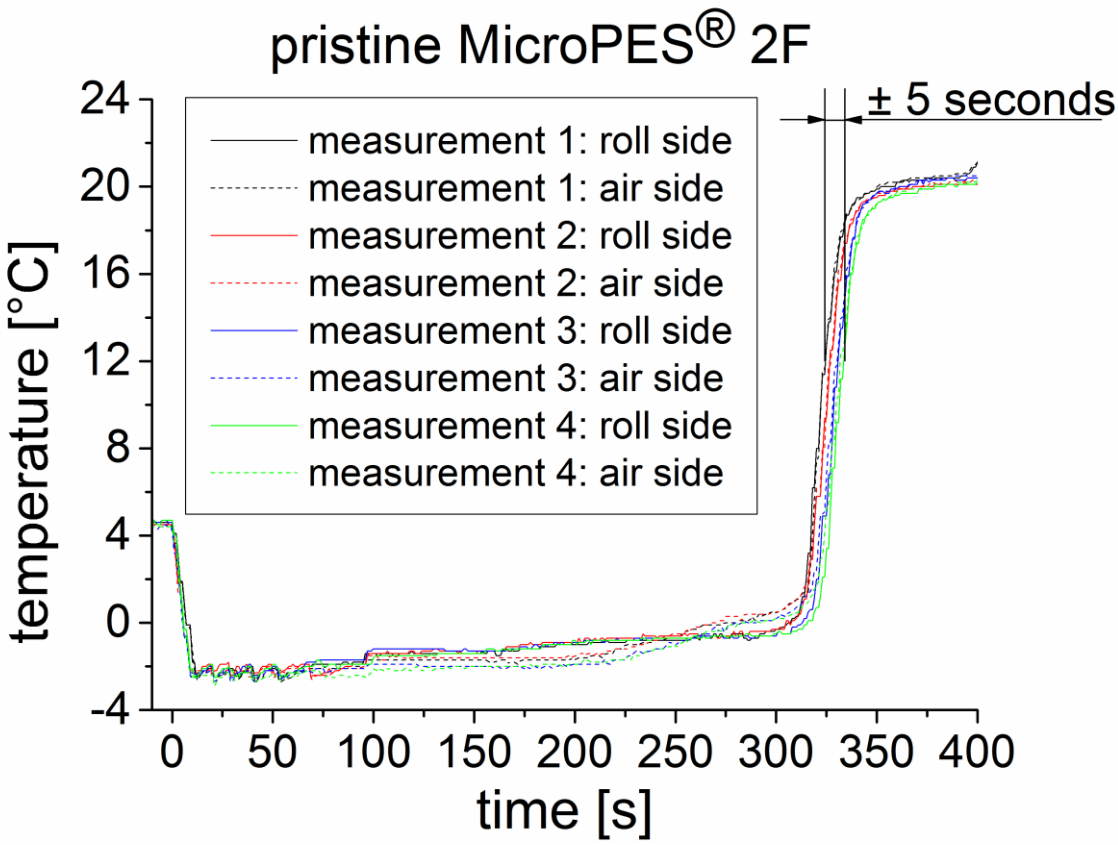

Fig. 19: Investigation of the reproducibility of the modified experimental setup at a pristine MicroPES® 2F. Four different samples were used to record the profiles.

2.5.1.1. Reference temperature profiles

In order to obtain reference measurements for both pristine membranes, temperature profiles of the membranes and SEM images of a surface were recorded with the new setup (see Fig. 20 and Fig. 21). Both profiles in Fig. 20 reflect the asymmetrically layered structure of the membrane. The drying process starts at time zero after the thermal equilibrium was reached. After the sharp temperature drop, due to cooling as a result of the vaporisation of water, the temperature remains nearly constant. First vaporisation of the thin closed water film at the surface occurs, followed by the drying of the surface pores. Representative SEM image sequences recorded at the roll side and the air side of a DuraPES® 600 are shown in Fig. 21. The specified times give the duration after the pressure change and thus the start of membrane drying. Darker regions in the image indicate pores that have already dried. After 200 sec the water from the surface pores at the roll side has already evaporated, while the smallest pores at the air side are still filled with water. The recorded image sequences also make it possible to obtain the start and end of the drying of the surface pores. The double arrows inserted in Fig. 20 mark these times for the air side. The left arrow indicates the drying out of the first big pores, the right arrow marks the drying out of all surface pores.

After the surface pores have dried out, a step in the temperature profiles can be observed. Generally both the height and the length of the steps in the profiles measured at the two

membrane surfaces differ from one another. This temperature increase is caused by the diffusion of water vapour through the already dry surface pores. The measured temperature is an average of the temperature of the cold water vapour diffusing out through the already dry surface pores and the temperature of the warmer surrounding water vapour diffusing into these pores. As a rough approximation, the height of the step is both a measure of the distance between the separation layer and the respective surface and the pore size in the support layer. The step in the temperature profile recorded at the air side is smaller because of the smaller distance between the separation layer and the surface. The length of the step correlates with the thickness of the separation layer, but also adjacent layers with comparable pore sizes could contribute. The lengths of the individual segments of the temperature profile and thus the overall drying time will also depend on the hydrophilicity of the membrane layers. As different segments of the drying profile represent processes in different membrane layers, a change in the temperature profile should indicate which layer is mainly responsible for this change. Additionally, the SEM images recorded at the membrane surface provide additional information about processes occurring directly at the surface and the drying of the surface pores.

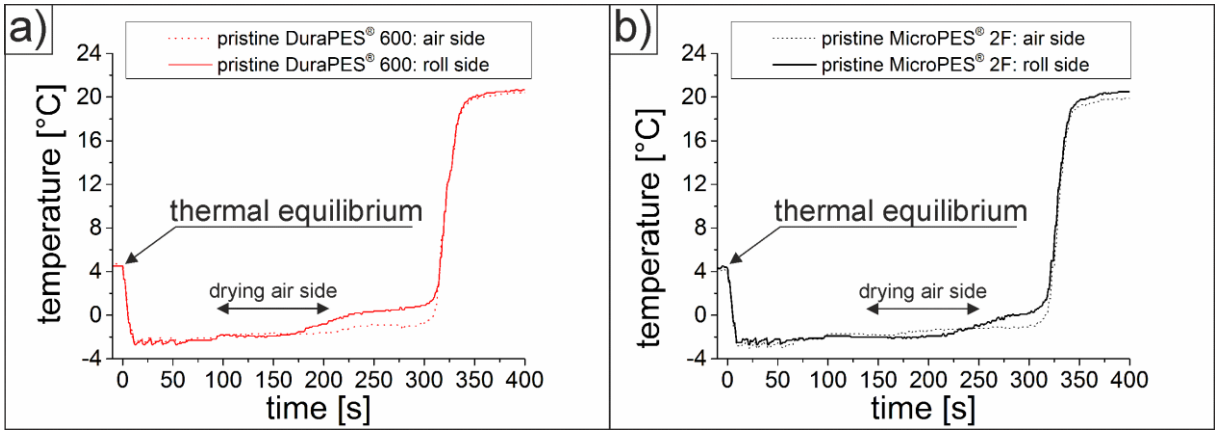

Fig. 20: Temperature profiles recorded during the drying process of a pristine a) DuraPES® 600 and b) MicroPES® 2F microfiltration membrane.

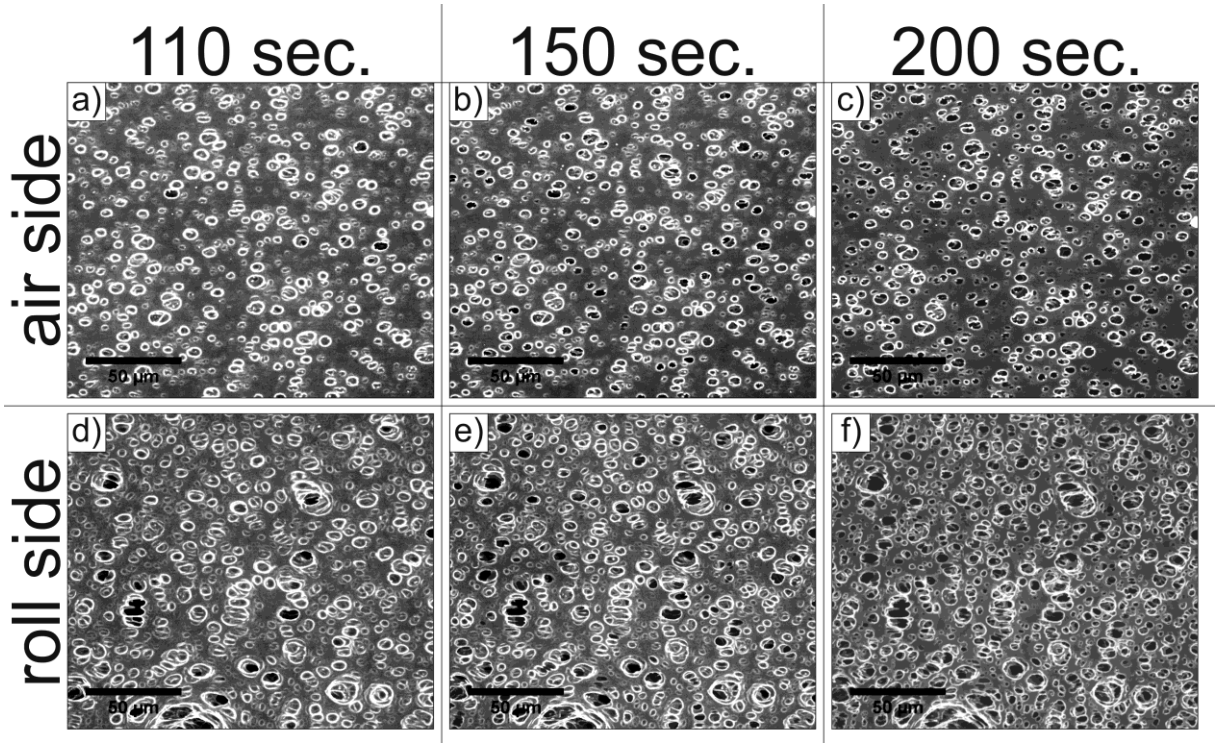

Fig. 21: ESEM image sequences of the DuraPES® 600 membrane recorded during the drying process at both the air side (a) – c)) and roll side (d) – f)) at the respective time after initialising the drying process.

2.5.1.2. Treatment of different membranes with the same dose

One incentive for the *in situ* experiments and the recording of the temperature profiles was the expectation that this technique allows a spatially resolved analysis of changes in the membrane structure or membrane properties. In a first test, the two membranes already investigated were treated with the same relatively high NaClO dose of 30,000 ppm.day. This was done by soaking the membranes in a 30,000 ppm NaClO solution for 24 h. This also enables a direct comparison of the two different membranes in terms of membrane degradation and whether or not the amount of degradation is dependent on the membrane type. The resulting temperature profiles are shown in Fig. 22, where two different time axes were used to enable a better comparison. Fig. 22 a) and c) show that the overall drying times decrease, while Fig. 22 b) and d) demonstrate that both the length and height of the last temperature steps remain unchanged. This indicates that the separation layers were not affected by the treatment. The ESEM image series additionally reveal that the drying times of the surface pores at the air side also remain constant for both membranes investigated. Thus the overall decrease in the drying time of the treated membranes is due to the time necessary to evaporate the thin closed water film at the membrane surface. The decrease in the total drying time was stronger for the MicroPES® 2F membrane than for the DuraPES® 600 membrane. This could be due to the smaller surface pores of the MicroPES® 2F membrane. As a consequence, the contact area between the water film and the membrane material is larger than in the DuraPES® 600 membrane. The actual reason for the decrease in drying times is most probably a

decrease in the hydrophilicity of the membrane material directly at the surface, due to degradation of the PVP. It is not surprising that this effect is strongest at the surface. The IR maps in Fig. 14 show that the PVP concentration is by far the highest at the membrane surfaces.

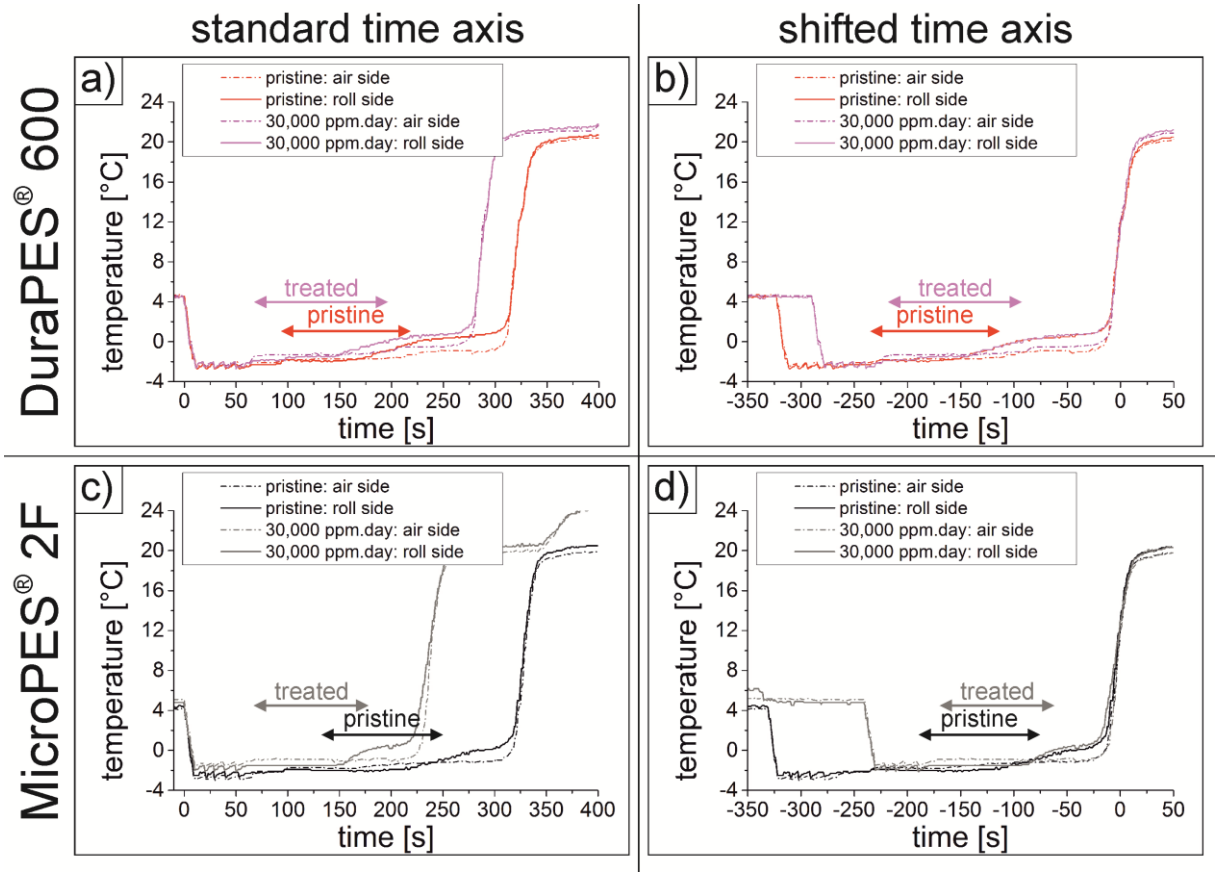

Fig. 22: Temperature profiles of different membranes after treatment with the same dose of 30,000 ppm.day (NaClO with a concentration of 30,000 ppm). The double arrows indicate the start and end of the drying of the surface pores at the air side. Two time axes were used for a better visualisation of the drying behaviour of the DuraPES® 600 at a) and b), and the MicroPES® 2F at c) and d).

2.5.1.3. Impact of different cleaning agent concentrations

The impact of varying doses of the cleaning agent NaClO on membrane degradation was studied on the MicroPES® 2F membrane. The MicroPES® 2F membrane was chosen because, as shown in the previous chapter, the degradation with the same dose of NaClO is higher for this membrane than for the DuraPES® 600 membrane. This should enable the detection of changes in the temperature profile at much lower doses. The concentration of free chlorine was varied between 4,000 ppm and 15,000 ppm. The soaking time was varied from 1 h up to 24 h to achieve a lowest dose of 167 ppm.day and a highest dose of 15,000 ppm.day. A detailed list of the doses used in the experiments can be found in Tab. 1.

Tab. 1: NaClO doses used in the investigation of the MicroPES® 2F membrane.

Concentration [ppm]	Time [h]	Dose [ppm.day]
4,000	1	167
4,000	24	4,000
15,000	5	3,125
15,000	24	15,000

The lowest concentration of 4,000 ppm caused a small but insignificant change in the overall drying time for both treatment times (see Fig. 23 a)). To avoid confusion caused by too many contiguous profiles, only the temperature profiles recorded at the air side were plotted. Irrespective of the dose, again no changes were found in those segments of the profiles which represent the drying of the separation layer. By increasing the concentration to 15,000 ppm of free chlorine in the solution, a clear change in the temperature profile was observed, see Fig. 23 b). Even at a lower dose of 3,125 ppm.day a clear decrease in the overall drying time was found in comparison to a higher dose of 4,000 ppm.day at a concentration of 4,000 ppm NaClO. Fig. 23 b) also demonstrates that a large difference in the dose is not necessarily accompanied by a large difference in the drying time. This proves that the amount of membrane degradation introduced by the treatment depends mainly on the concentration of the cleaning agent and that the duration of the treatment and thus the dose is less important. Likewise, higher concentrations do not lead to significant changes at the segment of the temperature profile indicating the drying of the separation layer. Thus the main changes of the membrane properties are always due to degradation at the topmost layer, which changes from hydrophilic to more hydrophobic behaviour. This corroborates the results described in the previous section.

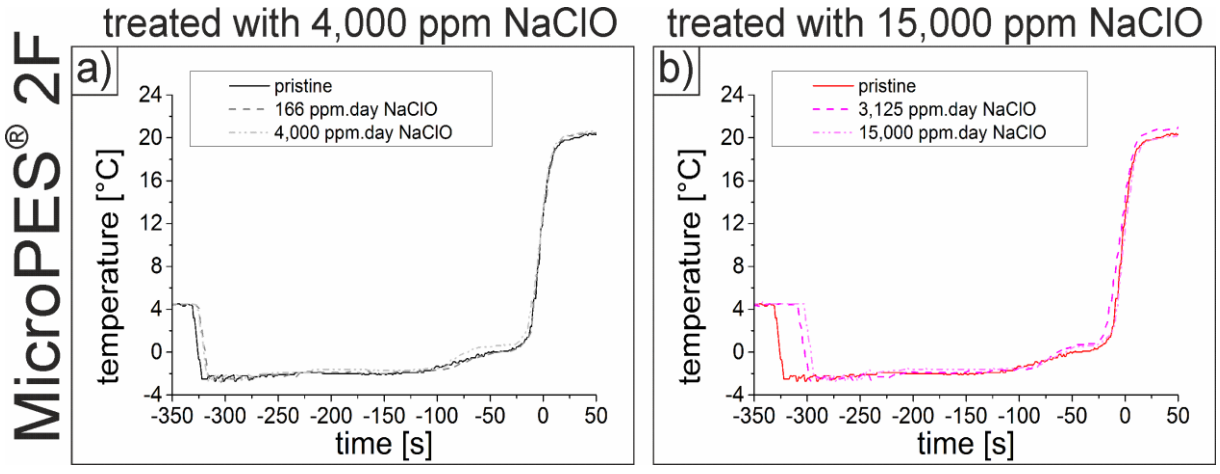

Fig. 23: Temperature profiles of the MicroPES® 2F membrane treated with various free chlorine concentrations at different lengths for time. a) concentration of 4,000 ppm and b) concentration of 15,000 ppm.

It must be pointed out, however, that the membranes were only soaked in the solutions used for the treatment. The results could be different if they were flushed with the solutions, causing a continuous exchange of the solution in the pores and so keeping them in constant contact with fresh solution.

2.5.1.4. Impact of various cleaning agents

Besides NaClO, NaOH and occasionally CA are also used for membrane cleaning and disinfection. In this investigation, two different concentrations of each solution and different soaking times were used to obtain the doses stated in Tab. 2.

Tab. 2: Solutions of NaOH and CA with the respective concentrations, lengths of time and the resulting doses.

Cleaning agent	Concentration [ppm]	Time [h]	Dose [ppm.day]
NaOH	3,000	24	3,000
NaOH	3,000	48	6,000
NaOH	3,000	96	12,000
CA	2,000	24	2,000
CA	2,000	48	4,000
CA	2,000	96	8,000

The membranes were again examined after the treatment using the *in situ* wetting and drying setup. The results can be seen in Fig. 24. The results obtained for both agents were similar to those obtained for the previously discussed NaClO: the higher the dose the larger the decrease in overall drying time. The strongest effect was observed after treatment with NaOH at 12,000 ppm.day. A comparison with the results from the membranes exposed to NaClO showed that the decrease in drying time was nearly the same as for a treatment at 30,000 ppm.day (at a concentration of 30,000 ppm). This indicates that not only the dose but also the chemical used has a great effect on membrane degradation after treatment. Nevertheless, neither of the chemicals caused a significant change in the length of the last temperature step, indicating the drying of the separation layer. Treatment with one of these cleaning agents thus does not lead to a substantial degradation of the inner layers of the membrane but mainly to changes in the properties of the topmost layers. As discussed above, these results also indicate a decrease in the PVP concentration in those regions, making the membrane more hydrophobic.

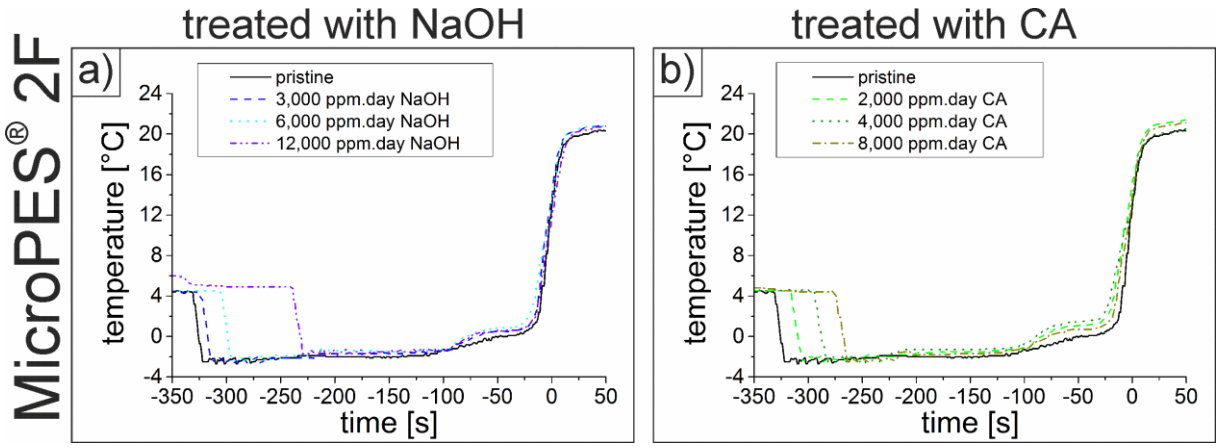

Fig. 24: Temperature profiles of a MicroPES® 2F membrane after treatment with various doses of a) NaOH and b) CA.

2.5.2. Infrared spectroscopy

The *in situ* wetting and drying experiments in the ESEM have shown that treatment with one of the three cleaning agents caused primarily a change in properties at the membrane surface. Another method, infrared spectroscopy, was applied to confirm these results. The spectrometer provides several modes. Macro ATR-IR was used to reveal changes of the PVP concentration at both membrane surfaces. Subsequently measurements using both the macro imaging and transmission imaging modes were performed at cross-sections of the membranes to map the PVP distribution across the cross-section. The results will be presented and discussed in the following chapters.

2.5.2.1. Macro ATR-IR investigation

Macro ATR-IR spectra were recorded at both surfaces of the MicroPES® 2F membranes. After integration over the intensities of the characteristic bands of PES and PVP the PVP / PES ratio was calculated. The changes in this ratio were compared with the changes of the overall drying time ascertained by the ESEM measurements. To obtain a more reliable result, two measurements were performed for each membrane surface and the results were finally averaged over all four measurements. Fig. 25 shows the results for all three investigated cleaning agents as a function of the dose. In all cases the PVP / PES ratio initially drops significantly, followed by a smoother decrease at higher treatment doses. Like the wetting and drying experiments in the ESEM, these results also show a distinctive decrease in the PVP concentration – and thus an increase in hydrophobicity – at the membrane surfaces after treatment with one of the cleaning agents. Additionally, they reveal that the drying time and the PVP concentration do not have to be in direct correlation to each other. Both characteristics show different slopes. Yet it can be assumed that the correlation between the PVP / PES ratio and hydrophilicity and also drying time is not linear. This could be due to the fact that the IR measurements are only surface sensitive, whereas the ESEM measurements comprise the

whole membrane volume. It is also well known that too high PVP concentrations reduce the hydrophilicity of the membranes again. Other studies have proved that the relationship between the PVP concentrations in PES ultrafiltration membranes and the respective contact angles is also nonlinear [42]. Additionally, this investigation revealed a correlation between the hydrophilicity of the membrane and its surface roughness. But the PVP / PES ratio cannot be affected by the surface roughness. Thus, as different parameters govern the outcome of different measurement methods, the changes in membrane properties and behaviour measured with these methods will not necessarily run completely along the same slope. The PVP / PES ratio will also not always give full account of all the damage mechanisms occurring in the material. Occasionally both PES and PVP may be damaged by the treatment, with the ratio remaining constant. But the IR measurements possibly show that there is a certain PVP concentration range within which the membrane properties do not undergo essential changes. Nevertheless, the ATR-IR measurements show that the PVP concentration verifiably decreases at the membrane surface after treatment with one of the cleaning agents.

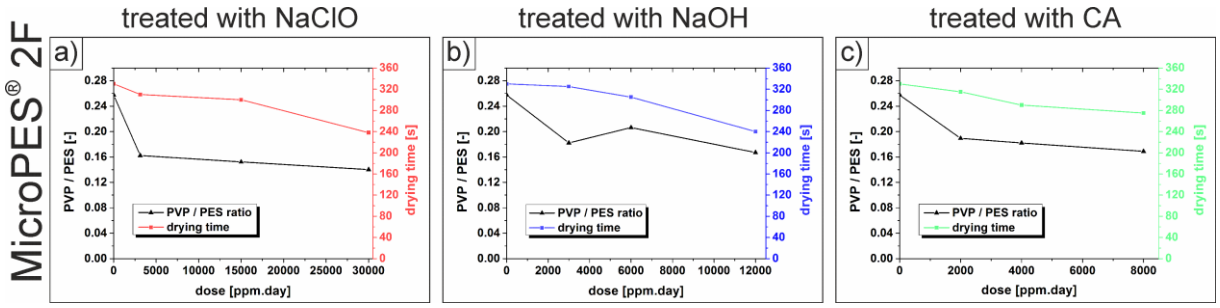

Fig. 25: PES ratio at the membrane surface and total drying time of membranes as a function of the chemical agent and the dose used for treatment. The PVP / PES ratios were measured by macro ATR-IR, the drying times by *in situ* experiments in the ESEM. a): 3125 ppm.day (15,000 ppm*5 h); 15,000 ppm.day (15,000 ppm*24 h), 30,000 ppm.day (30,000 ppm*24 h); b): 3000 ppm.day (3000 ppm*24 h), 6000 ppm.day (3000 ppm*48 h), 12,000 ppm.day (3000 ppm*96 h); c) 2000 ppm.day (2000 ppm*24 h), 4000 ppm.day (2000 ppm*48 h), 8000 ppm.day (2000 ppm*96 h).

2.5.2.2. Transmission FT-IR investigations

The spatially resolved IR measurements across the cross-sections were carried out in transmission mode. Fig. 26 shows four results of the PVP / PES distribution over the membrane cross-section in dependence on the pre-treatment. A different colour setting than given in the maps in chapter 2.4.2 was used and the same scale was chosen for all maps for better comparability. The biggest changes occur after treatment with 4,000 ppm.day of CA, see Fig. 26 e). The fact that CA has a large impact on the membrane is also shown in Fig. 24 b), where even low doses led to a substantial decrease in the overall drying time. The membrane treated with NaOH showed slight changes at the air side, whereas the other regions were not significantly affected, see Fig. 26 d). Fig. 26 b) and c) depict the results for the membranes treated with NaClO. In both cases the greatest changes can be observed at the roll side. It has to be mentioned, however, that all examinations represent only a small region where only a small amount of PVP is present. Thus no reliable quantitative concentration

values can be calculated and only a qualitative analysis of the results is acceptable. But a comparison of the PVP / PES map of the cross-section of the pristine membrane with the maps of the treated cross-sections shows a distinct decrease in the PVP concentration of the membranes after treatment. This confirms the results obtained from the *in situ* ESEM wetting investigation, where the overall drying time decreased after membrane treatment. The shorter drying time is due to the decrease in the PVP concentration and thus the hydrophilicity of the membrane.

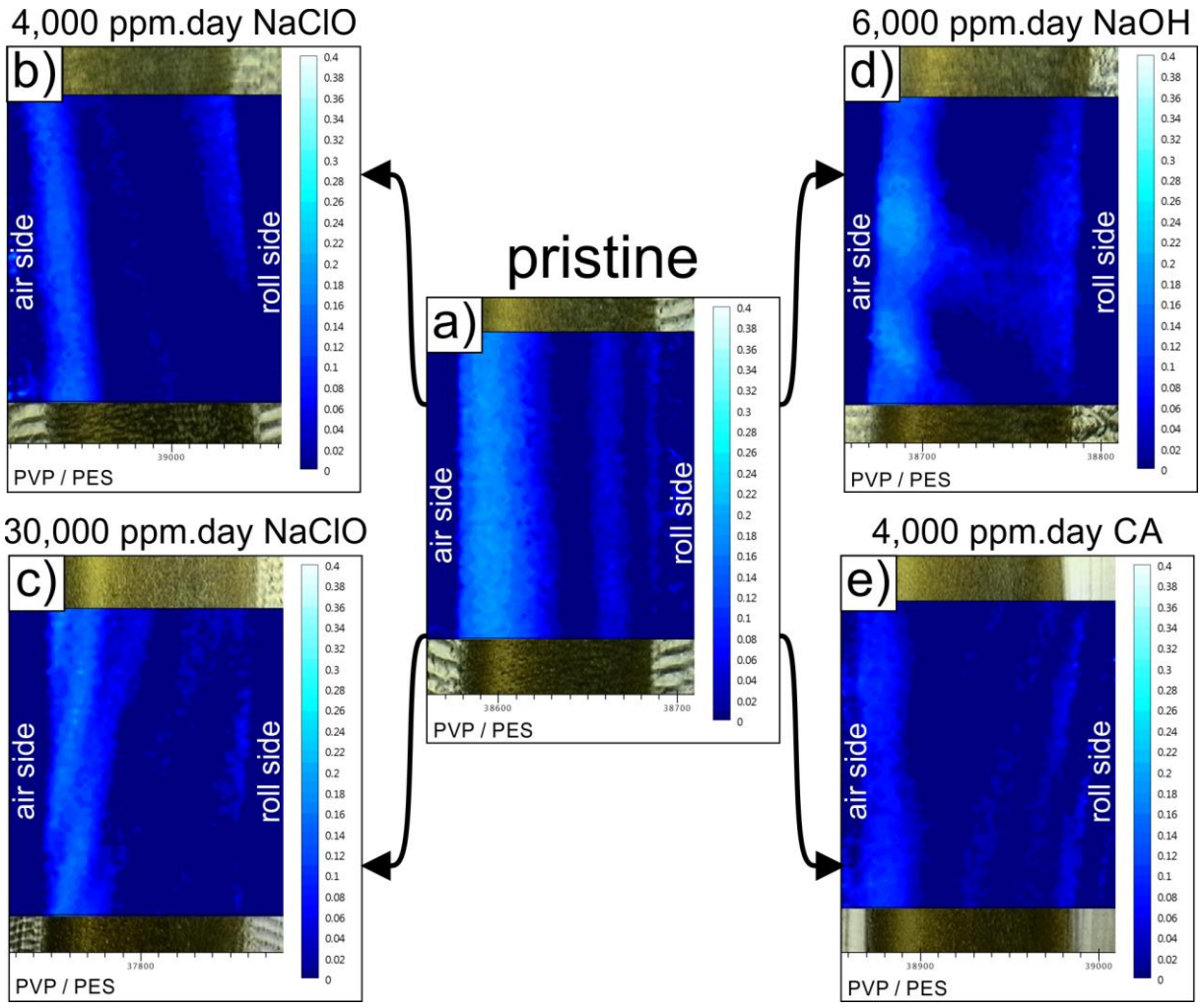

Fig. 26: IR maps of the PVP / PES ratio across the membrane cross-section of a MicroPES® 2F membrane: a) pristine, b) treated with NaClO at 4,000 ppm.day (concentration of 4,000 ppm) and c) 30,000 ppm.day (concentration of 30,000 ppm), d) treated with NaOH at 6,000 ppm.day (concentration of 3,000 ppm) and e) treated with CA at 4,000 ppm.day (concentration of 2,000 ppm). The background consists of light microscopic images of the membrane recorded in the same area as the maps.

It has to be mentioned that small PVP signals in the resin were also detected in the maps, see e.g. Fig. 26 e). The division of a small intensity at the characteristic band of PVP by an intensity close to zero at the PES band leads to a disproportionately large PVP / PES ratio. The small signal at the PVP band in the spectra recorded in the resin could be due either to a

dissolution of PVP in the resin during the embedding process or to impurities in the resin with a band overlapping with the characteristic band of PVP. Nevertheless, the method not only enables the investigation of flat-sheet membranes, but more or less of every type of polymeric membrane. A pristine hollow fibre ultrafiltration membrane from Membrana© was examined as an example, see Fig. 7 b). The resulting IR maps at Fig. 27 show that here again the PVP concentration is not evenly distributed across the whole membrane cross-section and is highest at the inner tube surface.

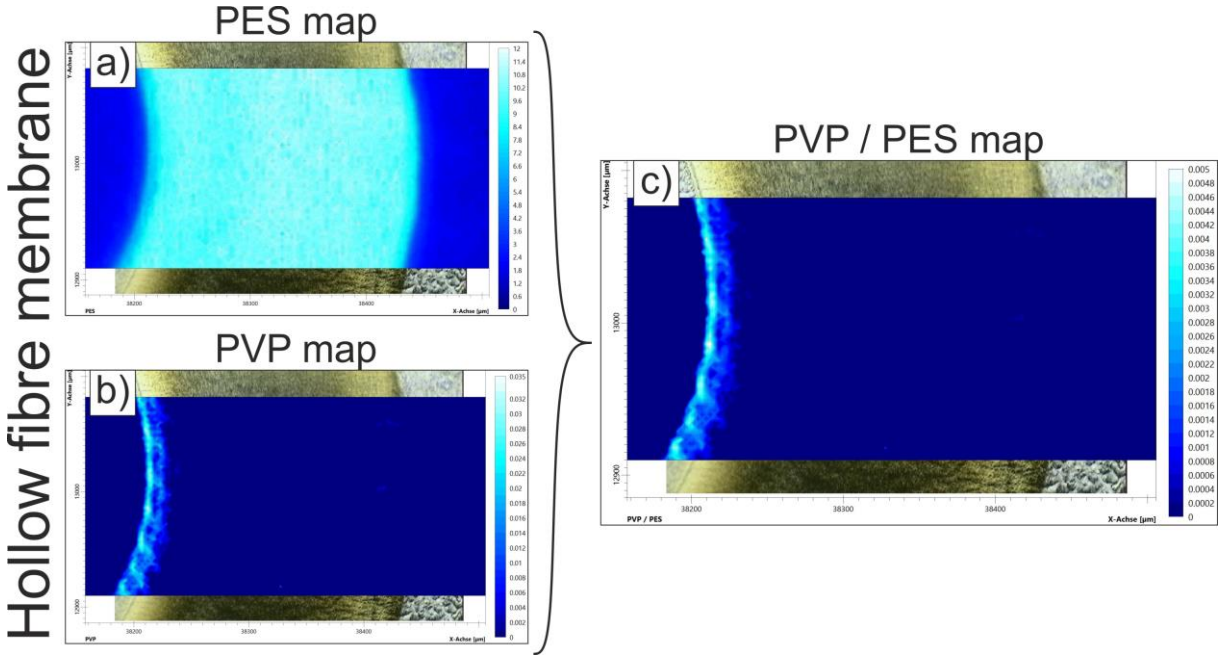

Fig. 27: IR maps of a pristine hollow fibre membrane of a) PES, b) PVP and c) the PVP / PES ratio. The background consists of light microscopic images of the membrane recorded in the same area as the maps.

To examine the effects of NaClO on other types of PES and PVP based membranes, pristine and treated versions of a flat sheet membrane (see Fig. 7 a)) provided by the University of Rennes[2] and a multi-pore membrane (see Fig. 7 c)) provided by the University of Poitiers[3] were additionally investigated. Fig. 28 a) shows the PVP / PES maps for the flat sheet membrane after the production process. Fig. 28b) shows the membrane after 20 h treatment with a 400 ppm NaClO solution. In the pristine membrane the PVP concentration is highest at one surface and decreases continuously across the cross-section towards the opposite surface. In comparison to the pristine membrane the treated one shows a clear decrease in the PVP concentration practically throughout the cross-section, but an especially strong one at the

[2] Université de Rennes, Institute des Science Chimiques de Rennes, Rennes, France

[3] Institute de Chimie des Milieux et Matériaux de Poitiers, Univeristé de Poitiers, Ecole de Ingénieurs de Poitiers, Poitiers, France

surface with the originally highest concentration. The mismatch between the light microscopic background image and the IR map is due to the serial imaging process. One image consists in most cases of two maps and the stage shift between the two images is not always perfect.

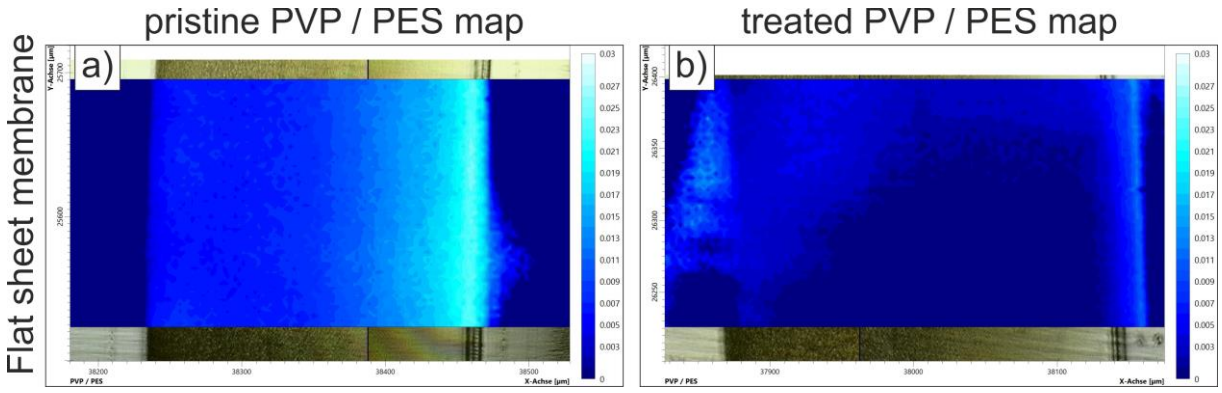

Fig. 28: PVP / PES maps of a) a pristine PES based flat-sheet membrane and b) after 400 ppm NaClO treatment for 20 h.

The same analyses were performed for the multi-pore membrane. Fig. 29 shows the result of a representative area of both the pristine and treated membranes. Only a part of the cross-section was investigated because the membrane was too thick to fit into one recording. The map of the pristine membrane in Fig. 29 a) shows that PVP was detected only at the inner tube surface. Subsequently, a treated membrane was investigated at the same position. A 15 ppm NaClO solution was used to flush the membrane for 180 h to obtain a dose of 2,700 mg.h/L. PVP was no longer detectable at the inner tube surface, as shown by the PVP / PES map.

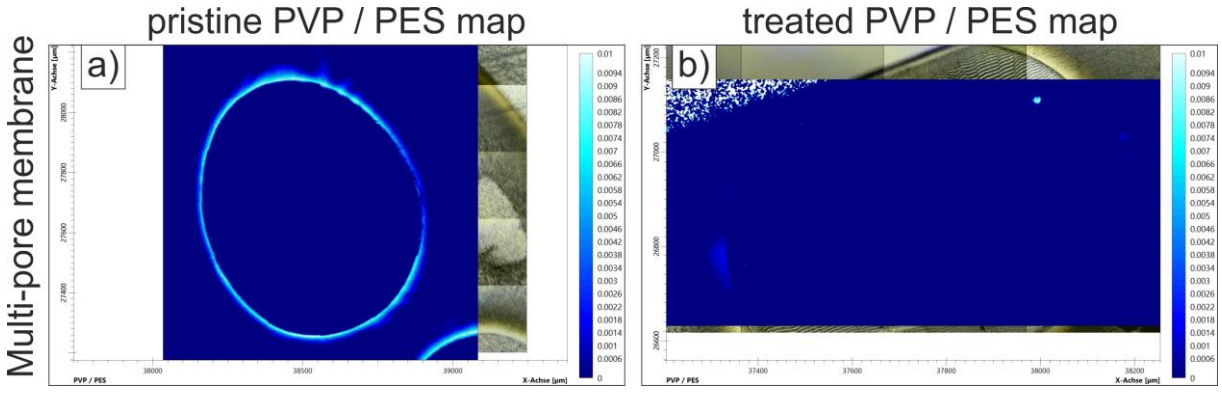

Fig. 29: Maps of both a) a pristine and b) a treated multi-pore membrane. The treatment was performed by flushing the membrane with a 15 ppm NaClO solution for 180 h to obtain an exposure dose of 2,700 mg.h/L.

All investigations by transmission IR spectroscopy proved that it is possible to obtain spatially resolved maps of the main components. The PVP concentration in all pristine membranes was unevenly distributed over the respective cross-section. A comparison of the IR maps of pristine membranes and membranes treated with NaClO always showed a decrease in the PVP concentration, irrespective of the membrane type or treatment dose. This microscopic method thus provides additionally to the ESEM investigation a supplementary possibility to obtain spatially resolved results of the PVP degradation process due to chemical treatment. But these maps only provide information about one cross-section, whereas in the wetting and drying experiments a large membrane volume is investigated, resulting in better statistical significance.

2.5.3. Droplet imbibition test

The MicroPES® 2F membrane used in most previous experiments was also used for the droplet imbibition test. For a theoretical discussion of the process see chapter 2.4.3. Because the imbibition of water and the membrane drying in the ESEM are partly governed by different parameters and additionally by a different dependency of parameters controlling both processes, the results gained by both methods do not necessarily show a linear correlation, as was also the case for the IR measurements. But the results gained by the imbibition test should also show the same tendency as those obtained from the wetting and drying experiments and the infrared measurements. As already discussed in section 2.4.3, the only parameters which can cause a change in the imbibition time are related to the material properties, namely surface tension and viscosity, both of which are connected with the hydrophilicity of the surface.

Fig. 30 shows the imbibition time as a function of the dose of different cleaning agents. A sharp initial increase in the imbibition time can be observed for all agents. But whereas the membranes treated with NaClO show no significant change at higher doses, the imbibition time further increases with increasing doses of NaOH and CA. Because the imbibition time is dependent on the material properties, the results indicate that the topmost layers of the membrane have become more hydrophobic. These results are in accordance with the results obtained from the ESEM and IR spectroscopy measurements, which also show a degradation of PVP in the membrane.

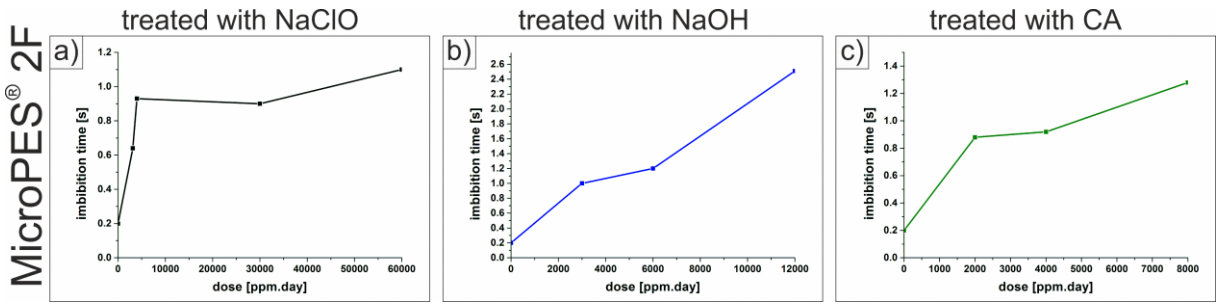

Fig. 30: Imbibition time of 1 µl ultrapure water as a function of membrane treatment: a) treated with NaClO, b) NaOH and c) CA.

2.6. Conclusion and Outlook

Experiments were carried out to study the impact of three cleaning agents, sodium hypochlorite, sodium hydroxide and citric acid, on polyethersulfone and polyvinylpyrrolidone based multi-layered microfiltration membranes. To do this, the two different multi-layered membrane types DuraPES® 600 and MicroPES® 2F were investigated both in pristine condition and after treatment with the cleaning agents and the results compared. The main aim was to ascertain whether wetting and drying experiments in the ESEM are a suitable method to find out whether the treatment caused membrane degradation, and if so, to identify the membrane layer most affected by the treatment, and also to elucidate the type of chemical attack that caused this degradation. The changes in membrane structure / properties may be caused not only by cleaning procedures, but also by membrane ageing or fouling.

The membranes were treated by soaking them in solutions with different concentrations for various lengths of time resulting in different treatment doses. The wetting and drying experiments in the ESEM proved that the topmost layers of both membranes became more hydrophobic after the treatment, but that the internal layers, especially the separation layer, were not affected. This was concluded from a decrease in the overall drying times of the membranes, whereas the drying times for the inner membrane layers did not change. Because PVP increases the hydrophilicity of the membrane material, the results indicate its degradation at the respective layer. Furthermore, the results show that the treatment is more dependent on the concentration of the respective agent in the solution than on the treatment dose, i.e. the length of soaking time. A higher concentration but lower dose leads to a greater change in drying times than vice versa. Additionally, the amount of degradation is highly dependent on the chemical used. At low doses, a larger effect was achieved by the treatment with citric acid than with the other two chemicals. But in general, the applied dose must be relatively high to obtain a measurable effect. The presented method proved in principle to provide reliable and spatially resolved results.

FT-IR measurements were used to verify the results obtained by the ESEM experiments. The membrane surfaces were first examined by macro ATR-IR to investigate possible changes in the PVP concentration after treatment with the cleaning agents. It was shown that the PVP concentration rapidly decreased at low doses, followed by a smoother PVP reduction at higher doses. These measurements thus confirmed the results obtained from the wetting and drying experiments in the ESEM. However, the increase in degradation as a function of dose obtained by the two methods did not show a linear correlation. The main reason for this may be a nonlinear correlation between the amount of PVP at the membrane surface and its hydrophilicity. Subsequently, transmission IR spectroscopy was used to record spatially resolved PVP / PES maps across the membrane cross-sections. The highest PVP concentration in the MicroPES® 2F membranes was found at the surface on the air side, a smaller amount at the surface on the roll side, whereas nearly no PVP was detected in the central region. A comparison of the PVP distributions in IR maps recorded at the cross-sections of pristine membranes with those of treated membranes proved that the treatment with CA caused the greatest changes, even at low doses. This also agrees with the results obtained from the drying experiments in the ESEM. A decrease in the PVP concentration was also determined for the membranes treated with the other cleaning agents. It should be mentioned, however, that only a few cross-sections were mapped and the low PVP concentration and the

pore size distribution allow only a qualitative interpretation of the results. The results obtained from the drying measurements in the ESEM, in contrast, comprise a large volume, resulting in a much higher statistical significance. Additionally they also provide information about changes in the membrane properties caused by degradation mechanisms not detectable by IR spectroscopy, such as changes in the membrane structure.

The strongest degradation was always observed at the membrane surfaces, which may be due to the fact that the PVP concentration is highest there. The main mechanism thus definitely seems to be damage of the PVP or its dissolution from the matrix.

A third method used to observe membrane degradation involved dropping ultrapure water droplets on the membrane surface and accurately measuring the imbibition time. A distinct increase in the imbibition time already at low cleaning agent concentrations is a clear evidence of a rapid decrease in hydrophilicity. A steady increase in the imbibition time was found for higher doses of NaOH and CA, whereas the imbibition time for NaClO treated membranes remained nearly constant. Again, the nonlinear correlation between these results and those obtained from the ESEM experiments is due to the fact that the imbibition time depends on parameters other than the drying time of the membrane and that the former is restricted to degradation at the membrane surface. Nevertheless, the results of the imbibition test also indicate a damage of PVP after exposure to one of the cleaning agents.

Further investigations could simulate a more application-related treatment scenario by flushing the membranes instead of only soaking them in the solution. The transmembrane flow could possibly lead to a stronger degradation already at lower doses and to a measurable effect also at the inner layers of the membranes because of the permanent exchange of cleaning agent. To enable a quantitative interpretation of the IR measurements, it will be necessary to investigate larger areas and to find a resin which does not dissolve one of the two components. But both IR spectroscopy and drying experiments in the ESEM allow spatially resolved investigations of the impact of the cleaning agents on polymeric microfiltration membranes. The droplet imbibition test provides an additional convenient method to investigate changes in the surface properties. By combining all three methods a comprehensive insight into the membrane degradation process can be obtained.

3. Fracture of polymers and 3D reconstruction

3.1. Introduction

Polymers are widely used in almost every industrial field. They are used in aeronautics, automotive and household appliances because many of their physical properties can be tuned and also due to their resistance to many chemicals and their easy processability. This is why fundamental research on the different properties of different types of polymers and blends is a focus of great interest for many industries and universities. One widely used polymer is polypropylene (PP), which is additionally available with a large variety of filler particles to adjust the desired properties of the material. This thesis investigates the fracture behaviour of ethylene propylene rubber (EPR) and linear-low density polyethylene (LLDPE) modified PP. The former is used for producing blends for, e.g., the automotive industry [3]. As PP forms a stiff matrix and the rubber inclusions provide a balanced stiffness-impact behaviour, this hetero polymer has physical properties suitable for car parts. Another frequently used PP modifier is LLDPE, which was investigated by different methods to study its behaviour under different conditions [43], [44]. A topic which is frequently investigated experimentally is the resilience against physical impacts, the ramification of the material and the formation of cracks or crazes.

A variety of theoretical approaches to describe the formation of crazes and crack propagation in polymers and polymeric blends has been developed [45]. A frequently used experimental technique for testing the fracture behaviour of polymers is tensile testing [46], [47], which enables the direct measurement of , e.g., the maximum tensile strength, maximum elongation and strength at break, and subsequent calculation of other material properties like the Young´s modulus or Poisson´s ratio. Specially designed tensile stages can also be mounted in the specimen chamber of an ESEM [9]. It is thus possible to perform tensile tests and simultaneously record high resolution images at the crack tip during the whole process. The microstructures developing at the crack tip and their modification during the tensile test can be directly observed at high magnification and great depth of focus. Nevertheless, the information that can be gained is limited to structural changes occurring at the sample surface, whereas no insight is provided, e.g., into the cracks formed inside the sample. This requires a 3D reconstruction of the bulk of the material using one of several techniques available. One of these methods is X-ray computer tomography [48]. Its resolution is limited, however, and the differences in the densities of the organic components of a polymer blend may be too small to give a reliable phase contrast. Therefore investigations often resort to slice-and-view techniques, where different kinds of microscopes can be used for the imaging process [49]. But the respective 3D distribution is then just a snapshot at a predefined stress / strain during the tensile test.

The method used in this thesis is serial block-face scanning electron microscopy (SBEM) which was introduced in 2004 by Denk and Horstmann [50]. An ultramicrotome is mounted inside the specimen chamber of a scanning electron microscope. This setup enables an automated slice-and-view process at high resolution, with the images recorded at the freshly cut block face. The method was developed in the field of life science, where most of the SBEM publications can be found (exemplarily see [51]–[54]). However, also first results in materials science application of SBEM for the investigation of polymers and composite materials were published in 2009 [55]. These were followed by publications on membranes or porous monoliths [10], [56], different materials including particles [57], [58] or metals [59], [60]. Zankel

et al. [55] published first investigations on polymer blends after tensile testing, but primarily focused on the methodological aspect. Special aspects of 3D reconstruction and data processing are not discussed in this publication. In this thesis the cracks formed by tensile testing and the distribution of the filler particles in the matrix are investigated by SBEM. The 3D reconstruction of the cracks formed by tensile testing in polymeric materials and the distribution of the filler particles in the matrix can be obtained from the resulting image stack following proper sample preparation (see Fig. 41). These results, in combination with the stress-strain diagrams can lead to a deeper insight into the crack formation processes.

Michler and Baltá-Calleja [45] introduced a theoretical approach, where the average interparticle distance and the ratio between the shear modulus of the filler particles and matrix strongly contributes to the crack formation in organic particle modified polymers, with the particles themselves being organic. The interparticle distance is the minimal distance between the surfaces of neighbouring particles, see Fig. 31 b), labelled as “A”. The particles themselves are assumed to be spherical objects. Stress enhancement occurs if the shear modulus of the filler particles G_P is much smaller than that of the matrix G_M: $G_P \ll G_M$. As shown in the schematic in Fig. 31 a), the resulting stress concentration around the filler particle, drawn as a black bold line, is dependent on the angle φ relating to the direction of the applied load σ_0. The angle dependent stress concentration $\sigma_{\delta\delta}/\sigma_0$ reaches its maximum at an angle φ = 90°. This can lead to an increase in the stress concentration between the particles if the filler interparticle distance becomes less than twice the particle diameter, as schematically shown in Fig. 31 b). Thus the smaller the distance, the more likely that crazes or cracks will be formed in the matrix between the particles.

Furthermore, S. Wu already showed in 1988 [61] that the transition between tough and brittle behaviour of nylon/rubber blends is dependent on the surface-to-surface interparticle distance. He also stated that the transition should be independent of the volume fraction of the rubber in the blend and the particle size. But this theory is now much contested. Especially in the theoretical considerations the particles are assumed to be spherical objects which are randomly distributed in the matrix. But as shown in the images of the cross-sections of the EPR08 or LLDPE (see Fig. 32 a) and c)) samples, this requirement is generally not fulfilled. Other publications discuss additional parameters which can be responsible for a failure in the matrix under an applied load. This includes the elongation of the particles and their orientation to the applied load [62], [63], [64], the crystallinity of the sample [65], the testing speed [66] or the notch radius [67], to name but a few. Some of these parameters can be excluded as the same testing speed and notching procedure were applied in all tests. But for the investigation of other parameters, like the influence of the interparticle distance, 3D reconstructions of the samples will be necessary in order to obtain reliable information about crack propagation. This can be achieved by a distance transformation of the filler particle surfaces and by comparing the location of the cracks within the resulting distance map. This will be discussed in detail in chapter 3.5.5.1.

Most of the microscopic investigations of polymer fracturing are restricted to the imaging of the fracture surface after the sample has completely fractured. But from these images it is difficult to extract which microscopic processes were mainly responsible for the fracturing and which rather tend to prevent crack growth. In the investigations presented here the focus was put on the very early stages of the fracturing process, at forces / stresses far below the yield, where the formation of crazes / cracks / voids has just started. Therefore it should be easy to

derive a correlation between, e.g., particle distributions, interparticle distances and crack / craze formation from the respective 3D reconstructions.

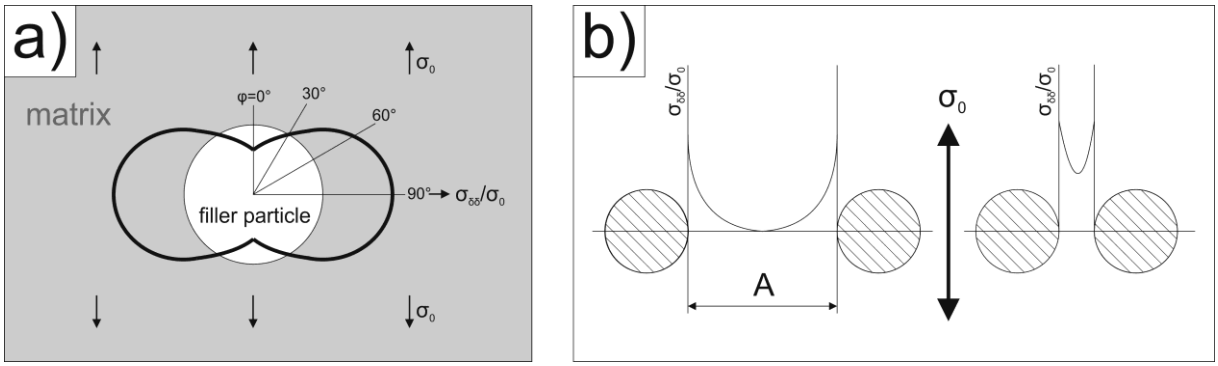

Fig. 31: Schematic of stress concentration around spherical particles marked as a bold black line in a) and its dependence on the interparticle distance in b). Adapted from [45].

3.2. Investigated polymeric blends

The fracture behaviour of three different types of polymeric blends was investigated. The matrix of all three consists of iPP, with the second phase being around 20 wt% of either EPR (two blends) or LLDPE (one blend) filler particles (specimens by courtesy of Borealis Polyolefine GmbH, Linz, Austria). Materials with the same amount of filler particles have been chosen to obtain results which are independent of this parameter. The blends differ not only in their composition but also in the particle size distribution and the shape of the particles. This can be seen in Fig. 32, where both blends EPR08 and EPR10 have approximately the same amount of EPR filler particles, but the particle size distribution and particle shapes differ. Apart from these microscopic parameters, macroscopic ones may also vary like the melt flow index (MFI), see Tab. 3. This index characterises the flow behaviour of thermoplastic polymers [68]. To this aim, a small amount of the polymer must be melted in special equipment and pressed through a capillary with a specific diameter and length applying constant pressure. Subsequently the weight which flows through the capillary is measured every ten minutes by a precise scale and typically given in grams per ten minutes.

Tab. 3: Specification of the investigated polymeric blends.

Name	MFI [g/10 min]	Filler particle amount [wt.%]	Filler particle amount [vol.%]
EPR08: SVA 1244	6.9	20	20.0
EPR10: SVA 1246	2.3	20	20.0
LLDPE: 54732-3	unknown	20	20.5

The specific densities of iPP (approx. 0.92 g/cm³), EPR (approx. 0.86 g/cm³) and LLDPE (approx. 0.92 g/cm³) [69] can be used to calculate the amount of filler particle in vol.%. This amount can be used to check the accuracy of the segmentation algorithm, because the filler particle amount should be the same in the reconstructed volume as in the original material.

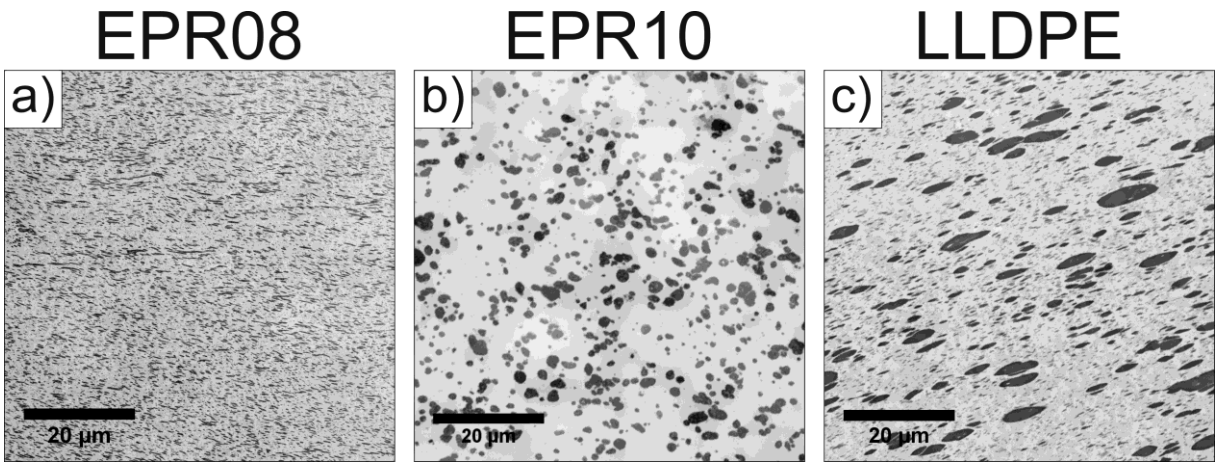

Fig. 32: Cross-section of all three investigated polymer blends with same image width of 70 µm for a better comparison of the particle distribution.

All tests were performed on V notched specimens (depth: 2 mm) of 80 x 10 x 4 mm³ in size. Before performing the tensile tests, the specimens were cut to a length of 62 mm to fit into the tensile stage and pre-cracked with a razor blade (depth: 0.5 mm). Crack propagation will happen in this region due to the high stress concentration at the tip of this prefabricated crack. Because of the small field of view in the microscope, prior knowledge of the region of strongest damage is necessary.

All of the preparatory steps, i.e. crack initiation, mounting at the tensile stage, demounting and ultramicrotome slicing, could possibly already cause craze formation. To test this, samples were subjected to the whole procedure, except the tensile test itself. The TEM image in Fig. 33 a) demonstrates that the preparation did not induce any visible damage. But if additionally a tensile test is performed and stopped at a force of 7 % yield, first crazes start to appear (see Fig. 33 b). Thus, at least in the case of polypropylene, the first crazes appear already at very small forces / stresses.

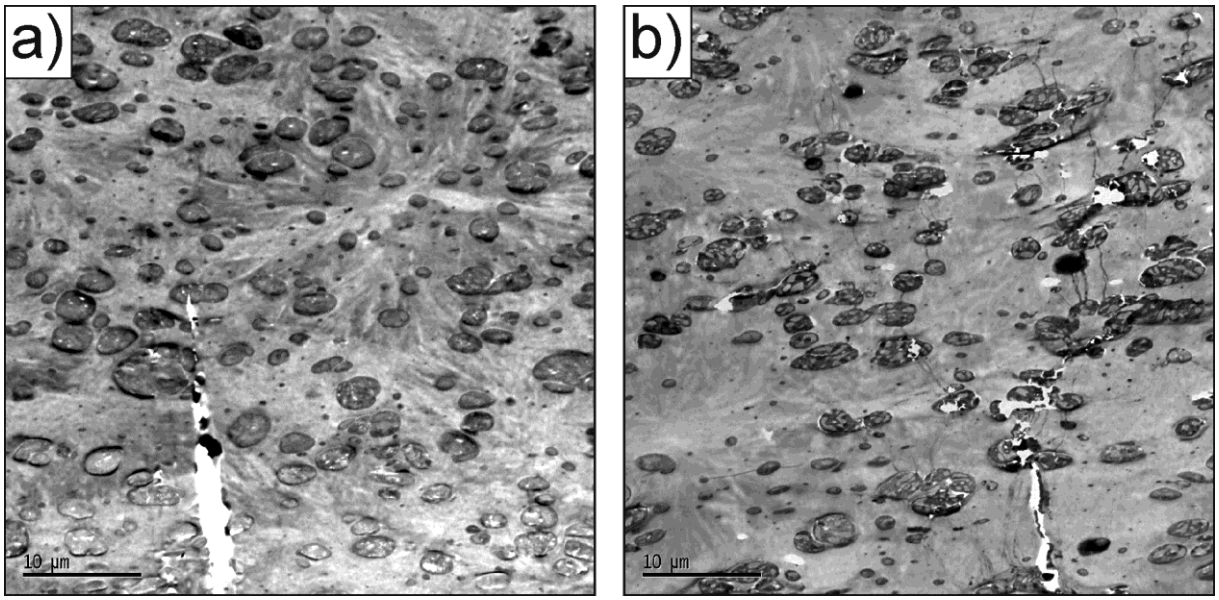

Fig. 33: TEM images at the crack tip a) after pre-cracking with a razor blade and b) after an additional tensile test stopped at a force of 7 % yield; tested sample: iPP 20 wt% EPR particles, MFI of 4.8 (images by courtesy of Dr. E. Ingolic). The crack initiation with a razor blade can be seen at the bottom.

3.3. Sample preparation

Samples must fulfil several requirements for slicing and imaging by *in situ* ultramicrotomy. They have to fit on the sample holder and their width should not exceed that of the diamond knife, the phases in the sample should provide sufficient contrast for SEM imaging and they should be sliceable by ultramicrotomy, i.e. they should be neither too ductile nor too brittle. If the samples are powdery, thin, flexible or porous they must first be embedded in a suitable resin for fixation. As only bulk specimens were used in the present investigations, they only had to be trimmed to an appropriate size by using a trimmer and conventional ultramicrotomy. Hence the samples were trimmed to a cubic size of around 0.6 x 0.6 x 0.6 mm^3 and glued onto a rivet, the sample holder [49]. BSEs were used for imaging because they provide sufficient materials contrast for the differentiation between matrix and particles, and also visualise the cracks/crazes. Yet in the materials to be investigated the density differences between matrix and particles were too small to give sufficient contrast. They were also too ductile to be cut with a diamond knife without previous hardening. Staining, which is the addition of heavy atoms to specific structures, solved both these problems. It highlights stained features, in the present case the filler particles and cracks, and additionally hardens the material. A schematic of the staining process and the resulting chemical reactions can be found in Fig. 34, where staining is performed with RuO_4 (ruthenium tetroxide). To do this, the sample was fixed inside an airtight container holding a small amount of ruthenium trichloride [70]. In order to start the reaction to achieve the necessary RuO_4 vapour, a 5 % aqueous solution of sodium hypochlorite was poured over the ruthenium crystals. The samples were kept inside the sealed container for at least 12 h to obtain the maximum penetration depth.

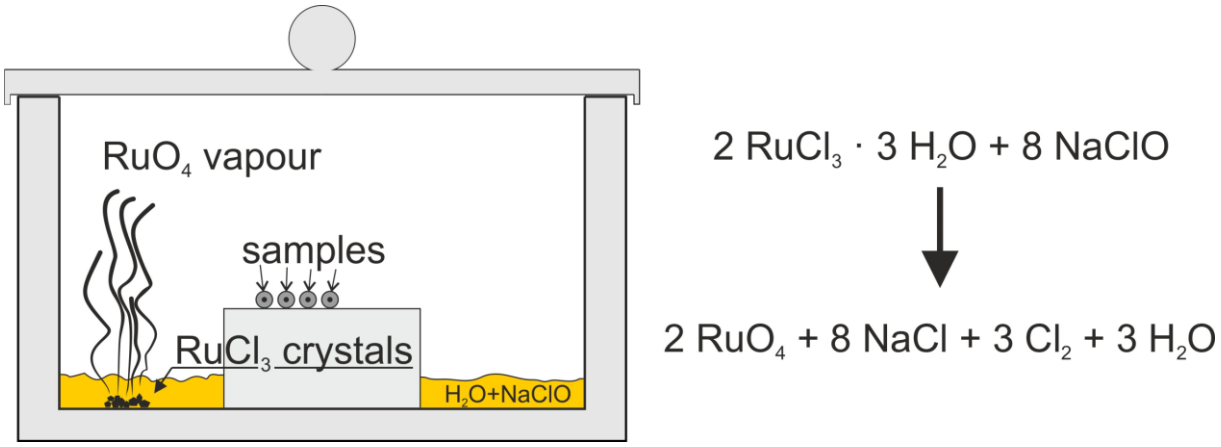

Fig. 34: Schematic of the staining process of polymer samples with RuO_4.

Three samples of pure isotactic PP were prepared to determine the penetration depth of ruthenium tetroxide into the investigated material. They were cut parallel and normal to the flow direction out of two different materials in order to obtain sample and direction independent results. The exposure time to the ruthenium environment was set to at least 14 h. The sample was then cut using an ultramicrotome, see Fig. 35 a). The whole sample was additionally coated with a thin carbon layer by carbon filament evaporation to obtain an electrically conductive surface and enable investigations under high vacuum in the SEM. All analyses were performed with an acceleration voltage of 10 kV and a working distance of around 11 mm. Two techniques were used for measuring the depth profile of the ruthenium concentration into the samples. The first technique uses the EDS (energy dispersive X-ray spectrometry) system, while the second method involves measuring the contrast variation in the BSE images. As the BSE signal intensity is dependent on the mean atomic number at the beam position, the ruthenium penetration depth profile can also be obtained by evaluating the grey level intensity distribution in a BSE image. Therefore, before performing the first EDS measurement, a BSE image was recorded to be able to compare the EDS profiles with those obtained from the grey level variations. Subsequently the stained area was subdivided into equidistant rectangular zones of the same size, approximately 2.9 x 42.0 µm², see Fig. 35 b). To make the measurements comparable, the X-ray spectrum for every zone was collected for a period of 300 s. The distances given in Fig. 35 are those to the mesa shape surface (shape of trimmed sample), which is characterised by higher surface roughness compared to the smooth microtome cut (marked as a green line in Fig. 35 b)).

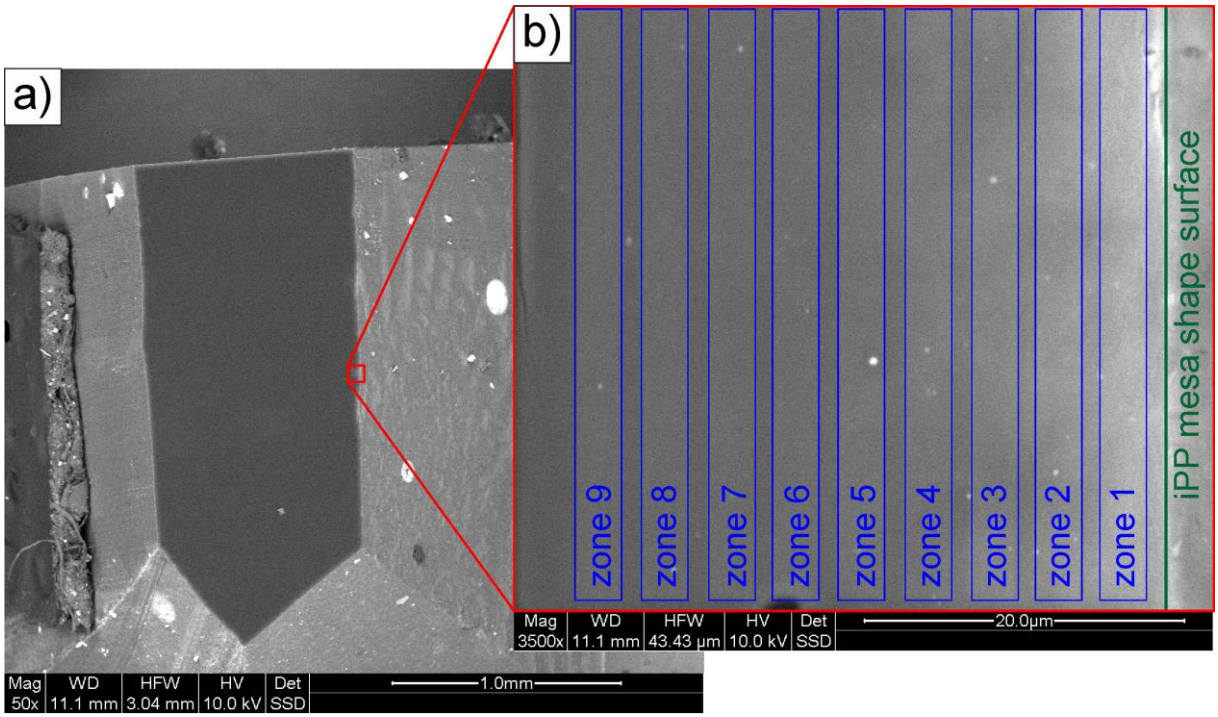

Fig. 35: Isotactic polypropylene; a) sample overview, showing the microtome cut with the investigated area marked in red; b) magnified image of the investigated area with the regions for EDS analysis marked in blue and the mesa shape surface in green.

Three measurements each were performed on two different samples and the Ru concentration profiles calculated from both the EDX spectra and the BSE images displayed in Fig. 36. The ruthenium concentration was calculated using only the net counts of the Ru-Lα peak. Because the maximum counts differ for every measurement, their maxima were normalised to one for better comparability. The results can be seen in Fig. 36 a), where additionally the average of all six examinations were calculated using the program Origin 9.0G (OriginLab, Northampton, MA). The mean grey levels per zone in the BSE images were calculated using the Fiji program. These results were also normalised to one and their average calculated, see Fig. 36 b). Additionally, the standard deviation was calculated for both averaged profiles, see Fig. 36 c). It can be seen that the profiles obtained by both the EDS and BSE measurements show practically the same downward slope, an approximately exponential decrease in ruthenium concentration with depth. Thus the maximum penetration depth of the stain is around 35 µm. As a consequence, serial sectioning and imaging by SBEM is only possible to this depth, which finally restricts the size of the volume for 3D reconstruction.

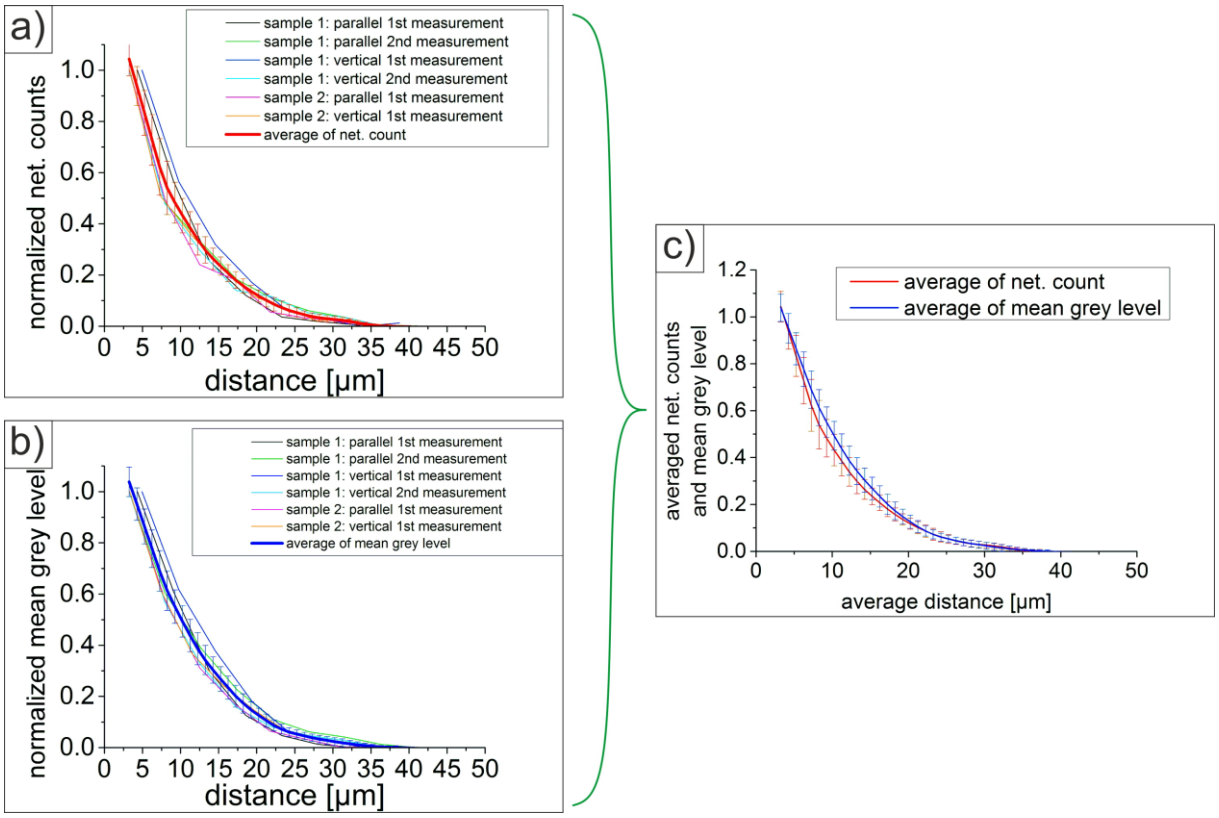

Fig. 36: iPP stained with RuO_4; a) Ru X-ray intensity as a function of specimen depth; b) grey level (BSE) as a function of specimen depth; c) comparison of average depth profiles from both methods.

3.4. Experimental setup

Two different devices must be used consecutively to enable the 3D reconstruction of the inner structures of polymers, in this case the cracks and filler particles. The first device is an *in situ* tensile stage which can be mounted inside the specimen chamber of the ESEM Quanta 600 FEG. The second one requires the door of the microscope specimen chamber to be replaced by another door with a special *in situ* ultramicrotome mounted on it. The two methods will be discussed in more detail in the following.

3.4.1. *In situ* tensile tests

The *in situ* tensile tests were carried out using the tensile stage Microtest 5000 (MT5000) from Deben (Suffolk, UK), see Fig. 37. This tensile stage can be mounted and operated inside the ESEM specimen chamber. The jaw velocity of the stage can be varied between 0.05 and 5 mm/min [9]. The velocity used was 1 mm/min for all investigations in order to obtain comparable results. Three exchangeable load cells are available, with maximum loads of 125 N, 1,250 N and 5,000 N. The force–elongation diagram of all three investigated samples can be seen in Fig. 38. Additionally an inset shows a notched pristine EPR10 sample, where the arrows indicate the direction of the force applied during the tensile test. Because the maximum load for the tested polymeric samples was around 650 N, the 1,250 N load cell was chosen for the tensile tests.

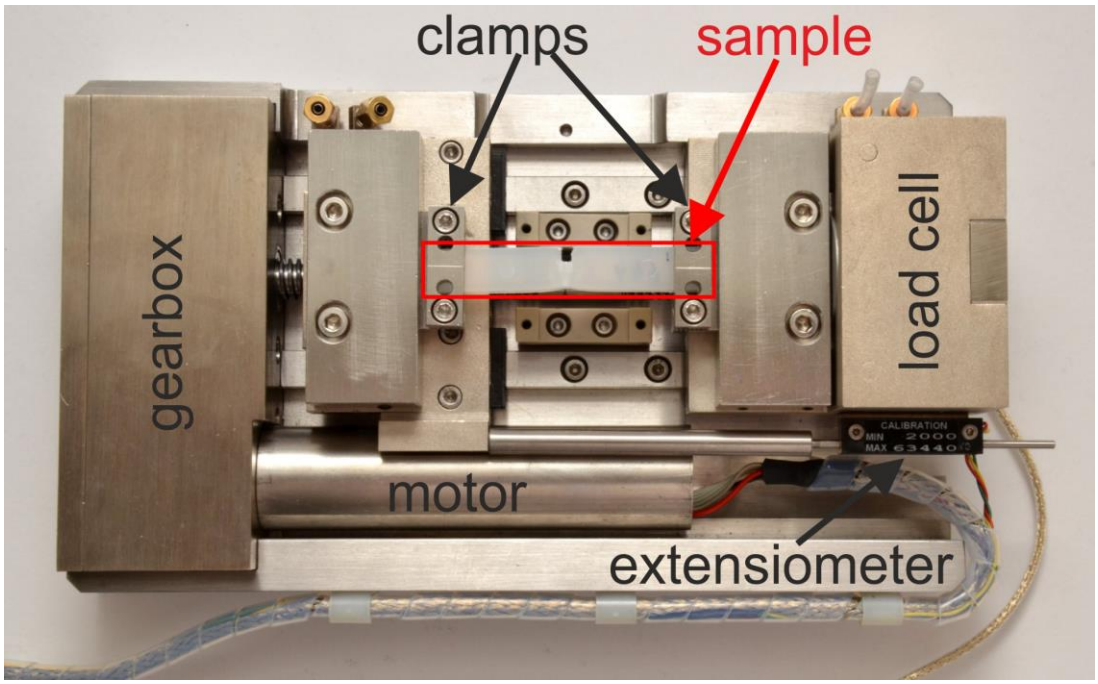

Fig. 37: *In situ* tensile stage MT5000 with a mounted polymer sample (after tensile testing).

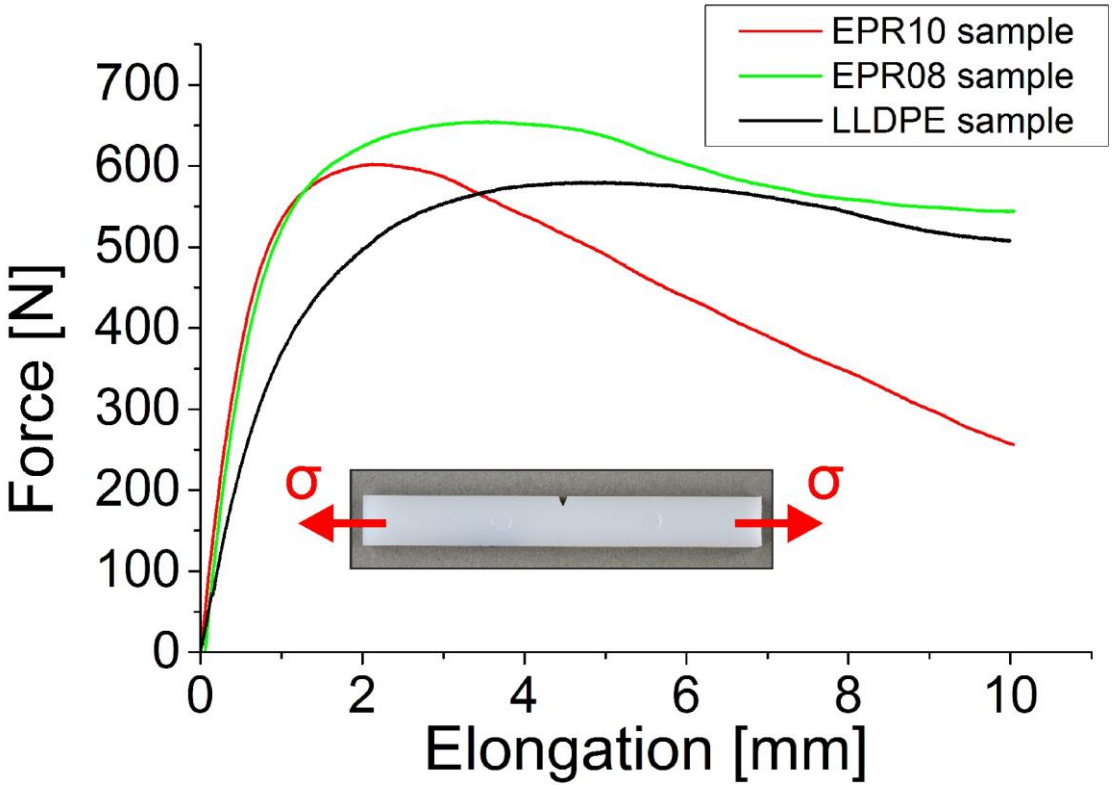

Fig. 38: Force–elongation diagrams of all three investigated polymer samples (test velocity: 1mm/min); the inset shows a notched untested EPR10 sample with arrows indicating the direction of the applied forces.

With this setup it is possible to obtain the force–elongation diagram, while simultaneously recording ESEM images at high magnification and a large depth of focus of the microstructures evolving at the crack tip. To obtain a time resolved measurement, either a video or an image sequence can be recorded by the ESEM. A representative force–elongation diagram of a tested EPR10 sample with the respective image sequence can be found in Fig. 39, where the progress at the crack tip can be correlated with the elongation. For the samples which were further investigated by 3D reconstruction the tensile tests were stopped at a predefined value of yield in the nearly linear region of the respective diagram in Fig. 38. This region is approximately represented by image 2) in the sequence. At these low forces the pre-crack has not widened enough and thus the view at the crack tip is still blocked. Thus unfortunately a correlation between the surface structures formed during the tensile test and those emerging in the bulk and made visible by the 3D reconstruction is not possible for these forces.

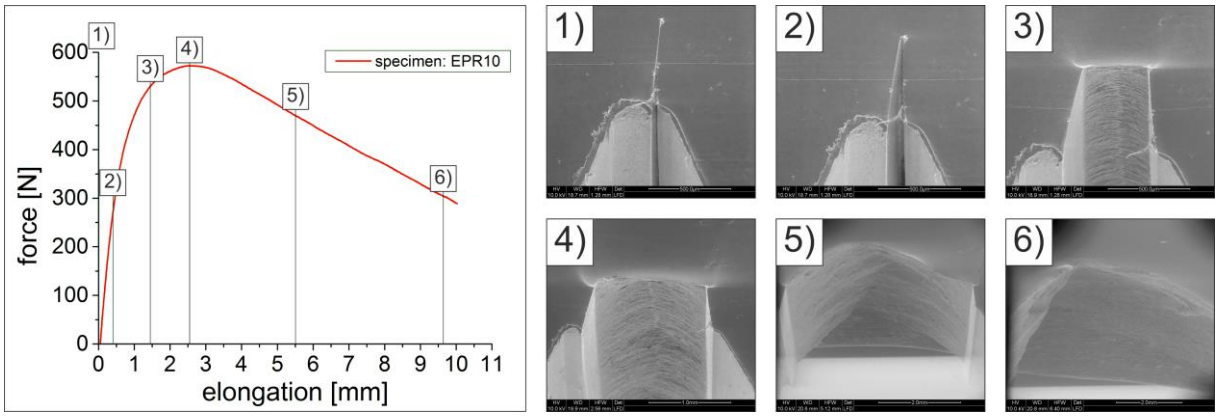

Fig. 39: Force-elongation diagram of an EPR10 specimen with appropriate SEM images at the crack tip at marked positions.

3.4.2. In situ ultramicrotomy (SBEM)

A successful 3D reconstruction first requires a slicing of the material in equidistant steps and image recording at the respective positions. The step size is dependent on the smallest structures to be reconstructed, but is often between 50 nm to 100 nm. One method which enables automated serial sectioning and imaging of materials is serial block-face scanning electron microscopy (SBEM) [49]. In comparison with other methods like serial sectioning and imaging by a focused ion beam (FIB) a much larger sample volume can be prepared within the same timeframe. A schematic of the setup for SBEM, with the ultramicrotome 3View™ from Gatan (Gatan GmbH, Munich, Germany) mounted in the ESEM Quanta 600 FEG is shown in Fig. 40. As an ESEM can be operated at low vacuum, also non-conductive materials can be directly recorded without the necessity of a conductive layer on the sample, see chapter 1. The achievable resolution in x and y direction is around 5 nm for polymeric samples, the resolution in z direction is given by the step size. The step size and thus slice thickness can be chosen in a range from 30 nm to 100 nm. The instrument records images of the block face after each cut. Although the process can be fully automated, monitoring by the user is necessary. The slices tend to adhere to the rear side of the diamond knife due to electrostatic forces and

accumulate there. Every now and then this debris can drop onto the block-face and thus mask the image recorded at the respective block-face. This can be prevented by a periodic cleaning of the diamond knife.

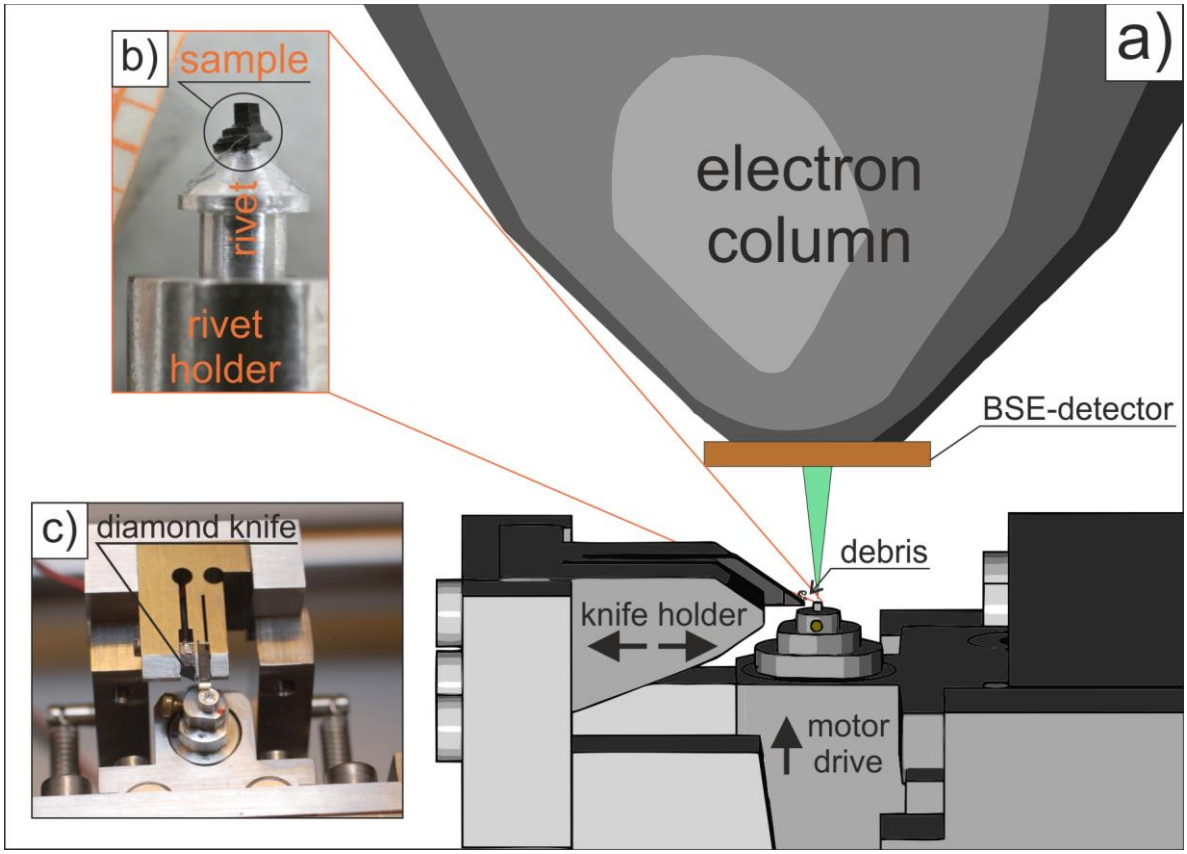

Fig. 40: a) Schematic of the *in situ* ultramicrotome with the BSE detector, b) the sample glued on the rivet and mounted in the holder and c) the diamond knife.

Because the size of the filler particles in the samples is around 500 nm (along the smaller axis for elongated particles), see Fig. 32, a slice thickness of 100 nm was chosen to obtain reliable results. This slice thickness also proved sufficient for the reconstruction of the cracks. The procedure shown in the schematic in Fig. 41 thus provides information about the 3D spatial relationship between the filler particles and the cracks generated during the tensile test.

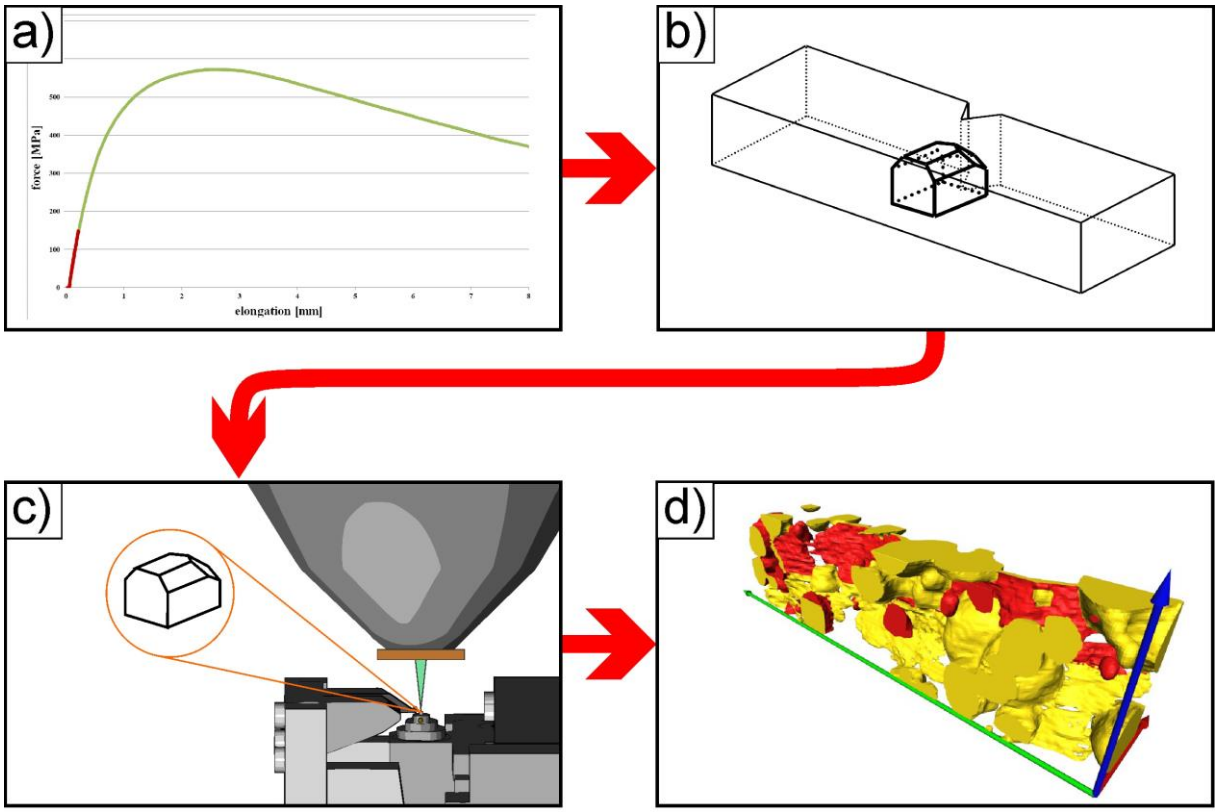

Fig. 41: Schematic of the 3D reconstruction procedure: a) tensile test stopped at a predefined force; b) extraction of region of interest (ROI) with subsequent preparation (RuO4 staining); c) serial sectioning and imaging (SBEM); d) Image processing and 3D reconstruction.

3.4.3. Interaction between electron beam and sample

The irradiation of materials with electrons during the investigations in an electron microscope can damage the material [71]. The critical parameters are the electron energy (acceleration voltage) and the probe current, but whether damage occurs is of course mainly dependent on the kind of material analysed [72]. The resulting change in the specimen properties or structure due to electron irradiation depends on various parameters. Different processes can be involved and damage the specimen. They are typically separated into a primary and secondary category [6]. The primary category includes ionisation or displacement of an atom or excitation of an atom or an atom group. The secondary category includes increase in temperature, emission of X-rays, light or electrons, electrostatic charging, cross-linking or bond scission of the molecules or contamination of the surface due to the formation of a carbonaceous coating. In the case of organic materials like polymers the major causes of damage are atomic or molecular excitation, the ionisation of single atoms, bond scissioning and cross-linking. If water vapour is used as the imaging gas the interaction of electrons with the gas molecules can lead to the formation of reactive radicals which then attack the materials. Thus by using unsuitable microscope settings a degradation of the specimen can emerge. Typically chain scission of the polymer molecules can occur and lead to depolymerisation. It is therefore essential to choose suitable settings for every material investigated in order to avoid at least visible changes of the material. Polymer damage can usually be prevented by choosing very low acceleration voltages (AV) and low electron doses[72]. But in some cases it is not possible to

achieve a suitable image contrast when, e.g., the beam energies or the dwell times are set too low. The microscope settings for image recording will thus be specified in the further discussion, but only a very generalised description of different electron beam impacts on the material will be given.

The first example in Fig. 42 shows the impact of a too high electron dose on the iPP / LLDPE sample. The sample was at first only scanned across the red marked region, followed by an overview image at lower magnification. An acceleration voltage of 7 kV, a spot size (SS) of 4 (determines the probe current), a dwell time of 10 ns, a water vapour pressure of 0.3 Torr and a pixel size of 7.4 x 7.4 nm² were chosen for the scan across the marked region. Specimen damage is clearly visible in the red marked region. These settings thus do not produce reliable images. The resulting image stack from the SBEM is therefore not suitable as a basis for 3D reconstruction. Lower doses must be applied to avoid damage by adjusting the relevant microscope parameters.

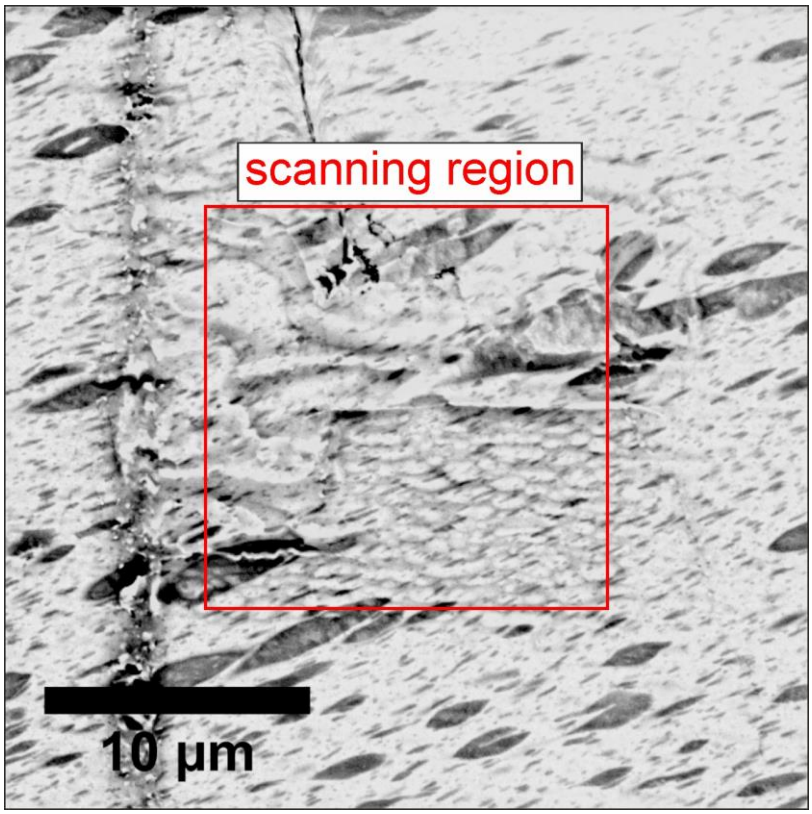

Fig. 42: iPP, modified with LLDPE; SEM image recorded following a scan across the region marked in red. Microscope settings for marked region: AV of 7 kV, SS 4, water vapour pressure 0.3 Torr, pixel size 7.4 x 7.4 nm² with 10 ns dwell time.

Fig. 43 shows a SEM image of an EPR10 sample which was recorded after the serial sectioning and imaging had been stopped at a depth of about 10 µm. As the diameter of the interaction volume is larger than the slice thickness, the marked region is exposed to electron irradiation from at least two scans. Thus the electron dose applied inside the region is higher than that applied outside. In comparison to the former microscope settings, the acceleration voltage was slightly increased to 7.4 kV, the water vapour pressure doubled to 0.6 Torr and,

more importantly, the pixel size increased to 80 x 80 nm². It has to be mentioned that the usage of this larger pixel size was only suitable for this type of sample, because only in these samples is the size of both the filler particles and the cracks large enough to be imaged with sufficient detail. The image in Fig. 43 was also obtained by scanning during sectioning and imaging across the marked region and then lowering the magnification to record a final overview image. In contrast to Fig. 42, no damage can be seen in the marked region. On the contrary, the contrast in that region is higher than outside and all features are clearly visible. Wavelike structures evolved outside the marked region and the contrast continually decreases with increasing distance from the boundary. The wavelike structures seem to be a result of irradiation with electrons which were scattered by the gas molecules in the microscope chamber. As shown in Fig. 3, the higher the chamber pressure the stronger the scattering and thus the larger the skirting. As the pre-set water vapour pressure was twice that used in the procedure resulting in Fig. 42, electron scattering also increases, causing this structural change. This would indicate that as long the dose lies within a certain range, the main mechanism is a cross-linking of the molecules, which leads to hardening of the irradiated material. This conclusion can be drawn because outside the marked region smearing of the material appears earlier than inside, see example in Fig. 44 b). This was also confirmed by other investigations.

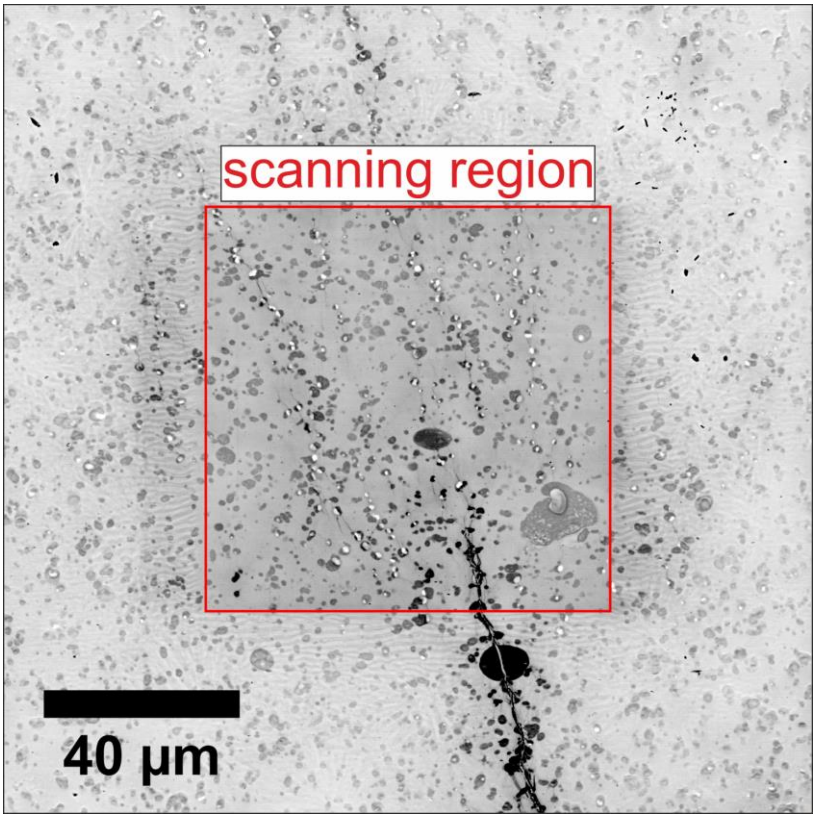

Fig. 43: Overview image of the surface of an EPR10 sample after stopping the SBEM routine at a depth of around 10 µm and recording image stacks in the scanning region with the following microscope settings: AV = 7.4 kV, SS = 4, p = 0.6 Torr, pixel size of 80 x 80 nm² with a dwell time of 10 ns; the crack tip is visible at the bottom.

Two images of the same sample but recorded at different slicing depths are displayed in Fig. 44 a) and b), showing the beam damage as a function of the material properties. Both images were recorded after stopping the slicing process and lowering the magnification for the recording of an overview image. A lower acceleration voltage (4.0 kV) was used than for image recording in Fig. 43, while the SS and dwell time were kept the same and the water vapour pressure was slightly reduced. The corresponding pixel size was 13.5 x 13.5 nm² during the SBEM process. The first stop was made after 110 slices (see Fig. 44 a)), thus reaching a depth of around 11 µm beneath the sample surface. The image reveals small but no distinct changes in the scanning region. In contrast, the image shown in Fig. 44 b), which was recorded at a depth of approximately 25 µm, reveals some damage both inside and outside the area irradiated during the SBEM procedure. As shown in chapter 3.3, the RuO_4 concentration decreases with increasing depth. Thus also the hardening of the material due to ruthenium staining decreases. This softening leads to a smearing at the cut surface of the material outside the marked area. No smearing is detected inside this area, but ripples in the polymer matrix can be observed, similar to those appearing in Fig. 43 at the boundary of the marked region. But the contrast between the filler particles and the matrix is much stronger inside the marked area than outside, indicating hardening of the material by irradiation in this region.

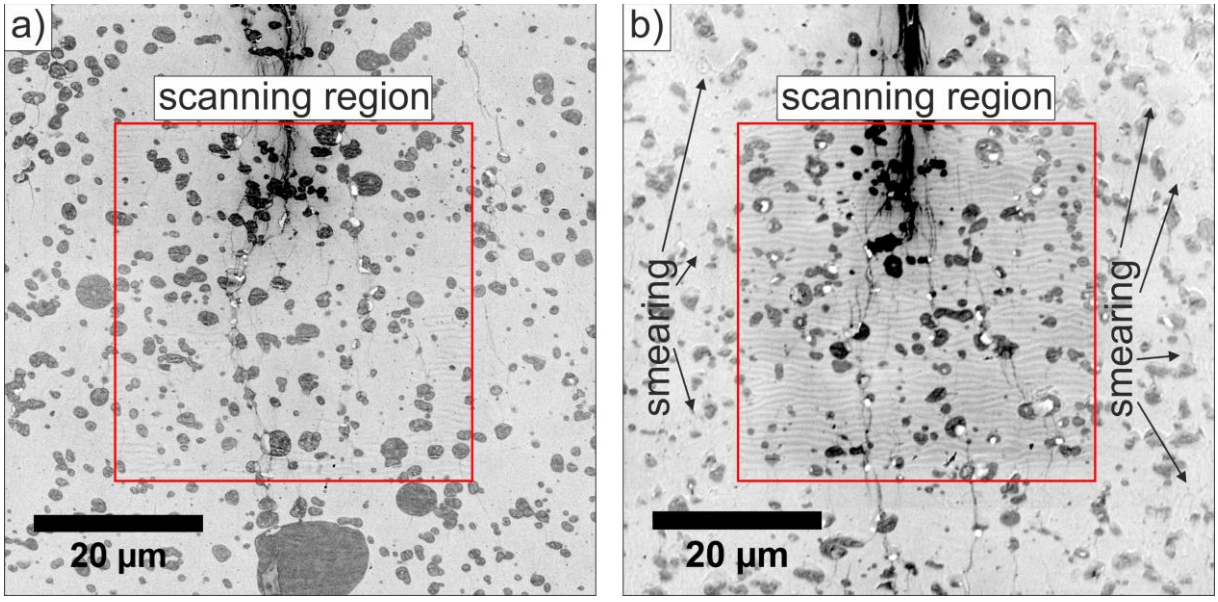

Fig. 44: Overview image of the scanning region after stopping the SBEM process after approx. 11 µm at a) and at 25 µm at b) where a smearing of the material occurs outside the window. Microscope settings for the scanning region: AV = 4.0 kV, SS = 4, p = 0.42 Torr, pixel size = 13.5 x 13.5 nm², dwell time = 10 ns.

The examples in Fig. 42 – Fig. 44 show that the beam induced damage is dependent on the material properties and the microscope settings used.

Not only the specimen damage of the investigated material but also the image information depth depends on the acceleration voltage. As explained in chapter 3.4.2, the applied slicing thickness was 100 nm, thus the information depth should be lower than this setting to prevent convolution of information from different slices. A suitable electron energy was estimated using the Monte Carlo simulation program casino™ [73]. Because BSEs were used for imaging, only

the respective results are presented. The simulation was only done for pristine PP because the exact composition of the sample after staining was not known and the Ru atoms used for staining are not homogeneously distributed in polymer blends. But after the staining process the penetration depth should decrease due to an overall density increase. Fig. 45 shows the result for two simulations at acceleration voltages of 7 kV (top) and 3 kV (bottom). The images on the left show the calculated electron trajectories of the primary electrons inside the material, with backscattered electrons (BSE) in red. The horizontal orange line marks the slice thickness of 100 nm. The two images on the right show the normalised number of BSEs as a function of depth. It can be seen that at an acceleration voltage of 7 kV the penetration depth of BSEs exceeds the slice thickness, whereas for 3 kV the vast majority of the backscattered electrons appear at a much lower depth, with a maximum at approximately 50 nm. An acceleration voltage of around 3 kV was thus used for imaging during the SBEM process, with the additional advantage that both beam damage and skirting decreased.

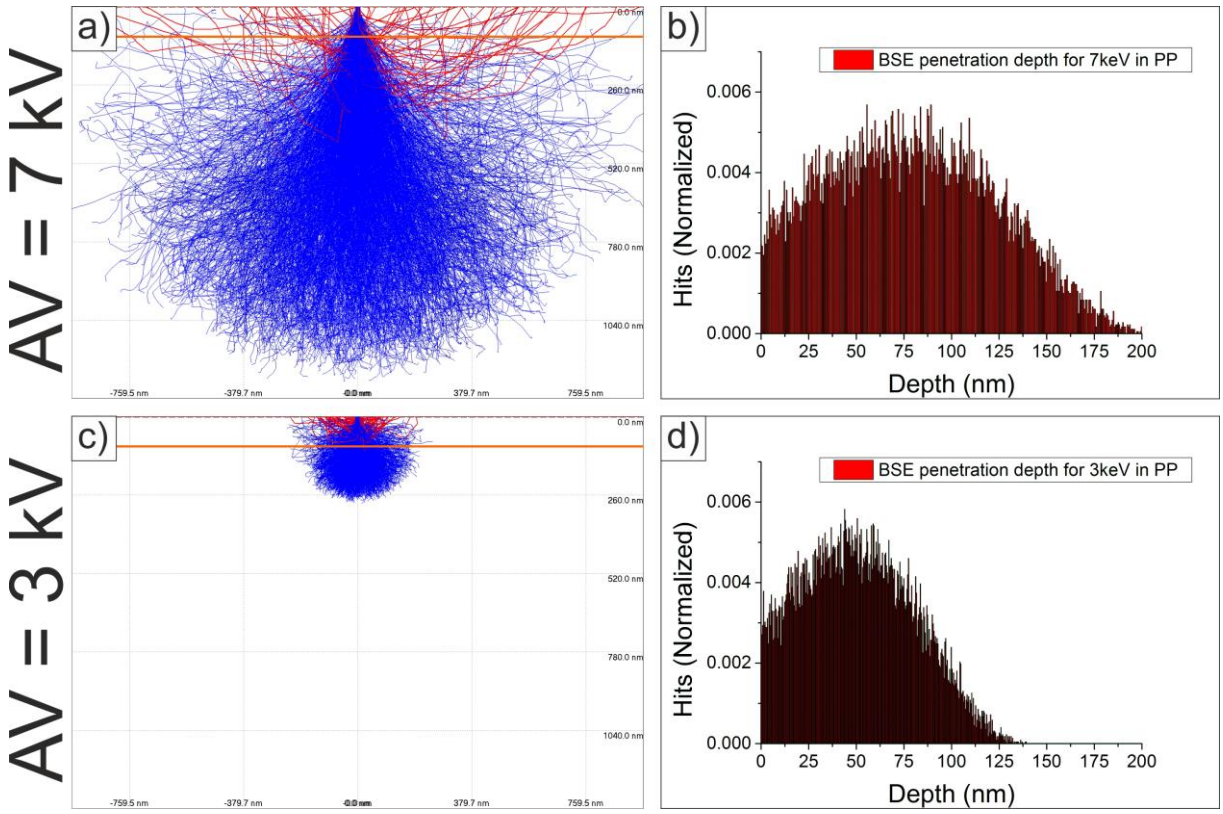

Fig. 45: pristine PP: Casino™ Monte Carlo simulations for electrons accelerated with a voltage (AV) of 7 kV (a) and b)) and 3 kV (c) and d)); left: electron trajectories, with red lines corresponding to BSE trajectories; right: depth distribution of the BSEs.

The image stacks obtained were subsequently used for the 3D reconstruction. However, because, e.g., the concentration of the stain decreases with progressive cutting depth, the image contrast also changes. Different image processing options can be used to correct these changes. The processed images can subsequently be segmented to enable the 3D reconstruction of both image features, the filler particles and cracks.

3.5. Digital image processing

The image stacks obtained by SBEM must be segmented to enable 3D reconstruction of the cracks and filler particles inside the PP matrix. As mentioned in chapter 3.4.2, the images must first be processed, as for instance to compensate for contrast changes due to the staining depth profile. Image processing was carried out mainly using the freeware Fiji because it offers a great variety of image filters and segmentation tools [39]. Fiji is a distribution of the image processing software ImageJ with a big bundle of plugins enabling different scientific image analyses. Additionally, the program Avizo® (FEI Visualisation Science Group, Bordeaux, France) was used for 3D reconstruction.

Fiji provides various routines for the segmentation of images. The higher the contrast between the objects of interest and their background and the less noisy the images the more efficiently they work. The following chapter covers the methods which enable noise reduction and contrast enhancement to obtain satisfactory and reliable segmentation results which can be used for a successful 3D reconstruction.

3.5.1. Noise reduction

Because the cracks originating from the tensile test have a width of around 100 nm, high resolution images must be taken. As the samples are sensitive to irradiation damage, short dwell times must be chosen, resulting in noisy images. Several noise reduction filters can be used to get rid of the noise. Most of these filters are linear filters which are specified either by their convolution kernel or their transfer function. The image filter used in this thesis will be briefly discussed in the following chapters and a detailed description of most of these processing methods can be found in [74].

3.5.1.1. Neighbouring averaging and convolution

One relatively simple routine is neighbouring averaging, where the brightness of each pixel is calculated by summing over the brightness values of neighbouring region pixels divided by the number of pixels used. Typically, odd square block size boxes 3 x 3 or 5 x 5 in size were used for averaging over the neighbouring region. For a 3 x 3 size box the signal-to-noise ratio can be improved by a factor of 3, if there is random noise in the image. However, small features in the image will be suppressed because the lateral resolution is dramatically reduced.

A more elaborate way to remove noise is convolution, i.e. the use of a kernel operation. This method involves replacing every pixel with the average of itself and its neighbours by use of equation (7):

$$P^*_{x,y} = \frac{\sum_{i,j=-m}^{+m} W_{i,j} \cdot P_{x+i,y+j}}{\sum_{i,j=-m}^{+m} W_{i,j}}, \tag{7}$$

where $P^*_{x,y}$ is the new average pixel, $P_{x+i,y+j}$ one neighbouring pixel in a 2m + 1 dimension squared box and $W_{i,j}$ the weight array. For simple averaging this weight array only contains ones, thus every pixel in the square has the same weight. Noise reduction can be improved by using a larger neighbourhood size, but the blurring at edges increases, see Fig. 46.

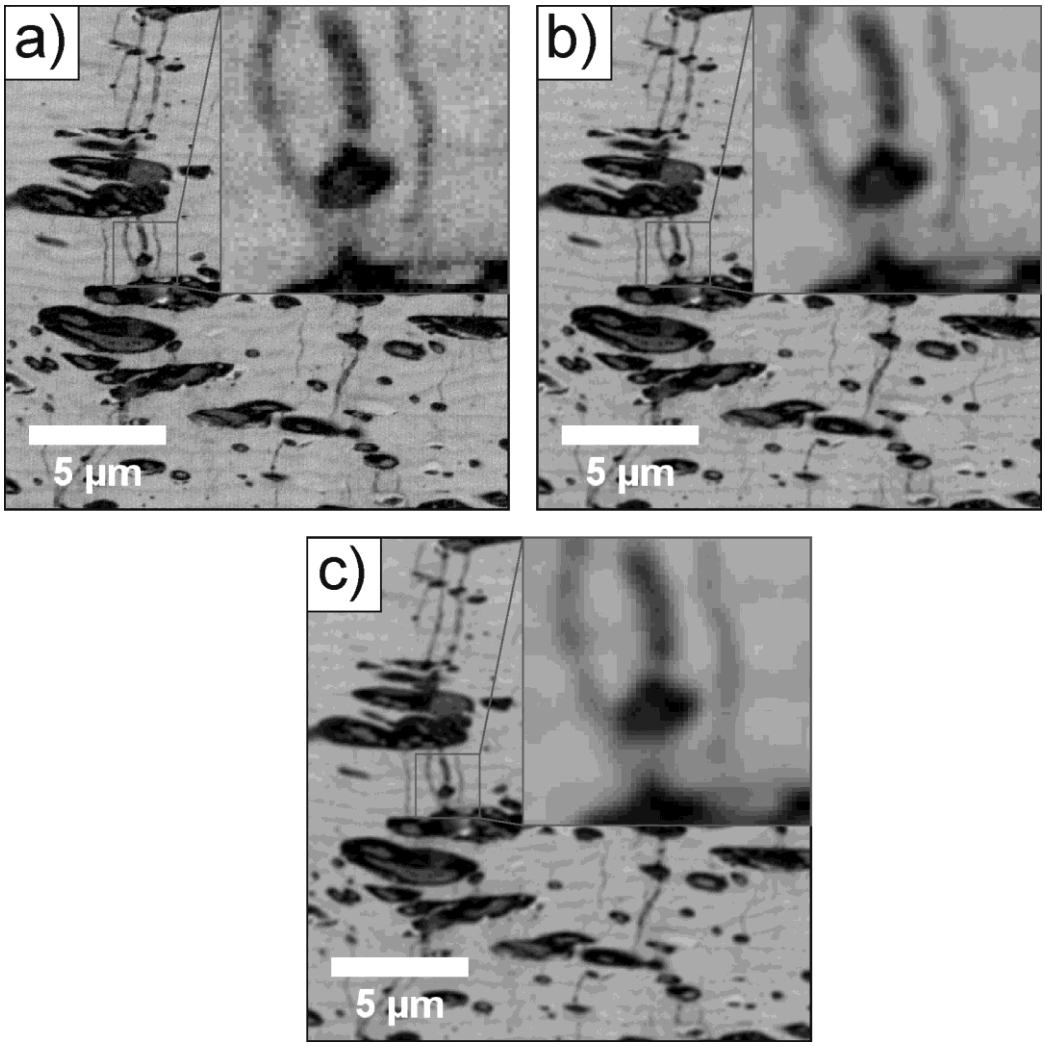

Fig. 46: Neighbouring averaging by convolution with 1s in the matrix as weight: a) original image, b) 3 x 3 kernel and c) 5 x 5 kernel convolution.

This blurring can be minimized by using a higher weight for the central pixel:

$$\begin{bmatrix} 1 & 1 & 1 \\ 1 & 4 & 1 \\ 1 & 1 & 1 \end{bmatrix}.$$

Here the 4 is multiplied with the central pixel of the original image with the result that this pixel dominates the averaging, thus reducing the blurring at the edges, see Fig. 47.

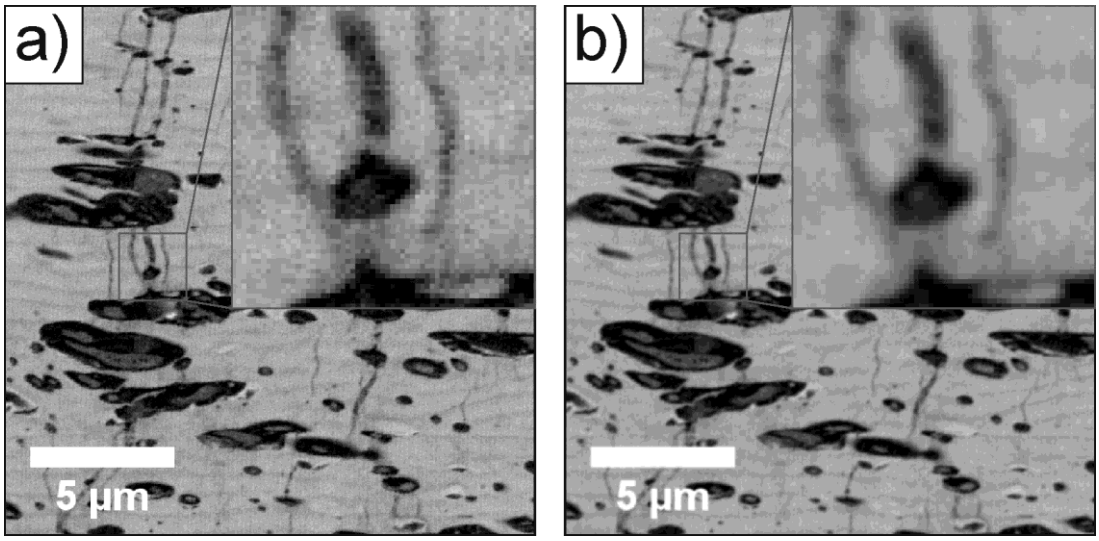

Fig. 47: Noise reduction by image convolution: a) original image and b) same image after filtering with a weighted 3 x 3 convolution filter.

These types of noise reduction filters are based on the local averaging of pixels and show a more or less distinct blurring of edges in the images. As a consequence, the fine cracks in the images will be blurred, which makes successful segmentation nearly impossible. Therefore more complex noise filters must be applied, which filter the noise but simultaneously preserve the edges of the image features. The two filters used in this thesis will be explained in the following two chapters.

3.5.1.2. Non-local mean filter

A more sophisticated filter technique is the so called non-local mean (NLM) denoising filter, which can also be implemented into Fiji. This filter calculates the average grey value of the most representative pixels inside a search window around the pixel to be denoised [75]. The denoising process is given by equation (8):

$$\hat{u}(p) = \frac{1}{C(p)} \sum_{q \in B(p,r)} u(q)\, \omega(p,q) \;\; with\; C(p) = \sum_{q \in B(p,r)} \omega(p,q)\,, \tag{8}$$

with $\omega(p,q)$ a weighting function and $C(p)$ a normalising factor. The central pixel p of the image $u(p)$ will be denoised, while $B_{(p,r)}$ defines the pixel neighbourhood of a size (2r + 1) x (2r +1). This limits the search area of the representative pixels around the pixel to be denoised and thus reduces the computation time. The region is set to a fixed size of 21 x 21 px² for small and moderate operator chosen $\hat{\sigma}$ values and 35 x 35 px² for higher $\hat{\sigma}$ values, because a larger region must be scanned to evaluate the representative pixels for noise reduction. The weighting function $\omega(p,q)$ typically depends on the squared Euclidean distance $d^2 = \sum_i (p_i - q_i)^2$ of the respective p and q pixels. The function implemented in Fiji additionally uses an exponential kernel for the computation:

$$\omega(p,q) = e^{-\frac{\max(d^2-2\sigma^2,0.0)}{h^2}}, \tag{9}$$

with σ the standard deviation of the noise and h a filtering parameter which depends on σ. Hence the NLM filter calculation results in the replacement of each pixel with the average of the most resampling pixels inside a neighbouring window, where the resemblance is calculated by the weighting function. The result is a denoised image, where fewer image details get lost than with other filters, see Fig. 48. Fiji provides several options to adjust this filter to the image. The first option is the previously mentioned $\hat{\sigma}$. The higher this value is set, the more high frequency information will be smoothed, resulting in a loss of details in the image, as can be seen in Fig. 48 c). This value can be calculated automatically by ticking the "Auto estimate sigma" option, which estimates the value by a fast noise variance calculation [76]. The second value which can be chosen is the smoothing factor, which sets the intensity of the smoothing. In most cases the standard smoothing factor of one and a low $\hat{\sigma}$ give the best results, see Fig. 48 b). This filter can also be applied on image stacks with every image being filtered separately. Subsequently, the filtered images can be used for the segmentation processing routines or other image processes because noise is effectively reduced.

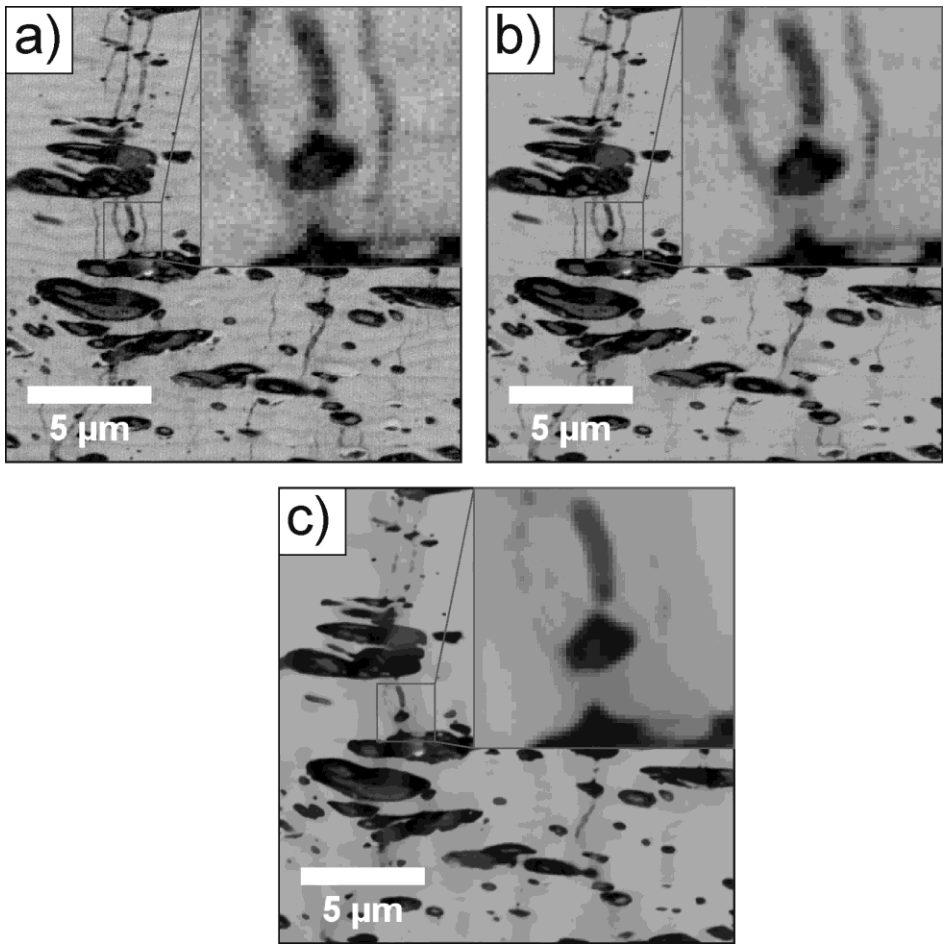

Fig. 48: Image noise reduction with non-local mean filtering: a) original image and b) same image after applying a non-local mean filter with a $\hat{\sigma}$ value of 7 and c) 30 (both with a smoothing factor of one).

3.5.1.3. Kuwahara filter

Critical objects for segmentation are small or narrow regions which can be blurred by a linear noise reduction procedure such as neighbouring averaging. More sophisticated filters have been developed to take this disadvantage into account. One of these so called adaptive noise reduction filters is the non-linear smoothing filter according to Kuwahara [77], which smoothes the image but tries to retain the edges. This filter takes the region of a square window around the central pixel $P(x,y)$ and divides it into four smaller square sub-regions of the same size, like a chequerboard. Subsequently the standard deviation $\sigma_i(x,y)$ and the arithmetic mean $m_i(x,y)$ of every sub-region are calculated and the following operator is used to determine the value of the central pixel $\phi(x,y)$:

$$\phi(x,y) = \begin{cases} m_1(x,y) & if\ \sigma_1(x,y) = min_i\ \sigma_i(x,y) \\ m_2(x,y) & if\ \sigma_2(x,y) = min_i\ \sigma_i(x,y) \\ m_3(x,y) & if\ \sigma_3(x,y) = min_i\ \sigma_i(x,y) \\ m_4(x,y) & if\ \sigma_4(x,y) = min_i\ \sigma_i(x,y) \end{cases}. \tag{10}$$

This means that the operator sets the central pixel to the mean value of that region which has the lowest standard deviation, i.e. which is most homogeneous. This enables edge preserving filtering, while smoothing the other regions. The window size allows adjusting the size of the objects to be preserved. In Fig. 49 two different window sizes were applied to a NLM filtered image. The previous NLM filtering step was used to obtain a smoothed image, which enables the usage of smaller Kuwahara window sizes. Without this preceding step, small variations in the background would be enhanced. The effect of the different window sizes can be seen in Fig. 49 b) and c). Whereas the small cracks are preserved using the smaller window size of 5 x 5, they are smeared out using a window size of 11 x 11. For both window sizes the larger features (filler particles) are only enhanced at their edges. Thus the object sizes to be preserved in the final image can be defined by adjusting the window size. To remove the smaller regions altogether, the filter can be used in an iterative process. The smaller regions are more and more smeared out after every iteration. This can be used to separate smaller objects from larger ones in the segmentation process, which will be explained in more detail in section 3.5.4.6.

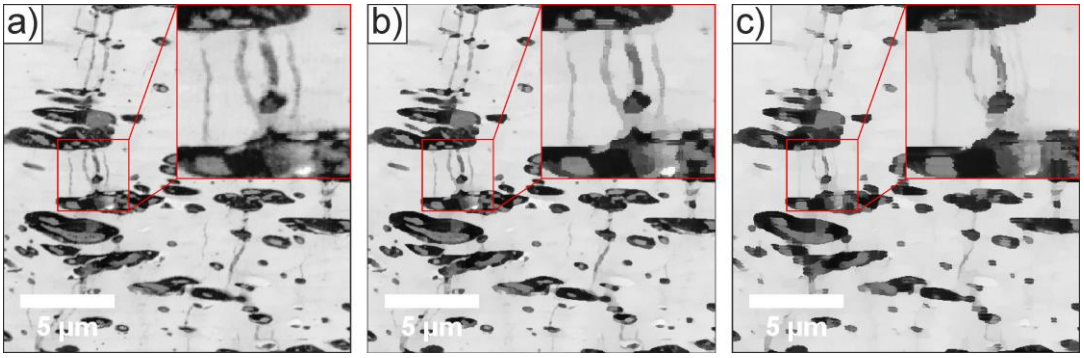

Fig. 49: Kuwahara noise filtering: a) a NLM filtered image, which was used for applying the Kuwahara filter with a window size of b) 5 x 5 and c) 11 x 11.

3.5.2. Non-uniform brightness distribution

In some cases, the contrast and brightness in the images or image stacks change non-uniformly for a variety of reasons. Charging often occurs at some areas of the sample despite the presence of water vapour in the ESEM chamber. This can be caused, for example, by strongly non-uniform RuO_4 staining. Non-uniform contrast and brightness in the images can also be caused by the sample mounting. When mounting the sample at the ultramicrotome in the ESEM, the sample block face can often not be oriented exactly parallel to the diamond knife. Therefore, because of the tilted sample surface, part of the sample is already cut at the start of the slicing process, with the rest of the sample surface below the cutting level. When finally the whole sample block face is cut, some regions have been sliced more often than others. Because the staining concentration decreases with increasing depth, these regions show less contrast. This can lead to small but identifiable contrast differences inside the scanning region. As the staining depth is only around 35 µm, see chapter 3.3, even small tilt angles can have a large effect.

3.5.2.1. Non-uniform contrast in image stacks

Different image processing methods are available to get rid of these contrast / brightness variations. The method depends on whether brightness variations can be found within single images or whether variations appear between images within the image stack. The software provides procedures which equalise the contrast variations within a whole image stack [78]. The process is divided into two steps. In the first step, the grey level histogram is calculated from all images in the series and the contrast and brightness are adjusted according to a reference image. The reference image can be chosen by the user, but an image with high contrast and uniform brightness should be selected. In the second step, the histogram of all other images is adjusted to the histogram of the reference image. An example of the effect of the filter can be seen in Fig. 50, where the original images with different brightness and contrast are shown at the top and the respective images after application of the filter at the bottom.

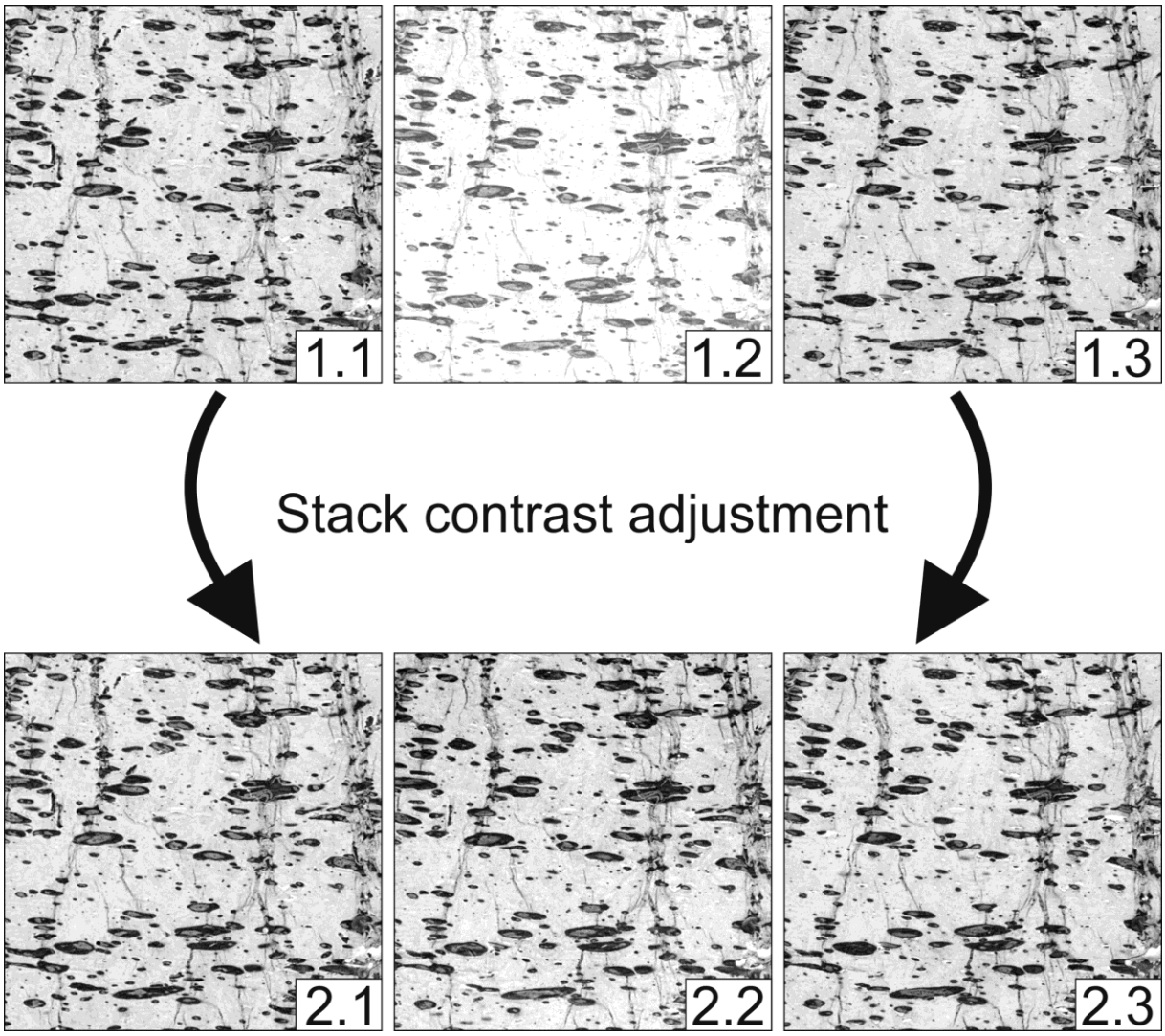

Fig. 50: Image contrast adjustment of non-uniformly illuminated images: top: original image sequence; bottom: after application of the image filter.

3.5.2.2. Non-uniform contrast within one image

Non-uniform brightness distribution within one image can be adjusted using Fourier transformation. Because this transformation can be very CPU-intensive (central processing unit) typically the fast Fourier transform (FFT) method is used to transform images from spatial domain to frequency domain [74]. A function can be transferred into frequency domain by the following equation:

$$F(u) = \int_{-\infty}^{+\infty} f(x) e^{-i2\pi ux} dx \,. \tag{11}$$

The transformation back from the frequency domain to spatial domain is:

$$f(x) = \int_{-\infty}^{+\infty} F(u) e^{2\pi i u x} du \,. \tag{12}$$

The discrete form of the equations (11) and (12) can be used to calculate the forward and inverse Fourier transform of an image into frequency domain and back into the spatial domain. The incentive to work in frequency domain is that many image operations are much faster and require less computational effort than in the spatial domain. In Fig. 51 three examples demonstrate the effect of different filter masks applied in the inverse transform. The first mask, see Fig. 51 b), filters low frequencies out of the original image, leaving only high frequencies. In images high frequencies usually appear at edges because of the quick change in the brightness level. An edge detecting filter can thus be realised by filtering the accurate frequencies, see Fig. 51 c). The second example shows the realisation of a smoothing filter, where high frequencies were filtered from the original image. By scaling the size of the white circle in the middle of Fig. 51 d) the filtered frequencies can be adjusted. An example of the filter mask that will be often used in this section is shown in Fig. 51 f). This bandpass filter allows compensating an inhomogeneous background while the foreground stays nearly the same. This results in an evenly illuminated image where the filler particles as well as the cracks are preserved, as can be seen in Fig. 51 g).

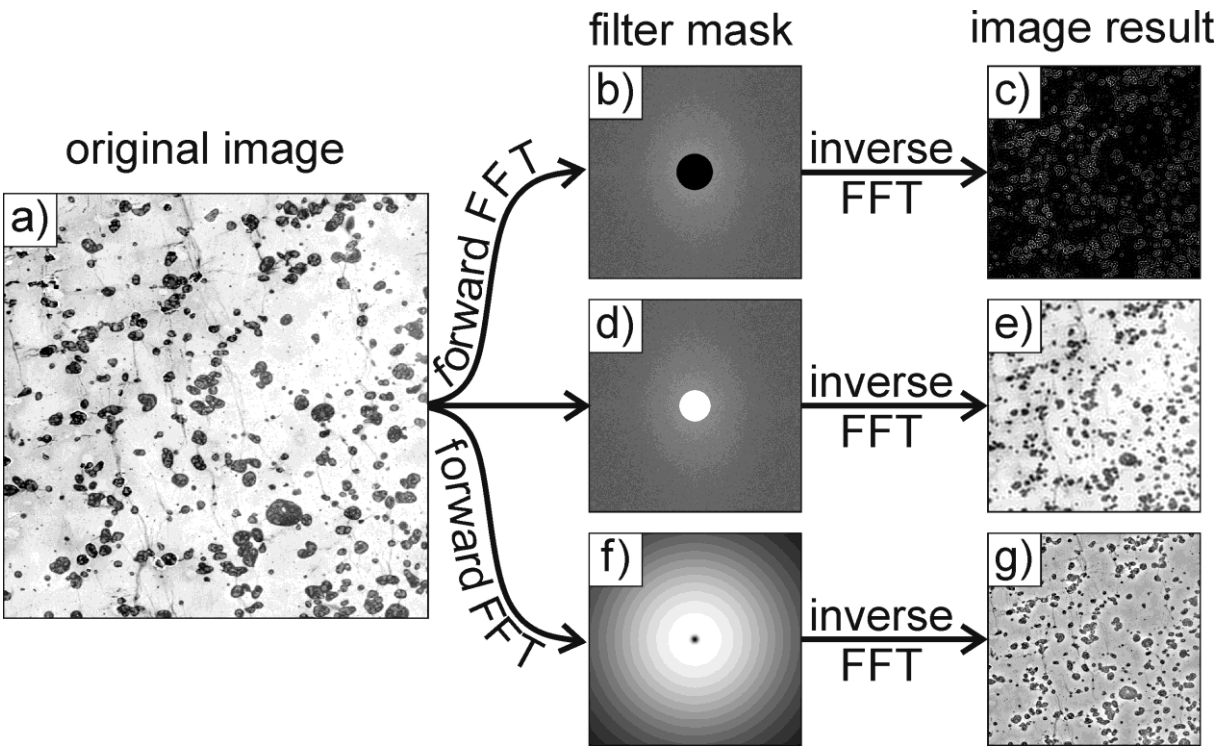

Fig. 51: Image filtering by FFT: a) original image, b) low frequency filter with c) the resulting image, d) filter which passes high frequencies with e) the resulting image and f) bandpass filter with g) the resulting image after applying the filter on the original image.

Another method to compensate a non-uniform background within one image is background subtraction. The algorithm is based on the so called “rolling ball” method, which was described by S. Sternberg in the 1980s [79]. The image is transformed into a 3D, surface where the grey value corresponds to the height in the image. The filter equates a ball rolling along the valleys of this 3D surface. The respective regions, representing the background of the image, are subsequently subtracted from the original image. The user can select the radius of the ball, which should be at least as large as the largest feature in the image. Fig. 52 shows an image with a non-uniform brightness distribution at a), the filtered background at b) and the background corrected image at c).

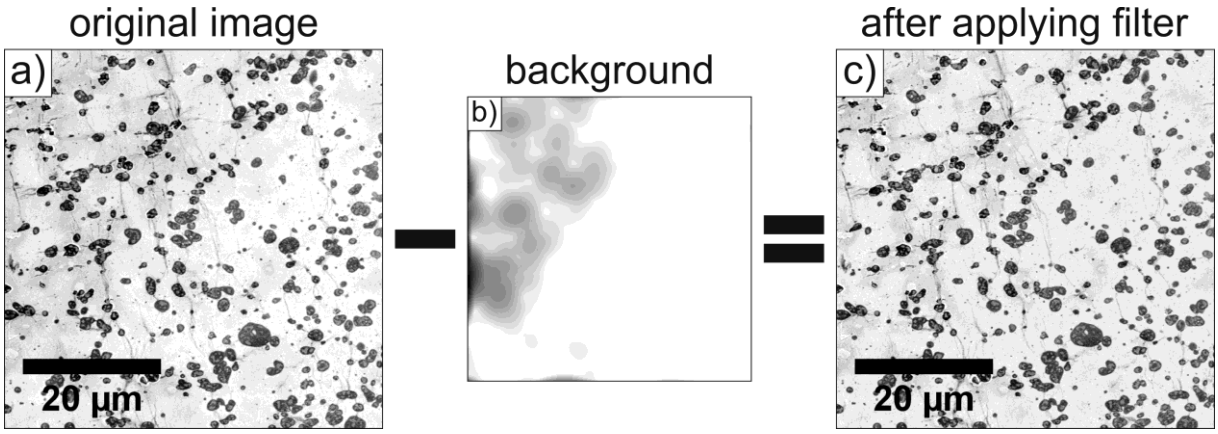

Fig. 52: Non-uniform brightness distribution correction by background subtraction: from the original image a) the calculated background b) was subtracted to obtain the background adjusted image c). The calculated background contrast at b) was increased for better visibility.

The grey level intensity profiles of the images were calculated to check the improvement in the image after background filtering independently of the visual comparison. The profile of the original image in Fig. 53 shows a clear grey level intensity increase from the left (position 0 µ) to the right edge (position 55 µm). After application of the FFT bandpass filter, the average grey level intensity became constant, but also the overall intensity was shifted to lower values, see Fig. 53 a). Additionally, the image contrast was lower where the contrast corresponds to the maximum intensity change within the respective profile. But this could be corrected by a subsequent adjustment of brightness and contrast. Nevertheless, the profile shape seems to remain constant, indicating no significant changes in the image information. The average grey level intensity profile for the image after background subtraction by the “rolling ball” method was also linearised, but without a shift in the overall intensity change, see average profiles in Fig. 53 b). A comparison of the two unmodified profiles also reveals no significant changes in contrast. Thus the background subtraction method typically provides suitable corrected images without substantial changes in the mean grey level intensity or image contrast, which do not require subsequent correction.

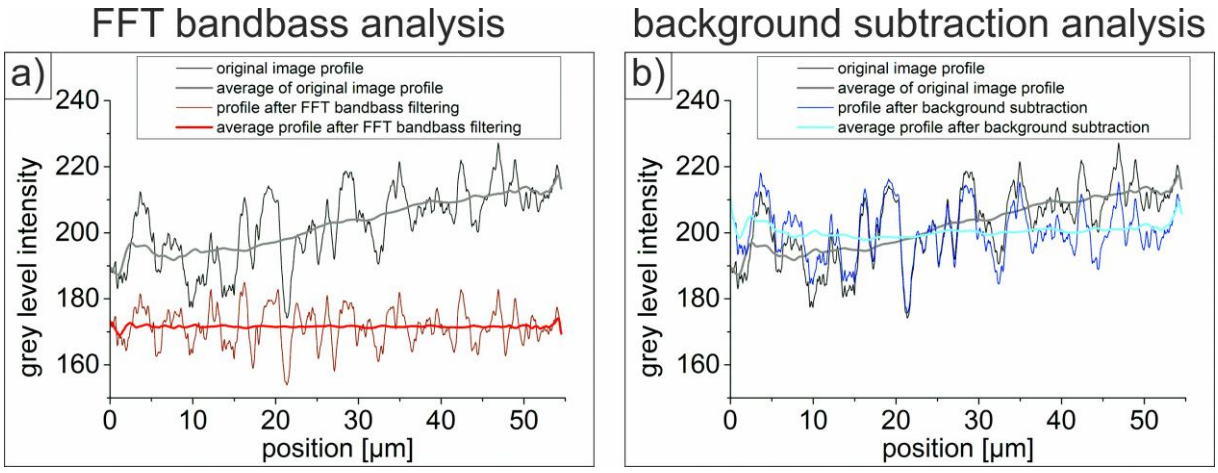

Fig. 53: Comparison of the grey level intensity profile of the original with a) the same image after FFT bandpass filtering and b) the corresponding profile after background subtraction.

Thus both filters can be used to compensate brightness artefacts in either a single image or all images in the stack. Typically, the background subtraction, or occasionally the FFT bandpass filter, was used for every single image with a non-uniform distribution of background brightness. Subsequently the stack contrast adjustment filter adjusts the contrast and brightness distribution in all images in the stack. These image stacks can subsequently be used for the image segmentation process.

3.5.3. Contrast enhancement

Because most image segmentation techniques are based on the exploitation of differences in the image brightness distribution, an increased contrast between the foreground and background can enhance the accuracy of the segmentation result. Several methods for contrast enhancement, based on different algorithms, have been developed. One frequently used method is gamma correction, which is based on modifying the brightness distribution by a non-linear histogram adjustment. The following equation is used to recalculate the grey level intensity of every pixel in the image [80]:

$$new\ pixel\ intensity = \left[\frac{old\ pixel\ intensity}{255} \cdot gamma\right], \tag{13}$$

where $gamma$ can be chosen by the user. If $gamma < 1$ then the brightness of faint objects is increased, whereas images appear darker if $gamma > 1$. Because the features in the image in Fig. 54 a) are dark the gamma value was set to 3 in Fig. 54 b). The histogram shows an overall decrease in brightness, while some grey values are not occupied especially in the region next to white (255), which leads to a loss of image information. Another method, histogram equalisation, was therefore used to obtain a more reliable and also reproducible contrast enhancement. The non-uniformly distributed grey values are reassigned to obtain a

histogram as flat as possible [74]. For an 8-bit image (brightness values: 0…255) the reassignment can be calculated by:

$$k = 256 \cdot \sum_{i=0}^{j} \frac{N_i}{T}, \tag{14}$$

where for each grey level value j a new assigned value k is calculated. To this aim the sum of the pixels with a grey value smaller than or equal to j is divided by the total number of pixels (T) in the image and multiplied by the maximum grey level value. All pixels in the original image with grey level j are replaced by the value k. Fig. 54 c) shows the resulting image with the corresponding histogram. In contrast to the gamma correction method, the full range of the histogram is used. But this method often does not sufficiently enhance the contrast in dark or light regions.

Therefore an adaptive calculation method was introduced by K. Zuiderveld [81], which is based on the calculation of histograms for several distinct image regions. This method enhances the local contrast especially at edges of image features. The variant used to obtain Fig. 54 d) is called contrast limited adaptive histogram equalisation (CLAHE) and limits the contrast amplification to prevent overmodulation of noise or background pixels. Different calculation parameters can be chosen by the user: *block size*, *histogram bins*, *max. slope* and the option for a faster calculation. The *block size* feature allows the user to set the size of the local region around the selected pixel. This size should be larger than the features to be preserved and enhanced in contrast compared to the matrix. The example shown in Fig. 54 d) shows the results for a block size setting of 11. The parameter *histogram bins* is used to set the smoothing factor of the resulting image. The fewer bins are set the larger is the smoothing effect. As no image smoothing was desired, this parameter was set to 256 in the example. The third parameter *max. slope* allows the user to adjust the maximum clipping level of the calculation. This is the limiting factor of the contrast amplification of the CLAHE calculation and involves clipping the calculated histogram of every region by the pre-defined value prior to calculating the transformation function. Commonly, the value is set very low, e.g. 3 in the shown example. All three values are set in a range which only slightly increases the local contrast to prevent contrast enhancement in the background. But the CLAHE procedure can be applied to the image repeatedly in order to reveal an increased contrast amplification while the background pixels do not change significantly. This contrast enhancement allows better segmentation of smaller features because of their increased dominance.

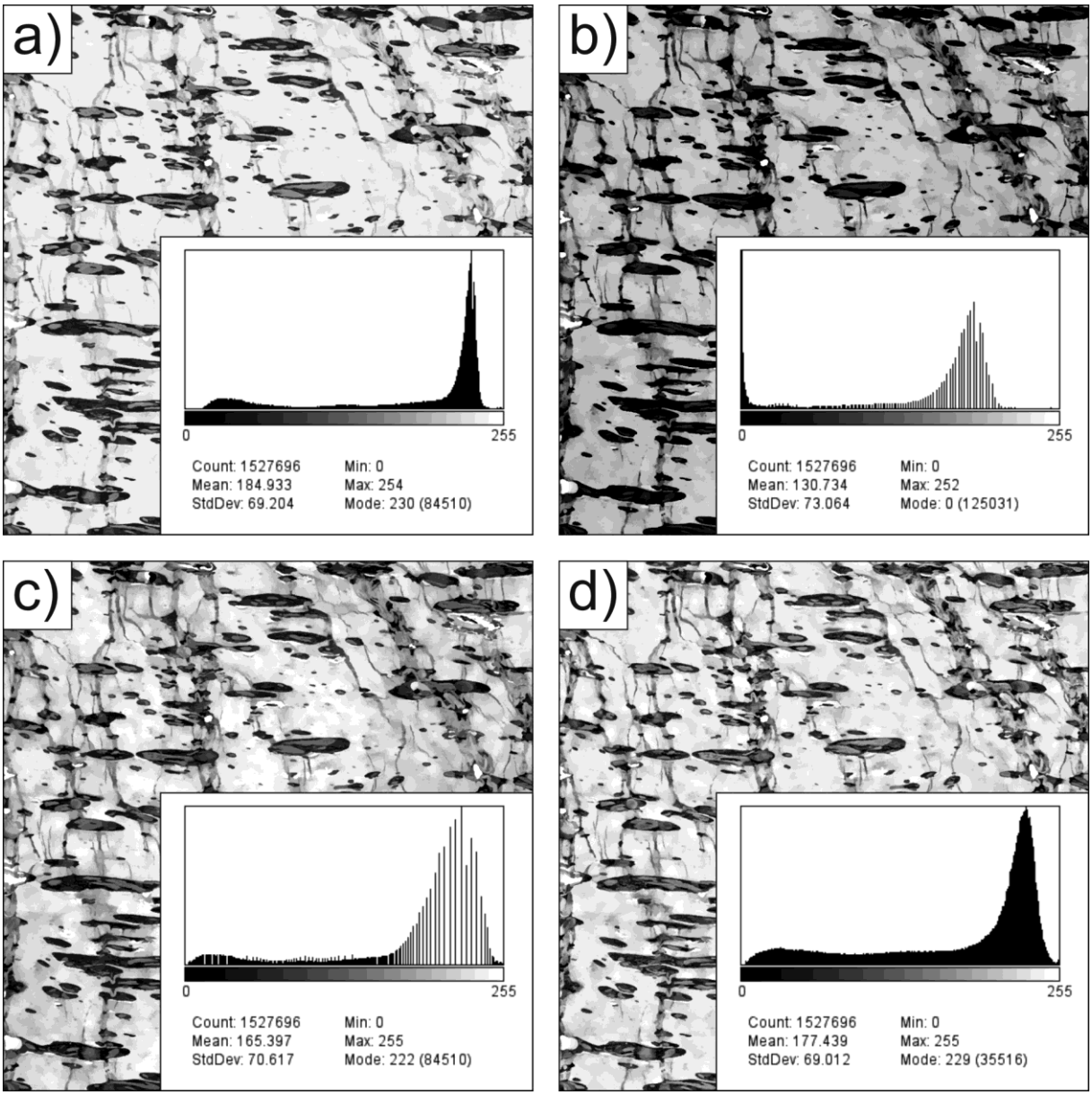

Fig. 54: The original image with corresponding histogram at a) and several contrast enhancement results: b) gamma correction, c) histogram equalisation and d) enhanced local contrast (CLAHE). For detailed description and parameters see text.

3.5.4. Image segmentation

3D reconstruction requires the filtered images to be segmented into objects of interest, also called labels. In this case filler particles and cracks are set as foreground, while the PP matrix serves as the background. Several different methods are available to perform the segmentation. In the following chapters the advantages and disadvantages of frequently used simple and more sophisticated methods will be discussed.

3.5.4.1. Segmentation quality evaluation

Since a range of different segmentation algorithms are available, a strategy was elaborated to evaluate the quality of the respective segmentation processes. At the start an image must be prepared which represents the ideal segmentation, also called ground truth (GT). To do this, an image with the size of 82.5 x 82.5 µm² and a pixel resolution of 4.096 x 4.096 px² was segmented by hand to obtain a reference segmentation image (RSI) for comparison with the images obtained by the different segmentation processes and to assess the accuracy of the respective process.

The RSI was used to introduce different methods for evaluating the accuracy of the segmentation results. The first and simplest approach is to compare the segmented areas with the areas of the respective features (filler particles or cracks) in the RSI, where the area of the filler particles was 22.9 % with respect to the total image area and those for the cracks was 1.4 %. A comparison of these values with the values resulting from the different segmentation algorithms does not provide information about the correct position of the segmented features and whether they have been attributed to the right label. Thus it provides only an initial qualitative validation of the segmentation result. To obtain a more comprehensive parameter, the area difference coefficient (ADC) is introduced:

$$ADC_i = \frac{\mathrm{X}_i}{\mathrm{Z}_i} \cdot 100 \;\; with \;\; i \ldots F, C \,, \tag{15}$$

where X_i is the area in the segmentation result, and Z_i the respective area in the RSI image. Here the index i was used to differentiate between the filler particles F and the cracks C. The calculated coefficient represents the correlation of the respective area with the RSI result in percent. If the coefficient is greater than 100 the respective area in the segmentation result is larger than that of the RSI and vice versa. Nevertheless, the coefficient still provides only information about the comparability of the area but not about the correct pixel position in the image. Another approach was thus developed to take this into account, the fractional equivalent coefficient (FEC):

$$FEC_i = \frac{(\mathrm{X}_i - \mathrm{Z}_i)_{difference}}{\mathrm{Z}_i} \cdot 100 \,, \tag{16}$$

with the subtraction in the numerator an image operation calculated by the image processing software. The results of this subtraction are either pixels which were not detected by the respective segmentation algorithm or are the result of oversegmentation. The smaller this coefficient, the better the congruence of the positions of the features in both images and also their shape and size. Both coefficients will subsequently be used to enable a qualitative evaluation of the images after the different segmentation processes. But whereas they are definitely suitable for the segmentation of particles, this may not be the case for the cracks, which represent lines rather than areas.

3.5.4.2. Global threshold

A simple segmentation procedure is global thresholding, where pixels within a defined range of grey values belong to the foreground and the residual pixels to the background. Usually such images are displayed as black and white binary images, but there is no convention if the foreground or background is black or white. The program used allows an interactive thresholding, where the foreground pixels are marked in red in a preview window, as can be seen on the left image in Fig. 55. The foreground region can be chosen by adjusting two slides, which set the minimum and maximum grey level within the image histogram, see Fig. 55 centre. Application of these thresholds generates a binary image, with the segmented structures coloured in black in the right image.

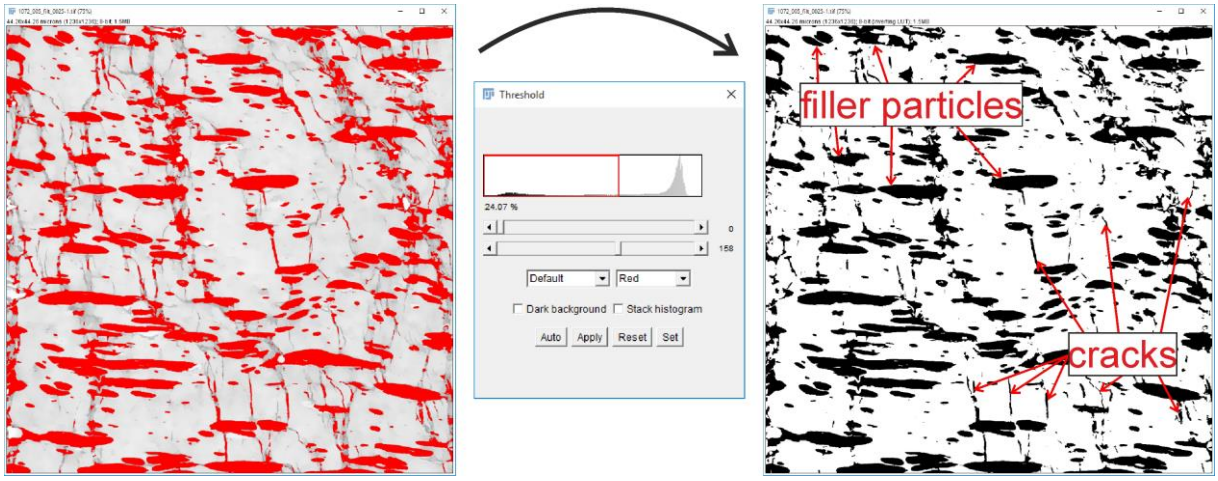

Fig. 55: Example of separating an image by thresholding; left: preview of segmentation, with foreground pixels marked in red; centre: threshold settings with inserted histogram and slide bars to choose the grey level range; right: thresholded (binary) image, with foreground in black.

Because the grey level range is user defined the segmentation result varies depending on the user. To get some idea about the variation in the results, the grey level range for all images is first chosen such that the area fraction of the segmented structures is the same as that obtained from the RSI. The upper threshold value defining the grey level range for segmentation is then successively lowered or increased for all images, including the RSI, until an under- or oversegmentation is definitely observed. Subsequently, the segmented area fraction and its percentage increase compared to the RSI area fraction are calculated. To investigate how large the image area must be in order to obtain statistically sound results the threshold variations in the RSI were compared with the same variations in a combination of 30 other images, providing a much larger area. The area of the RSI was approximately 6,800 µm², while in comparison the total area of the 30 other images was around 148,500 µm², with the area of each of these images being smaller than that of the RSI. From Fig. 56 it can be seen that, with one exception, the results for both areas are comparable. The results, again with the exception of the +20 grey level shift of the upper threshold, show an approximately linear area de- or increase with a de- or increasing grey level range, and the maximum changes were

found to be approximately +9 % or -15 %. The linear change is due to the circumstance that the histogram values in the region of the grey level range chosen are approximately constant, thus also the resulting changes in the foreground area are linear, see inserted histograms in Fig. 56 b) and c). As the shift of the upper threshold comes close to +20 grey levels, the grey level range chosen for the segmentation starts, including the histogram peak visible in Fig. 56 b) and c) and resulting from the bright background (the PP matrix). And this peak causes the steep increase in the area fraction at the +20 grey level shift and the big difference in the size of the segmented areas. The exact grey level at which this peak starts to rise varies slightly between individual images.

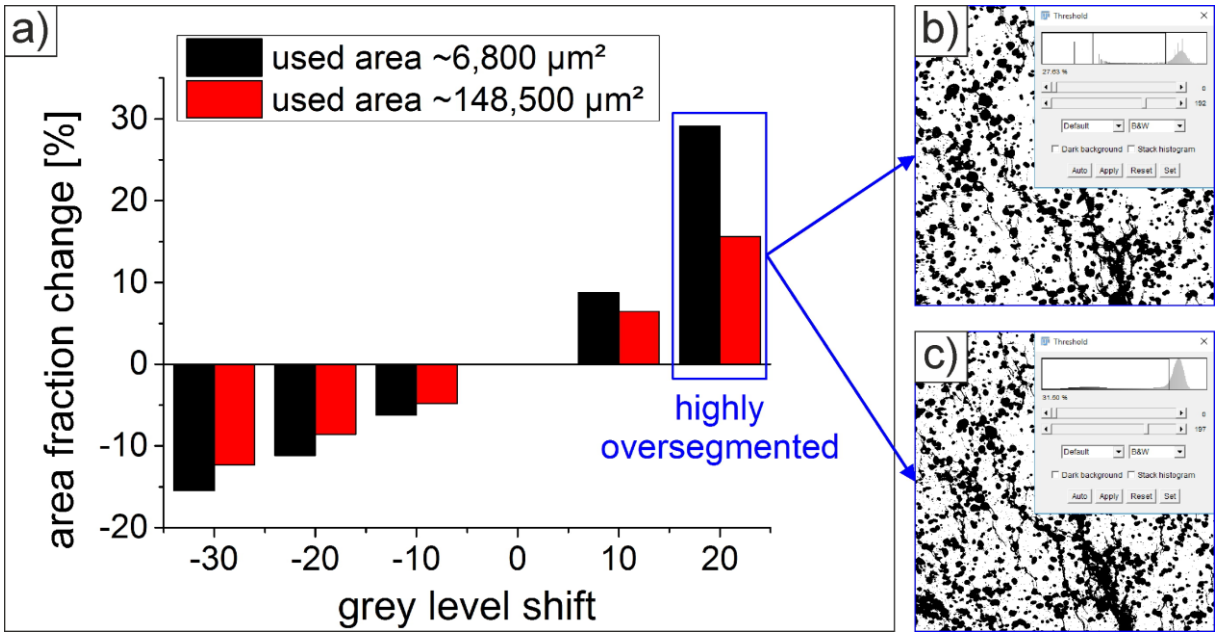

Fig. 56: a) Change in the size of the segmented area in dependence on the shift of the upper threshold and in dependence on the size of the whole image area; the change is relative to the segmented area at a shift of zero; b) and c) segmented images and the respective histograms for two different values of the upper threshold; see text for detailed description.

Typically, the variation of the selected threshold region is assumed to lie below the performed values in the range of ± 10 grey levels, which results in a maximum change in the foreground area of approximately ± 8 %. This global threshold technique allows fast segmentation of a whole image stack, but unfortunately is not suitable for the segmentation of only one object (filler particles or cracks). The right image in Fig. 55 demonstrates that by trying to separate only the filler particles, some cracks were also selected. Nevertheless, a segmentation of both image features is easily achievable.

Because global thresholding makes is possible to obtain only labelled images containing both image features, the accuracy of the segmentation process was calculated including the sum of the areas of filler particles and cracks. A NLM and subsequently Kuwahara (3 x 3 window) filtered image of the original recording was segmented by choosing a grey level range which gives the same percentage for the segmented area as was determined for the RSI

(24.3 % of the total area). Unsurprisingly, the respective ADC_{total} was 99.7 %, but also the FEC_{total} was very small at 11.6 %. This proves that the global threshold technique is an accurate segmentation method. A visual comparison of the original and the segmented image showed that most of the mis-segmented pixels are in regions with very fine cracks and at the edges of the two image features. The use of an image filter strategy described in chapter 3.5.4.6 also enables the separate segmentation of both image features. This method thus turns out to be an easily applicable, fast and reliable segmentation method if the background has been sufficiently smoothed.

3.5.4.3. Edge detection

Another simple segmentation method is based on detecting strong changes in the grey levels along a line. This edge detection method uses local steps in the brightness to identify boundary regions. Several different filters are available. A commonly used one is the Sobel filter, which calculates the derivatives of the image in two orthogonal directions using a row and a column mask. The magnitude of the edge is given by equation (17):

$$Magnitude = \sqrt{\left(\frac{\partial B}{\partial x}\right)^2 \cdot \left(\frac{\partial B}{\partial y}\right)^2}, \tag{17}$$

where B represents the brightness at the respective image place. The calculation thus combines the gradual brightness change in both directions x and y. The resulting binary image in Fig. 57 b) shows that nearly all edges of both image features, the filler particles and the cracks, were detected. As this method cannot differentiate whether the detected edge belongs to a crack or a filler particle, however, it is not suitable for the segmentation process, because it requires obtaining separate representations of the two features. Also, only the edges and not the whole area of, e.g., the filler particles are segmented in the binary image. Nevertheless, this method can be used to compute merged images, like that shown in Fig. 57 c), to enhance edges for images with weak contrast. Subsequently, these images could be used to obtain better segmentation results using other segmentation methods. But the merging often increases the size of the segmented areas, in particular a widening of the crack structures can be observed. This method was thus used only occasionally when individual images of an image stack showed very low contrast.

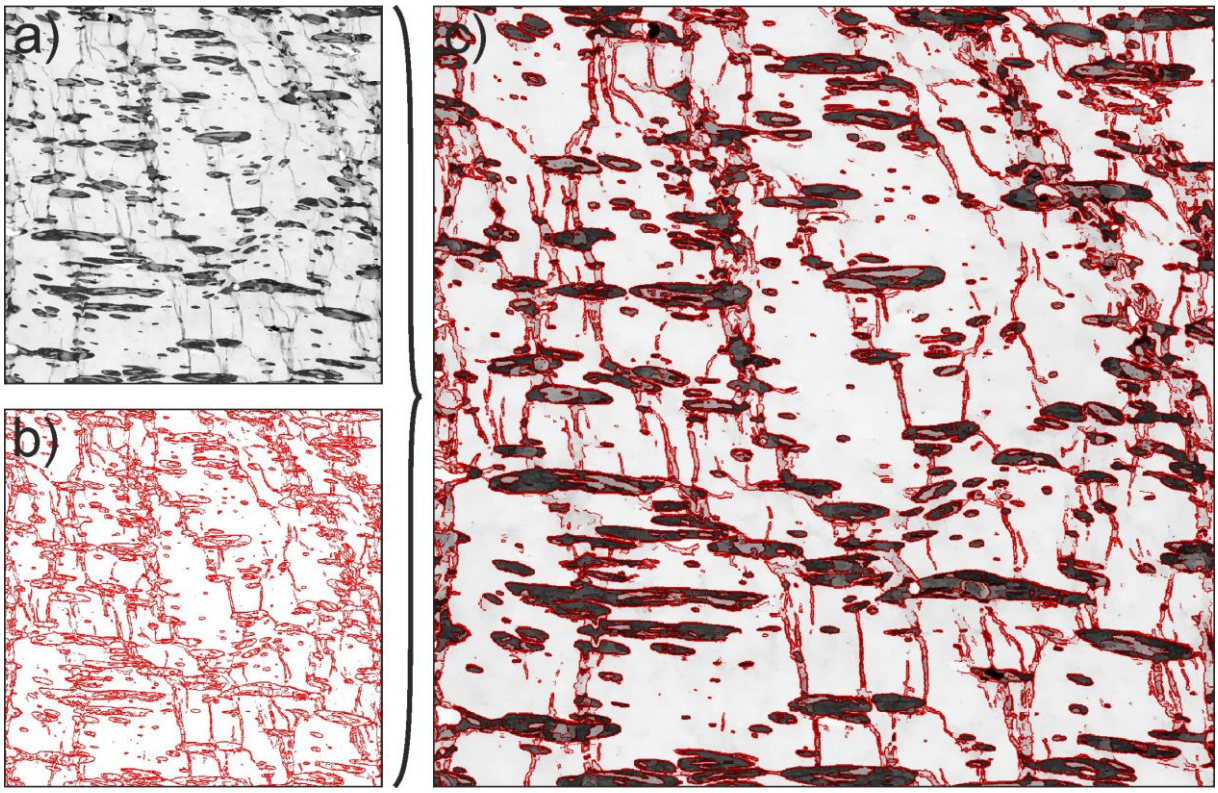

Fig. 57: Example of edge detection using a Sobel filter: a) the original NLM filtered image, b) the detected edges and c) the two images merged for comparison. For a better visualisation the edges were coloured red.

3.5.4.4. Auto local threshold

Other established segmentation methods are based on local thresholding. Some routines calculate the threshold for each pixel using a selected image characteristic within a user defined window area. In the program used the image characteristics contrast, mean, median, middle grey value or more sophisticated calculation methods such as the Niblack, Phansalkar, Otsu, Sauvola or Bernsen method can be selected [80]. To identify the most accurate segmentation method, the same image as the RSI was segmented using the standard values provided by the program for each method. Subsequently, both accuracy coefficients (ADC and FEC) were calculated, see Tab. 4:

Tab. 4: Comparison of the accuracy of different auto local threshold methods

Method	ADC [%]	FEC [%]
Mean	101.9	13.4
Median	204.8	111.2
Middle grey value	76.5	23.8
Contrast	76.8	23.7
Bernsen	76.1	24.5
Niblack	94.8	10.7
Otsu	82.6	18.4
Phansalkar	79.6	20.9
Sauvola	76.6	23.7

The FEC is weighted higher than the ADC because it provides more reliable information about the segmentation quality. Thus the method which provides the most accurate segmentation results is the method according to Niblack, which will be discussed in more detail. This method treats every pixel in the images separately and the following equation (18) determines whether it is a foreground or a background pixel [82]:

$$pixel_{backgr.} = (pixel_{select} > mean + k * stdrtdev. - c)\,, \tag{18}$$

where the parameters k and c can be chosen by the operator. In general, the selected pixel is set as a background pixel if its brightness is higher than the calculated value. The mean and standard deviations are calculated in a user predefined window around the selected pixel. The offset value c is not implemented in the original calculation but is used in Fiji to shift the grey level intensity of the selected background pixel up or down. A negative value means that brighter pixels in the original image will be indicated as foreground pixels, and vice versa for positive values. The value k allows the user to choose if the foreground in the original image is bright (set to a positive decimal number) or dark (negative decimal number). The accurate parameter must be chosen individually for each filtered image stack. As can be seen in Tab. 4, the FEC is 10.7 % if standard values for k (k = -0.2) and c (c = 0) are used. By adjusting these two parameters an ADC of 98.1 % and a FEC of 5.6 % can be achieved. But this result has to be interpreted with care, because a comparison of the results gained by the Niblack segmentation method with the original image demonstrates that most of the unlocated features are cracks and not filler particles, see Fig. 58. This means that the Niblack method is very accurate in segmenting the filler particles, but can only locate larger cracks and fails to segment fine cracks with low contrast related to the background.

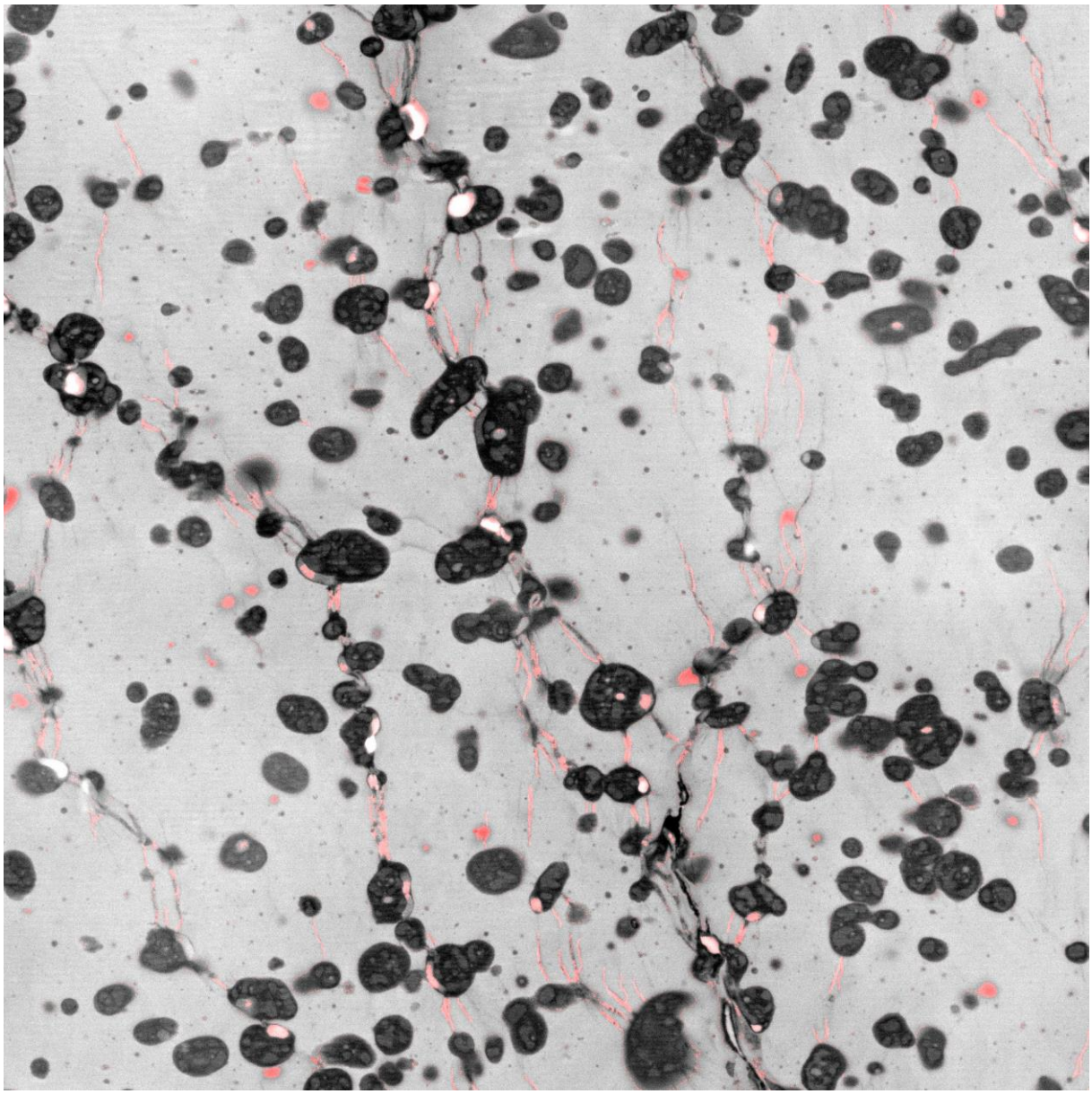

Fig. 58: Overlay of the original image with those features not detected by the Niblack segmentation method, with the latter marked in red.

Nevertheless, in comparison with the global threshold method, the method according to Niblack provides a slightly better segmentation result but also needs a higher computational effort and is thus more time intensive. But a discrimination between the two image features, filler particles and cracks, is not possible in this case either. In chapter 3.5.4.6 a segmentation method will be introduced that can be used to obtain separate segmented image stacks for each of the two features.

3.5.4.5. Trainable WEKA segmentation

One of the most sophisticated methods for image segmentation is to train the computer to identify different objects in an image. One method implemented in the software Fiji is the Waikato Environment for Knowledge Analysis (WEKA) segmentation method, which enables the user to specify the objects of interest and uses different machine learning algorithms to train the computer to identify them [83]. The result is an automatically generated labelled image based on the trained image features. The user can select different training features from a wide variety on offer, which can be seen on the right side of Fig. 59, a description of the individual options can be found on the plugin webpage[4].

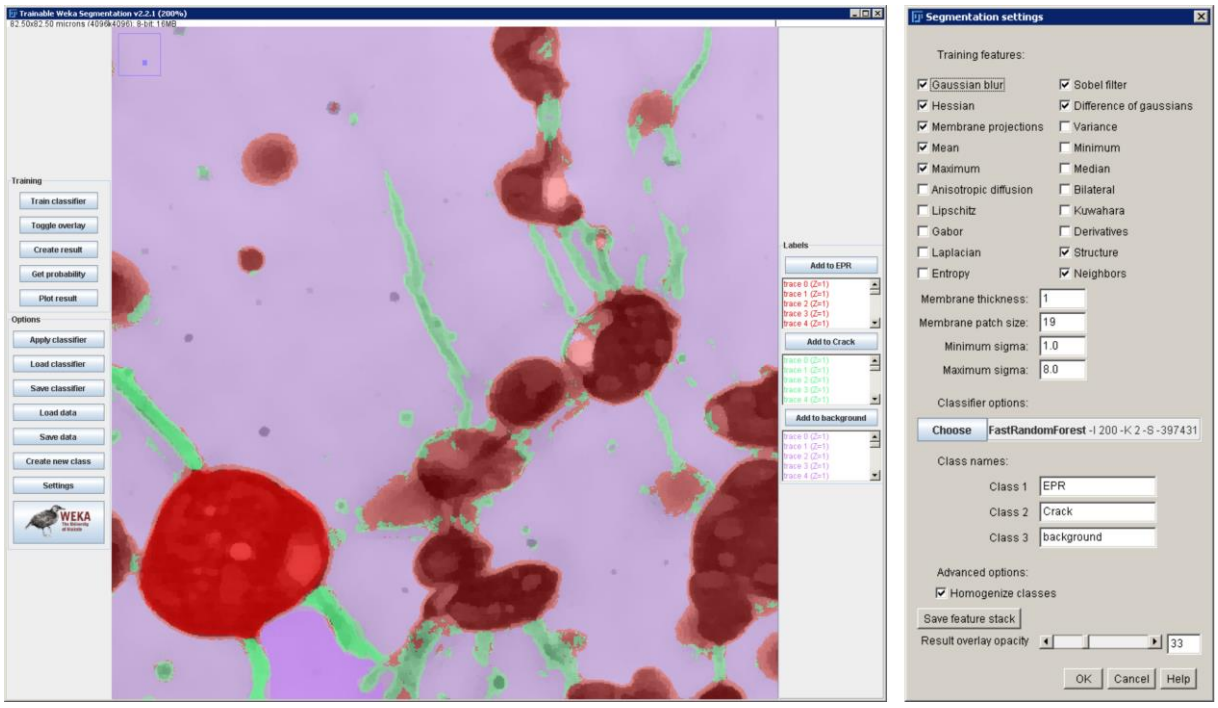

Fig. 59: User interface of the WEKA segmentation tool; left: graphical user interface, right: list of possible settings of the WEKA segmentation tool.

To initialise the segmentation process, the user must first specify the different labels inside the image manually. This involves marking the different phases and assigning them to the appropriate label. Due to the large variation within one phase (phases: filler particles, cracks, background), around 30 marks per phase must be set for a reliable segmentation. By ticking the different trainable features in the setting menu the user can select the features to be trained for the marked phases. Generally the quality of the segmentation results increases with the number of training features selected. Nevertheless, as the method is very CPU and memory intensive, the amount of learned features depends on the computer setup used and the image

[4] http://imagej.net/Trainable_Weka_Segmentation; last access Sept. 2016

or stack size. Because the computation can be parallelised a Dell© workstation with two six core Xeon processors running at 3 GHz and 48 GBytes of RAM (random access memory) was used. This allows one image of 4.096 x 4.096 px² and the settings shown in Fig. 59 (right) to be trained and segmented in about 10 min. Once the training has been completed, the whole image is segmented into the three predefined objects and the result is overlaid with the original image to check for wrongly assigned regions. By assigning these regions the correct labels the segmentation result can be improved with an iterative process of trainings. This iterative segmentation process produces a separate labelled image for each image feature, like the one shown in Fig. 60 b).

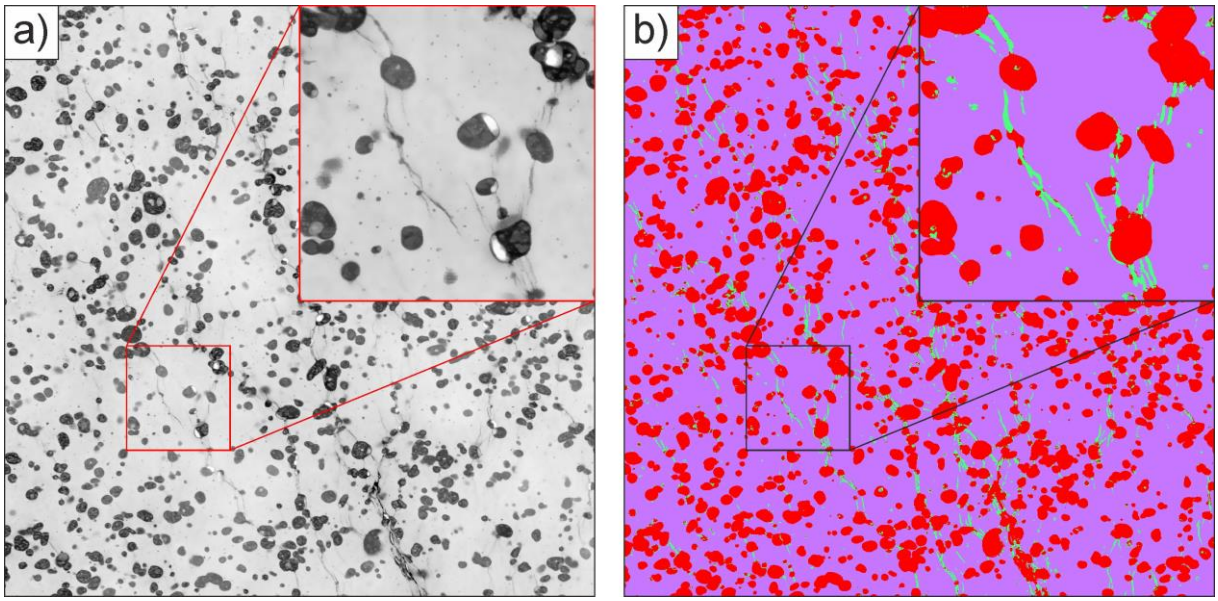

Fig. 60: Original image, b) image after segmentation by an iterative WEKA process, with filler particles marked in red, cracks in green and the background (polypropylene matrix) in purple. Magnified sections of the images in the inserts in the upper right corners.

The coefficients introduced in chapter 3.5.4.1 were again calculated separately for both image features in order to check the segmentation quality. An ADC of 125.3 % and a FEC of 29.1 % were calculated for the label including only the filler particle. The respective values for the cracks are 149.5 % for the ADC and 128.4 % for the FEC. This high oversegmentation, especially for the cracks, is mainly due to two reasons. Firstly, some regions were labelled incorrectly, even when a higher number of marks were set and more image features were implemented in the WEKA process, see Fig. 61 a). This image shows an overlay of the segmentation result and the original image for better visualisation, with the filler particles marked in red and the cracks in green. Secondly, an overestimation of the edge regions took place. A clear oversegmentation can be seen at the edge regions of both the cracks and the particles, resulting in a larger area in the respective segmented labels. This oversegmentation at the edges is illustrated by Fig. 61 b) and c), which show the differences of the areas of the filler particles and cracks respectively, as calculated by comparing the WEKA segmented image with the RSI. Because the crack area is much smaller than the filler particle area, this

overestimation at the edges leads to a larger error in the segmentation of the cracks. But this result must be treated with caution, because a visual comparison of the filler particles and cracks detected by the WEKA method with the respective labels in the RSI shows a good agreement in the detection rates of the two image features. This means that this method can locate even fine cracks. And the vital issue is the detection of the cracks, while their exact width is not of real importance, at least not in this investigation. The 3D reconstructions should mainly provide information about the size of the fracture surfaces and the location of the cracks related to the position of the neighbouring filler particles. Thus, neither the ADC nor the FEC coefficients may be the most suitable parameters for estimating the segmentation accuracy.

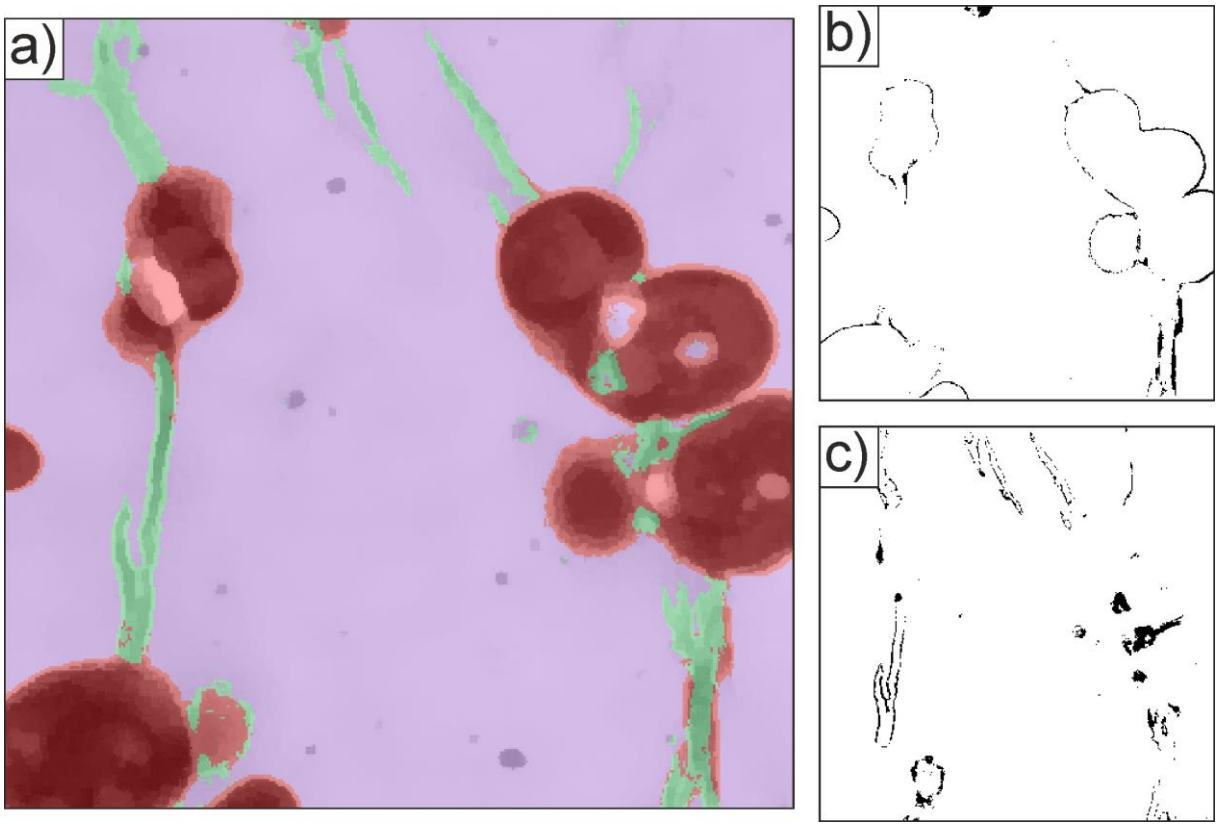

Fig. 61: Investigation of WEKA oversegmentation: a) overlay of the original image with the respective segmentation result, b) pixels which are matched incorrectly to the filler particle labels and c) the respective incorrectly matched pixels of the crack labels.

The WEKA algorithm has proven to be a convenient segmentation method, especially in detecting fine cracks. But there are limitations in segmenting a big dataset due to the limited amount of memory available. To overcome this issue the stacks can be divided into sub-stacks which can be segmented separately and finally again linked to obtain a larger 3D reconstructed volume. But it has to be mentioned that the segmentation of big datasets can be very time consuming because of the iterative process which has to be performed for every individual sub-stack. An image segmentation strategy which is less sensitive to oversegmentation, combining different already discussed image filters and segmentation methods, will be established and discussed in the following chapter.

3.5.4.6. Applied image segmentation strategy

An image segmentation strategy was developed to provide a suitable and reliable method to obtain one labelled image for each image feature (filler particles and cracks) [Michael Rastel, Diploma Thesis, Graz University of Technology, 2017]. A selection of image processing procedures was successively applied to the image stacks. The whole procedure is schematically shown in Fig. 62. The path involving the Kuwahara filter is less time consuming but usually the path involving the WEKA process is more accurate. Because the parameter setting for every individual procedure must be slightly adapted for the different image stacks, only a general description will be given.

The first steps serve to obtain an image stack where the noise is filtered, the contrast enhanced and a uniform grey value distribution in every image feature is achieved. This enables the usage of simple segmentation algorithms or to enhance the accuracy of more advanced methods. Therefore the NLM and Kuwahara filters are initially applied to reduce the noise in every image of the stack separately. The choice of a small “sigma” and “smoothing factor” for the NLM filter and repeated filtering preserves even small image features. The subsequently applied Kuwahara filter with a small window size is used for edge enhancement, see Fig. 62 b). Moreover, the contrast in the processed images is enhanced by background subtraction. To obtain the same grey value distribution in every image of the stack, the “stack contrast adjustment” procedure is finally applied to the whole stack, with one representative image presented in Fig. 62 c). The “CLAHE” process is used to additionally increase the contrast between the foreground and background. In order to prevent excessive contrast enhancement, the process is applied several times with low “block-size” and “max. slope” values, followed by NLM filtering, see the result in Fig. 62 d). Image segmentation can now be performed by the “auto local threshold” technique according to Niblack, preferably using large window sizes and standard options. As can be seen in Fig. 62 e), the segmented image now contains both features, the filler particles and the cracks.

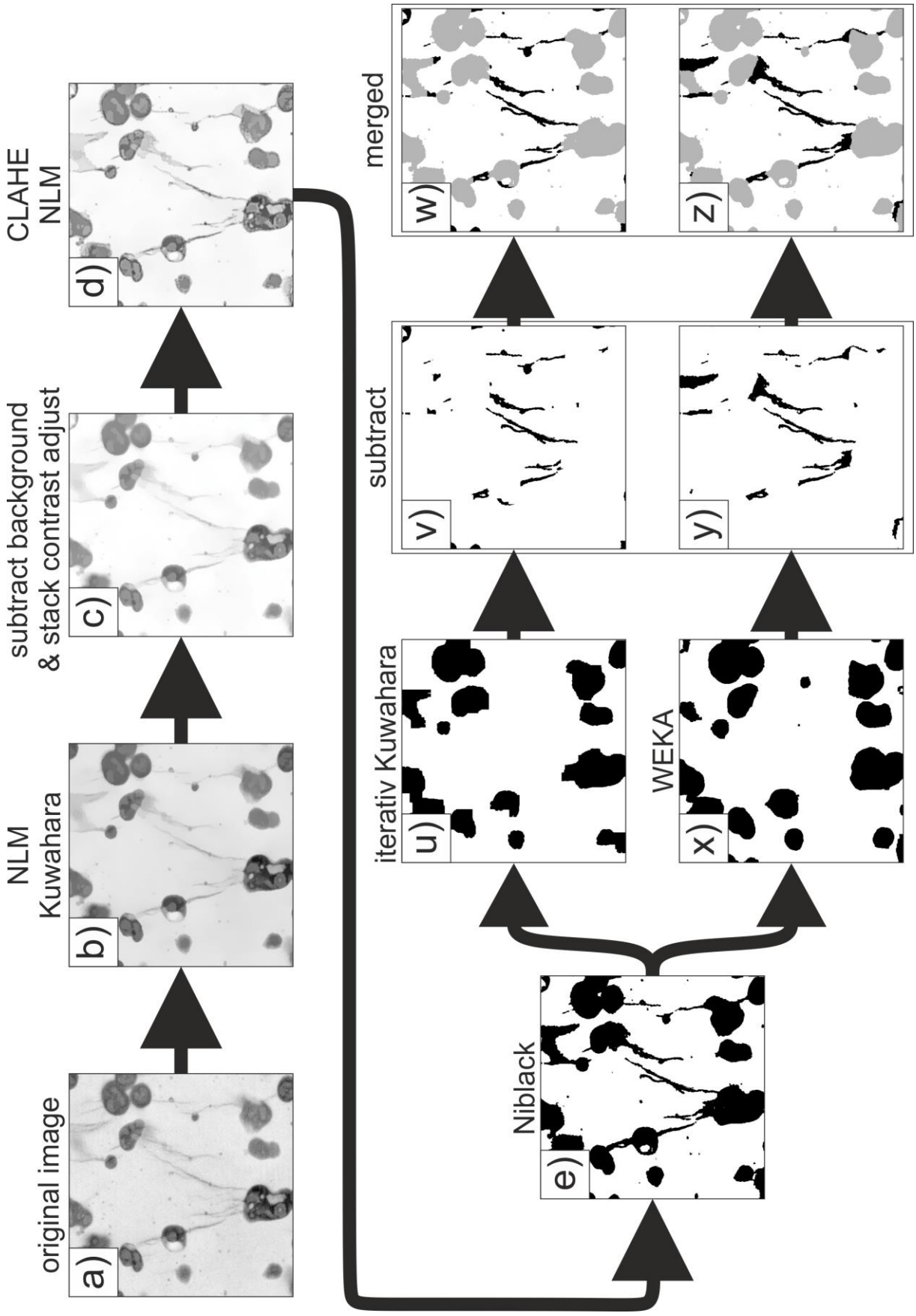

Fig. 62: Schematic of the segmentation strategy used. Detailed description can be found in the text.

Two different methods were established to obtain separate images for each of the two features, as schematically drawn in Fig. 62. The first method uses the circumstance that different window sizes of the Kuwahara filter smooth image features of different sizes. To remove the cracks, the Kuwahara filter must therefore be applied repeatedly with an increasing window size until only the filler particles are left. This iterative process can be applied to grey level images as well as binary images, as schematically shown in Fig. 63, where the filter was first applied five times with a window size of 5 x 5 to the original image a) to obtain image b). Subsequently, a larger window of 11 x 11 was applied to obtain image c) and so forth. But because the edges of the filler particles were slightly smaller due to the filtering, the resulting labels are also smaller than the labels in the initial segmented image a). To compensate for this, the labels can be dilated appropriately. The dilation process adds one pixel to every edge in the binary image every time it is applied, thus the area of all filler particles increases. The resulting image (dilated version of d)) is then subtracted from the original a) to obtain a binary image where only the cracks are left, because negative values are set to zero in principle. The respective images in the schematic drawing in Fig. 62 range from u)–w), with u) the result of the iterative Kuwahara process, v) after subtraction of image u) from image e) and w) the merged version containing both the filler particles and cracks, but with different brightnesses for the two features.

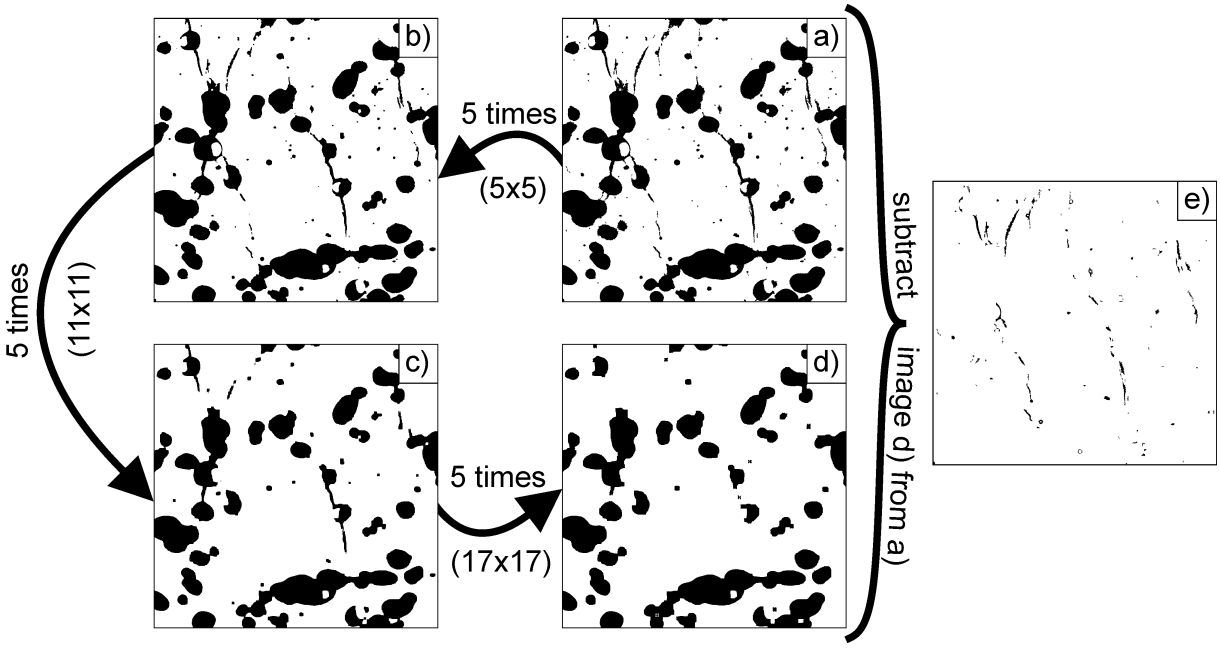

Fig. 63: Schematic of the iterative Kuwahara filtering process applied to a binary image: a) image segmented by the Niblack method, b) the same image after applying a 5 x 5 window Kuwahara filter 5 times, c) after subsequently applying an 11 x 11 Kuwahara filter 5 times and d) a 17 x 17 Kuwahara filter 5 times. To obtain only the cracks in e) a dilated version of image d) was subtracted from image a).

The second possibility to separate the cracks and filler particles in the binary image in Fig. 62 e) is by use of the WEKA segmentation algorithm. As mentioned in chapter 3.5.4.5, this algorithm is very accurate in segmenting both image features, but produces a clear

overestimation at all edges (see Fig. 61). This issue can be used to obtain binary images where only the filler particles are present, which are however slightly larger than the filler particles obtained by the Niblack algorithm, see Fig. 62 x). Subtracting the result obtained by the WEKA process from the Niblack result leaves only the cracks (Fig. 62 y)). But because the filler particles in the binary images of the WEKA result are definitely too large, these binary images are not directly used for the 3D reconstruction of the EPR particles. Instead, the already segmented cracks were subtracted from the initial Niblack result to obtain a better result, as shown in Fig. 62 z).

In some cases the crack labels for both segmentation methods must additionally meet a special constraint before they can be subtracted from the overall segmentation because of occasional mis-segmentation. Fiji enables grouping of the labels according to their shape. The circularity C of objects is given by:

$$C = 4\,\pi\,\frac{A}{p^2}, \tag{19}$$

with A the area and p the perimeter of the respective binary object. If the object is a perfect circle C is 1.0 and approaches 0.0 the more elongated the object is. This parameter can be used to filter out wrongly segmented filler particles from images containing only the segmented cracks, because generally the circularity of the filler particles is higher than that of the cracks, which tend to resemble lines. This is mainly true for the EPR10 and partly true for the EPR08 and LLDPE sample, see Fig. 32. Most of the wrongly segmented filler particles can be removed by choosing the appropriate value.

The accuracy of the segmentation strategy was verified by calculating the respective ADC and FEC for the two different segmentation strategies presented in Fig. 62. The Kuwahara filter produced an ADC of 107.3 % and a FEC of 11.5 % for the filler particles, and an ADC of 67.6% and a FEC of 92.7 % for the crack labels. The calculations for the WEKA segmentation algorithm gave an ADC of 105.7 % and a FEC of 9.5 % for the filler particles and an ADC of 91.9 % and a FEC of 94.7 % for the cracks. Thus the segmentation strategy including the WEKA process produced a slightly but not distinctly better segmentation result. Hence both segmentation algorithms are capable of separating the filler particles from the cracks.

Which strategy is chosen to segment an image stack depends mainly on the computing power available, because the WEKA process needs a higher computational effort than the iterative Kuwahara process. A routine was programmed for the WEKA image segmentation strategy using a combination of MATLAB® R2016a (the MathWorks, Inc., Natick, Massachusetts, United States) and Fiji. It provides automated execution of the different image processes on a whole image stack. The code for this routine can be found in the Appendix.

3.5.5. 3D rendering and analysis of the segmentation result

A 3D model of both structures, the filler particles and the cracks, was rendered using the program Avizo® 9.0 (FEI Visualisation Science Group, Bordeaux, France), because it provides several measurement and analysis tools additionally to model visualisation. Since it offers a huge variety of options only a brief introduction will be given in this chapter. A detailed description of all options and settings can be found in the user guide [84].

A screenshot of the user interface is shown in Fig. 64, where the major parts are marked in different colours. After loading the segmented image stacks the voxel size must be defined. Here the x- and y-values are the pixel sizes of the images which were recorded during the SBEM process. The z-value matches the slice thickness, i.e. 100 nm for the present work. These settings are also shown in the properties area in Fig. 64 b) if the respective module is selected in the project view, see Fig. 64 a). The project view shows all available options, see Fig. 64 c). As the loaded image stacks are already segmented, only the rendering modules were used for calculating the reconstruction. After rendering the model it can be presented in the 3D viewer in Fig. 64 d). Typically the “surface rendering” option was used because it provides a reliable and smooth model. In this option small triangles are calculated on the whole surface of each structure. The size of the triangles depends on the rendering settings, but the smaller their size the smoother the surface. The maximum possible amount of triangles or voxels which can be displayed depends on the computer efficiency. With the computer used (see setup details in chapter 3.5.4.5), some segmentation results contained too much triangles/voxels (up to about $2.5 \cdot 10^9$ voxels) which could not be displayed. To be able to also display larger volumes the voxel number often had to be down-scaled. The module options also contain the measurement and analysis tools. As already described in chapters 3.5.4.5 and 3.5.4.6, the segmentation algorithms used lead to a relatively large error, especially for the crack labels. The measurement results obtained from the 3D model should thus also be interpreted with caution. Nevertheless a qualitative analysis is always feasible either within one reconstruction or in a comparison between the different reconstructions. The results of these analyses are either numeric values listed in a table, see Fig. 64 e) or displayed in the 3D viewer. The combination of both should provide a new insight into crack propagation in polymers during fracturing.

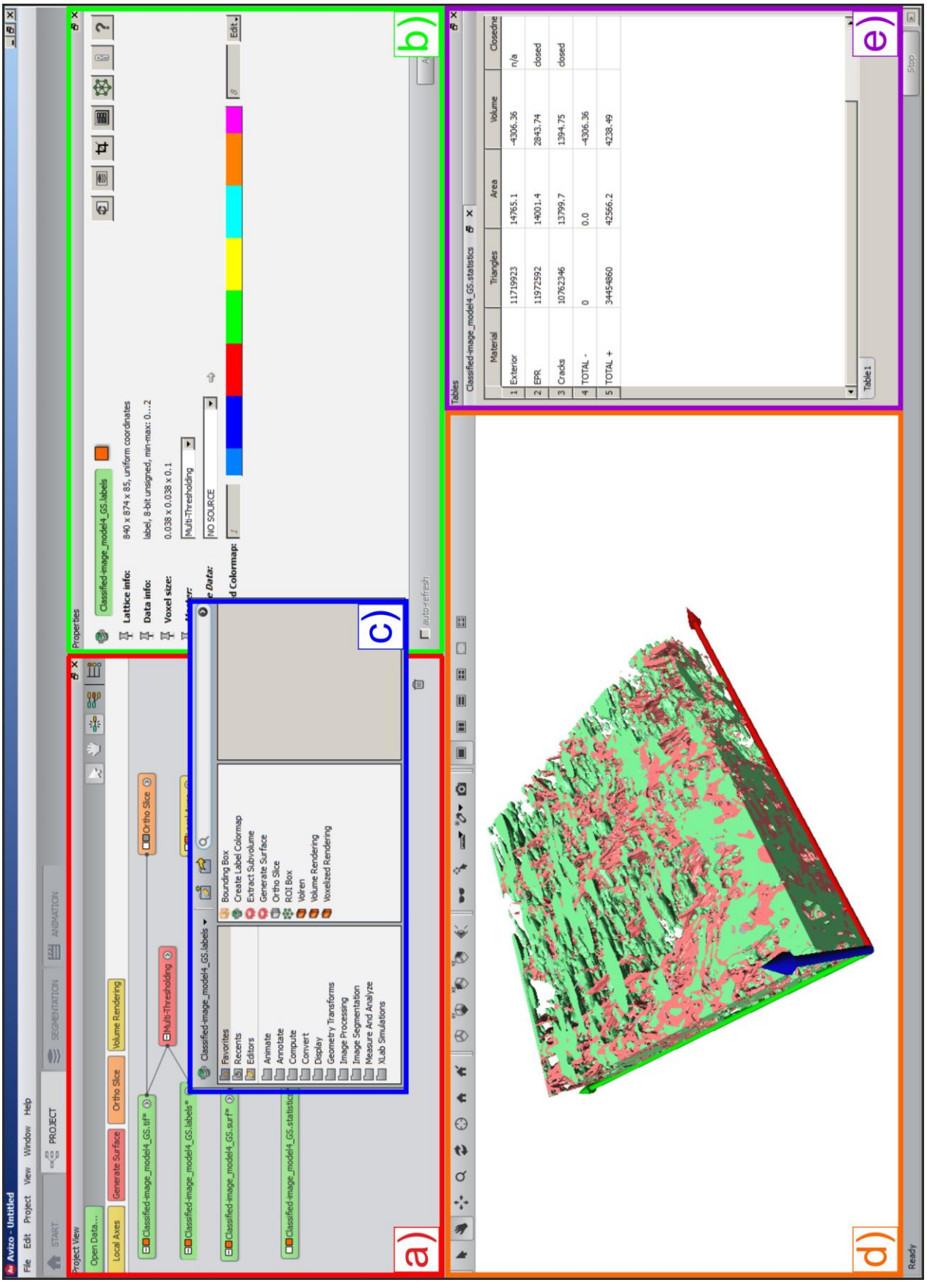

Fig. 64: Screenshot of the Avizo® user interface with a) the project view, b) the properties area, c) the available options for the respective module, d) the 3D viewer and e) the table with calculated results.

3.5.5.1. Distance transformation

As mentioned in section 3.1, interparticle distance distributions may play an important role in the interpretation of the fracture behaviour of particle modified polymers. More or less all methods for the calculation of 3D distance maps are based on the labelling of each pixel/voxel outside the reconstructed objects (in this case the filler particles) with respect to its distance to the nearest object boundary. Avizo® offers several calculation methods under the options "Image Processing >> Distance Maps": Chamfer distance map, Chessboard distance map, Closest boundary points, Euclidean distance map and Geodesic distance map. The Euclidean distance transformation (EDT) was used for the calculations although it is more time consuming because it involves a higher computational effort. This method is often used because of its rotation invariant properties [85]. The Euclidean distance d_e between the foreground p_i (EPR particle) and the background q_i can be calculated by:

$$d_e(p,q) = \sqrt{\sum_{i=1}^{n}(q_i - p_i)^2} \quad with \begin{cases} n = 2 \ldots\ldots 2D\ (x,y) \\ n = 3 \ldots 3D\ (x,y,z) \end{cases}. \tag{20}$$

This calculation takes into account that the diagonal neighbours of a pixel/voxel are farther away than the off-diagonal neighbours. In the resulting distance map pixels/voxels contain floating values which can be displayed or used for further statistical analyses. An example of a distance map of a 2D distribution of particles is shown in Fig. 65 a). The grey level of the distance map indicates the distance to the nearest particle surface. With this distance transformation it is possible, for example, to analyse the distribution of the interparticle distances between the filler particles or the average distance of the cracks in respect to the filler particles. By multiplying the image of the segmented cracks (binary image in Fig. 65 b)) with the distance map (Fig. 65 a)) the resulting image contains only information concerning the distance of the cracks to the nearest particle surfaces, as shown in Fig. 65 c). Now this can be used to initially calculate the average grey value of the distance map a), giving an average distance of the particles. Subsequently the average grey value of all cracks in image c) is calculated. If the average grey value of the cracks is significantly smaller than the average grey value of the total distance map this indicates that the cracks are mainly positioned in regions with a small interparticle distance between the filler particles, e.g. where agglomeration of the particles occurs.

The image obtained by the GT segmentation was investigated using this technique to prove that this concept provides sound results. In addition to the segmented cracks obtained, randomly orientated and distributed lines (with approximately the same thickness as the average cracks) were manually drawn in an image the same size as the GT images, see Fig. 65 d). The average grey value resulting after multiplication of this map with the distance map should be approximately the same as the average value of the distance map itself. At first the average grey value of the 2D EDT (one slice) was calculated with Avizo®, giving a value of 30.2. The corresponding average value for the random drawing similar to Fig. 65 e) was 29.3 and that for the cracks similar to Fig 30.7. This indicates that the average distance between the cracks and filler particles is approximately the same as the average distance between the particles. Subsequently the concept was tested by use of a 3D reconstruction of the same

sample (EPR08, tensile test stopped at 25 % yield). The resulting average grey value for the overall 3D distance map was 9.9. For testing the random drawn lines, the slice was extended to the same volume as the WEKA segmentation by taking it as an image sequence. After multiplying this volume with the overall 3D distance map, the resulting grey level average was also 9.9. This confirms that the drawn lines are at least randomly distributed in the 3D volume. This result also indicates that an overestimation of the particle distance in 3D can be expected when calculating the distance only from a 2D image. But as mentioned in previous chapters, this result must be treated with caution, because of the inaccuracy in the segmentation process and the large standard deviations of the calculated average values themselves. A comparison of the average grey value of the overall distance map with that obtained by multiplying it with the image containing the segmented cracks thus gives a good estimate of the average position of the cracks related to the filler particles. To reduce this comparison to just one parameter the grey value average of the cracks $\emptyset_{cracks}$ is divided by the grey value average of the distance map $\emptyset_{total}$:

$$DMc = \frac{\emptyset_{cracks}}{\emptyset_{total}}. \tag{21}$$

If the DMc value is significantly smaller than one then the cracks are located in areas where the interparticle distance is smaller than their average distance and if it is larger than one vice versa. This should provide new insight into how the distribution of the interparticle distances influences the cracking behaviour of particle modified polymers.

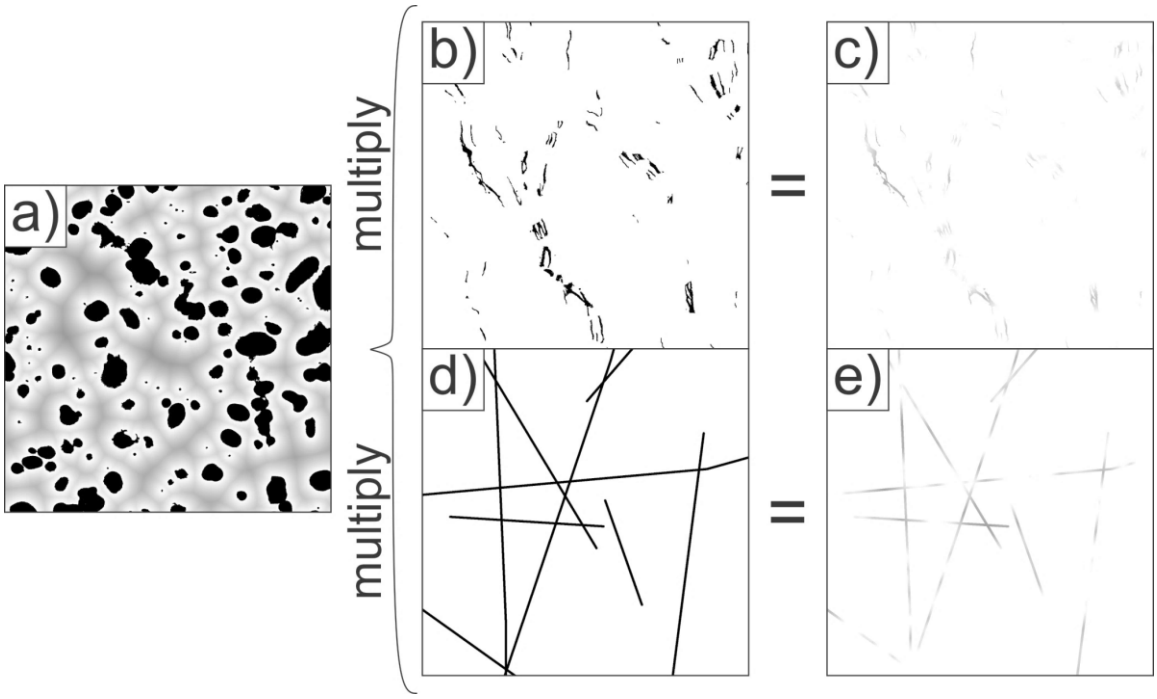

Fig. 65: Image multiplication of the distance map a) with a binary image of the cracks b) resulting in the image displayed in c), which is a map indicating the distance of the cracks to the nearest particle surface; d) image of manually drawn and randomly distributed lines and e) the image after multiplication with the distance map.

3.6. Results and discussion

All samples prepared by SBEM could be 3D reconstructed using the image processing methods introduced in the previous chapters and the subsequent rendering of the segmentation results. This process enables the visualisation of the spatial relationship between the filler particles and cracks. The 3D models additionally enable further simulations and/or calculations, e.g. of the 3D distance distribution of the particles. This can provide a new insight into the fracture behaviour of PP blended either with EPR or LLDPE filler particles and especially the impact of interparticle distance on crack formation and propagation at the very early stages of the fracture process.

3.6.1. PP-EPR08 blend sample

This sample was sliced and imaged by SBEM after stopping the tensile test at a force of approximately 50 % yield (see the respective force – elongation diagram in Fig. 38). An overview of the cross-section of part of the sample is shown in Fig. 66 a), with the position of the extracted part being marked in the inset. The direction of the applied tensile force is also specified in the image. At the top of image a) the precrack is visible (see section 3.4.1). The whole image stack contained 100 slices, so that the reconstruction size in z-direction was 10 µm (100 nm slice thickness). The overall image area in Fig. 66 b) was 107.42 x 189.87 µm² with a resolution of 3,000 x 5,300 px², resulting in a pixel size of 35.8 x 35.8 nm². It has to be mentioned that none of the pixel sizes given were directly measured, but were obtained by dividing the image size by the pixel number. This resolution was sufficient to image both features, the EPR particles and cracks with adequate accuracy, see detail view Fig. 66 c). With a dwell time of 10 µs the acquisition time per image was around 160 s. The segmentation of the resulting image stacks was carried out using the image segmentation strategy along the WEKA path described in chapter 3.5.4.6 (see also Fig. 62). It is worth noting that an image mapping of the whole sample surface would be possible in principle, but both the recording time per slice and the data amount would increase accordingly. Furthermore the requirements on the computer system, where the segmentation processes and the 3D reconstructions are performed, would increase.

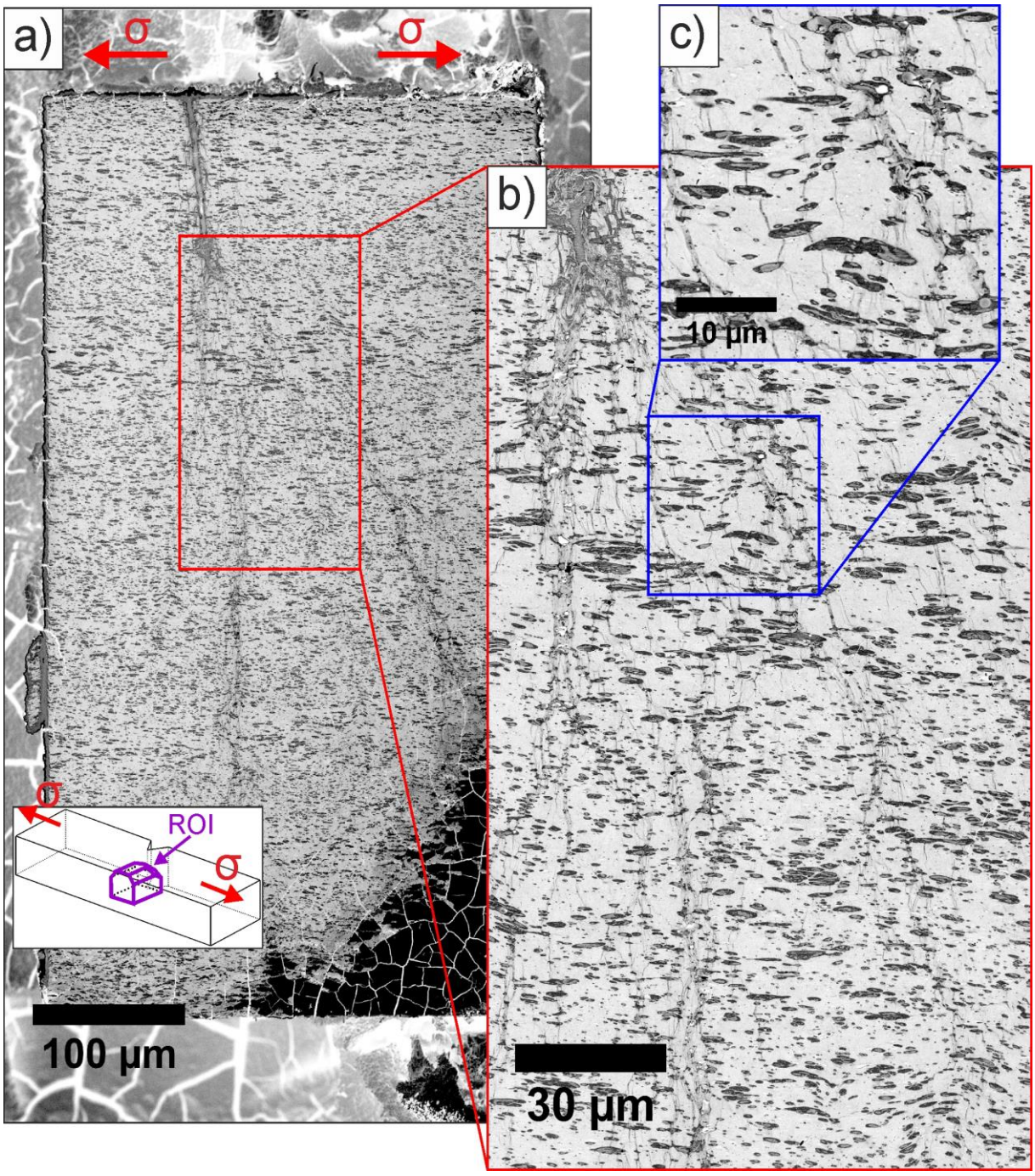

Fig. 66: Sample EPR08; Overview of the whole area of a microtome cut across the extracted part marked in purple in the inset of a); images b) and c) are magnified sections, with b) giving the size of the images recorded for the 3D reconstructions. The arrows show the direction of the force during the tensile test.

3.6.1.1. 3D reconstruction

After completion of the segmentation using the WEKA algorithm procedure (see Fig. 62), the segmented images were rendered using Avizo®. Because the whole segmented volume of 107.4 x 189.8 x 10.0 µm³ contains around $1.6 \cdot 10^9$ voxels and could not be rendered in one step, only a sub-volume of 30.2 x 31.5 x 8.5 µm³ is presented in the figure below. Fig. 67 a)

shows only the cracks in blue, b) only the EPR filler particles in green and c) a merged reconstruction of both structures. The direction of the force during the tensile test was parallel to the x-axis and the pre-crack is located close to the lower left corner (on the z-axis). As expected, nearly all cracks run relatively perpendicular to the tensile test direction, whereas the elongated axis of the EPR particles is parallel to the testing direction, which was the flow direction during injection moulding.

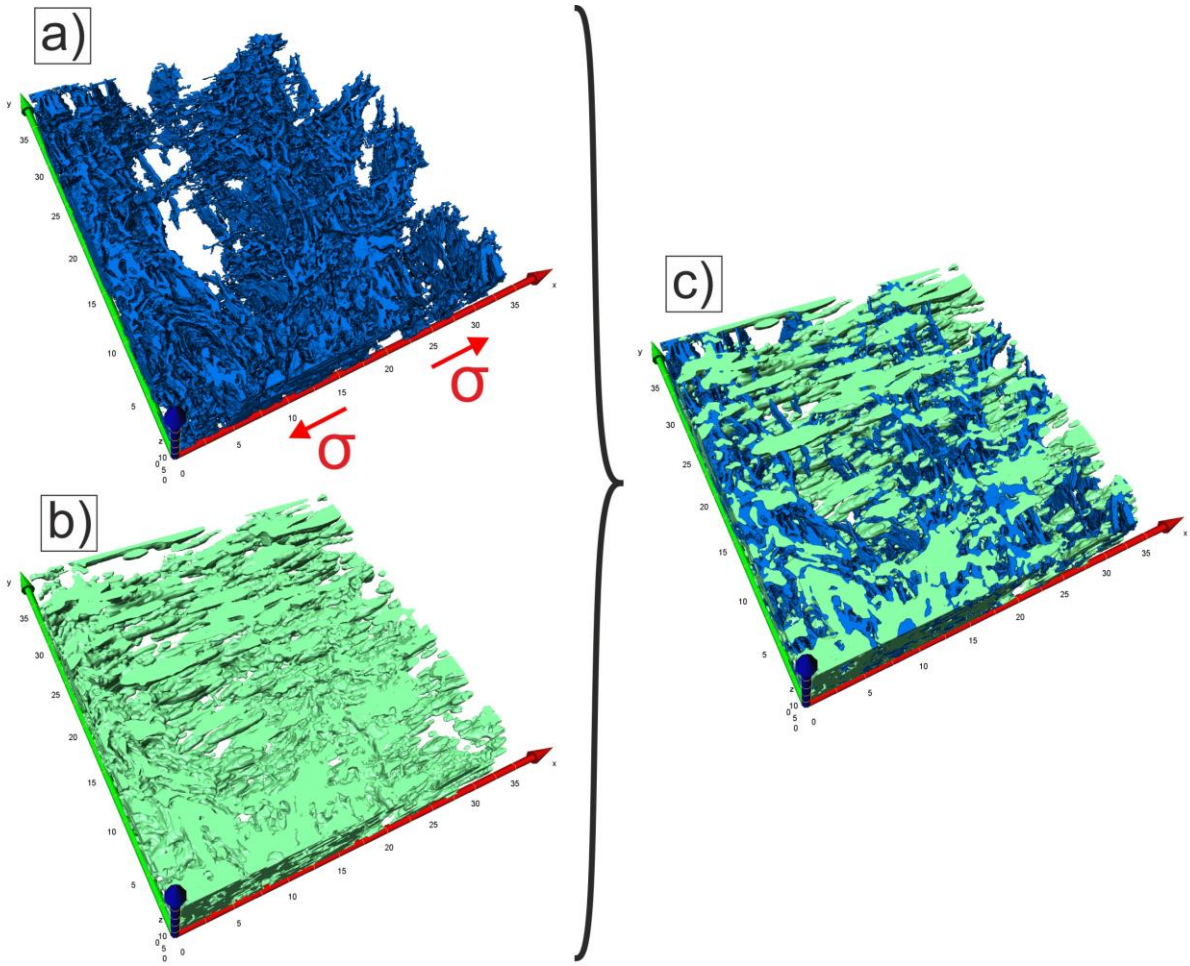

Fig. 67: 3D reconstruction of sample EPR08 with the tensile test stopped at 50 % yield: a) shows the cracks, b) the filler particles and c) the merging of both features (shown volume: 30.2 x 31.5 x 8.5 µm³).

The reconstruction allows the distribution of the filler particles and cracks in the respective region to be illustrated. Especially Fig. 67 c) gives the impression that the density of cracks is highest in regions with also high filler particle density. But it is hardly possible to verify whether or not one or more filler particles are encompassed by an individual crack and what the crack surface looks like. Therefore smaller representative volumes (sub-volume) were cropped from the whole volume to obtain a better feeling for the structure of the crack surfaces and their connectivity to the EPR particles, see Fig. 68. Fig. 68 presents two single crack surfaces, and it can be seen that they consist of connected regions encompassing many filler particles with interparticle distances generally less than the radii of the neighbouring particles. As explicated

in chapter 3.1 the stress concentration between filler particles reaches its maximum at an angle of 90° to the applied load. But these results were gained from calculations for spherical particles, and some investigations revealed a different behaviour for elongated particles. The stress concentration was found to be highest at the tip of the elongated particles in case they are oriented at a right angle to the applied force [64]. They concluded that the interparticle distance and the stress field around the filler particles are mainly responsible for the mechanical toughness of the polymer. Therefore the distance map will also be calculated for this polymer to obtain information about at least a neighbourhood relationship between cracks and EPR particles.

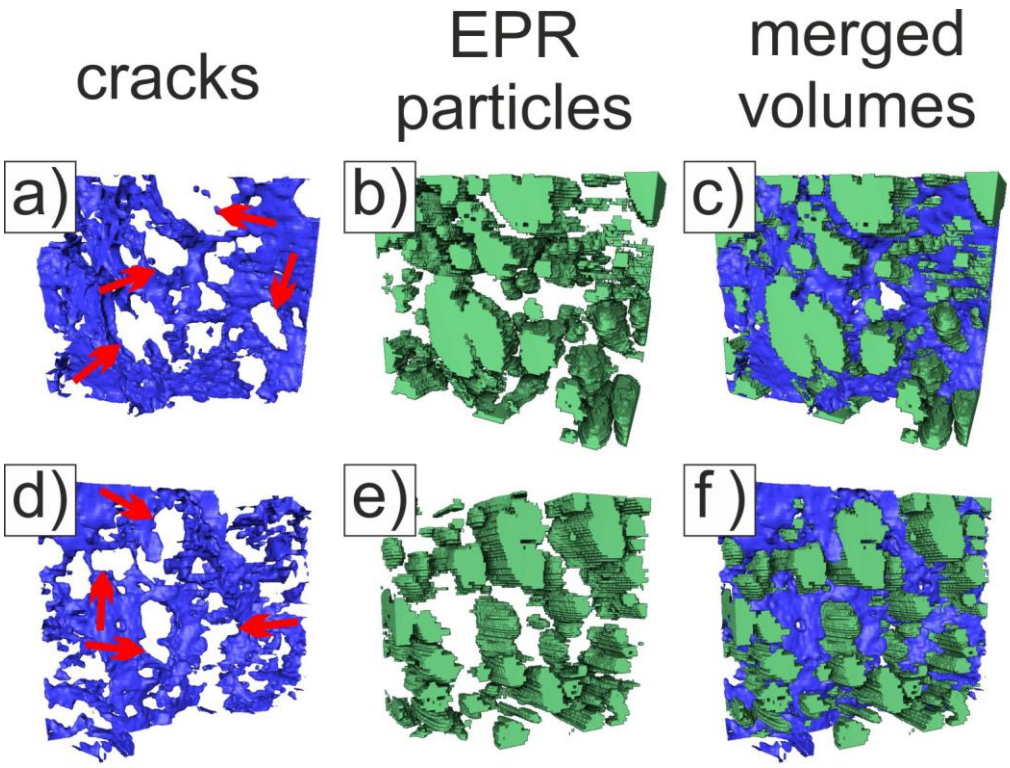

Fig. 68: Two sub-volumes of the whole 3D reconstruction in Fig. 67, with each of the two volumes showing just one fracture surface; a) and d) show the crack surfaces, b) and e) the EPR particles and c) and f) particles and cracks merged. The arrows in a) and d) point to the positions of EPR particles (shown volume: 1.1 x 9.6 x 8.4 µm³).

3.6.1.2. Distance map

As described in chapter 3.5.5.1, the separate 3D reconstruction of the filler particles and that of the cracks can be used to gain information about the position of the cracks in relation to the filler particles and to calculate the interparticle distances. Avizo® provides two methods for the calculation of the distance maps. The first one calculates the distribution of the particle distances for each slice separately, providing a stack of 2D distance maps. The second one also includes the third dimension to reveal the interparticle distances of the objects in all three dimensions. But both options are only available for either single images or already 3D

reconstructed objects. Therefore instead of the previously mentioned EDT (Euclidean distance transformation, see section 3.5.5.1 Fig. 67), a slightly different method was used for this special case: the adapted Chamfer distance transformation (CDT). This transformation is an approximation of the EDT but needs less computational effort [84]. But as the resulting pixels or voxels are given in a different data format (32 bit floating real instead of 8 bit unsigned character), the results are not directly comparable to the distance maps obtained by the EDT. The initial investigation performed with this transformation suggested that there might be a difference in the distribution of the interparticle distances calculated on the one hand from the 2D images and on the other hand from the 3D reconstructions (see chapter 3.5.5.1). But the EDT in 2D is only available for one slice and so the CDT will be used for the 2D / 3D comparison to obtain a statistically more significant result.

Additional calculations were performed for subdomains to ascertain that the areas / volumes chosen for the calculations were large enough to obtain reliable results. The whole area in Fig. 69 a) comprises 85 images with 20,353.8 µm², the subdomain 204.5 µm², the whole volume in Fig. 69 b) is 107.4 x 189.3 x 8.5 µm³ and the subdomain 14.3 x 14.3 x 8.5 µm³. As Fig. 69 a) and b) prove, the differences in the interparticle distance distributions in the whole regions and their subdomains are rather modest. On the contrary, there is a distinct difference between the results from the 2D (Fig. 69 a)) and the 3D analysis (Fig. 69 b)). The 3D analysis gives much shorter distances than the 2D analysis.

The 2D analysis, however, is based only on images cut in flow direction (FD) of the injection moulded samples. Yet the particles are elongated and rather ellipsoidal in shape. Results gained from images cut perpendicular to the flow direction might thus provide different results. Therefore Fig. 69 c) also shows results from cuts perpendicular to the flow direction including the average between both directions. The individual lines parallel and perpendicular to the FD are averages of five images. But the 3D reconstruction gives still smaller distances. A difference in the distance distribution between regions close to the boundaries and the centre can be often found in injection moulded polypropylene and is not surprising.

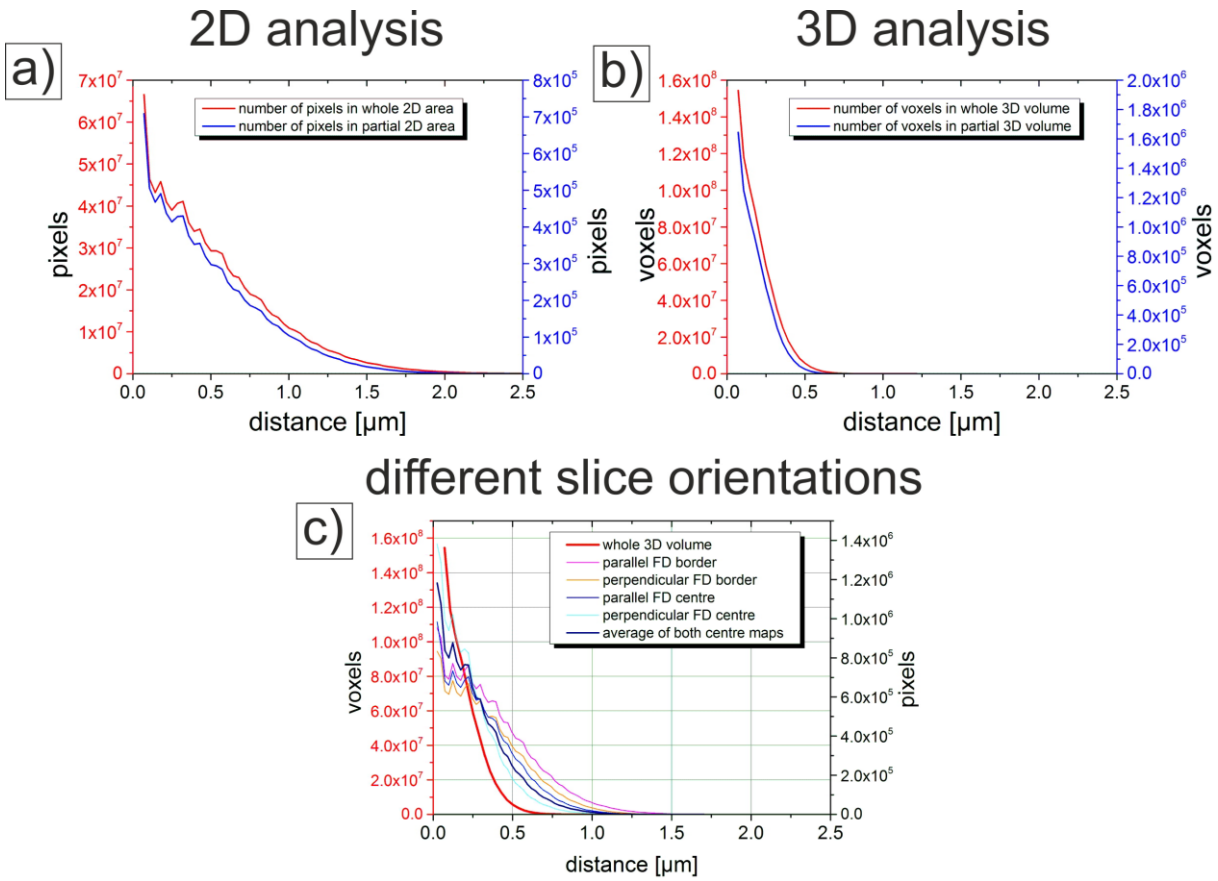

Fig. 69: Number of pixels / voxels outside the particles as a function of the distance of these pixels / voxels to the nearest particle surface calculated by CDT in a) 2D and b) 3D for the PP-EPR08 sample (tensile test stopped at 50 % yield); this is a substitute for the distribution of the interparticle distances, the actual distance is roughly twice the value appearing in the graphs; c) comparison of the 3D particle distance distribution with 2D distributions gained from slices cut in different directions; details can be found in text.

The distance map for the reconstructed EPR particles was calculated by the EDT for a volume of 107.4 x 189.8 x 10.0 µm³. The resulting Fig. 70 a) shows the same sub-volume as presented in Fig. 67. The transparent regions are those where the particles shown in Fig. 70 c) were originally based. The colour map ranges from dark red, which represents short interparticle distances, to light yellow regions, which represent the regions with the longest interparticle distances. For an easier comparison of crack locations within this distance map, they were additionally rendered in Fig. 70 b). It seems that the cracks are mainly located in regions with a high density of EPR particles, thus short interparticle distances. The resulting calculated DMc (see section 3.5.5.1) value was 0.74, which also indicates that the cracks developed preferentially in regions where the interparticle distance is smaller than the average EPR interparticle distance. The reliability of this value was verified by multiplying the distance map by randomly distributed lines (compare Fig. 65) and calculating the respective DMc. As the respective value was 1.04 the DMc can be assumed to be reliable. This indicates that the interparticle distance is an essential parameter for crack formation even if the applied force is perpendicular to the main axis of the ellipsoidal particles.

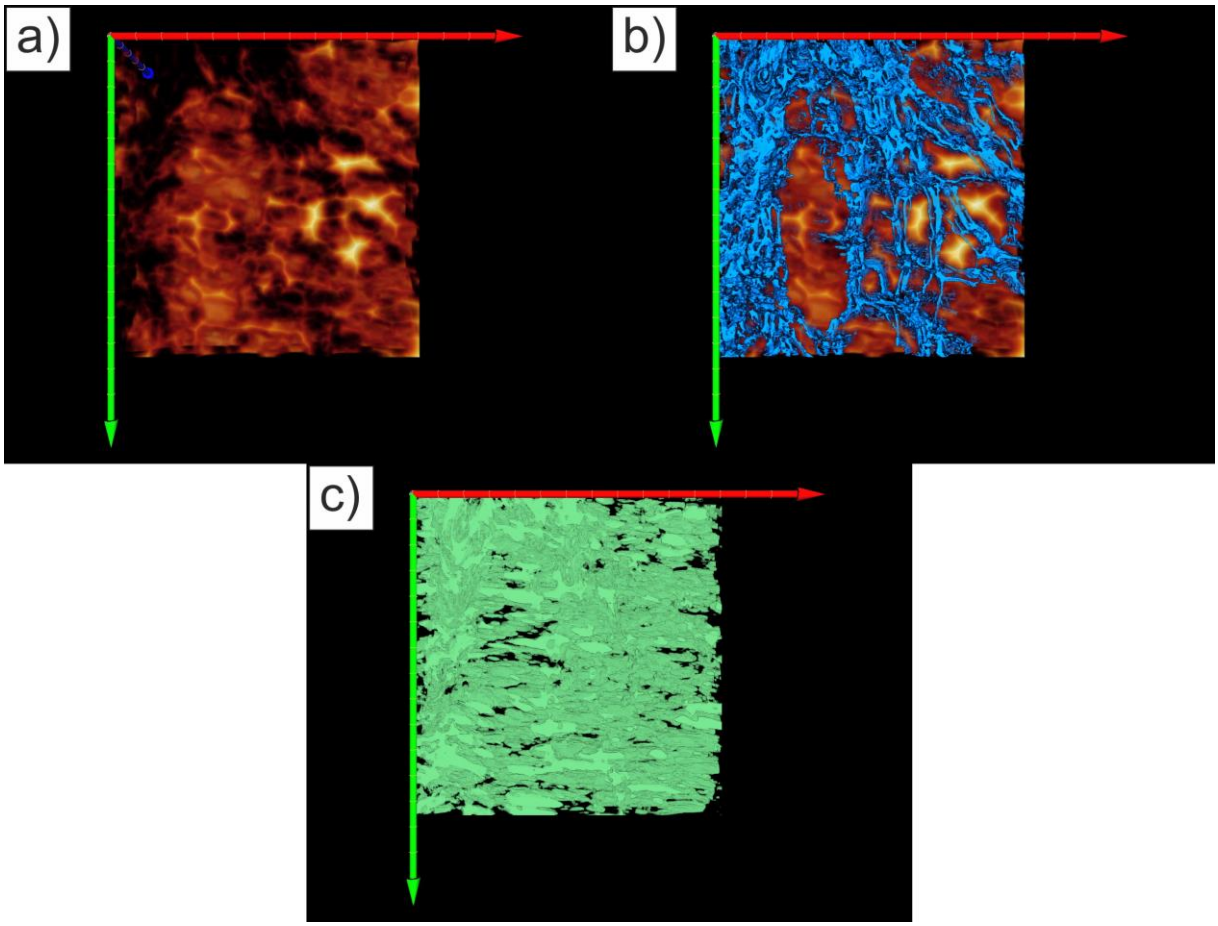

Fig. 70: a) EDT (Euclidean distance transformation) performed on a partial volume reconstruction of the EPR08 sample (tensile test stopped at 50 % yield); b) merged image of a) and 3D reconstruction of the cracks, c) 3D reconstruction of the EPR particles which was used for calculating the distance map in a) (shown volume: 30.2 x 31.5 x 8.5 µm³).

3.6.2. PP-EPR10 blend sample

The second investigated PP sample blended with EPR (EPR10) is shown in Fig. 32 b). Here the same amount of EPR was added as in the EPR08 sample, but the particles were much larger and rather spherical in shape. This time the tensile tests were stopped at both 25 % and 50 % yield. This makes it possible to gain information about the progress of crack formation at different strains. Fig. 71 shows the cross-sections of the two samples. Unsurprisingly the overviews of both samples in Fig. 71 a) and d) show much farther widespread crack propagation in the sample tested to 50 % yield than in the 25 % sample. This can also be seen in the images recorded during the SBEM process, see Fig. 71 b) and e). To resolve all image features in the SBEM images the resolution for the 25 % yield tested sample was set to 4,096 x 4,096 px², which gives a pixel size of 20.1 x 20.1 nm². The resolution for the second sample was set to 4,000 x 4,000 px² with a pixel resolution of 36.6 x 36.6 nm². This gives approximately the same number of pixels as for the EPR08 recordings, thus also the acquisition time per image was nearly the same in both cases, i.e. 160 s/image. Also the same segmentation strategy was applied to obtain binary image stacks of both investigated samples.

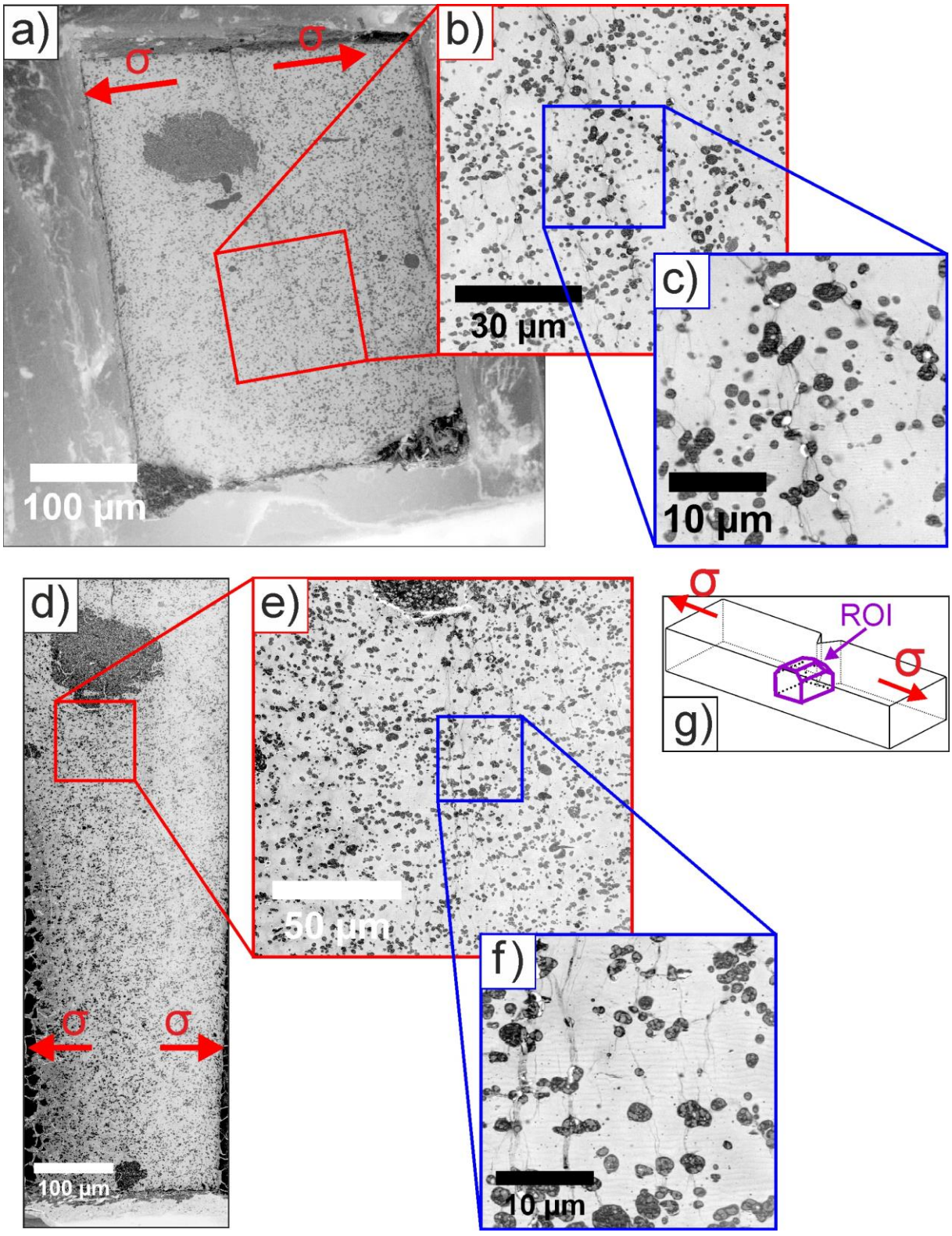

Fig. 71: Cross-sections of EPR10 samples; a) – c): tensile test stopped at 25 % yield; d) – f): tensile test stopped at 50 % yield; a) and d) show an overview of the whole sample, b) and e) the recorded area during the SBEM process and c) and f) a magnified region. The pre-crack starts at the top boundary in both cases.

3.6.2.1. 3D reconstruction

The results for the PP-EPR10 sample where the tensile test was stopped at approximately 25 % yield will be discussed first. Fig. 72 shows the whole reconstruction of a) only the cracks, b) only the filler particles and c) both merged. It can be seen that a relatively large number of cracks were generated in the PP matrix although the tensile test was already stopped at 25 % yield. It should be mentioned that the volume of 70 x 70 x 10 µm³ represents only a part of the total volume containing cracks. The direction of the applied force was parallel to the x-axis, as drawn in Fig. 72 a). A detailed look at the reconstruction reveals some regions with a high crack density in addition to smaller isolated crazes, see Fig. 72 a). The preferential crack propagation is perpendicular to the applied force. Additional information about the spatial relationship between the cracks and the filler particles can be obtained by overlaying the two 3D reconstructions. But the merged image in Fig. 72 c) hardly provides insight into the spatial relationship between the EPR particles and cracks because in the large volume, the particles conceal the cracks. Therefore two subdomains were extracted, see Fig. 73.

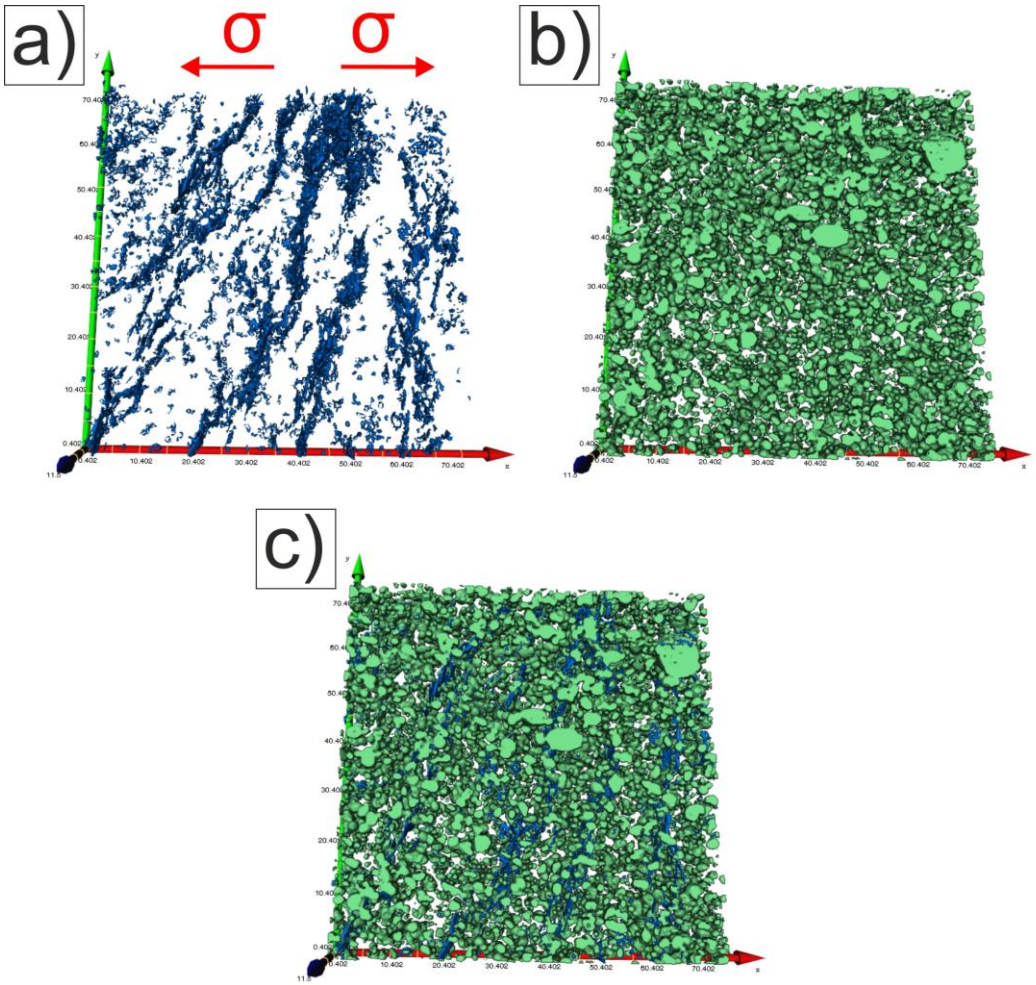

Fig. 72: 3D reconstruction of the EPR10 sample, with the tensile test stopped at 25 % yield: a) only EPR cracks, b) only EPR particles and c) both merged (shown volume: 70 x 70 x 10 µm³).

Similar to the results obtained for the EPR08 sample where the tensile test was stopped at 50 % yield, see Fig. 68, also in this case the cracks in the PP matrix encompass many EPR particles of various sizes, see merged images in Fig. 73 c) and f).

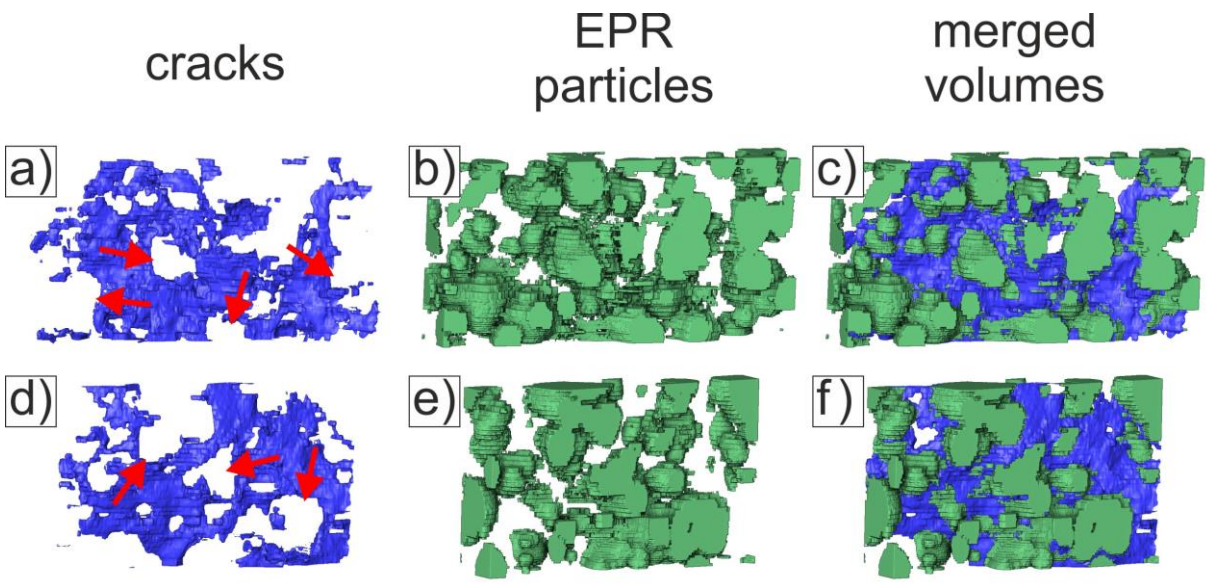

Fig. 73: EPR10 sample with the tensile test stopped at 25 % yield: a) and d) show the reconstruction of two cracks, with the arrows marking the positions of EPR particles; b) and e) reconstruction of the particles and c) and f) the merging of cracks and particles (shown volume: upper row: 2 x 11 x 7 µm³; lower row: 2 x 9 x 7 µm³).

The same procedure was also performed for the sample where the tensile test was stopped at around 50 % yield. The 2D overview image in Fig. 71 d) already reveals that the density of the cracks and their spread is much larger than for the sample tested to 25 % yield. A larger area was therefore recorded during the SBEM preparation to obtain a larger 3D reconstruction of a larger volume (142.5 x 142.5 x 11.0 µm³ (110 slices)). The distribution of the cracks can be seen in Fig. 74 a) and that of the EPR particles in Fig. 74 b). As expected, at least at the same distance from the crack tip, the crack surfaces seem to be larger than those found in the sample tested with a maximum load of 25 % yield. Nevertheless the merged volume in Fig. 74 c) again provides just an overview of the total distribution of both image features because of the crowded representation. Hence two subdomains were extracted also for this sample, see Fig. 75.

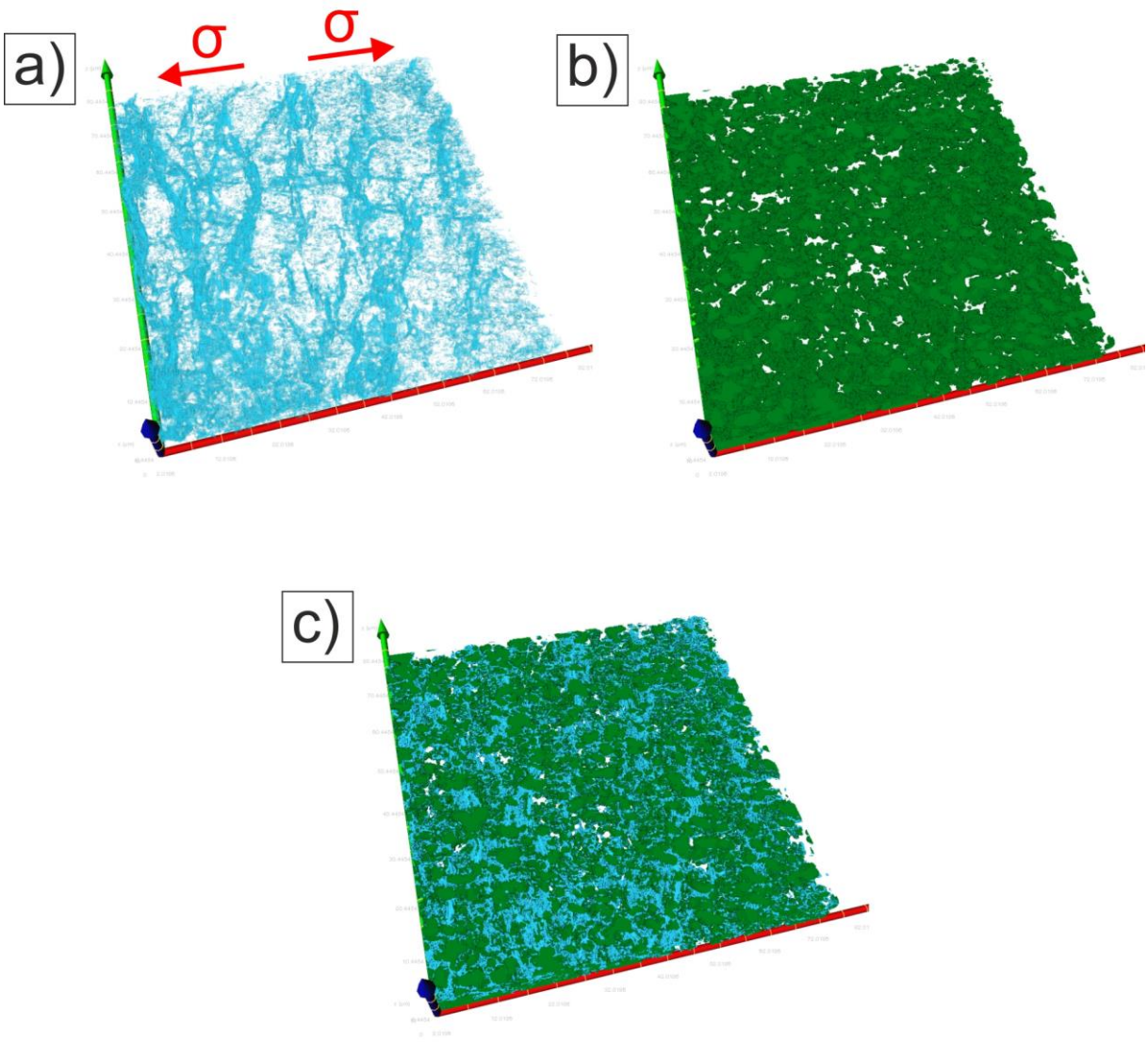

Fig. 74: 3D reconstruction of the EPR10, tensile test stopped at 50 % yield; a) shows the reconstructed crack surface, b) the EPR particles contained and c) both 3D images merged (shown volume: 142.5 x 142.5 x 11.0 µm³).

As in the previously discussed samples, it can also be seen here that one crack can encompass many EPR particles, with the interparticle distance between most of these particles being less than twice their average diameter. The outcome of this is again that cracks seem to be generated more likely in regions with a high density of EPR particles and thus short interparticle distances.

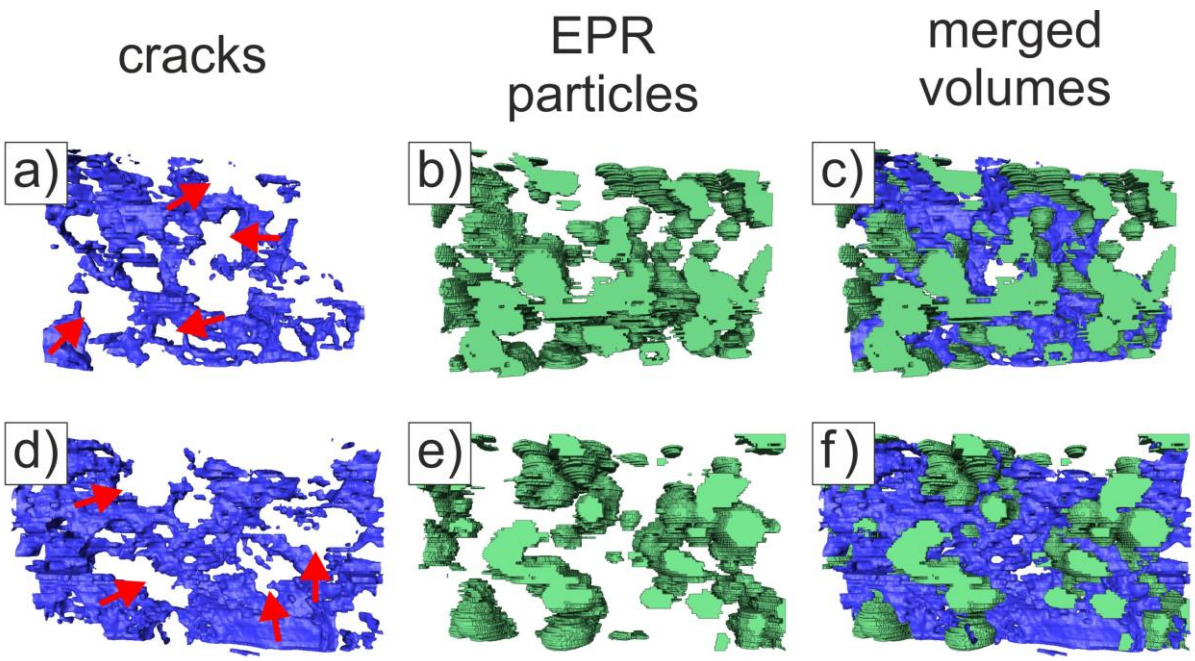

Fig. 75: EPR10 sample with the tensile test stopped at 50 % yield: a) and d) show the reconstruction of two crack surfaces, with the arrows marking the positions of EPR particles; b) and e) reconstruction of the particles and c) and f) the merging of cracks and particles (shown volume: 2.5 x 14.9 x 8.9 µm³).

3.6.2.2. Distance maps

The EDT was calculated for both EPR10 samples to examine the average position of the cracks in respect to the filler particles and as a substitute for the distribution of the interparticle distances. Fig. 76 a) shows the resulting map for the sample with the tensile test stopped at 25 % yield; the 3D reconstruction of the EPR particles used for the calculation can be seen in Fig. 76 c). Both were merged to obtain the spatial correlation of the map with that of the cracks, see Fig. 76 b). This gives the impression that cracks propagate preferentially along regions where short interparticle distances dominate. To confirm this, the DMc (see section 3.5.5.1 and equation (21)) was also calculated, giving a value of 0.40. Additionally the DMc was calculated for the image shown in Fig. 76 a) and multiplied with randomly distributed lines, giving a value of 1.00. This proves that the cracks are not evenly distributed between the particles but are rather found in regions where the interparticle distance is less than the average interparticle distance.

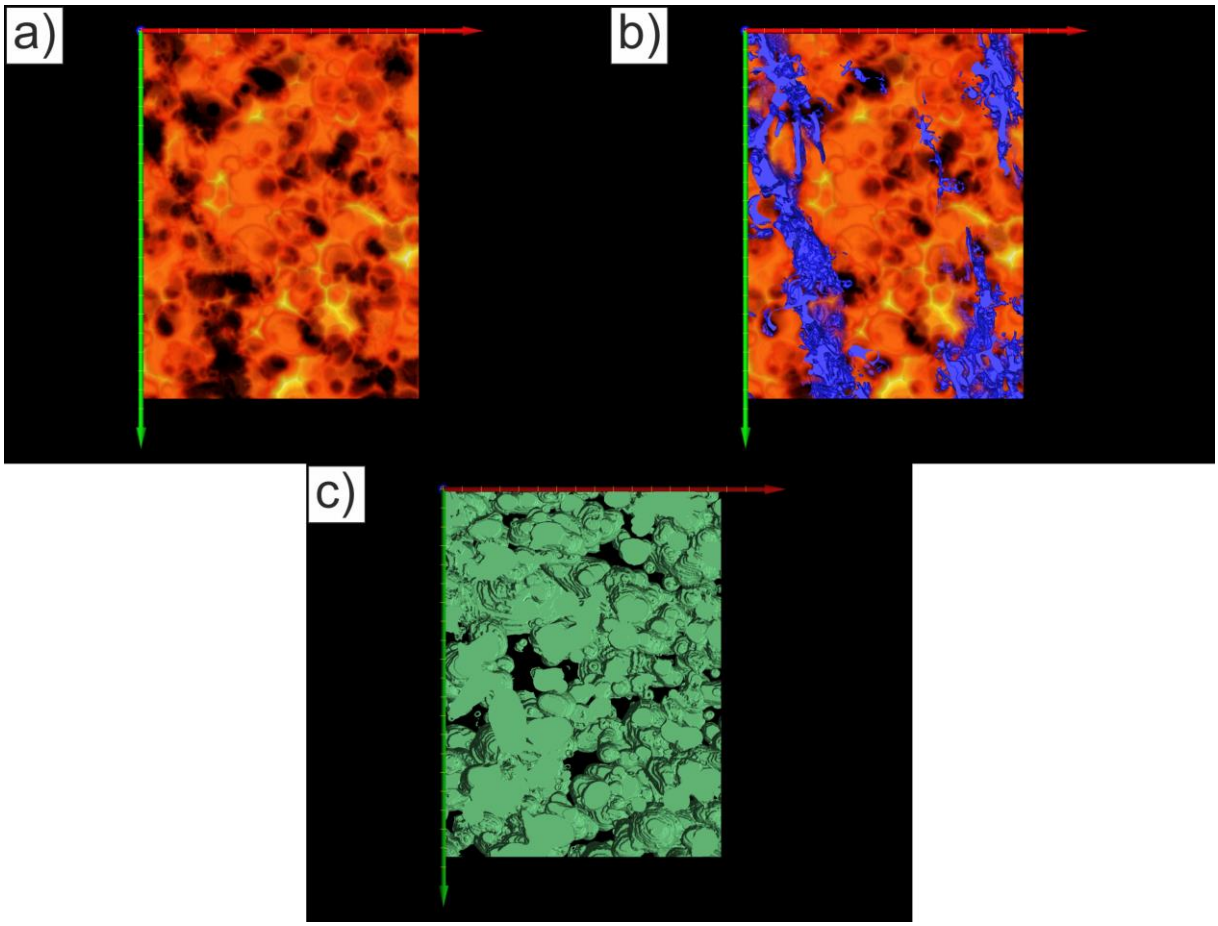

Fig. 76: EPR10 sample (25 % yield): a) distance map, greater brightness means larger interparticle distances; b) additionally merged with the crack distribution; c) 3D reconstruction of the EPR particles used for the distance transformation (shown volume: 14.7 x 19.5 x 6.4 µm³).

The same procedure was performed for the EPR10 sample where the tensile test was stopped at 50 % yield. The appropriate distance map calculated by the EDT is shown in Fig. 77 a). Fig. 77 b), where the cracks are merged with the distance map, also partly illustrates the spatial correlation between the interparticle distance and the cracks. The 3D reconstruction of the particles used for calculating the distance map is shown in Fig. 77 c). Again the cracks appear mainly in the regions with highest particle density and thus shortest interparticle distances. The calculated DMc value was 0.53, again confirming the more visual impression for the multiplication with the crack regions, and 1.01 for those multiplied with the randomly drawn lines. These results confirm those obtained from the preceding two examples, that the cracks are generated mainly in regions with short interparticle distances between the filler particles.

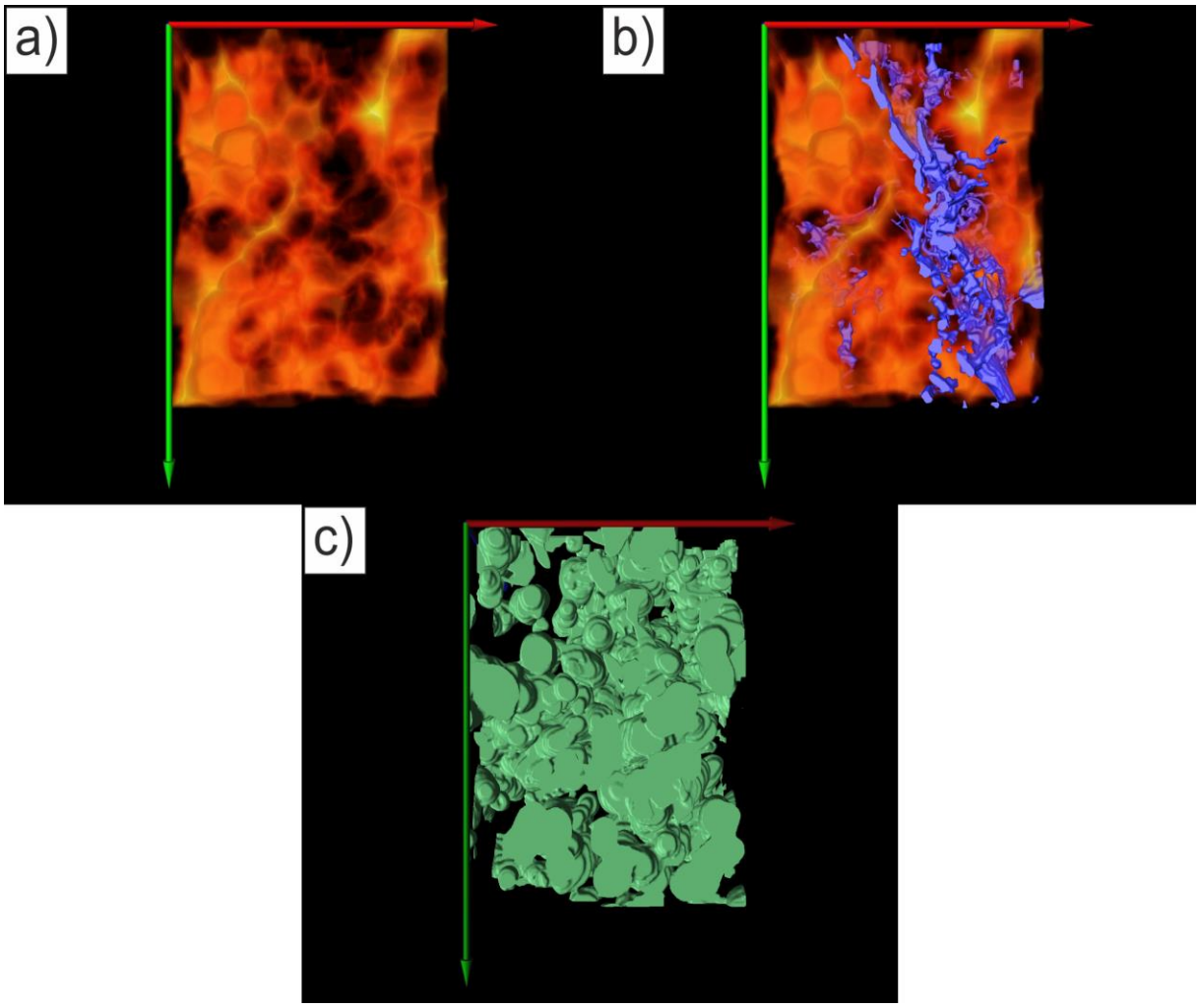

Fig. 77: a) 3D distance map of the EPR10 sample (tensile test stopped at 50 % yield), the greater the brightness, the larger the interparticle distances; b) distance map merged with the cracks; c) 3D reconstruction of the EPR particles used for the calculation of the distance map (shown volume: 12 x 15 x 7 µm³).

3.6.3. PP-LLDPE blend sample

As in the case of the EPR10 sample, the tensile tests of the LLDPE samples were also stopped at the two pre-defined values of 25 % and 50 % yield. Cross-sections of the two tested samples can be seen in Fig. 78 a) and d). Independently of the maximum tensile force applied, the samples demonstrated a different fracture behaviour from the EPR modified samples. They show only voids instead of cracks and contrary to the EPR modified samples, where the crack distribution is widely dispersed over the PP matrix already next to the pre-crack tip, the voids formed in the LLDPE modified samples are more concentrated along a straight line perpendicular to the applied stress. Thus the main damage mechanism for this material seems to be debonding of the particles from the matrix in connection with strong shear forces acting on the particles. This can be best seen in Fig. 78 f). Obviously, the damaged region is much longer and more distinct under higher tensile force than observed in the tests stopped at 25 % yield. But its width is still remarkably small. The crazes or cracks typical of the EPR modified samples (see e.g. Fig. 66 c) and Fig. 71 c) and f)) after tensile testing do not appear in the

LLDPE modified samples, not even at higher magnifications in Fig. 78 c) and f). Instead, when exposed to higher stresses the small voids seem to connect, forming larger ones. But the 3D reconstruction should provide a better insight. The reconstructed volume for the sample stopped at a force of 25 % yield was 44.7 x 109.7 x 22.8 µm³, that for the sample stopped at 50 % yield was 57 x 108 x 22 µm³. Because the voids in the images are very bright objects they can easily be segmented by global thresholding of the already filtered and grey scale adjusted images, whereas the segmentation of the filler particles was carried out using the same procedure as for the previous samples.

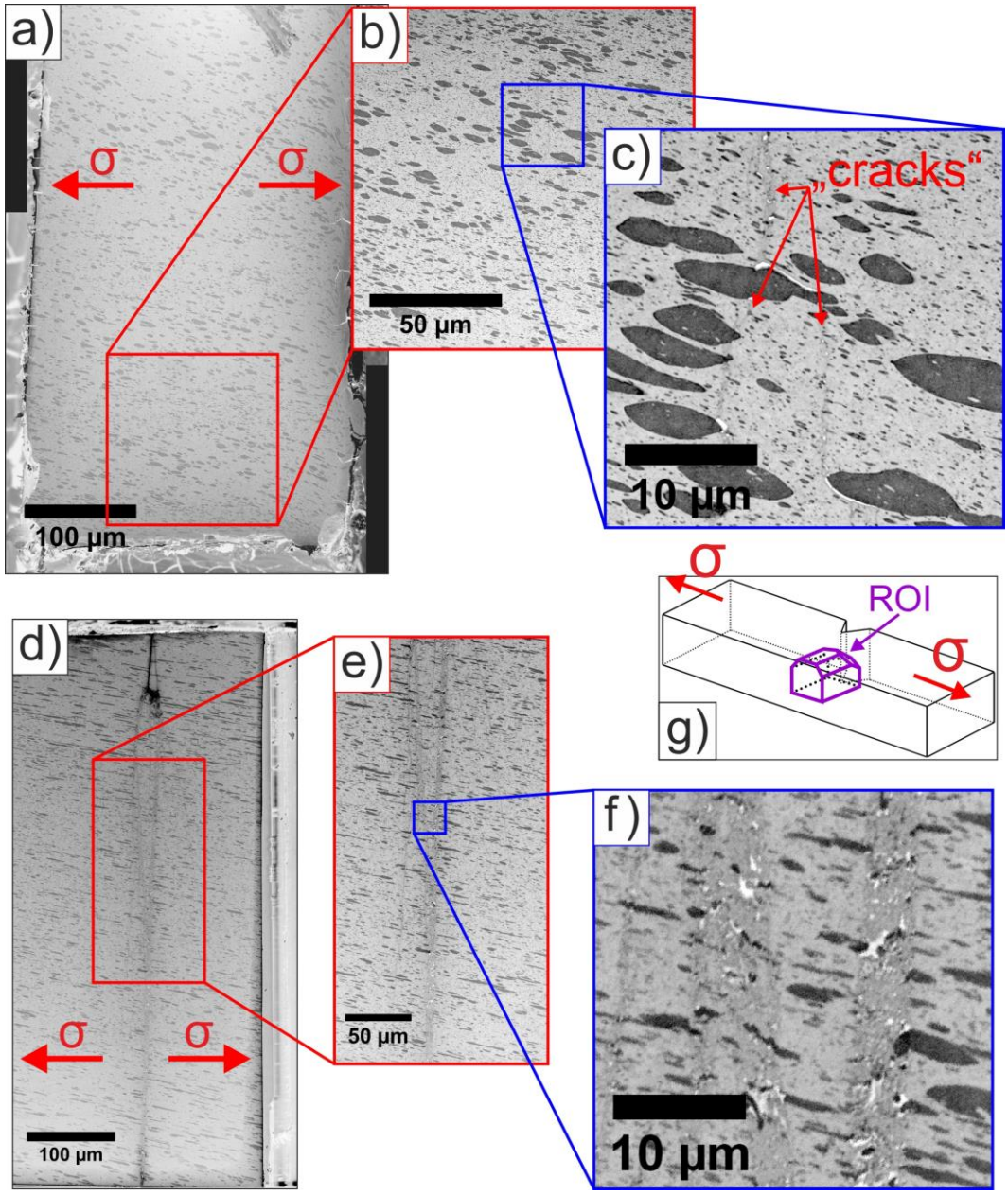

Fig. 78: Cross-sections of LLDPE modified samples; a) – c): tensile test stopped at 25 % yield; d) – f) tensile test stopped at 50 % yield; (a) and d): overview, b) and e): SBEM image area, c) and f): magnified sections; g): shows the position of the extracted volume for the 3D reconstructions. The pre-crack is at the top of the overview images.

3.6.3.1. 3D reconstruction

As mentioned in chapter 3.6.3 a different segmentation strategy was applied for these samples than for the PP samples blended with EPR. As the grey value distributions in the regions where the material seems to be damaged (slightly darker) and the surrounding PP matrix are very similar, it was not possible to separate these two regions. Hence, the 3D reconstructions for these samples only show the LLDPE filler particles and the voids. The 3D reconstruction of the sample where the tensile test was stopped at 25 % yield can be seen in Fig. 79. The image a) shows only the voids, cross-sections of which can e.g. be seen as bright white areas in Fig. 78 f). They are more or less concentrated along two sheet-like regions which are perpendicularly orientated to the applied stress, which acted along the x-axis.

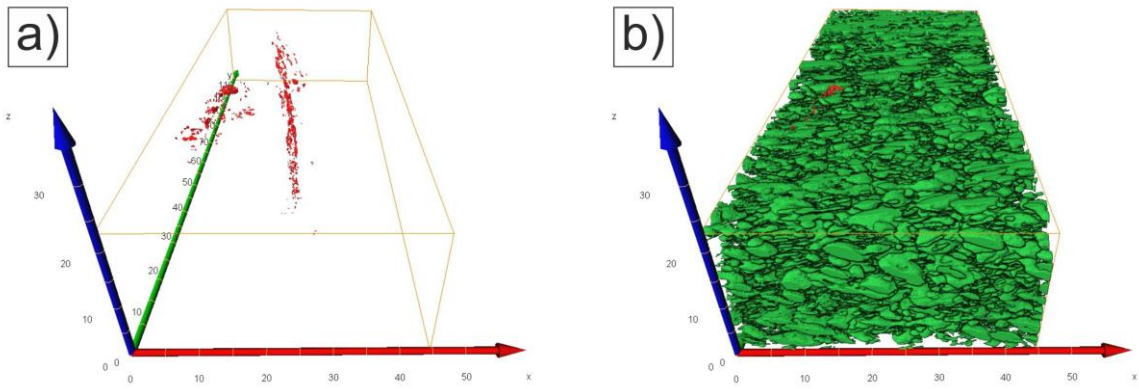

Fig. 79: 3D reconstructions of the LLDPE modified sample with the tensile test stopped at 25 % yield. Image a) shows only the voids and b) additionally the rendered filler particles (shown volume: 44.7 x 109.7 x 22.8 µm³).

To obtain a more detailed view, two subdomains were cropped from the reconstruction in the region where voids are present. Fig. 80 a) and d) shows only the reconstructed voids. It can be seen that only small unconnected volumes of voids are present in the material. When overlaid with the appropriate LLDPE filler particles (Fig. 80 c) and f)) it seems that the voids mainly emerge in regions of high particle density.

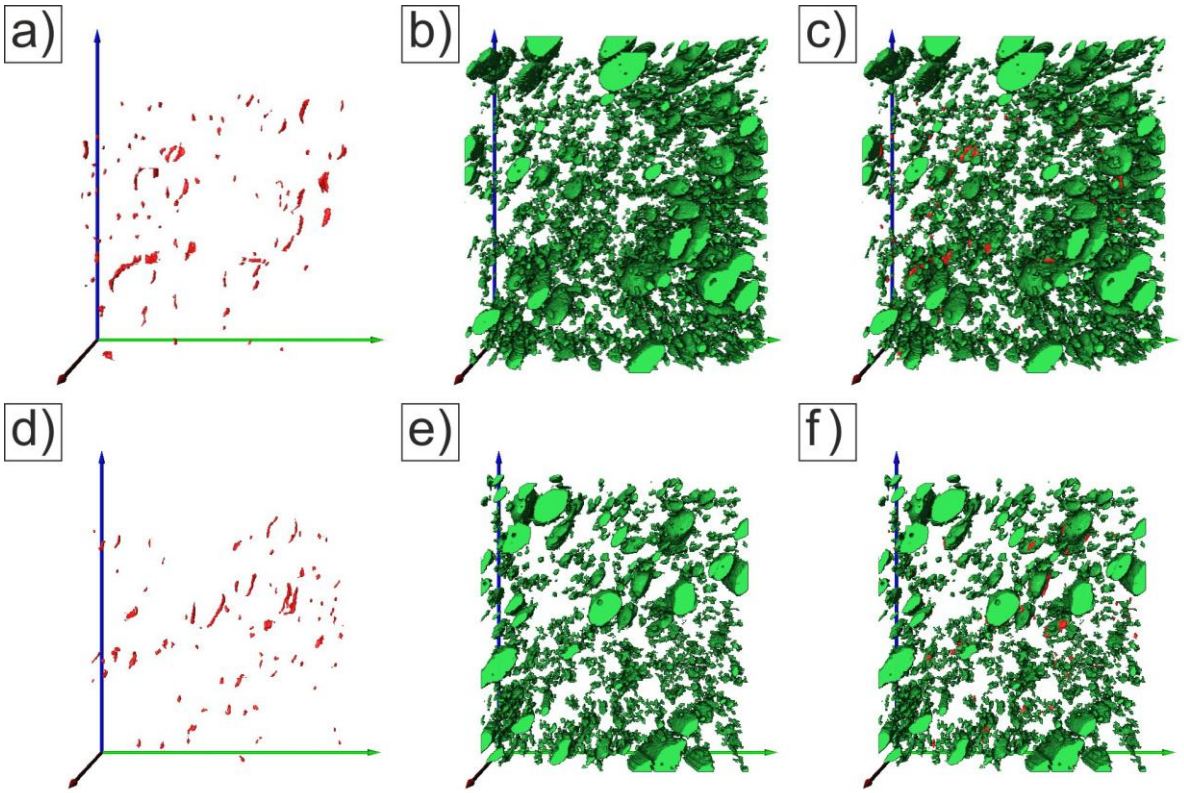

Fig. 80: Extracted subdomains for the LLDPE modified sample (tensile test stop: 25 % yield): a) and d) show the voids, b) and e) the filler particles in the same region and c) and f) both merged (shown volume: 1.0 x 20.0 x 22.8 µm³).

The tensile test of the second LLDPE sample was stopped at 50 % yield. As the overall recorded area is very large, the 3D reconstruction in Fig. 81 shows only a subdomain (57 x 108 x 22 µm³). The reconstruction of the voids marked in red in Fig. 81 a) shows that they are located along a 2-dimensional area without great lateral spread in 3 dimensions. The tensile test direction was parallel to the x-axis, thus perpendicular to void propagation. Both the number of voids and their volume are much larger than in the sample stopped at 25 % yield. Even if only a small sample volume is reconstructed by additionally rendering the LLDPE filler particles it is hardly possible to interpret the spatial relationship between the voids and the particles, see Fig. 81 b). To obtain a deeper insight different cross-sections were rendered in addition to the total reconstruction.

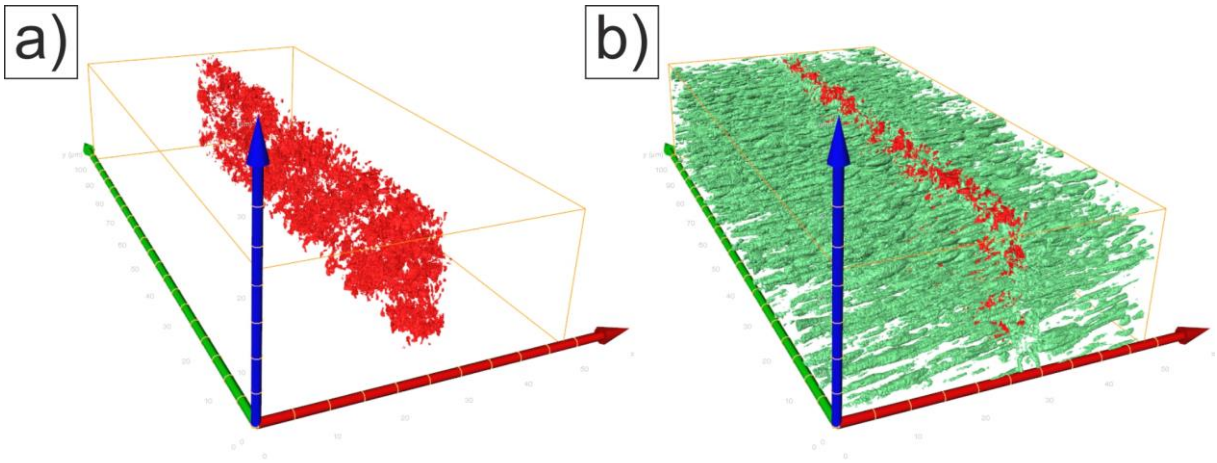

Fig. 81: 3D reconstruction of the LLDPE modified sample with the tensile test stopped at 50 % yield. a) shows the voids and b) additionally the LLDPE particles (shown volume: 57 x 108 x 22 µm³).

The question whether small voids actually merge to form larger volumes was investigated using an Avizo® module which enables the separation of objects of a certain volume. Several larger voids are representatively shown in Fig. 82 with every single colour corresponding to one connected region. Two different views were chosen: x-y in a) and c) and y-z in b) and d). The y-z view shows the cross-sections of the LLDPE particles (grey) in addition to the voids, illustrating the full 3D reconstruction of the voids. The position of these cross-sections in the volume is shown as a black line in the corresponding x-y view. The great advantage of this representation is that the voids are not hidden behind the particles. This reconstruction reveals on the one hand that some voids are much larger than the largest cross-sections of the particles and thus cannot result from the debonding of just one particle from the matrix. On the other hand this proves that the large voids appear in regions of high particle density. This is not surprising, because in such regions small voids develop close to each other and can finally merge to form larger voids.

An additional result can be obtained by viewing the region around the voids in the x-z direction. The 2D images already show a deformation of the LLDPE particles in the damaged regions, see e.g. Fig. 78 f). To obtain a more detailed view of these particles several cross-sections around the damaged regions were extracted, with two of them shown in Fig. 83 a) & b). Both images reveal a clear deformation of the otherwise horizontally orientated LLDPE particles. This bending of the particles seems to be induced by shear forces. It causes a stretching of the particles at one side and a compression at the opposite side, which will most probably promote the debonding of the particle from the matrix. But the basic cause of these shear forces is still unclear.

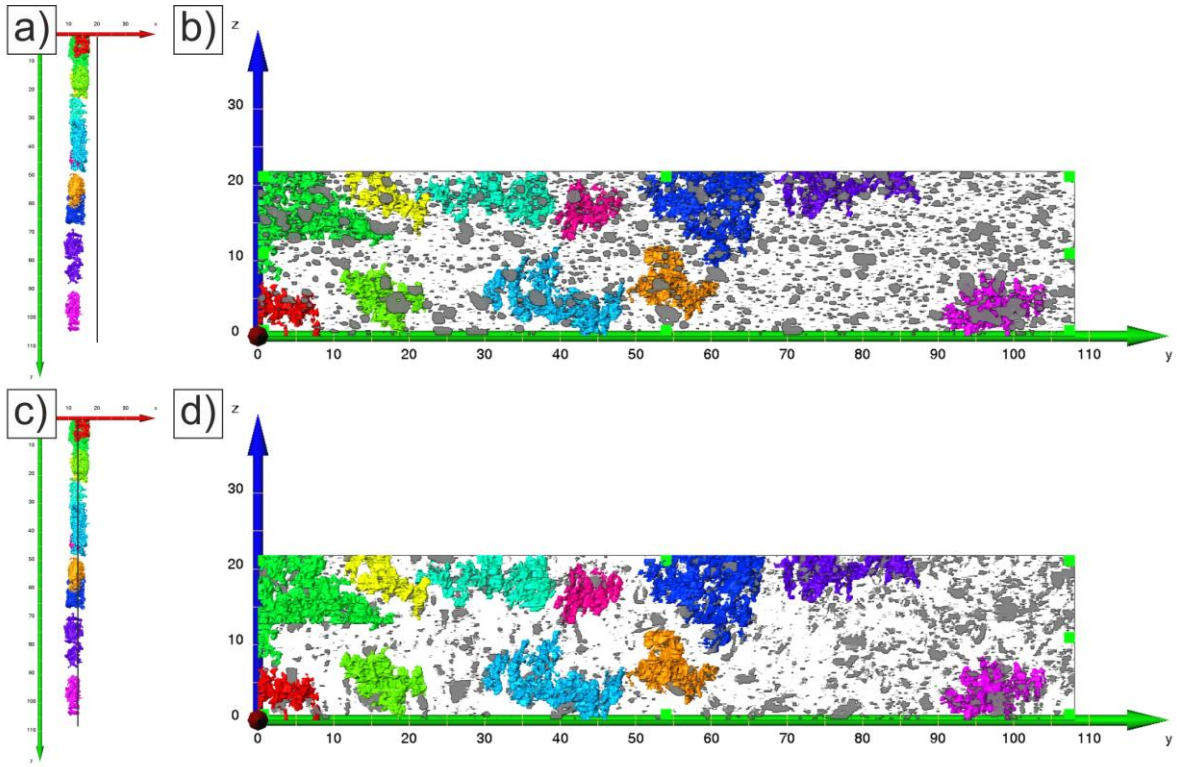

Fig. 82: Display of several large voids (different colours) consisting of many connected small voids at two different views (x-y left and y-z right) and the cross-sections of the LLDPE particles in grey at positions marked by a black line in a) and c) (shown cross-sectional areas right: 108 x 22 µm²).

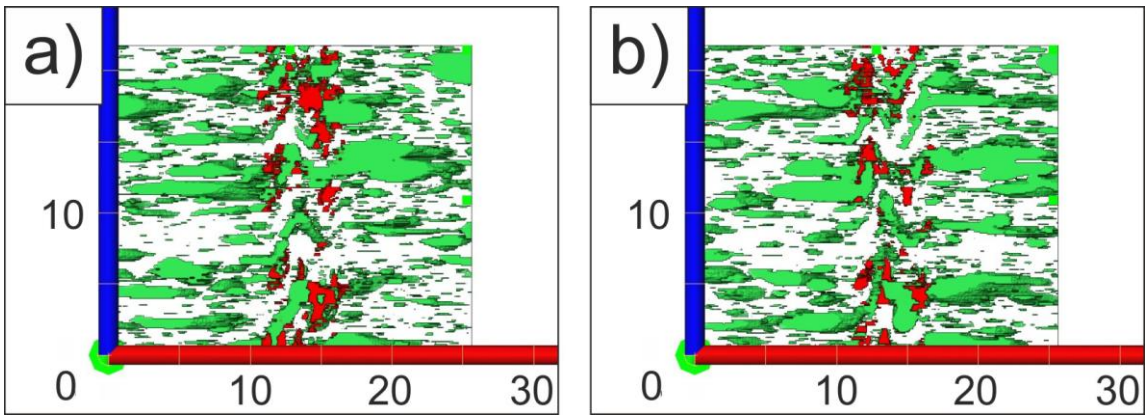

Fig. 83: Cross-sections in x-z direction showing the particle (green) deformation in the region of the voids (red) (shown cross-sectional area: 26 x 22 µm²).

3.7. Conclusion and outlook

Crack formation caused by tensile tests in three different EPR and LLDPE modified polypropylene samples was investigated. Initially, tensile tests were performed to strain the material, but the tests were stopped at predefined values far below the yield force. Subsequently, a part of the fracture region was cut out from the sample and prepared by

conventional microtomy and staining. RuO_4 was used to stain both EPR and LLDPE filler particles in the PP matrix. By measuring the ruthenium concentration as a function of depth by EDS it was found that the stain penetration depth was around 35 µm. Hence this is the maximum depth to which serial sectioning and imaging can be performed using SBEM to obtain the image stacks for 3D reconstruction. The staining depth thus also limits the reconstruction volume in z-direction. Nevertheless, these volumes were large enough to obtain significant and reliable results.

For the 3D reconstructions, an image segmentation method had to be developed, which enables the segmentation of both the filler particles and the crazes / cracks or voids. Initially a sequence of different image processing techniques was used to remove image noise. Image noise arises due to the fact that low beam energies and short dwell times had to be used for image recording in order to avoid beam damage to the polymers. After noise reduction and contrast enhancement the images can be segmented by combining two different techniques, the auto local threshold according to Niblack and the WEKA algorithm. This segmentation strategy was successfully applied to the EPR modified samples. The LLDPE modified samples were segmented by use of global thresholding only.

The first polymer investigated was PP blended with 20 % EPR as filler particles (sample EPR08). The samples were fabricated by injection moulding and the EPR particles had an ellipsoidal shape, with the long axis oriented in the flow direction. The tensile test was stopped at 50 % yield. After image segmentation, a 3D reconstruction of a volume of 30.2 x 31.5 x 8.5 μm^3 was performed. It could easily be seen that many cracks or crazes had already formed at this stage. The cracks were mostly encompassed several EPR particles of different sizes but at close distance. The 3D reconstruction of the EPR particles was subsequently used to calculate the interparticle distances between the particles by Euclidean distance transformation (EDT). The merging of the distance map with the reconstructed cracks gives the impression that the cracks / crazes originated mainly in regions with high particle density, i.e. low interparticle distances. A separate parameter, named DMc, was defined to obtain a more quantitative value. DMc was defined to be 1 when the cracks are randomly distributed and <1 when they are close to regions with high particle density and thus small interparticle distances (see section 3.5.5.1). The calculated DMc value for this sample was 0.74, thus the cracks seem to be located mainly in close neighbourhood to particles with small interparticle distances. But this result must be interpreted with caution because of unavoidable mis-segmentations, which are due to the fact that the automated procedures do not perfectly segment and reconstruct fine features in particular. The interparticle distance thus seems to be a vital parameter in crack / craze formation, at least for some types of polymers. Early-stage crack formation between particles with small interparticle distance will cause energy release and stop the progress of fracturing. Isolated agglomerates of particles can therefore be advantageous, whereas long paths with particles arranged at short interparticle distance could have detrimental effects.

The particles in EPR10, another EPR modified sample, exhibited more spherical particles with a larger average diameter than those in the EPR08 sample. The tensile test was stopped at both 25 % and 50 % yield to additionally obtain information about possible changes in the fracture behaviour at different stages of the tensile test. But apart from an increase in the size of the damaged region, no essential changes were observed. The DMc values calculated for

the samples were around 0.40 for the tensile test stopped at 25 % and 0.53 for that stopped at 50 % yield.

The tensile tests performed on the PP samples blended with 20 % LLDPE were also stopped both at 25 % and 50 % yield. But as already shown by single images of the cross-sections, the fracture mechanism is completely different from those observed for the EPR modified samples. In contrast to the spread-out cracks / crazes in the matrix of the EPR modified samples, only small straight regions perpendicular to the applied force are damaged. None of the cracks typical of the tested EPR modified samples were found. Instead, shearing of the LLDPE particles and debonding of the particles from the matrix occurred. The resulting voids were rather small for the tensile test stopped at 25 % yield. Much larger voids, often consisting of small but connected voids appeared, appeared in the 3D reconstruction of the samples where the tensile test was stopped at 50 % yield. A closer look at the reconstructions reveals that the area of some of the cross-sections of the big voids is much larger than that of the cross-sections of the LLDPE particles. But this could also be caused by a break-out of particles during the sectioning process due to debonding. Additional shear deformation of the filler particles occurred in the damaged regions. But again, debonding and void formation mainly took place in regions with many particles with short interparticle distance. Nevertheless, the results prove that apart from the interparticle distance, the bonding between particles and matrix also has a strong influence on crack formation in polymeric blends.

The image processing and segmentation strategy developed in this work significantly reduces the time and effort in the preparations necessary for the 3D reconstructions. But the segmentation process can still be improved, resulting in a higher precision of the reconstruction itself. Unfortunately the depth to which SBEM can be used is limited by the penetration depth of the stain. This depth is around 35 µm in the case of polypropylene, but could drop to zero for other polymers.

Polypropylene is a semi-crystalline material. Thus also the crystal structure and the size and distribution of the spherulites may influence the fracture progress. A common procedure to make these structures visible is chemical etching. But this cannot be combined with serial sectioning and imaging in the ESEM. As J.H. Rask *et al.* demonstrated already in 1993, etching is also possible by electron irradiation of the sample in the ESEM [86]. This could also open the possibility of integrating the spherulites in the 3D reconstructions and to obtain the spatial relationship between the cracks and the crystalline structures. It would especially be interesting to find out whether the cracks split the spherulites or whether they run along their boundaries.

List of publications

Peer – reviewed article:

Nachtnebel, Manfred; Fitzek, Harald; Mayrhofer, Claudia; Chernev, Boril; Pölt, Peter. *Spatial localization of membrane degradation by in situ wetting and drying of membranes in the scanning electron microscope*. Journal of membrane science, Band 503, 2016, S. 81-89.

Journal article:

Zankel, Armin; Wernitznig, Stefan; Nachtnebel, Manfred. *Synergy of SEM and Ultramicrotomy: SBEM Spreading from Life Sciences to Materials Science*. Imaging & microscopy, Band 18 Nr. 4, 2016, S. 34-36.

Book chapters:

Nachtnebel, Manfred; Zankel, Armin; Mayrhofer, Claudia; Pölt, Peter; Gahleitner, Markus. *3D-Reconstruction of cracks in polymers – New insight in the fracture behaviour?* Deformation and Fracture Behaviour of Polymer Materials. in print 2017. Edit. 1.

Zankel, Armin; Nachtnebel, Manfred; Mayrhofer, Claudia; Wewerka, Karin. *Characterisation of polymers in the scanning electron microscope from low voltage surface imaging to the 3D reconstruction of specimens*. Deformation and Fracture Behaviour of Polymer Materials. in print 2017. Edit. 1.

Conference proceedings:

Pölt, Peter; Nachtnebel, Manfred; Zankel, Armin; Mayrhofer, Claudia; Gahleitner, Markus. *Analysis of the fracture behaviour of polymers – 2D compared to 3D.* Polymertec 16. 2016. S. 104.

Nachtnebel, Manfred; Mayrhofer, Claudia; Pölt, Peter. *3D-reconstruction of cracks in polymer blends*. Multinational Congress on Microscopy. 2015. S. O-216-34-35.

Nachtnebel, Manfred; Fitzek, Harald; Mayrhofer, Claudia; Brandl, Christian; Chernev, Boril; Pölt, Peter. *Characterization of microfiltration membranes by in-situ wetting in the ESEM and FT-IR mapping.* ASEM Workshop Advanced Electron Microscopy. 2015. S. 32-32.

Zankel, Armin; Nachtnebel, Manfred; Müllner, Tibor; Pölt, Peter. *In situ ultramicrotomy in the variable pressure/environmental scanning electron microscope for the assessment of polymeric materials.* Microscopy Conference., 2015. S. 507-507.

Pölt, Peter; Nachtnebel, Manfred; Fitzek, Harald; Chernev, Boril. *In-situ analysis of PES microfiltration membrane degradation in the ESEM.* Microscopy Conference. 2015. S. 501-502.

Nachtnebel, Manfred; Zankel, Armin; Mayrhofer, Claudia; Gahleitner, Markus; Pölt, Peter. *3D-reconstruction of cracks in polymers - New insight into the fracture behaviour?* Internationale Wissenschaftliche Tagung Polymerwerkstoffe. 2014. S. 216-220.

Nachtnebel, Manfred; Pölt, Peter. *In situ characterisation of Microfiltration Membranes in the ESEM.* Aachener Membran-Kolloquium. 2014. S. 461-466.

Pölt, Peter; Nachtnebel, Manfred; Zankel, Armin.. *In situ characterisation of polymers in the ESEM.* Microscopy for Global Challenges, 2014. S. MS-6-O-2276.

Pölt, Peter; Nachtnebel, Manfred; Zankel, Armin. *In situ testing of soft materials in the Environmental Scanning Electron Microscope.* International Conference on Electron Microscopy and Annual Meeting of the Electron Microscope Society. 2014. S. 24-25.

Conference talks:

Nachtnebel, Manfred; Mayrhofer, Claudia; Pölt, Peter. *3D-reconstruction of cracks in polymer blends.* 2015. 12th Multinational Conference on Microscopy 2015, Eger, Hungary.

Nachtnebel, Manfred; Fitzek, Harald; Mayrhofer, Claudia; Brandl, Christian; Chernev, Boril; Pölt, Peter. *Characterisation of microfiltration membranes by in situ wetting in the ESEM and FT-IR.* 2015. 5th ASEM Workshop, Graz, Austria.

Nachtnebel, Manfred; Pölt, Peter. *Characterisation of Microfiltration Membranes by Wetting Investigations in the ESEM.* 2014. ÖGP Jahrestagung, Pöllau, Austria.

Nachtnebel, Manfred; Pölt, Peter. *Characterisation of Microfiltration Membranes by Wetting Investigations in the ESEM.* 2014. 4th ASEM Workshop, Wien, Austria.

Conference posters:

Nachtnebel, Manfred; Fitzek, Harald; Brandl, Christian; Loulergue, Patrick; Teychene, Benoit; Pölt, Peter. *Spatial characterization of PES/PVP based membranes by FT-IR.* 2016.Advanced Materials Day 2016, Graz, Austria.

Nachtnebel, Manfred; Fitzek, Harald; Brandl, Christian; Loulergue, Patrick; Teychene, Benoit; Pölt, Peter. *Spatial characterization of PES/PVP based membranes by FT-IR.* 2016. PERMA-MELPRO, Prague, Czech Republic.

Zankel, Armin; Nachtnebel, Manfred; Müllner, Tibor; Pölt, Peter. *In situ ultramicrotomy in the variable pressure/environmental scanning electron microscope for the assessment of polymeric materials.* 2015. MC 2015, Germany

Nachtnebel, Manfred; Fitzek, Harald; Mayrhofer, Claudia; Brandl, Christian; Chernev, Boril; Pölt, Peter. *Spatially Resolved Characterisation of Microfiltration Membranes by two Different Microscopic Methods.* 2015. Euromembrane 2105, Aachen, Germany

Nachtnebel, Manfred; Pölt, Peter. *Characterisation of Microfiltration Membranes by Wetting Investigations in the Environmental Scanning Electron.* 2014. 15th Aachener Membran Kolloquium, Aachen, Germany

Nachtnebel, Manfred; Zankel, Armin; Mayrhofer, Claudia; Gahleitner, Markus; Pölt, Peter. *Fracture Behaviour Investigation in Polymers by 3D-Reconstruction of Cracks.* 2014. Advanced Materials Day 2014, Graz, Austria

Nachtnebel, Manfred; Pölt, Peter. *In situ Wetting Investigations of Microfiltration Membranes in the ESEM.* 2013. Advanced Materials Day 2013, Graz, Austria

Bibliography

[1] B. Pellegrin, R. Prulho, A. Rivaton, S. Thérias, J.-L. Gardette, E. Gaudichet-Maurin, and C. Causserand, “Multi-scale analysis of hypochlorite induced PES/PVP ultrafiltration membranes degradation,” *J. Memb. Sci.*, vol. 447, pp. 287–296, 2013.

[2] Y. Hanafi, A. Szymczyk, M. Rabiller-Baudry, and K. Baddari, “Degradation of Poly(Ether Sulfone)/Polyvinylpyrrolidone Membranes by Sodium Hypochlorite: Insight from Advanced Electrokinetic Characterizations,” *Environ. Sci. Technol.*, vol. 48, no. 22, pp. 13419–13426, Nov. 2014.

[3] G. Grestenberger, G. D. Potter, and C. Grein, “Polypropylene/ethylene-propylene rubber (PP/EPR) blends for the automotive industry: Basic correlations between EPR-design and shrinkage,” *Express Polym. Lett.*, vol. 8, no. 4, pp. 282–292, 2014.

[4] M. Von Ardenne and D. Beischer, “Untersuchung von Metalloxyd-Rauchen mit dem Universal-Elektronenmikroskop,” *Zeitschrift für Elektrochemie und Angew. Phys. Chemie*, vol. 46, no. 4, pp. 270–277, 1940.

[5] H. Fitzek, H. Schoettner, J. Wagner, F. Hofer, and J. Rattenberger, “High-quality imaging in environmental scanning electron microscopy - optimizing the pressure limiting system and the secondary electron detection of a commercially available ESEM,” *J. Microsc.*, vol. 262, no. 1, pp. 85–91, Apr. 2016.

[6] D. J. Stokes, *Principles and Practice of Variable Pressure/Environmental Scanning Electron Microscopy (VP-ESEM)*. West Sussex: John Wiley & Sons, Ltd, 2008.

[7] A. Reichmann, A. Zankel, H. Reingruber, P. Pölt, and K. Reichmann, “Direct observation of ferroelectric domain formation by environmental scanning electron microscopy,” *J. Eur. Ceram. Soc.*, vol. 31, no. 15, pp. 2939–2942, Dec. 2011.

[8] E. Stabentheiner, A. Zankel, and P. Pölt, “Environmental scanning electron microscopy (ESEM)—a versatile tool in studying plants,” *Protoplasma*, vol. 246, no. 1–4, pp. 89–99, Oct. 2010.

[9] P. Poelt, A. Zankel, M. Gahleitner, E. Ingolic, and C. Grein, “Tensile tests in the environmental scanning electron microscope (ESEM) – Part I: Polypropylene homopolymers,” *Polymer (Guildf).*, vol. 51, no. 14, pp. 3203–3212, Jun. 2010.

[10] H. Reingruber, A. Zankel, C. Mayrhofer, and P. Poelt, “Quantitative characterization of microfiltration membranes by 3D reconstruction,” *J. Memb. Sci.*, vol. 372, no. 1–2, pp. 66–74, Apr. 2011.

[11] A. Jansson, “Development of novel in situ techniques for the study of water interaction with soft materials,” Chalmers University of Technology, 2013.

[12] FEI company, “The Quanta FEG 200, 400, 600 User´s Operation Manual.” FEI company, p. 298, 2003.

[13] J. I. Goldstein, *Scanning electron microscopy and x-ray microanalysis*, vol. 3. New York, NY [u.a.]: Kluwer Academic, Plenum Publ, 2003.

[14] J. H. Butler, D. C. Joy, G. F. Bradley, and S. J. Krause, “Low-voltage scanning electron microscopy of polymers,” *Polymer (Guildf).*, vol. 36, no. 9, pp. 1781–1790, Apr. 1995.

[15] C. P. Royall, B. L. Thiel, and A. M. Donald, “Radiation damage of water in environmental scanning electron microscopy,” *J. Microsc.*, vol. 204, no. 3, pp. 185–195, Dec. 2001.

[16] M. Higashi, J. Morita, N. Shimada, and T. Kitagawa, “Long-term-hydrophilic flat-sheet microfiltration membrane made from chlorinated poly (vinyl chloride),” *J. Memb. Sci.*, vol. 500, pp. 180–189, Feb. 2016.

[17] H. Susanto and M. Ulbricht, “Photografted Thin Polymer Hydrogel Layers on PES Ultrafiltration Membranes: Characterization, Stability, and Influence on Separation Performance,” *Langmuir*, vol. 23, no. 14, pp. 7818–7830, Jul. 2007.

[18] M. Ulbricht, “Advanced functional polymer membranes,” *Polymer (Guildf).*, vol. 47, no. 7, pp. 2217–2262, Mar. 2006.

[19] Y. Wyart, G. Georges, C. Deumié, C. Amra, and P. Moulin, “Membrane characterization by microscopic methods: Multiscale structure,” *J. Memb. Sci.*, vol. 315, no. 1–2, pp. 82–92, May 2008.

[20] E. Zondervan and B. Roffel, “Evaluation of different cleaning agents used for cleaning ultra filtration membranes fouled by surface water,” *J. Memb. Sci.*, vol. 304, no. 1–2, pp. 40–49, Nov. 2007.

[21] H. Reingruber, A. Zankel, C. Mayrhofer, and P. Poelt, “A new in situ method for the characterization of membranes in a wet state in the environmental scanning electron microscope,” *J. Memb. Sci.*, vol. 399–400, pp. 86–94, May 2012.

[22] M. Mulder, *Basic pricipals of membrane technology*, 2nd editio. Dordrecht: Kluwer Academic Publishers, 1996.

[23] Z. L. Xu and F. A. Qusay, “Polyethersulfone (PES) hollow fiber ultrafiltration membranes prepared by PES/non-solvent/NMP solution,” *J. Memb. Sci.*, vol. 233, no. 1–2, pp. 101–111, 2004.

[24] M. Ulbricht, O. Schuster, W. Ansorge, M. Ruetering, and P. Steiger, “Influence of the strongly anisotropic cross-section morphology of a novel polyethersulfone microfiltration membrane on filtration performance,” *Sep. Purif. Technol.*, vol. 57, no. 1, pp. 63–73, Oct. 2007.

[25] P. J. Flory, “Thermodynamics of High Polymer Solutions,” *J. Chem. Phys.*, vol. 9, no. 8, p. 660, 1941.

[26] M. L. Huggins, “Solutions of long chain compounds,” *J. Chem. Phys.*, vol. 9, no. 8, p. 440, 1941.

[27] L. Xu and F. Qiu, “Simultaneous determination of three Flory-Huggins interaction parameters in polymer/solvent/nonsolvent systems by viscosity and cloud point measurements,” *Polymer (Guildf).*, vol. 55, no. 26, pp. 6795–6802, 2014.

[28] H. Strathmann and K. Kock, “The formation mechanism of phase inversion membranes,” *Desalination*, vol. 21, no. 3, pp. 241–255, 1977.

[29] Membrana, “DuraPES® 600.” Membrana, Wuppertal, Germany, p. 1, 2012.

[30] Membrana, “MicroPES® 2F.” Membrana, Wuppertal, Germany, p. 1, 2012.

[31] G.-D. Kang, C.-J. Gao, W.-D. Chen, X.-M. Jie, Y.-M. Cao, and Q. Yuan, “Study on hypochlorite degradation of aromatic polyamide reverse osmosis membrane,” *J. Memb. Sci.*, vol. 300, no. 1–2, pp. 165–171, Aug. 2007.

[32] Y. Kwon and J. O. Leckie, “Hypochlorite degradation of crosslinked polyamide membranes I . Changes in chemical / morphological properties,” vol. 283, pp. 21–26, 2006.

[33] R. Prulho, S. Therias, A. Rivaton, and J. L. Gardette, “Ageing of polyethersulfone/polyvinylpyrrolidone blends in contact with bleach water,” *Polym. Degrad. Stab.*, vol. 98, no. 6, pp. 1164–1172, 2013.

[34] E. Arkhangelsky, D. Kuzmenko, and V. Gitis, “Impact of chemical cleaning on properties and functioning of polyethersulfone membranes,” *J. Memb. Sci.*, vol. 305, no. 1–2, pp. 176–184, Nov. 2007.

[35] N. Porcelli and S. Judd, “Chemical cleaning of potable water membranes: A review,” *Sep. Purif. Technol.*, vol. 71, no. 2, pp. 137–143, Feb. 2010.

[36] H. Reingruber, “New microscopic methods for the characterization of microfiltration membranes,” TU-Graz, 2012.

[37] P. R. Griffiths and J. A. de Haseth, *Fourier Transform Infrared Spectrometry*, 2nd editio. John Wiley & Sons, Ltd, 2007.

[38] A. M. Glauert, *Fixation, Dehydration and Embedding of Biological Specimens*. Cambridge, England: North-Holland publishing company, 1975.

[39] J. Schindelin, I. Arganda-Carreras, E. Frise, V. Kaynig, M. Longair, T. Pietzsch, S. Preibisch, C. Rueden, S. Saalfeld, B. Schmid, J.-Y. Tinevez, D. J. White, V. Hartenstein, K. Eliceiri, P. Tomancak, and A. Cardona, “Fiji: an open-source platform for biological-image analysis,” *Nat. Methods*, vol. 9, no. 7, pp. 676–682, Jun. 2012.

[40] W. Zhang and B. Hallström, “Membrane characterization using the contact angle technique I. methodology of the captive bubble technique,” *Desalination*, vol. 79, no. 1, pp. 1–12, Dec. 1990.

[41] R. Wallach and Q. Wang, “An extension of Miller scaling to scale sorptivity by contact angle,” *Water Resour. Res.*, vol. 49, no. 10, pp. 6927–6932, Oct. 2013.

[42] B. Vatsha, J. C. Ngila, and R. M. Moutloali, “Preparation of antifouling polyvinylpyrrolidone (PVP 40K) modified polyethersulfone (PES) ultrafiltration (UF) membrane for water purification,” *Phys. Chem. Earth, Parts A/B/C*, vol. 67–69, pp. 125–131, 2014.

[43] Y. Wang, B. Na, Q. Fu, and Y. Men, “Shear induced shish-kebab structure in PP and its blends with LLDPE,” *Polymer (Guildf).*, vol. 45, no. 1, pp. 207–215, 2004.

[44] X. M. Zhang and A. Ajji, “Oriented structure of PP/LLDPE multilayer and blends films,”

Polymer (Guildf)., vol. 46, no. 10, pp. 3385–3393, Apr. 2005.

[45] G. H. Michler and F. J. Baltá-Calleja, *Nano- and Micromechanics of Polymers*. München: Carl Hanser Verlag GmbH, 2012.

[46] J. R. Davis, *Tensile testing*, 2nd ed. ASM International, 2004.

[47] W. Grellmann and S. Seidler, *Polymer Testing*. München: Carl Hanser Verlag GmbH & Co. KG, 2007.

[48] J. Viguié, T. Savart, P. Duru, J.-C. Rouch, and J.-C. Remigy, “Characterisation of 3D porous macrostructure of hollow fibre membranes using X-ray tomography—Effects of some spinning process conditions,” *J. Memb. Sci.*, vol. 435, pp. 11–20, May 2013.

[49] A. Zankel, J. Wagner, and P. Poelt, “Serial sectioning methods for 3D investigations in materials science,” *Micron*, vol. 62, pp. 66–78, Jul. 2014.

[50] W. Denk and H. Horstmann, “Serial Block-Face Scanning Electron Microscopy to Reconstruct Three-Dimensional Tissue Nanostructure,” *PLoS Biol.*, vol. 2, no. 11, p. e329, Oct. 2004.

[51] J. H. Macke, N. Maack, R. Gupta, W. Denk, B. Schölkopf, and A. Borst, “Contour-propagation algorithms for semi-automated reconstruction of neural processes,” *J. Neurosci. Methods*, vol. 167, no. 2, pp. 349–357, Jan. 2008.

[52] S. Lang, P. Drouvelis, E. Tafaj, P. Bastian, and B. Sakmann, “Fast extraction of neuron morphologies from large-scale SBFSEM image stacks,” *J. Comput. Neurosci.*, vol. 31, no. 3, pp. 533–545, Nov. 2011.

[53] K. L. Briggman, M. Helmstaedter, and W. Denk, “Wiring specificity in the direction-selectivity circuit of the retina,” *Nature*, vol. 471, no. 7337, pp. 183–188, Mar. 2011.

[54] M. Helmstaedter and P. P. Mitra, “Computational methods and challenges for large-scale circuit mapping,” *Curr. Opin. Neurobiol.*, vol. 22, no. 1, pp. 162–169, Feb. 2012.

[55] A. ZANKEL, B. KRAUS, P. POELT, M. SCHAFFER, and E. INGOLIC, “Ultramicrotomy in the ESEM, a versatile method for materials and life sciences,” *J. Microsc.*, vol. 233, no. 1, pp. 140–148, Jan. 2009.

[56] T. Müllner, A. Zankel, C. Mayrhofer, H. Reingruber, A. Höltzel, Y. Lv, F. Svec, and U. Tallarek, “Reconstruction and Characterization of a Polymer-Based Monolithic Stationary phase using Serial Block-Face Scanning Electron Microscopy,” *Langmuir*, vol. 28, no. 49, pp. 16733–16737, Dec. 2012.

[57] T. Koch, D. Salaberger, A. Zankel, H. Reingruber, A. Steiger-Thirsfeld, Y. Voronko, and S. Seidler, “Methods for Characterizing the 3-D Morphology of Polymer Composites,” *Macromol. Symp.*, vol. 315, no. 1, pp. 115–124, May 2012.

[58] A. Trueman, S. Knight, J. Colwell, T. Hashimoto, J. Carr, P. Skeldon, and G. Thompson, “3-D tomography by automated in situ block face ultramicrotome imaging using an FEG-SEM to study complex corrosion protective paint coatings,” *Corros. Sci.*, vol. 75, pp. 376–385, Oct. 2013.

[59] T. Hashimoto, M. Curioni, X. Zhou, J. Mancuso, P. Skeldon, and G. E. Thompson, “Investigation of dealloying by ultra-high-resolution nanotomography,” *Surf. Interface Anal.*, vol. 45, no. 10, pp. 1548–1552, Oct. 2013.

[60] G. E. Thompson, T. Hashimoto, X. L. Zhong, M. Curioni, X. Zhou, P. Skeldon, P. J. Withers, J. A. Carr, and A. G. Monteith, “Revealing the three dimensional internal structure of aluminium alloys,” *Surf. Interface Anal.*, vol. 45, no. 10, pp. 1536–1542, Oct. 2013.

[61] S. Wu, “A generalized criterion for rubber toughening - The critical matrix ligament thickness,” *J. Appl. Polym. Sci.*, vol. 35, no. 2, pp. 549–561, 1988.

[62] Q. Fu, Y. Wang, Q. Li, and G. Zhang, “Adding EPDM Rubber Makes Poly(propylene) Brittle,” *Macromol. Mater. Eng.*, vol. 287, no. 6, p. 391, Jun. 2002.

[63] Y. Wang, Q. Zhang, B. Na, R. Du, Q. Fu, and K. Shen, “Dependence of impact strength on the fracture propagation direction in dynamic packing injection molded PP/EPDM blends,” *Polymer (Guildf).*, vol. 44, no. 15, pp. 4261–4271, Jul. 2003.

[64] Y. Wang, Q. Fu, Q. Li, G. Zhang, K. Shen, and Y.-Z. Wang, “Ductile-brittle-transition phenomenon in polypropylene/ethylene-propylene-diene rubber blends obtained by dynamic packing injection molding: A new understanding of the rubber-toughening mechanism,” *J. Polym. Sci. Part B Polym. Phys.*, vol. 40, no. 18, pp. 2086–2097, Sep. 2002.

[65] D. Mileva, Q. Zia, and R. Androsch, “Tensile properties of random copolymers of propylene with ethylene and 1-butene: effect of crystallinity and crystal habit,” *Polym. Bull.*, vol. 65, no. 6, pp. 623–634, Sep. 2010.

[66] a. van der Wal, a. J. J. Verheul, and R. J. Gaymans, “Polypropylene–rubber blends: 4. The effect of the rubber particle size on the fracture behaviour at low and high test speed,” *Polymer (Guildf).*, vol. 40, no. 22, pp. 6057–6065, Oct. 1999.

[67] L. Huang, Q. Pei, Q. Yuan, H. Li, F. Cheng, J. Ma, S. Jiang, L. An, and W. Jiang, “Brittle–ductile transition in PP/EPDM blends: effect of notch radius,” *Polymer (Guildf).*, vol. 44, no. 10, pp. 3125–3131, May 2003.

[68] A. V. Shenoy and D. R. Saini, “Melt flow index: More than just a quality control rheological parameter. Part I,” *Adv. Polym. Technol.*, vol. 6, no. 1, pp. 1–58, 1986.

[69] H. Saechtlingen, K. Oberbach, and B. Meyer, *Kunststoff Taschenbuch*. Carl Hanser Verlag GmbH, 1995.

[70] T. Ganner, T. Aschl, M. Eibinger, P. Bubner, A. Meingast, B. Chernev, C. Mayrhofer, B. Nidetzky, and H. Plank, “Tunable mixed amorphous–crystalline cellulose substrates (MACS) for dynamic degradation studies by atomic force microscopy in liquid environments,” *Cellulose*, vol. 21, no. 6, pp. 3927–3939, Dec. 2014.

[71] R. F. Egerton, P. Li, and M. Malac, “Radiation damage in the TEM and SEM,” *Micron*, vol. 35, no. 6, pp. 399–409, Aug. 2004.

[72] A. Zankel, B. Chernev, C. Brandl, P. Poelt, P. Wilhelm, M. Nase, B. Langer, W. Grellmann, and H. J. Baumann, “Assessment of Beam Damage in Polymers Caused by

in situ ESEM Analysis using IR Spectroscopy," *Macromol. Symp.*, vol. 265, no. 1, pp. 156–165, May 2008.

[73] D. Drouin, A. Couture, D. Joly, X. Tastet, V. Aimez, and R. Gauvin, "CASINO V2 . 42 — A Fast and Easy-to-use Modeling Tool for Scanning Electron Microscopy and Microanalysis Users," *Scanning*, vol. 29, pp. 92–101, 2007.

[74] J. C. Russ, *The image processing handbook*, 5th editio., vol. 5. Boca Raton, Florida: CRC Press [u.a.], 2007.

[75] A. Buades, B. Coll, and J.-M. Morel, "Non-Local Means Denoising," *Image Process. Line*, vol. 1, pp. 490–530, Sep. 2011.

[76] J. Immerkær, "Fast Noise Variance Estimation," *Comput. Vis. image Underst.*, vol. 64, no. 2, pp. 300–302, 1996.

[77] G. Papari, N. Petkov, and P. Campisi, "Artistic Edge and Corner Enhancing Smoothing," *IEEE Trans. Image Process.*, vol. 16, no. 10, pp. 2449–2462, Oct. 2007.

[78] M. Čapek, J. Janáček, and L. Kubínová, "Methods for compensation of the light attenuation with depth of images captured by a confocal microscope," *Microsc. Res. Tech.*, vol. 69, no. 8, pp. 624–635, Aug. 2006.

[79] S. Sternberg, "Biomedical Image Processing," *Computer (Long. Beach. Calif).*, vol. 16, no. 1, pp. 22–34, Jan. 1983.

[80] T. Ferreira and W. Rasband, "ImageJ user guide," 2012.

[81] K. Zuiderveld, "Contrast Limited Adaptive Histograph Equalization," in *Graphic Gems IV*, San Diengo: Academic Press Professional, 1994, pp. 474–485.

[82] W. Niblack, *An Introduction to digital image processing*. Englewood Cliffs/N. J.: Prentice-Hall, 1986.

[83] R. R. Bouckaert, E. Frank, M. A. Hall, G. Holmes, B. Pfahringer, P. Reutemann, and I. H. Witten, "WEKA — Experiences with a Java Open-Source Project," *J. Mach. Learn. Res.*, vol. 11, pp. 2533–2541, 2010.

[84] VSG, "Avizo Reference Guide," 2012.

[85] F. Y. Shih and Y.-T. Wu, "Three-dimensional Euclidean distance transformation and its application to shortest path planning," *Pattern Recognit.*, vol. 37, no. 1, pp. 79–92, Jan. 2004.

[86] J. H. Rask, J. E. Flood, J. K. Borchardt, and G. a York, "The esem used to image crystalline structures of polymers and to image ink on paper," *Microsc. Res. Tech.*, vol. 25, no. 5–6, pp. 384–392, Aug. 1993.

Appendix

Macro for automated image segmentation

Initial MATLAB® program for filtering:

```
pfad='C:\\Users\nachtnebel\Desktop\Matlab_MAKRO\';      %path in form of:
'D:\\...\Matlab_MAKRO\'
stackname='Stack.tif';       %name of stack to filter 'NAME.tif'
n=4;      %Numbers of iteration for CLAHE

start=datestr(now, 'HH:MM:SS');
run([pfad,'Fiji.app\scripts\Miji.m']);
MIJ.run('Open...', ['path=[',pfad,stackname,']']);
z=MIJ.getCurrentImage;
slices=size(z,3);
MIJ.run('Non-local Means Denoising', 'sigma=4 smoothing_factor=1 stack');
MIJ.run('Non-local Means Denoising', 'sigma=4 smoothing_factor=1 stack');
MIJ.run('Non-local Means Denoising', 'sigma=4 smoothing_factor=1 stack');
MIJ.run('Non-local Means Denoising', 'sigma=4 smoothing_factor=1 stack');
MIJ.run('Kuwahara Filter', 'sampling=3 stack');
MIJ.run('Subtract Background...', 'rolling=150 light disable stack');
MIJ.run('Stack Contrast Adjustment', ' ');

a=MIJ.getCurrentImage;
MIJ.createImage('NLM', a, true);
MIJ.run('Save', ['Tiff..., path=[',pfad,'NLM.tif]']);

MIJ.run('Close All');
MIJ.exit
pause(60);
MIJ.start


MIJ.run('Open...', ['path=[',pfad,'NLM.tif]']);

for l=1:n      %4x
  MIJ.run('Set Slice...', 'slice=1');
    for k=1:slices   %4x CLAHE for every single image
      MIJ.run('Enhance Local Contrast (CLAHE)', 'blocksize=11
                        histogram=256 maximum=3 mask=*None*');
      MIJ.run('Next Slice [>]');
    end
  MIJ.run('Non-local Means Denoising', 'sigma=4 smoothing_factor=1
                  stack');
end

MIJ.run('8-bit');    %Niblack needs 8bit
MIJ.run('Auto Local Threshold', 'method=Niblack radius=300 parameter_1=0.1
            parameter_2=0 stack');
b=MIJ.getCurrentImage; %next three lines for saving
MIJ.createImage('NLM', b, true);
```

```
MIJ.run('Save', ['Tiff..., path=[',pfad,'NIBLACK.tif]']);
stop=datestr(now, 'HH:MM:SS');

MIJ.run('Close All');  %Memory Reset
MIJ.exit
```

Second MATLAB® program for segmentation:

```
pfad='C:\\Users\nachtnebel\Desktop\Matlab_MAKRO\';
run([pfad,'Fiji.app\scripts\Miji.m']);
MIJ.run('Open...', ['path=[',pfad,'NLM.tif]']);
c=MIJ.getCurrentImage;
e=zeros(size(c));    %zize of result stack WEKA
MIJ.run('Trainable Weka Segmentation');

for k=1:size(c,3)    %every single image (Memory limited)
  d=c(:,:,k);
  MIJ.createImage('NLM', d, true);  %select one image from stack

  MIJ.run('Trainable Weka Segmentation');
  IJ=ij.IJ();              %Makro2: load classifier
  macro_path=[pfad,'makro2.txt'];
  pause(2);              %Pause because of classifier time
                                      limitation
  IJ.runMacroFile(java.lang.String(macro_path));


  e(:,:,k)=MIJ.getCurrentImage;    %save single image in stack
  MIJ.run('Close All');
  MIJ.exit
  pause(5);
  MIJ.start

MIJ.createImage('NLM', e, true);    %create stack from variable e
MIJ.run('8-bit');
MIJ.run('Save', ['Tiff..., path=[',pfad,'WEKA.tif]']);
DateVector(k,:) = datevec(datestr(now, 'HH:MM:SS'));
end
save zeiten.mat DateVector;

MIJ.run('Open...', ['path=[',pfad,'NIBLACK.tif]']);
MIJ.run('8-bit');

IJ=ij.IJ();     %3 lines for makro: create 3-class stack
macro_path=[pfad,'makro3.txt'];
IJ.runMacroFile(java.lang.String(macro_path));

finish=datestr(now, 'HH:MM:SS');

start
stop
finish
```

used ImageJ Macros in the second MATLAB® program: Makro2

```
dir = File.directory + "classifier" + ".model"
call("trainableSegmentation.Weka_Segmentation.loadClassifier", dir);
call("trainableSegmentation.Weka_Segmentation.getResult");
```

Makro3:

```
selectWindow("WEKA.tif");
run('Invert', 'stack')
run('Erode', 'stack');
run('Erode', 'stack');
run('Erode', 'stack');
run('Erode', 'stack');
run('Erode', 'stack');

imageCalculator("Subtract stack", "NIBLACK.tif","WEKA.tif");
run('Invert', 'stack')
run('8-bit')
run("Analyze Particles...", "size=5-Infinity circularity=0.00-0.50 show=Masks stack");
run("Multiply...", "value=0.5 stack");
dir0 = File.directory + "CRACKS" + ".tif"
saveAs("Tiff", dir0);

run('Close All')
dir1 = File.directory + "NIBLACK" + ".tif"
open(dir1);
run('8-bit')
dir2 = File.directory + "CRACKS" + ".tif"
open(dir2);

imageCalculator("Subtract create stack", "NIBLACK.tif","CRACKS.tif");
dir4 = File.directory + "EPR" + ".tif"
saveAs("Tiff", dir4);
```